

N72-13391-415

NASA SP-282

W

**FIFTH AEROSPACE
MECHANISMS SYMPOSIUM
CASE FILE
COPY**

A symposium held at
GODDARD SPACE FLIGHT CENTER
Greenbelt, Maryland
June 15-16, 1970



NATIONAL AERONAUTICS AND SPACE ADMINISTRATION

FIFTH AEROSPACE MECHANISMS SYMPOSIUM

Proceedings of a conference held at
Goddard Space Flight Center
Greenbelt, Maryland
June 15-16, 1970

Prepared at NASA Goddard Space Flight Center



Scientific and Technical Information Office
NATIONAL AERONAUTICS AND SPACE ADMINISTRATION
Washington, D.C.

1971

FOREWORD

The Fifth Aerospace Mechanisms Symposium, held at the NASA Goddard Space Flight Center, Greenbelt, Maryland, on June 15-16, 1970, was sponsored by Goddard, the University of Santa Clara, and Lockheed Missiles & Space Company. The symposium brought together approximately 200 representatives from 66 organizations concerned with the use of mechanisms in space.

The organizing committee included Joseph V. Fedor and Bowden W. Ward, Goddard Space Flight Center; George G. Herzl and Alfred L. Rinaldo, Lockheed Missiles & Space Company; Richard K. Pefley and Stein Weissenberger, University of Santa Clara; and Marcus Comuntzis and Paul W. Bomke, Jet Propulsion Laboratory. The review panel for papers submitted at this symposium consisted of Stein Weissenberger; Joseph V. Fedor, Alfred L. Rinaldo, and George G. Herzl, chairman, who edited the submitted papers in cooperation with Mrs. Hope H. Guss of Goddard Space Flight Center.

Management representatives of the sponsoring organizations who gave active support and encouragement were John F. Clark, Goddard Space Flight Center; Wayland C. Griffith, Lockheed Missiles & Space Company; and Robert Parden, University of Santa Clara.

Additional assistance in preparing for this symposium was provided by Mrs. Alberta C. Moran and Richard W. Rice, Goddard Space Flight Center. They handled many of the details of the meeting.

The meeting was divided into four sessions with the following co-chairmen:

- | | | |
|------|----------------------------|--|
| I. | June 15, Morning Session | Frank T. Martin
Goddard Space Flight Center
Vladimir Chobotov
The Aerospace Corporation |
| II. | June 15, Afternoon Session | Raymond F. Bohling
NASA Headquarters
A. D. Galbraith
Lockheed Missiles & Space Company |
| III. | June 16, Morning Session | Bernard A. Kulp
Eglin Air Force Base
Kenneth S. Bush
Langley Research Center |
| IV. | June 16, Afternoon Session | F.R.E. Crossley
University of Massachusetts
Stein Weissenberger
University of Santa Clara |

A highlight of this symposium was the presentation by V. S. Syromyatnikov of the U.S.S.R. of the paper entitled "Docking-Mechanism Attenuator with Electromechanical Damper." Following this presentation, a movie entitled "Docking of the Soyuz IV and

V" was shown. The paper and the dialogue accompanying the showing of related slides are included in these *Proceedings*.

Another special feature of this symposium was a panel discussion, "Nutation Dampers." Members of the panel were Barry E. Tossman, Applied Physics Laboratory—Johns Hopkins University; Thomas M. Spencer, Ball Brothers Research Corporation; Peter R. Kurzhals, Langley Research Center; and Joseph V. Fedor, Goddard Space Flight Center. The moderator was George G. Herzl of Lockheed Missiles & Space Company. The introductory remarks and questions and answers are a part of these *Proceedings*.

Bowden W. Ward, Jr.
Symposium Coorganizer for
GSFC

CONTENTS

Foreword	iii
Opening Remarks <i>George G. Herzl</i>	vii
Opening Remarks <i>Donald P. Hearth</i>	ix

SESSION I

The Apollo Docking System <i>Kenneth A. Bloom and George E. Campbell</i>	3
Dynamic Behavior of the Mercury Damper <i>Prescott D. Crout and Horace L. Newkirk</i>	9
Aerospace Vehicle Separation Mechanisms Selection, Design, and Use Considerations <i>I. B. Gluckman</i>	17
Rotary Relay for Space Power Transfer <i>H. Theron Haynie</i>	25
Response Characteristics of a Thermal-Heliotrope Solar-Array Orientation Device <i>Frederick H. Morse</i>	33

SESSION II

Docking-Mechanism Attenuator With Electromechanical Damper <i>V. S. Syromyatnikov</i>	43
Damper Design From a Structural Engineer's Point of View <i>Jay C. Chen</i>	59
Thermomechanical Piston Pump Development <i>Eric E. Sabelman</i>	65

Panel Discussion: Nutation Dampers

Introduction to Passive Nutation Dampers <i>George C. Herzl</i>	73
Nutation Dampers for Single-Spin Satellites <i>J. V. Fedor</i>	83

Nutation-Damper Design for Dual-Spin Spacecraft <i>T. M. Spencer</i>	87
Low Nutation-Rate Dampers <i>Barry E. Tossman</i>	97
Nutation Dampers for Manned Spacecraft <i>Peter R. Kurzhals</i>	103

SESSION III

A Scanning Mirror System for the Apollo Telescope Mount Ultraviolet Spectroheliometer <i>C. O. Highman</i>	113
A Release Mechanism With Mechanical Redundancy <i>John J. Paradise</i>	121
Accelerated Vacuum Testing of Long Life Ball Bearings and Sliprings <i>C. R. Meeks, R. I. Christy, and A. C. Cunningham</i>	127
A Motor Canister Designed for Prolonged Operation in Space <i>A. Wells</i>	137
Effects of Energy Dissipation in the Bearing Assemblies of Dual-Spin Spacecraft <i>M. P. Scher</i>	143
Metal-Silicate Friction in Ultrahigh Vacuum <i>E. I. Ofodile and J. Frisch</i>	149

SESSION IV

Meeting the Challenge of a 50,000-Hour-Lifetime Requirement <i>Charles E. Vest and Philip A. Studer</i>	159
A Lightweight Bimetallic Actuator for Spacecraft Thermal Control <i>Keith L. Schilling</i>	165
The Apollo 11 Laser Ranging Retro-Reflector Array <i>John E. McCullough</i>	171
Development of Payload Subsystem-Primate Mission-Biosatellite Program <i>James F. Hall, Jr.</i>	177
The Mariner Mars 1971 Gimbal Actuator <i>G. S. Perkins</i>	185
Organizations Represented at the Fifth Aerospace Mechanisms Symposium	193
List of Attendees	195
Prior Symposia in This Series	199

OPENING REMARKS

George G. Herzl
Lockheed Missiles & Space Company
Palo Alto, California

Fellow Engineers and Scientists; Ladies and Gentlemen:

It is my pleasure to welcome you to the symposium on behalf of the University of Santa Clara, NASA Goddard Space Flight Center, and Lockheed Missiles & Space Company. We are pleased to have with us participants from over 50 organizations from the United States and abroad, representing various government agencies, universities, and industry.

If I were to use only one word to convey the very essence of aerospace mechanisms, the subject of this symposium, I would use the word "imagination." Franklin P. Jones said long before the advent of the space age that "Anyone who still thinks that the sky is the limit, has no imagination." This is certainly true of our profession today. I am not referring to inventing any new exotic design principles. Imagination should be applied primarily, in my opinion, to make mechanisms as simple as possible, which is by no means an easy task. It may sound paradoxical, but it is relatively easy to accomplish any spacecraft function by complex means, and the virtue of a good design is to accomplish the same in the simplest possible way. Aerospace mechanisms inherently lend themselves to this task, and we have some fine papers at this symposium that illustrate the point. The benefits associated with simplicity in design are numerous, to mention only reliability and cost. Ever since the inception of the space age we have been constantly aware of the unprecedented reliability requirement, and I do not want to belabor this aspect here. These days the economic factor in design is becoming increasingly important, and while this factor is quite painful at times, I daresay that this is all to the good. It will ultimately lead to wider use of mechanisms, since they will replace in many instances more complex electronic counterparts. The current pause in aerospace activity gives us also a chance to evaluate the accumulated experience and consolidate progress to date, so that we will be better prepared for the resurgence that will follow. This symposium is a part of this effort and our proceedings are one of the principal sources of information in our field.

This meeting deals exclusively with aerospace mechanisms and is the first of its kind to be held on the East Coast of the United States. Dr. John Clark and Dr. William Pickering suggested that NASA sponsorship of the symposium should alternate between various NASA centers. Consequently, this year the sponsorship has moved to NASA Goddard from JPL, and the next symposium will be cosponsored by NASA Ames Research Center, and will be held there in September 1971. We are very pleased with this arrangement since it will bring the symposium closer to more aerospace engineers. Another first at this symposium is a paper and the attendance of a delegation from the Soviet Academy of Sciences. We are confident that this interchange of ideas will benefit everyone concerned, and that it is only the beginning of a professional dialogue in our field which was until now nonexistent.

The papers that have been selected for presentation represent the latest state of the art in our field. They describe various types of aerospace mechanisms, and it is hoped that we

will get many ideas from one another and from one project to another. We are especially appreciative of the preparation effort and cooperation of the authors whose papers are presented in this volume.

In addition, special thanks for making the symposium possible are due to the Very Reverend Thomas Terry, S.J., President, University of Santa Clara; Dr. John F. Clark, Director, NASA Goddard Space Flight Center; and Dr. W. C. Griffith, Vice-President, Lockheed Missiles & Space Company. The contribution of all phases of the symposium organization and planning by Joseph V. Fedor and Bowden W. Ward of NASA Goddard Space Flight Center, R. K. Pefley and S. Weissenberger, of the University of Santa Clara; P. W. Bomke and Marcus Comuntzis of the Jet Propulsion Laboratory; and A. L. Rinaldo of Lockheed Missiles & Space Company are greatly appreciated, as are the efforts of Mrs. Hope Guss of GSFC in the editorial preparation of this publication.

OPENING REMARKS

Donald P. Hearth
Deputy Director
NASA-Goddard Space Flight Center
Greenbelt, Maryland

It is my pleasure to welcome you on behalf of the Goddard Space Flight Center to the Fifth Aerospace Mechanisms Symposium. It is fitting that we host this symposium because GSFC has a keen interest in aerospace mechanisms, as is evidenced by the many satellites using these devices—for example, the Explorer, OGO, Tiros, OSO and OAO series—that GSFC has launched.

It is with added pleasure that I recognize the international flavor of this symposium. We have here today attendees from many areas of the world: the Soviet Union, England, Canada, and the United States, representing industry, universities, and various government agencies.

The primary purpose of this symposium is to provide open discussion and interchange of ideas and experiences related to problems of aerospace mechanisms. The boundaries of space technology have been expanding at an ever increasing rate as more and more successful orbital flights and other space achievements have been recorded. As a result, the scope of the design principles, details, and applications with which the aerospace mechanism designer must be familiar has grown in variety, complexity, and volume. It is to these needs that this symposium is dedicated.

The response to the symposium call for papers this year has been the greatest in the history of the symposium. It is hoped that the papers selected for presentation will give a broad but balanced spectrum of topics in the aerospace mechanisms field. Further, it is hoped that the wide range of topics in the program will make this symposium as informative as previous ones. If the interchange of ideas and experiences at this symposium plays a role in preventing major problems or failure in a flight program, then the cost effectiveness of this symposium will be of the highest order.

SESSION I

**Session Cochairman
Frank T. Martin
NASA—Goddard Space Flight Center**

THE APOLLO DOCKING SYSTEM*

Kenneth A. Bloom
George E. Campbell
North American Rockwell Corporation
Downey, California

The Apollo docking system is the means by which the Apollo command and service modules (CSM) and the lunar module (LM) are connected and disconnected during a lunar-landing mission. The system incorporates a CSM probe assembly that mates with a drogue assembly on the LM. Twelve automatic latches mounted on the CSM docking ring provide for structural integrity between the vehicles and for tunnel sealing during crew transfer. This paper includes a functional description of the flight hardware and discusses the alternate concepts that were evaluated to determine the system best suited to Apollo requirements.

I. INTRODUCTION

In May 1962, the National Aeronautics and Space Administration (NASA) prepared a preliminary outline for space docking. It was determined that a lunar-landing mission could be achieved by a combination of two space vehicles: the command and service modules (CSM) and the lunar module (LM). After initial transposition and docking (CSM to LM/S-IVB), the LM would undock in lunar orbit, descend to the moon, return to orbit, and redock with the CSM.

II. DESIGN CRITERIA

Through the use of a NASA-sponsored simulator program, the following docking vehicle parameters were established. These form the basic design criteria for the system:

(1) Initial contact-limit velocities

Axial velocity:	0.1 to 1.0 fps
Lateral velocity:	0.0 to 0.5 fps
Angular velocity:	0.0 to 1.0 deg/s

(2) Final contact-limit velocities (structure to structure)

Axial (transposition):	0.15 fps
Axial (lunar):	0.35 fps
Lateral and angular:	0.00 fps

(3) Allowable misalignment at initial contact

Radial:	1.0 ft
Angular:	10 deg
Rotational:	10 deg

III. ALTERNATE DESIGN CONCEPTS

On the basis of preliminary analysis and design studies, the decision was made to evaluate two basic docking concepts: extendable-tether and impact. Four extendable-tether systems and one impact system (center probe and drogue) were designed and evaluated. In addition, a NASA-designed ring-and-cone system and the Gemini docking system were evaluated.

A. Extendable-Tether Systems

The extendable-tether systems selected for design and evaluation included (1) the inflatable probe, (2) the stem, (3) the stem and cable, and (4) the inflatable tunnel. Each of these systems employed an LM-mounted drogue and provided for visual observation of latching. In each system, retraction was provided by a motor-driven reel.

1. Inflatable probe. The extendable-tether concept employed an inflatable tube to engage in the drogue. The tube was 4 in. in diameter and approximately 20 ft long. The inflating gas was expended as the probe was reeled in, bringing the vehicles together.

*This research was supported by NASA Contract NAS9-150.

2. Stem. The probing member in the concept was constructed of sheet metal and heat treated in the rolled position. When the sheet metal was released from the reel upon which it was wound, it formed a tube that had the structural characteristics of a seamless tube of the same diameter. The tube was then manually directed into the drogue from the crew compartment.

3. Stem and cable. The concept employed the same structural probing member as did the stem system, but it also included a cable within the tube to provide a single-cable tether after retraction of the tube.

4. Inflatable tunnel. A retractable tunnel or airlock permitted crew transfer without removal of equipment. The tunnel was inflated to approximately 5 psi, enhancing dynamic stability at initial contact.

B. Impact Systems

The impact systems selected for design and evaluation included (1) the center probe and drogue, (2) the ring and cone, and (3) the Gemini. Each of these systems employed a crew optical sight for alignment at initial latching.

1. Center probe and drogue. The initial design of this system included an air/oil attenuation capability in the center piston and three piston pitch bungees. The final design incorporated air/oil attenuation in pitch bungees instead of in the center piston. A drogue with latches to engage the probe head was installed in the LM. The final design required that the latches be placed in the probe head to reduce the weight of the LM. Pitch arms were included to provide centering of the drogue during retraction. Retraction was accomplished by an electrical reel mechanism.

2. Ring and cone. A 34-in.-diameter ring supported by air/oil attenuators located on the CSM was incorporated in this design. The ring was centered by a cone on the LM, and retraction was accomplished by reeled cables.

3. Gemini. In contrast to the ring-and-cone concept, this configuration incorporated an attenuation system located on the cone. This design was used successfully for the Gemini docking mission.

IV. COMPARISON OF DESIGN CONCEPTS

Two test vehicles were designed and built to permit comparison of the preliminary design concepts. Each vehicle was supported by air bearings to simulate docking vehicles. Comparable masses and inertias of the CSM and LM with simulated reaction-control-system (RCS) thrusting were scaled in proportion to the flight vehicles. The test incorporated full-scale docking hardware for the four extendable systems and the center probe and drogue system.

In addition to the vehicle testing operation, a two-dimensional mathematical analysis was performed to define the dynamic characteristics of all the systems. Unlike the simulator test, this analysis included the ring-and-cone system and the Gemini system. After completion of all evaluation and studies, the center probe and drogue system was recommended to NASA for Apollo docking. Although this system required an increase in crew effort, it was selected because it required minimum change to the basic vehicle structure, had lowest system weight, and demonstrated superior dynamic characteristics and latching capability.

V. FUNCTIONAL DESCRIPTION

The requirements imposed on the center probe and drogue concept dictated a functionally integrated design. These functions and the components that provide them are described in the following paragraphs.

A. Initial Vehicle Coupling

Initial vehicle coupling is achieved by means of a latch mechanism in the probe head and a drogue in the LM. The probe head, which is self-centering and is gimbal mounted to the probe piston, contains three spring-loaded capture latches. As the probe head bottoms in the drogue socket, the latches depress and automatically return to engage the opening in the socket. A trigger link at each latch is held depressed by the socket opening, allowing a spring-loaded spool to move forward and maintain a toggle linkage in an over-center locked position.

Release of the capture latches at undocking is accomplished by electrically energizing tandem-mounted dc torque motors located in the center piston. Release operation can be accomplished manually from either of

the docked vehicles. Release from the LM is accomplished by depression of the locking spool through an open hole in the probe head; release from the CSM is accomplished by rotation of a release handle at the back of the probe to rotate the motor torque shaft manually. The latches are designed to support a tension load under a probe preload of 10,000 lb.

The receiving end of the probe-head capture latches is a truncated-cone structure mounted in three support fittings in the upper end of the LM tunnel. It consists of a 1-in.-thick aluminum honeycomb core, bonded front and back to aluminum face sheets. The main tripod support structure interfaces with three tunnel mounting supports, one of which houses a simple locking lever to prevent drogue rotation.

The drogue structure, designed to a control weight of 20 lb, must withstand a probe-head impact load of 4700 lb at any point on its inner face sheet.

B. Shock Attenuation and Vehicle Centering

A centering beam is attached at one end to the probe center piston and at the other end to a sliding link and yoke, which are attached to the cylinder collar. A hydraulic shock attenuator also attaches to the centering beam and the collar between the piston attach point and the sliding link. This linkage is duplicated radially around the probe at three places 120 deg apart. As the center piston is compressed, the beam and link act as a simple lever to compress the attenuator. At the same time, through its kinematic displacement, the linkage expands to mate with the drogue cone and provide vehicle centering.

Individual contact by the drogue on one or two beams is attenuated by direct compression of the independent attenuator and sliding link.

The shock attenuators are air/oil fluid-displacement dampers. Damping is effected by means of a velocity-sensitive fluid restrictor located in the attenuator piston head. Each attenuator is hermetically sealed by a nesting metal bellows. Argon and helium are used to fill the bellows and compensator piston cavities. When compressed, this air spring provides a nominal 400-lb extension force in each attenuator. This stored energy aids the probe center spring in providing vehicle separation force at undocking.

C. Retraction

After the initial capture and stabilization of the vehicles, a closing force of 1000 lb minimum is created by the probe to draw the vehicles together. This force is generated by gas pressure reacting on the center piston within the probe cylinder. The pressure is created by a dry-nitrogen-gas system located inside the probe cylinder. The system consists of four hermetically sealed pressure vessels, each containing 6 in.³ of dry nitrogen gas at 5000 psi. Each vessel is capable of producing the 1000-lb retraction force.

The system is activated by electrically energizing an explosive initiator, which drives a small piercing piston through a sealed diaphragm in the throat of the pressure vessel. Internal porting in a common manifold allows high-pressure gas flow from the selected vessel to pass through the manifold and be regulated to a reduced flow and pressure in the cylinder.

D. Structural Connection

Twelve automatic locking latches are located radially around the inner surface of the CSM docking ring. The latches are self-contained, spring-energy devices, individually actuated by the closing motion of the two vehicles as they are being drawn together. Actuation of the latch and engagement of the LM ring is fully automatic, and crew operation is required only for manual disengagement of the latch before undocking.

Each latch is designed to withstand an ultimate tension load of 12,000 lb. The mechanism also must create a nominal draw-down force of 3000 lb within a total hook axial stroke of 0.150 in. This hook displacement stroke allows for maximum waviness at the sealing interface resulting from temperature/pressure distortion of the mating structures. Maximum manual operation force is limited by design to 40 lb.

E. Probe and Drogue Removal and Installation

A foldable probe assembly permits intravehicular crew transfer. Folding is accomplished by release of a single lock, providing an umbrella-like telescoping action; at lock release, the three support beams attached to a sliding collar retract from their sockets in the tunnel and fold into a smaller diametrical package. Folding is induced by the air-spring extension force of the three attenuators, which are attached to the sliding collar.

The mechanism that accomplishes probe installation is similar to an automobile bumper jack, and installation is achieved through approximately 20 pump strokes of the handle. Maximum handle force is 50 lb.

Removal of the drogue is accomplished by rotation of a locking lever in the support mount, which allows the drogue to rotate out of its sockets. Installation is accomplished in reverse order with the aid of ramps in the tunnel that guide the drogue into the support fittings.

F. Separation

An automatic extend latch attached to the probe cylinder body engages and retains the probe center piston in the retracted position. The mechanism is spring loaded for automatic engagement with a clevis roller on the probe-head collar and is remotely released by energizing dual rotary solenoids mounted on the mechanism housing.

Before vehicle separation in lunar orbit, manual cocking of the 12 ring latches must be accomplished. The separating force from the internal pressure in the tunnel area must now be transmitted from the ring latches to the probe and drogue. This balancing of load and the maintenance of interface sealing integrity require that the probe and drogue be preloaded through the capture latch/drogue interface.

This preload is accomplished by a manually operated torque shaft, supported at the side of the cylinder and incorporating a single-unit handle and torque-limiting clutch mechanism splined to the torque shaft. At the extend latch end of the torque shaft is an acme-threaded screw for translation of the latch while torque is applied to the shaft. The clutch limiter is preset to release at a torque that provides a nominal 6000-lb tension load at the latch.

G. Launch Abort

In event of a vehicle launch abort, the docking system must be separated from the CM to provide clearance for parachute deployment and subsequent recovery conditions. This separation capability is provided by connection of a passive tension link to the boost

protective cover and to the probe head by means of shear pins located in the probe head. For normal launch escape-tower jettison, the pins are sheared at the probe head, and the ring containing the probe and latches, is left intact. In an abort mode, the docking ring, including the probe and latches, is separated by an explosive charge ignited simultaneously with ignition of the launch-escape motors. The docking system then is allowed to separate with the boost protective cover.

H. System Testing

Parallel to the structural/operational development program was a program involving the astronauts and their ability to understand and operate the docking mechanism. The first real test of a man's ability to work a mechanism such as this in a zero-g environment was simulated in a one-g environment with the aid of mockups involving counterbalances. The initial probe and drogue design involved the use of special tools already provided in the astronaut tool kit. The number and complexity of the tasks to be performed proved to be too great an effort for the crewmen, and the design was modified. Integral handles for all operations were then provided, and better methods for simulating the zero-g operations were initiated. NASA established a water-immersion facility and scheduled a zero-g flight program using a KC-135 airplane. Use of the water-immersion facility established acceptable operating handle forces, and the zero-g flight program provided an operational environment similar to that of actual flight.

The Apollo docking system was qualified for flight through testing that verified the structural and functional capabilities of the system in mission flight environments. Facilities for testing dynamic capability included (1) a pendulum test facility using simulated vehicles with actual spacecraft masses and inertias and (2) a dynamic-docking test device using a closed-loop analog system with force feedback to simulate vehicle masses, inertias, and dynamics in a six-deg relative-motion system. Structural capability was verified also by loads generated from a three-dimensional mathematical mode and applied in a static condition. Mission environments were imposed on the docking hardware based on its actual position relative to the spacecraft. The system, in its final spacecraft configuration (Fig. 1), successfully completed all qualification test programs before the first docking-mission flight on 4 March 1969.

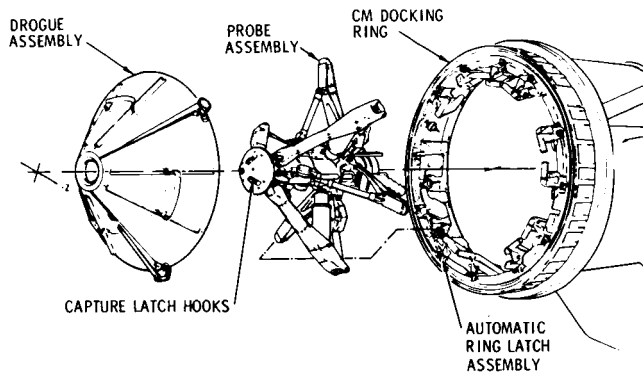


Fig. 1. Probe and drogue docking configuration

VI. CONCLUSION

Design of the Apollo docking system combined practically all the disciplines of mechanical engineering. Extensive system testing and actual spacecraft flight have proved the reliability of this merger. Operation of the mechanism in a previously unknown environment has proved no problem to a spacecraft crew. Man's first attempt to provide a mechanical interface in space and to transfer through it has been successfully accomplished. We are hopeful that the knowledge gained in the design and operation of the Apollo docking system will benefit future space programs.

DISCUSSION

Ray Bohling:

It wasn't clear to me just how the drawdown occurred. Were you depending on the propulsion force pushing the vehicles together or, after contact, on the mechanism actually pulling the vehicles together?

Campbell:

We are actually using the nitrogen-pressure retract system to draw the vehicles together. At the time capture latch is obtained, the crew receives a signal indicating capture and then initiates a switching circuit which fires the retract system.

Bohling:

I had missed the latching sequence.

Maitland McLarin:

I noticed you described the energy absorption mechanisms but you omitted rotational energy. Is there a mechanism to absorb this?

Campbell:

We do not absorb rotational energy. That's a good point. The head of the probe actually swivels freely. When the vehicles dock, they have a target alignment of 10 deg relative misalignment between the vehicles. We have run actual simulated tests at McDonnell-Douglas that show the vehicles closing. And we did actually impose rotation at the interface, proving there was no damage to the seals even if the vehicles were rotating at the point of interface contact. But we do not attempt to dampen rotary energy.

George Herzl:

Would you please describe the difference between the Apollo docking mechanism and the Gemini-Agena docking mechanism?

Campbell:

Essentially, the Gemini configuration was a large truncated cone which had a hexagonal array of six attenuators mounted on this cone section. This mechanism was mounted on the Agena. You can picture a much larger unit than we have, a truncated cone with a hexagonal array of shock attenuators supporting that.

The Gemini then docked directly into that truncated cone. All the energy was attenuated. And the drawdown was actually made through the cone. That system, by the way, weighs close to 500 pounds.

Norman Mayer:

On one of the Apollo flights there was considerable discussion during a docking operation concerning the rotational alignment. I had the impression, without investigating, that part of this was because the latches had not worked properly or the alignment was close to the marginal limits. Could you elaborate on that?

Campbell:

I hope I can without involving too long a discussion. The problem you speak of was on Apollo 10. I think it was spacecraft 106. And this gets into another area, but at the time of undocking, just prior to the LM separating and going to the moon, the crew was in the LM vehicle. By standard procedure, the crewman in the command module preloads the probe, which I haven't described because it's another subject. He makes a nut and bolt out of the probe, which essentially balances the internal pressure that's in the tunnels. Then he goes around to the 12 docking-ring latches and manually unlocks those.

At that time, the only mechanism holding the two vehicles together under pressure is the preloaded probe. It is preloaded to a 6000-pound load through a screw-jack mechanism on the side

of the probe. What NASA had elected to do at separation was to actually do a hot-gas fire check of the LM engines. Now, we were not aware of this requirement in rotation. When they did that the CSM was hanging onto the LM with the preloaded probe and they were doing a hot-gas firing of the LM which is intended to rotate the interface, which it did by some 2 or 3 deg. This had really no effect on the ability to separate.

At the time I think the concern was, at least from my standpoint, if the LM were to sit out there and keep spinning, it could eventually damage the interface seals. But the degree of rotation, as it turned out, was not critical. I hope I have answered your question.

Member of the audience:

What supplies power for the extension operation?

Campbell:

If I wasn't clear on that, it was my fault. Power for the extension is supplied by a large Elgiloy wire internal spring which provides fully automatic extension at the release of the extend latch.

The only function of the torque motor is to unlock the capture latch from the drogue.

DYNAMIC BEHAVIOR OF THE MERCURY DAMPER*

Prescott D. Crout
Massachusetts Institute of Technology
Consultant, U.S. Naval Weapons Center
China Lake, California

Horace L. Newkirk
U.S. Naval Weapons Center
China Lake, California

The dynamic behavior of the mercury nutation damper is investigated. Particular attention is paid to the eccentric annular mercury configuration, which is the final continuous ring phase that occurs in the operation of all mercury dampers. In this phase, damping is poorest, and the system is closely linear.

During the investigation, the hydrodynamic problem is treated as three dimensional, and extensive use is made of a variational principle of least-viscous frictional power loss. A variational principle of least-constraint is also used to advantage. Formulas for calculating the behavior of the mercury damper are obtained.

Some confirmatory experiments were performed with transparent ring channels on a laboratory gyroscope. Selected movie frames taken during wobble damping are shown along with the results of film measurements.

I. INTRODUCTION

The purposes of the present investigation are to examine the dynamic behavior of the mercury damper and to devise means for calculating this behavior. Since mercury dampers can operate in several different ways, depending upon the mercury configuration, the nature of the inner free surface, and the state of turbulence, and since any given damper operates in at least two very different manners, the overall behavior of a mercury damper may appear to be both complex and peculiar.

Any mercury damper acts more effectively when the mercury forms a broken ring rather than a continuous

ring. It follows that the transition from a broken ring to a continuous ring, which always occurs during the damping of spacecraft nutation, corresponds to a transition from a more effective to a less effective action of the damper. It is particularly important that the behavior of the damper in this unfavorable "continuous-ring" case be analyzed, and a considerable portion of this paper is devoted to this analysis. The more favorable "broken-ring" case is also treated; however, it is very much simpler than the unfavorable case just mentioned.

The viscous frictional power loss in the mercury is of primary importance in the elimination of the precession, or wobble. This loss satisfies a minimum principle that constitutes a powerful tool for the determination of the velocity distribution in the mercury and hence for the determination of the power loss itself. The pressure distribution is determined by another variational principle—the principle of least constraint—which is devised for this purpose.

*This paper is a comprehensive outline of the report by P. D. Crout entitled, "A Theoretical Investigation of the Dynamic Behavior of the Mercury Damper," U.S. Naval Ordnance Test Station (now U.S. Naval Weapons Center), China Lake, Calif., NAVWEPS Report 8611 and NOTS TP 3635, Nov. 1964, together with a description of some experimental results obtained by H. L. Newkirk.

When the wobble is small and the mercury is in the unfavorable continuous-ring configuration, the system is approximately linear and the wobble dies out exponentially. This is not true when the wobble is larger and the mercury is in the broken-ring configuration, in which case the wobble decreases parabolically. In both cases, however, specific formulas are obtained for the calculation of the behavior of the system.

II. MECHANICAL SYSTEM: ACTION OF THE DAMPERS

A mercury nutation damper consists of a circular channel, or race, partially filled with mercury. Two such dampers are mounted with their planes perpendicular to the axis of symmetry of the main spinning body, as shown in Fig. 1. The translational effects of two dampers on the main spinning body cancel each other, whereas the rotational effects add. Let A be the moment of inertia of the main body about the axis of symmetry, and B be the moment of inertia about a transverse axis through the center of gravity. We suppose that $A > B$; hence, the precessional angular velocity β is greater than the spin velocity v and is closely approximated by $A v / B$.

It will suffice to consider one of the two dampers: Looking down upon the upper damper and observing the system from reference axes that rotate with the precessional angular velocity β counterclockwise about the precession axis, we see the eccentric annular mercury configuration as shown in Fig. 2a, if the wobble is sufficiently small and if we (temporarily) neglect the friction between the mercury and the channel. The precession axis and the spin axis intersect the plane of the damper at points W and S , respectively.

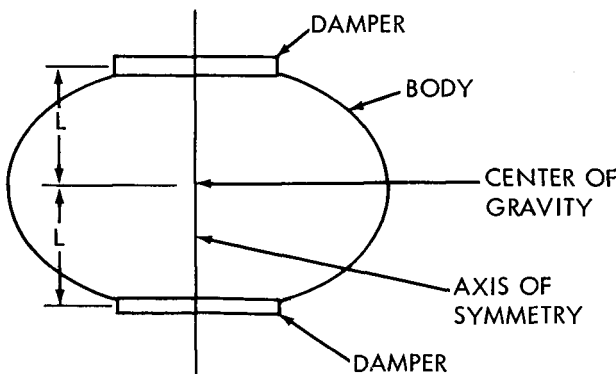


Fig. 1. Schematic diagram of main body and dampers

The mercury appears to be stationary, and the channel wall appears to be rotating clockwise with an angular velocity $(\beta - v)$. If we gradually "turn on" the friction between the mercury and the channel, the mercury configuration tends to be dragged clockwise, as indicated in Fig. 2b, and in this configuration the mercury will appear to flow clockwise.

In the calculation of the force exerted by the mercury upon the channel, and hence upon the main body, the fact that the observations are made from a rotating reference system is accounted for by the introduction of a centrifugal force field and also a Coriolis force field. This force is due to the centrifugal force field alone; its line of action passes through W , and its magnitude is the same as the centrifugal force acting

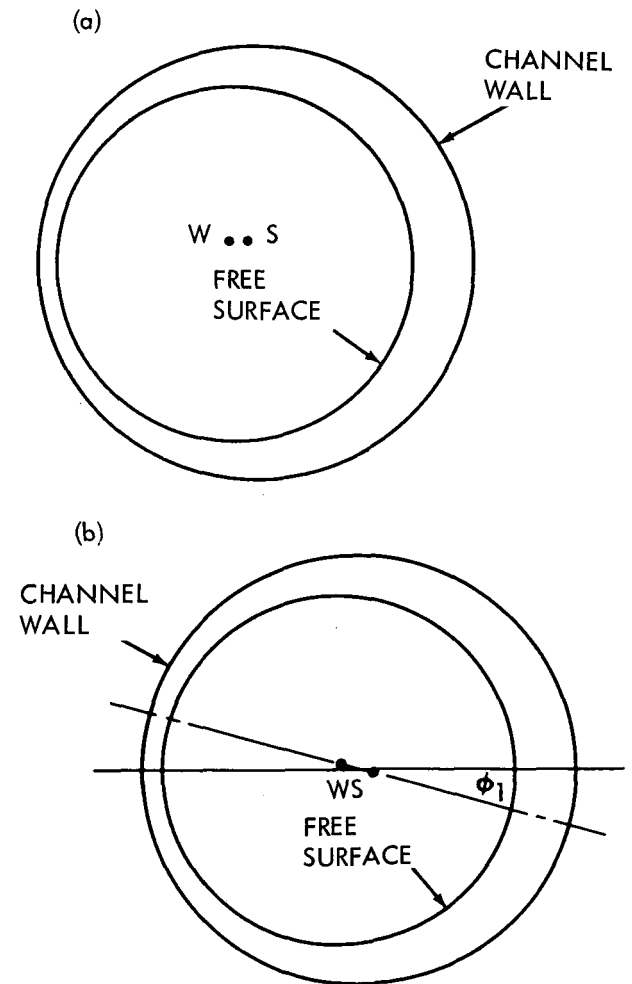


Fig. 2. Mercury configurations seen from rotating axes

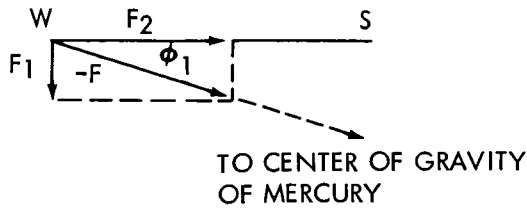


Fig. 3. Component forces exerted by mercury on channel

upon a mass point of mass M equal to that of the mercury, located at the center of gravity of the mercury and rotating about W with an angular velocity β . The force system is indicated in Fig. 3, where the magnitudes of the force components F_1 and F_2 are $(-My_0\beta^2)$ and $Mx_0\beta^2$, respectively, and x_0 and y_0 are the coordinates of the center of gravity of the mercury with respect to x - and y -axes having W as the origin and WS as the positive x direction. If we denote WS by ξ , a measure of the wobble, and time differentiation by a dot, it follows that the velocity component of W toward S is

$$-\dot{\xi} = \frac{-2My_0\beta^2L^2}{Av} \quad (1)$$

which gives the rate of decrease of the wobble. Expressions are also obtained for the rate of increase of the spin velocity and the decrease in the precessional velocity. However, x_0 and y_0 have yet to be determined.

III. RELATION OF THE VISCOUS FRICTIONAL POWER LOSS TO THE DAMPING: MINIMUM PRINCIPLE

The viscous frictional power loss P is $-My_0\xi\beta^2(\beta-\nu)$, which in the above expression gives

$$-\dot{\xi} = \frac{2PL^2}{Av\xi(\beta-\nu)} \quad (2)$$

from which we see that the viscous frictional loss P is the primary factor in the determination of $\dot{\xi}$ and hence in the elimination of the wobble.

Because the mercury is incompressible, the flow that we observe from our rotating reference system is

essentially stationary and may be considered to be composed of an infinite number of closed elementary tubes of flow, as indicated in Fig. 4. It is next proved rigorously that if the flow is stationary, and if the shape of the velocity field is held fixed so that the lines and tubes of flow are unaltered, then the flow will distribute itself among the various tubes in such a way that the viscous frictional power loss is a minimum. It is required only that the actual surface boundary condition be satisfied—that is, the velocity of the fluid must be that of the channel at the solid boundary surface provided by the channel. This minimum principle is extended to apply not only to the actual field of flow, but also to the field that results when the shape of the velocity field is altered by constraints.

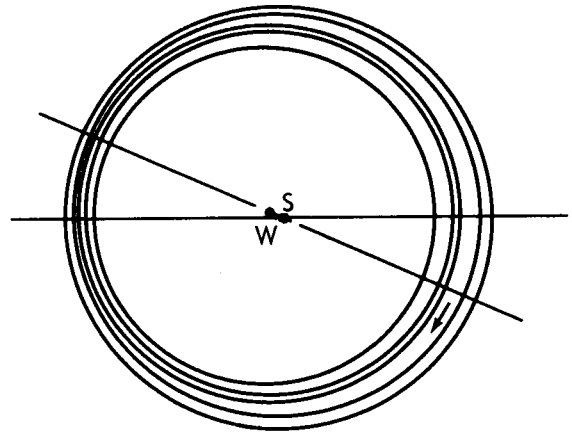


Fig. 4. Tubes of flow of mercury

IV. APPLICATION OF THE MINIMUM PRINCIPLE: DETERMINATION OF THE VELOCITY FIELD

The shape of the velocity field is specified closely by the relation

$$r = r_2 - \lambda(r_2 - a) - \lambda^2 b \left[1 - \left(\frac{z}{z_1} \right)^2 \right] \cos \theta \quad (3)$$

where λ is a parameter and the other quantities are as indicated in Fig. 5. Each line of flow is very nearly circular and, for a given height z and parameter λ , is expressed in polar coordinates. The worst eccentricity (shift in position of center) is b . The lines $z = \pm z_1$ and $\lambda = 0$ correspond to the solid boundary surfaces, and

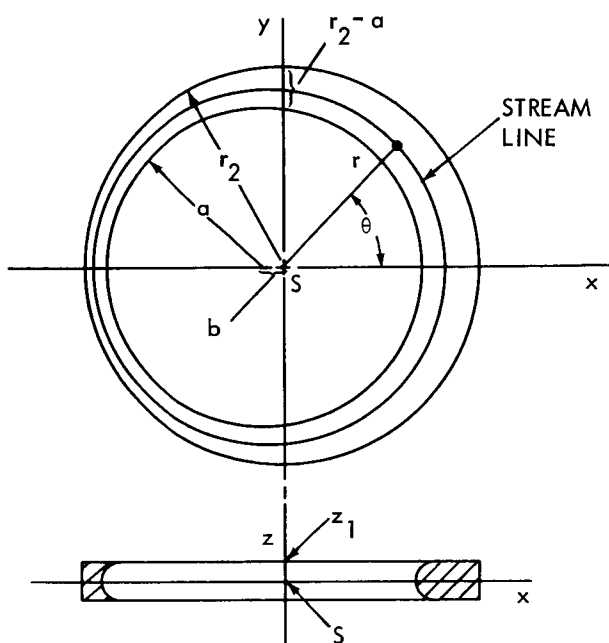


Fig. 5. Quantities used to specify velocity fields

$\lambda = 1$ corresponds to the inner free surface of the mercury. We note that at the solid bounding surfaces the fluid moves with the channel, and the eccentricity of the lines of flow is zero. It is also true that a is the radius of the inner free surface with no wobble.

We obtain a tube of flow corresponding to $d\lambda dz$ whose cross section is an elementary parallelogram that varies in shape as θ varies from 0 to 2π . Since the shape of the velocity field has been completely specified, the volume of mercury that flows per second in any $d\lambda dz$ tube can be expressed in terms of the velocity function $q(\lambda, z)$ as $q(\lambda, z)d\lambda dz$. The viscous frictional power loss P is now expressed in terms of $q(\lambda, z)$, after which $q(\lambda, z)$ is determined by the minimum principle. It is convenient to express $q(\lambda, z)$ as a Maclaurin series in b , which contains no odd-power terms.

V. DETERMINATION OF THE PRESSURE FIELD: PRINCIPLE OF LEAST CONSTRAINT

Having thus determined the velocity field and P , we next integrate the flow equation along a tube of flow and thereby determine the pressure in that tube, except for an additive constant which may be denoted by

$\psi(\lambda, z)$ because it depends upon the tube and hence upon λ and z . For any such function the resultant pressure field and also the velocity field, whose shape we specified, may be considered to be the ones actually obtained, provided that one introduces a suitable distribution F of body force and a distribution F_s of excess pressure over the free surface. F_s plays the role of a constraining surface. $F \equiv 0$ for the true fields; hence, by minimizing the constraint, which we define to be $\int_v F^2 dv$ taken throughout the volume of the mercury, we determine $\psi(\lambda, z)$ except for an unknown additive constant c_0 . Similarly, $F_s \equiv 0$ for the true fields; hence, by calculating F_s from the known internal and external pressure and the surface tension we minimize the "surface constraint," which we define to be $\int_a F_s^2 da$ taken over the free surface, and thereby determine c_0 and b . This completes the determination of the dynamic behavior of the mercury for a given wobble ξ .

In particular, we now know P , the viscous frictional power loss; hence Eq. (1) becomes

$$-\dot{\xi} = \frac{k_x L}{Av} \xi \quad (4)$$

in which the coefficient of ξ is a known constant. It follows that ξ , and hence the wobble, ultimately dies out exponentially with a damping factor

$$\alpha = -\frac{k_x L}{Av} \quad (5)$$

In addition, expressions are obtained that give the decrease in precessional velocity and the rate of increase of the spin velocity.

VI. CASE WHERE THE MERCURY CONFIGURATION IS CRESCENT-SHAPED

We shall next consider the case where the mercury is crescent-shaped (broken-ring configuration) and completely fills an angle $2\theta_m$ of the channel, with the flow being turbulent. Instead of Fig. 5 we now have the mercury configuration of Fig. 6. Expressions for the mercury volume and the off-center distance x of the center of gravity are now easily obtained in terms of r_1 , r_2 , z_1 , and θ_m .

If we observe the system as before, from axes that rotate counterclockwise with a precessional angular

velocity β , we see the configuration shown in Fig. 7. Taking moments about S , we obtain

$$|F_1| \xi = K_0 r_m^3 (\beta - v)^2 \quad (6)$$

Here, r_m is the mean radius of the mercury, and $r_m(\beta - v)$ is the velocity of the mercury relative to the channel. K_0 is a coefficient obtained from Chezy's formula. This coefficient depends upon the shape of the channel, the area of the surface of contact of the mercury with the channel, and the density and viscosity of the mercury.

Expressions for the three components of the torque exerted by the two dampers on the main body now follow directly, together with the relation

$$\sin \phi = \frac{K_0 r_m^3 (\beta - v)^2}{M \beta^2 \bar{x} \xi} \quad (7)$$

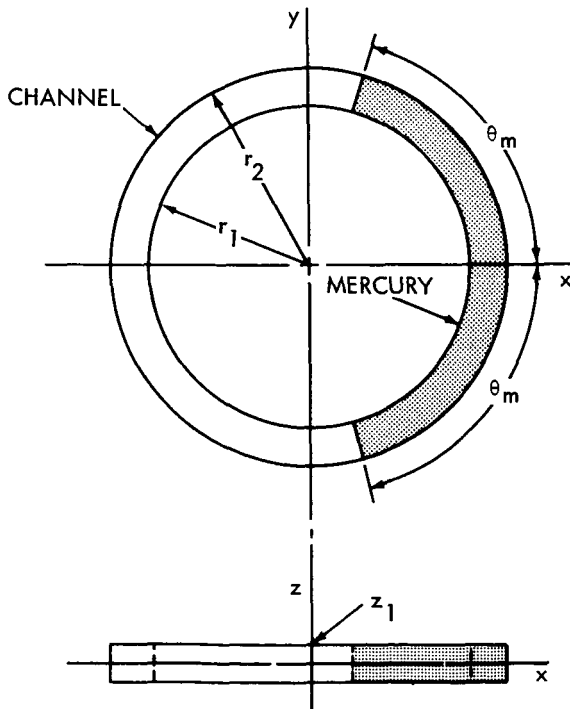


Fig. 6. Broken ring configuration

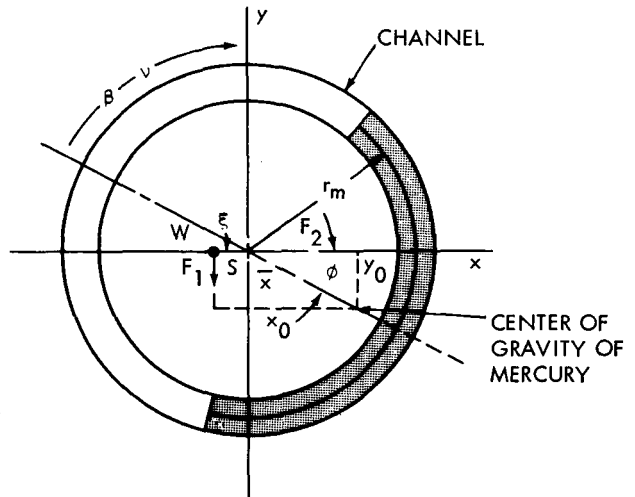


Fig. 7. Broken ring configuration seen from rotating axes

which determines ϕ . It follows from the expression for the x component of torque that

$$(Av - 2B\beta)\dot{\xi} = \frac{2L^2 K_0 r_m^3 (\beta - v)^2}{\xi} \quad (8)$$

which gives for the value of ξ at time t

$$\xi = \sqrt{\xi_0^2 - \frac{4L^2 K_0 r_m^3 (\beta - v)^2}{2B\beta - Av} t} \quad (9)$$

where ξ_0 is the initial value of ξ . Expressions are also obtained for the rate of increase of the spin velocity and for the decrease in the precessional velocity.

VII. CONCLUSIONS FROM THE THEORY

In addition to the fact that formulas have been obtained that enable us to calculate the dynamic behavior of the system for both the eccentric annular and the crescent-shaped (broken-ring) configurations, several other results are immediately evident from the above analysis. First, we see from Eq. (9) that, as the wobble ξ decreases during the course of the damping,

the smallest value of ξ that is compatible with the crescent configuration is that which renders $\sin \phi = 1$ in Eq. (7), i.e., $\phi = \pi/2$. For smaller values of ξ the configuration becomes eccentric annular. Second, we see from Eqs. (5) and (9) that, whereas ξ decreases exponentially for the eccentric annular configuration, it decreases parabolically for the crescent configuration, as shown in Fig. 8. The rate of damping increases as ξ decreases, and is greatest just before the crescent flow breaks and goes over into the eccentric annular. Finally, because the first part of the curve of ξ versus t is a parabola which is concave downward and the last part of the curve is a damped exponential which is concave upward, and because there is an intermediate part of this curve for which the flow is eccentric annular, but very eccentric, the ξt curve has a point of inflection if it is differentiable. In any case the curve can be approximated by a straight line over an appreciable range. Such a line is shown dotted in Fig. 8.

VIII. EXPERIMENT

A test of the theoretical analysis was performed with a bench-model gyroscope that had been used as a development tool for a twin-pendulum nutation damper used in the NASA AE a and b satellites. The results of this test provide qualitative confirmation of the theoretical results.

Fig. 9 shows the general nature of the gyro and a few frames of a movie of one of the mercury damper units tested on the gyro. The gyro is spun by twisting the

spindle by hand, by which manner an angular velocity of 6 to 8 rev/s is achieved. The total gyro weighs 1100 g (about 2-1/4 lb) and the mercury in the channel weighs 6.5 g. The bearing, located inside the gyro, consists of a U-joint with one shaft fixed to the upright support and the other to the spin bearings in the gyro body. Precision miniature ball bearing assemblies are employed, and these must be in top condition. Careful adjustments are made until the three bearing axes cross at a point on the gyro axis of symmetry. Coasting times in air are of about 15-minute durations so that the spin can be considered constant in a test requiring a few seconds. The two large rings around the body are copper. They are threaded onto the cylindrical aluminum body and held firmly in place by steel lock rings. The heavy copper rings can be screwed up or down to move the center of gravity along the symmetry axis and also to adjust the transverse moment of inertia. In the tests the moment ratio was $A/B = 1.22$.

The circular channel, or ring, containing the mercury was made of a transparent plastic disc bolted to the top of the gyro. Only one ring was used and not two symmetrically disposed, as in the theoretical development. Several discs were prepared, each having a channel of different rectangular cross-sectional dimensions, radial width, and thickness. However, all had the same cross-sectional area and outside radius.

Nutation was induced by a blow from a smooth pencil at the top of the spindle, as shown in the movie frames. The mercury appears light over the black

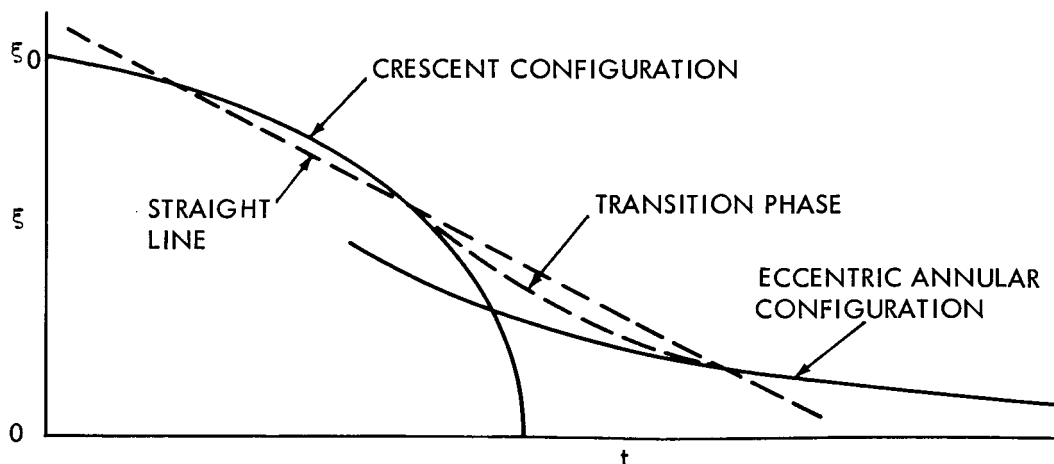


Fig. 8. Wobble ξ as a function of time t

backing of the plastic disc and seems to rush to one side in a wave formation, then to form the crescent shape associated with the fast damping. Further examination shows the mercury advancing in the channel, i.e., rotating faster than the gyro spin rate. The last frames show the mercury changed from the crescent to the eccentric annular shape.

Fig. 10 shows the *Y*-component, or projection, of the free-precession angle as a function of time for tests using two different channels. In test *A* the channel cross section is 1/4-in. wide (radially) by 1/16-in. thick; in test *B* the dimensions are 1/2-in. wide by 1/32-in. thick, as indicated in the sketches. All other parameters are the same in both tests. The thinner channel is evidently much more effective. Note that after the fast damping is

finished, the residual motion is poorly damped, as predicted; but the amplitude here is low, close to the size of the measurement error.

Although these initial experiments are inadequate to test the many aspects of this detailed theory, limited qualitative confirmation is surely demonstrated. There appears to be good qualitative agreement with a similar, approximately concurrent work.¹ Further tests would provide better accuracy in determination of the mercury shape and position, as well as the wobble angle, particularly at small angles; systematic parameter testing could then be undertaken.

¹Cartwright, W. F., Massengill, E. C., and Trueblood, R. D., "Circular Constraint Nutation Damper," *AIAA J.* 1(6): 1375-1380, 1963.

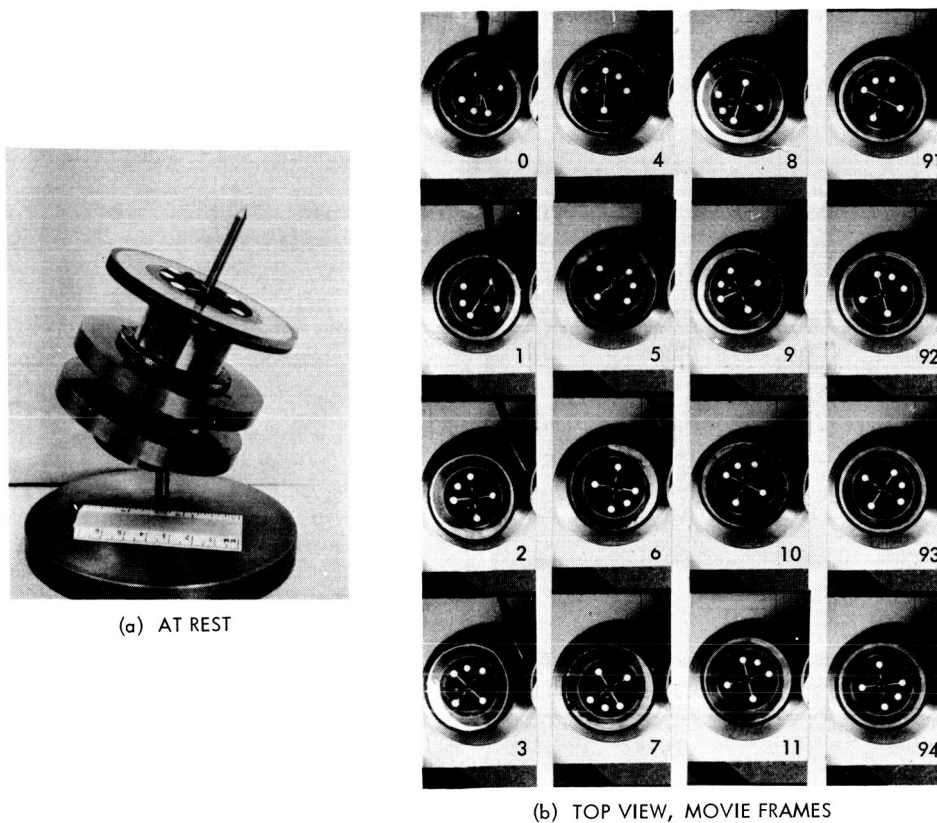


Fig. 9. Test gyroscope

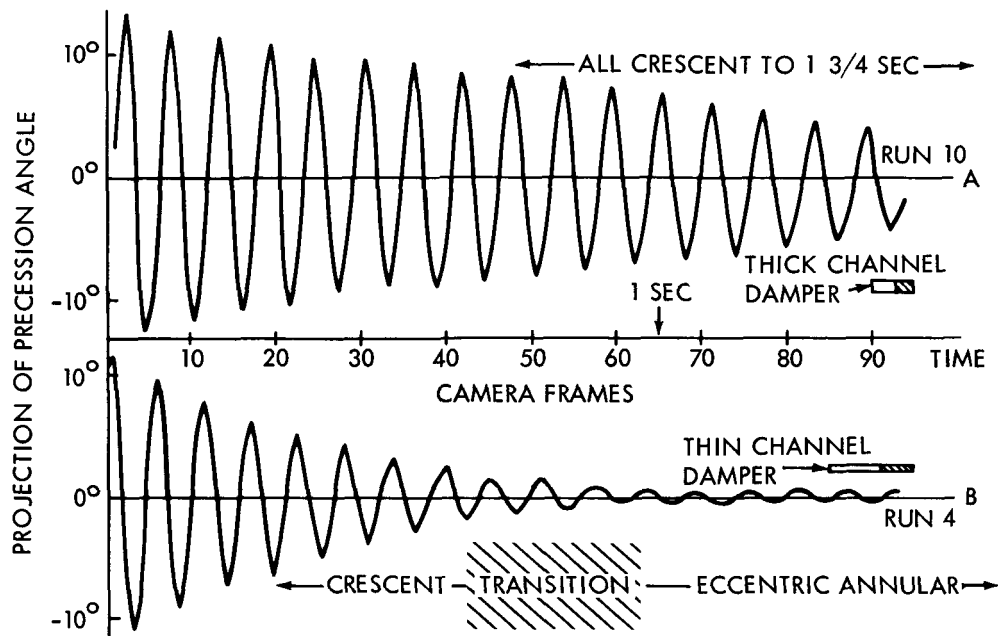


Fig. 10. Gyro free precession with different dampers (A. thick channel; B. thin channel)

DISCUSSION

Jay Chen:

Did you assume that the mercury flow in the damper is a channel flow?

Crout:

When the observer spins with it. Spinning around with it takes out the precessional angular velocity. Then you do see the flow in this channel.

Chen:

Can you tell me approximately what the Reynolds number is in this case?

Crout:

Well, most of the work is done for extremely small wobbles. And that's where the danger lies. The damping is lost when the wobble gets small, so the flow would be laminar.

Chen:

I see. What about the viscosity of the mercury?

Crout:

That plays a big role. In fact, in that theorem about the viscous frictional power loss, it plays a very prominent role. I have the derivation of that here if anyone is interested.

Robert Watson:

Have you attempted to optimize the capacity of mercury; what percentage of the annular ring should be filled with mercury?

Crout:

What I have are formulas which will calculate or determine the behavior of this, and then the experimental work can be done. I haven't gone into the experimental end at all, but if so much mercury is put in and the results are calculated, then some other amount is put in, the same formula can be used to calculate what would happen. And in that way, a comparison can be obtained. I imagine a digital computer would be pretty good at that.

Member of the audience:

Did you work on the dimensions of the cavity, for example, the depth of the cavity compared to the radius?

Crout:

No, I just have the formulas for computing what would happen in these different cases. I didn't put the numbers in or try to follow through on the design at all. My work was theoretical.

AEROSPACE VEHICLE SEPARATION MECHANISMS SELECTION, DESIGN, AND USE CONSIDERATIONS

I. B. Gluckman
Lockheed Missiles & Space Company
Sunnyvale, California

This paper describes and compares the principal types of separation systems and mechanisms used in spacecraft. Important parameters to be considered in tradeoff studies are discussed. Several examples of successful applications and failures and the lessons learned from them are discussed.

I. INTRODUCTION

The selection and design of systems and mechanisms for the separation of vehicle stages, fairings, and other aerospace structures are complex endeavors requiring detailed study, collection of background information, and objective decisionmaking. A serious problem is that, too often, adequate data on available designs are not readily available. Also, predesign tradeoff-study activity is sometimes limited by schedule and cost considerations. This paper is intended to facilitate these tasks.

A well-designed separation system must perform the separation function successfully and with minimum penalty on the vehicle and its performance. Design parameters to be considered are weight, shock, safety, reliability, strength, power requirements, and containment of fragments and gases. The effects of flight environment (temperature, vacuum, radiation, shock, and vibration) on the separation charge must also be considered, and costs and development effort are important factors.

Selection and integration of the separation system into the vehicle should be engineered for maximum compatibility. A wide variety of separation mechanisms are available to the designer, although modifications are usually required. The advantages and disadvantages of the two basic approaches—the point separation system and the linear separation system—are discussed in this paper. In addition to the attendant good points and success stories pervading their history of development and use, there have been, however, occasional mistakes and failures that yielded valuable lessons.

II. TYPES OF APPLICATIONS

The type of application strongly influences the selection of the separation mechanisms. There are two principal types of applications:

- (1) Single-point separation, in which programmed severance at one point only is required for accomplishing or committing the separation or actuation function of a system. A typical example is an antenna-boom release. In this case a point separation mechanism is the proper choice; a linear separation system does not usually lend itself to this type of application.
- (2) Multipoint separation, in which severance is required at two or more points or along a line. Examples are stage separations accomplished by severance of several spars and stringers, attachment points, or cutting of continuous stressed skin (monocoque). It is in this type of application that both point separation systems, utilizing several such devices, and linear separation systems are used. The discussions that follow pertain primarily to this type of application.

III. POINT SEPARATION SYSTEM

The point separation system consists of one or more discrete attachment points around the circumference or along the line of separation. The attachment points incorporate separation mechanisms, which are usually pyrotechnic, that separate on receipt of an electrical impulse imparted directly to each of these points.

Typical devices that fall into this category are explosive bolts, pin-pullers, pin-pushers, ball-lock ejectors, thrusters, and release nuts. The explosive bolt was the forerunner of these devices, and it was virtually the only choice for stage separation in the early days of missile technology. It has been used successfully for more than 20 years and is still being used. It consists of a hollow steel bolt containing an explosive charge which, upon initiation, causes the bolt to fracture along a weakened section. The explosive bolt is reliable and simple in design concept and has no moving parts. The actual design is sometimes complicated by high structural strength requirements, which introduce metallurgical and explosive train problems. Although the bolts have performed well in both ground and flight tests, they have exhibited two major inherent disadvantages: the creation of high localized shocks and the generation of fragments, debris, and ionized gases. These anomalies were blamed for causing telemetry blackouts and damage to nearby equipment in some applications. Some of the newer designs contain provisions for reduction, if not complete elimination, of these conditions.

The next generation of point separation mechanisms consisted of pressure-actuated devices such as pin-pullers, pin-pushers, and thrusters. These are pyro-actuated, piston-like mechanisms that sever an attachment either by the withdrawal of a pin or the breaking of a shear pin. Their reaction is milder than that of explosive bolts, and they usually contain the gases and debris. These features were the main reasons for their selection as replacements for explosive bolts in some applications. The mechanical design of these devices is more complex than that of explosive bolts because they have moving parts. Some of these devices also generate severe localized shocks during the sudden end-of-stroke piston deceleration. Nevertheless, these mechanisms have had a good flight history, and they are still used in applications where shock is tolerable.

In some of the more sophisticated designs of point separation mechanisms, the generation of shock is reduced considerably. Typical mechanisms are explosive release nuts and ball-lock devices, both of which are also piston-type mechanisms, but the energy absorbed in decelerating the piston is not transmitted to the structural members. This is accomplished by slotted, sliding components that permit disengagement of attachment interlocks in a radial direction (perpendicular to the piston movement). Explosive release nuts and ball-lock devices are popular and have a successful flight history.

Two disadvantages are mechanical complexity and high unit cost. An explosive release nut is used as a single-point release device for a horizon-sensor fairing on the Agena.

No matter how cleverly designed and reliable these devices are, two drawbacks are associated with point separation systems that use two or more such devices: lower statistical reliability and less inherent simultaneity when compared with linear systems. These parameters are discussed in Section V.

IV. LINEAR SEPARATION SYSTEMS

The linear separation system is an integrated, structural, frangible joint containing a length of detonating cord. The explosive shock created by the cord fractures the joint. This system was very popular during the last decade, particularly for large monocoque, or stressed-skin, airframes carrying heavy loads. There are two basic types (Fig. 1):

- (1) The unconfined mild detonating fuse (MDF)—flown successfully on Polaris, Agena (over 250 flights), and several other craft—and the unconfined flexible linear shaped charge (FLSC).
- (2) The confined systems, such as the Zipcord¹—which has been flown successfully on Abres, Isep, and Poseidon—and the more recent Super * Zip.² The latter has not yet been flown, but its development has been completed, and it is now being incorporated in a large fairing for the United States Air Force.

Although unconfined systems have been used for many years, they have two drawbacks: shock and contamination by products of combustion and metal fragments. These conditions could be tolerated in many but not all applications. In an effort to avoid potential problems, steps were sometimes taken to relocate shock-sensitive equipment or to provide protection by installing a protective gas shield behind the frangible joint. These perennial concerns led to design concepts that confined the detonating cord in a plastic or metal tube. Upon functioning of the cord, the plastic and/or metal jacket expands without rupturing and fractures the separation joint. All products of combustion are

¹LMSC Patent 3,373,686.

²LMSC patent pending.

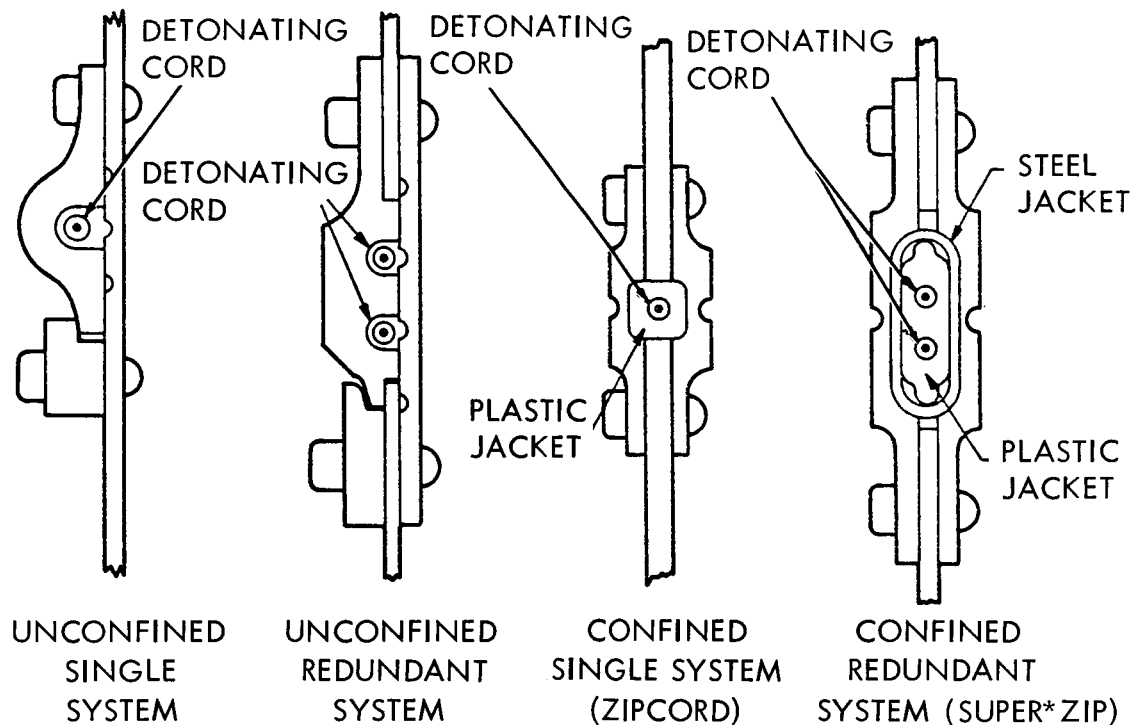


Fig. 1. Evolution of linear separation systems

retained. Significant reductions in shock are obtained; for instance, in a ground separation test of a 15-ft-long fairing, the maximum acceleration response at an instrument location was reduced from approximately 275 g for a conventional unconfined system to less than 100 g for Super * Zip.

V. COMPARISON BETWEEN MULTIPLE DEVICE POINT SYSTEM AND LINEAR SEPARATION SYSTEM

The primary considerations leading to introduction of the linear-separation concept were reliability and simultaneity. Byproducts were structural weight reduction and lower production cost. These and other pertinent parameters of both types of separation systems are compared in Table 1.

The reliability model for a point attachment/separation system using two or more devices is a series arrangement requiring successful operation of each device. The devices may have single or dual squibs. Failure of any device can result in a separation failure.

On the other hand, the reliability model for a linear separation system is a single primary device, usually initiated by redundant initiators. This is an oversimplification; nevertheless, it illustrates the basic difference (and advantage) in concept reliability of the linear separation system when compared with the multiple-point separation system. The reliability model for the single-point separation system is equivalent to that for the linear charge.

Instantaneous separation is an important factor in staging or fairing separation, especially in large and complex vehicles, because angular movements must be limited to prevent misalignment and possible mechanical interference during separation. Such performance requires simultaneity of separation of the various attachment points. In a multiple device point separation system using two or more independent units, the degree of simultaneity is dependent on the functioning-time dispersion among the various units. The dispersion can normally be reduced by increasing the current to the pyrotechnics to substantially more than the all-fire current. There are limits, however, to the current

available. Another method for the reduction of dispersion is the selection of faster-acting pyrotechnics and mechanical devices. Even under the best practical conditions of electric current supply and actuator selection, separation that would be as nearly instantaneous as that achieved with a linear separation system cannot be assured. For example, a time dispersion of up to 6 ms is a practical design criterion for a multiple-point separation system. On the other hand, total mechanical separation of a 5-ft-diameter linear-separation joint is accomplished in 1 ms because of the continuity of the

single charge and the high velocity of its detonation (6500 m/s or higher). Therefore, a linear separation system is superior to a point separation system having more than one device. There is no simultaneity problem with a single-point separation system.

Weight reductions of approximately 30 percent and more for the joint were achieved by changing to linear systems which simplified the structural design by eliminating the need for heavy bulkheads, attachment points, and Marmon clamps. Such simplification also resulted in

Table 1. Relative comparison of principal separation systems

Selection criteria	Multiple device point separation system	Linear charge	
		Unconfined	Confined
Contamination and fragments	From nil to moderate, depending on type of device	Moderate to maximum; may require internal debris shields	Nil
Simultaneity	Poor	Excellent	Excellent
Shock generation	High amplitude and frequency but localized; attenuates quickly (point source)	High frequency and amplitude; distributed	Less than unconfined; distributed
Weight	Heavy	Moderate	Moderate
Reliability (based on reliability model)	Low; decreases geometrically with number of devices used	High	High
Electrical power equipment	High	Low	Low
Pyro handling and installation effort required	Low	Moderate	Moderate
Cost for development	Low	Moderate	Higher than unconfined
Cost in production	High	Low	Low

Note: This comparison is applicable to functions involving separation at more than one point.

production cost savings. On the other hand, it is recognized that the earlier linear separation system which used unconfined detonating cord generated debris and that the shock levels were sometimes higher than those generated by a multiple-point attachment system. These disadvantages were later overcome or reduced by the introduction of the confined systems discussed above.

This paper does not intend to discredit multiple-point separation systems, some of which are still being used successfully; however, in the writer's opinion, the tendency is definitely toward the linear separation system for applications requiring simultaneous severance at two or more points of attachment or along a continuous line such as on a stressed skin (e.g., stage separation). In-depth tradeoff studies are always necessary for the selection of the proper system for the specific application.

VI. PROBLEMS AND FAILURES AND LESSONS LEARNED

After the designer has selected the proper system for his application, he proceeds with mechanism selection and/or design, development, and qualification. Subsequently, the user installs and flies the mechanism. In each of these phases, there are potential pitfalls regardless of which design is chosen. In the aerospace business, failures have yielded some expensive but useful lessons. Fortunately, these mishaps were few when compared with the successes.

The following are a few typical examples of problems and failures encountered in three categories: mechanism selection, design, and use. The lesson learned from each failure is also listed.

A. Mechanism Selection

1. Example of problem. About 8 years ago, the requirements for separation of large clamshell fairings (for Vela and Mariner) led to the selection of FLSC's having small core loads (5- and 7-grain/ft, respectively). There are V-shaped pyrotechnic linear charges approximately 1/8 in. in cross section and consisting of a lead-sheathed explosive, with a ratio of lead-to-explosive of about 15-to-1 by weight. The FLSC concept in larger core loads was known and proven at that time, but the miniaturized material was a new product that had been selected to reduce shock and debris. System development and qualification tests progressed normally, but

failures in the propagation of detonation along the cord developed late in the program, indicating that additional product development was necessary. Tight schedules, however, forced the FLSC to be abandoned for the Vela fairing in favor of the proven 10-grain/ft round cord, which was then flown successfully. The clamshell design with its linear separation system was abandoned for the Mariner fairing. Since that time, more work has been done on the low-core-load FLSC, and it appears that the product has matured.

2. Lesson learned. The initial selection of the 5- and 7-grain/ft material was premature. Use of unproven products should be avoided unless adequate lead time for developing and gaining confidence is provided. This applies particularly to state-of-the-art techniques and products, especially those involving miniaturization.

B. Mechanism Design

1. Example of problem. Failures encountered in development or qualification are often due to such mundane conditions as corrosion caused by dissimilar metals. A typical example of corrosion occurred when a pin-puller consisting of an aluminum housing and a piston and plug made of 4130 steel exhibited excessive corrosion and failed to function after temperature and humidity tests. The corrective action was to change the material for the internal parts to 17-4-PH and 303 stainless steel. The same pin-puller originally incorporated a detent spring (piano wire) mounted on the side of the piston. A failure was encountered in a ground test when the spring jammed and prevented retraction of the pin. Although careful manufacture and tightening of controls provided a temporary correction, a design correction was later implemented by replacing the long piano-wire spring with a snap ring.

2. Lesson learned. Materials should be selected for compatibility among themselves and should be non-reactive in environments encountered both on earth and in flight. Components that are difficult to manufacture to exacting specifications or close tolerances and difficult to test in a positive manner (such as piano-wire springs) should be avoided.

C. Mechanism Use

1. Example of problem. In May 1965, during the Gemini 9 target-satellite mission, the shroud failed to separate, although the two clamshell halves had split.

This was called the "angry alligator" incident by many because of the appearance of the partially separated shroud. The problem was traced to the failure of two quick disconnects to separate (Fig. 2). This condition was attributed to improper installation of the lanyards. Presumably, an error in procedures and a breakdown in communications were responsible.

2. Lesson learned. Installation procedures prepared by test and operation personnel should be reviewed carefully with the designer; the designer should be consulted if any question arises.

Two factors that must be considered in all phases discussed above are safety and human engineering. The importance attached to these two factors can easily determine the success or failure of a program.

VII. CONCLUSIONS

The aerospace designer has a variety of separation systems and mechanisms from which to choose. The preferred system for stage or fairing separation involving continuous, stressed (monocoque-structured) or multi-point-attachment separation planes is the linear system; for separation involving the severance of single-point attachments (e.g., antenna-boom releases), the point-separation mechanism is preferred. Many parameters must be considered in a proper tradeoff study; such a study should be conducted for each new application. Separation-system selection should be part of the initial structural design tradeoff effort. Although the flight success record of separation systems is quite impressive, there have been problems and some failures. Lessons learned from these should be applied to new endeavors.

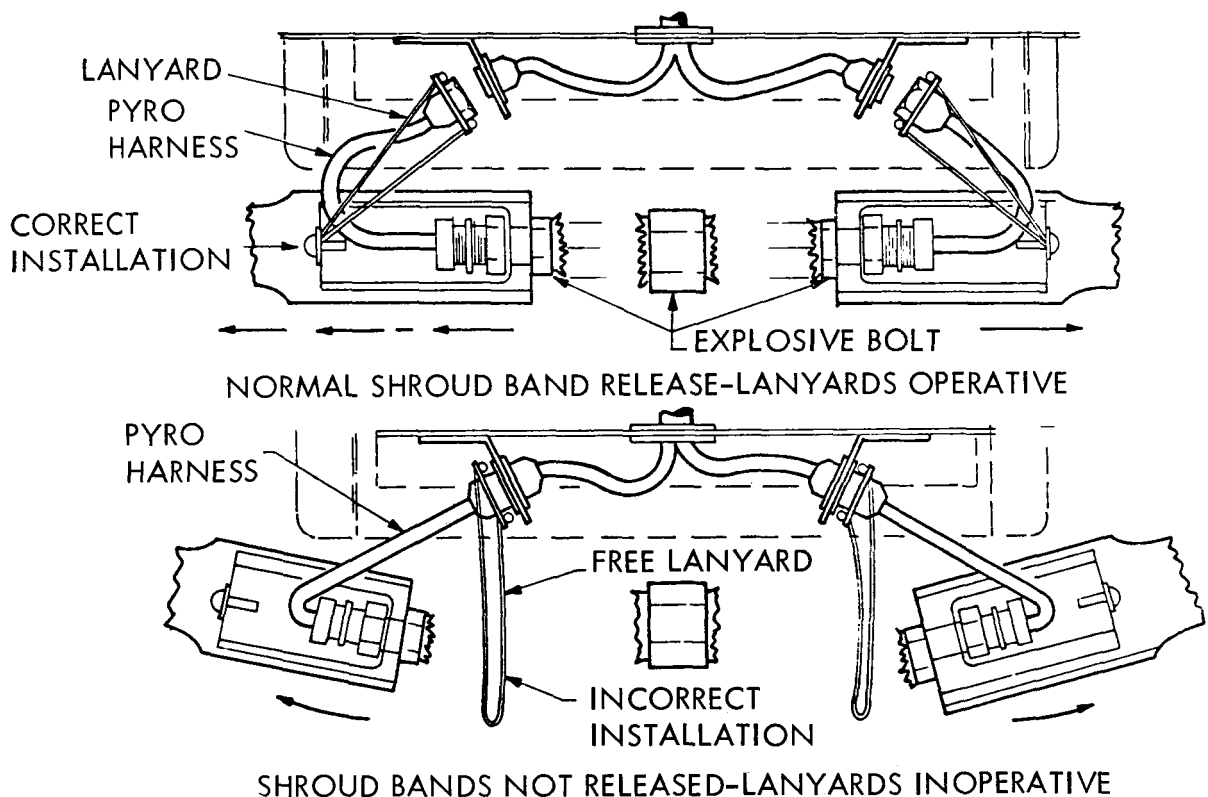


Fig. 2. Gemini 9 target satellite—shroud failure mode (May 1965)

DISCUSSION

H. Theron Haynie:

Do you find any reluctance among designers to use pin-pullers where they are liable to be under high-shear load at the time you actuate them?

Gluckman:

I find among designers a tendency to use pin-pullers because they are always there. Usually we have to draw their attention to

the fact that they have to be very careful about high-shear loads.

We've qualified our pin-pullers up to certain levels, and occasionally we find someone that wants to use them in an area where the load is considerably higher, and we recommend against it, unless we can qualify and test them.

You see, there are two squibs per pin-puller, but that's for redundancy. You should depend on only one squib functioning in the pin-puller satisfactorily at cold temperatures, which is the worst case. That's the way we run our worst case test.

ROTARY RELAY FOR SPACE POWER TRANSFER

H. Theron Haynie
Aerospace Systems Division
The Boeing Company
Seattle, Washington

The power clutch presented in this paper was designed for the transfer of electrical signals and power across rotating joints. Radio noise, friction, and wear are virtually eliminated. The design, construction, and applications are presented. This clutch eliminates the need of recycling solar arrays once each orbit by recycling only a low-inertia component of the power system.

I. INTRODUCTION

The complexity of the onboard experiments in spacecraft and the communications required to control and monitor experiments require very high power levels. For high spacecraft power requirements, both cost and weight are reduced when the solar cells are mounted on flat panels extended after the spacecraft has shed its protective cover. This configuration allows the spacecraft to maintain any selected attitude while the solar panels are oriented to face the sun. Some spacecraft designs require the recycling of the solar panels during the orbit night, with a flexible cable transferring power across the rotating joint. The disadvantages of this approach are the additional panel drive control circuits and the propellants required for attitude control of the spacecraft as the solar panels are stopped and reversed. The amount of time required to recycle is a disadvantage for some orbits.

An alternative approach is the use of a slipping and brush assembly at the rotary joint. Wear, friction, and radio noise are responsible for the limited use of this type of hardware. Liquid brushes and rotary transformers are presently being investigated, but they are not yet current technology.

The design described provides a "power clutch" of low moment of inertia that can be rapidly recycled once each orbit, while the array continues to track the sun position.

II. POWER CLUTCH DESIGN

The design described here and shown in Fig. 1 represents a different approach to power transfer. It is made up of three pairs of rotors and stators; each pair is a complete circuit. One conductor (see Fig. 2) is shown by the path of the black arrow through the assembly. Cable pairs are used to reduce the conductor size. Adjacent rotors and stators are insulated by a Teflon washer. Figure 3 shows a typical wiring circuit that can be quickly reset during an all-sunlight orbit. Figure 4 is a low-current housekeeping clutch with several circuits. Adjacent conductors are insulated by a Teflon washer.

A central tube of nylon, the structural backbone of the system, serves as the rotor pivot; it also houses the recycle actuator and guides the clamping piston. An extension handle protruding from the center enables manual actuation.

The stator assemblies are made up of circular plates with a metal-matrix solid-lubricant composite attached with silver foil diffusion bonding. The stators are held concentric by the nylon backbone tube and are prevented from rotating by the cabling connection. The composite lubricant is Boeing Compact 045-46, which prevents vacuum welding to the rotor.

The rotor assemblies (Fig. 2) are circular plates assembled to the conducting segment. The segments pivot around the nylon tube and are separated from each

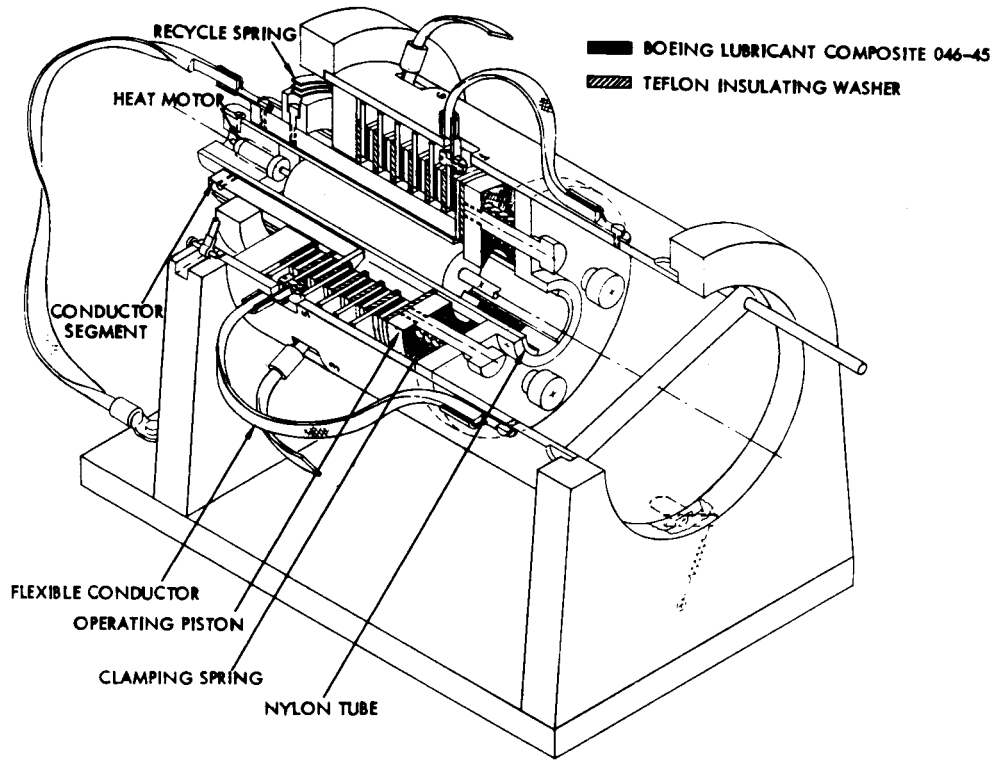


Fig. 1. Power clutch concept

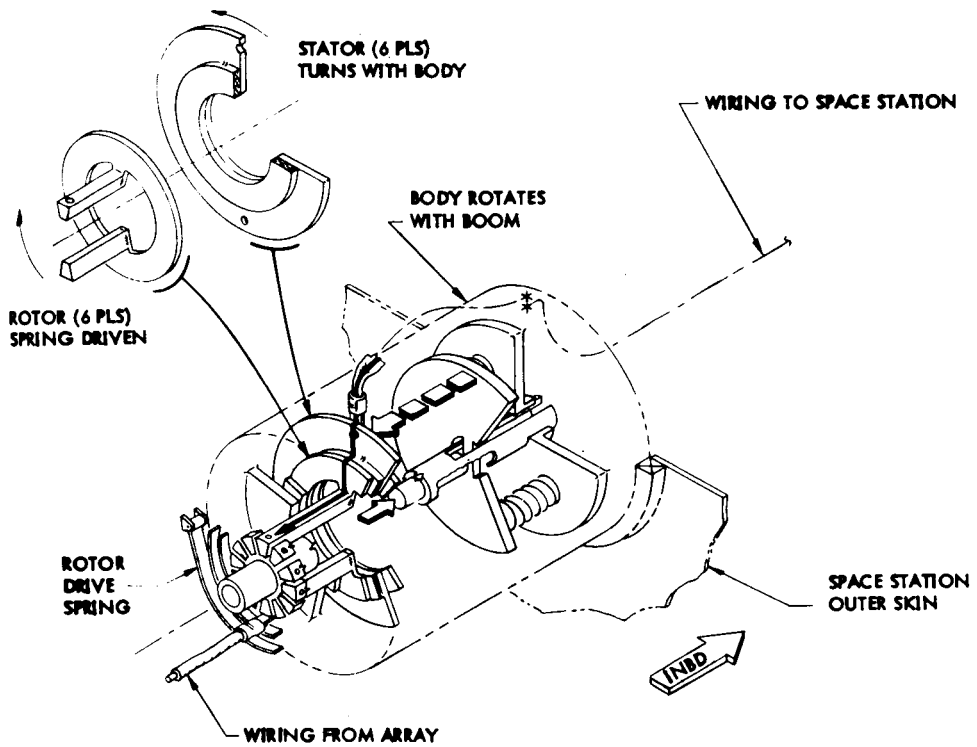


Fig. 2. Power clutch operation

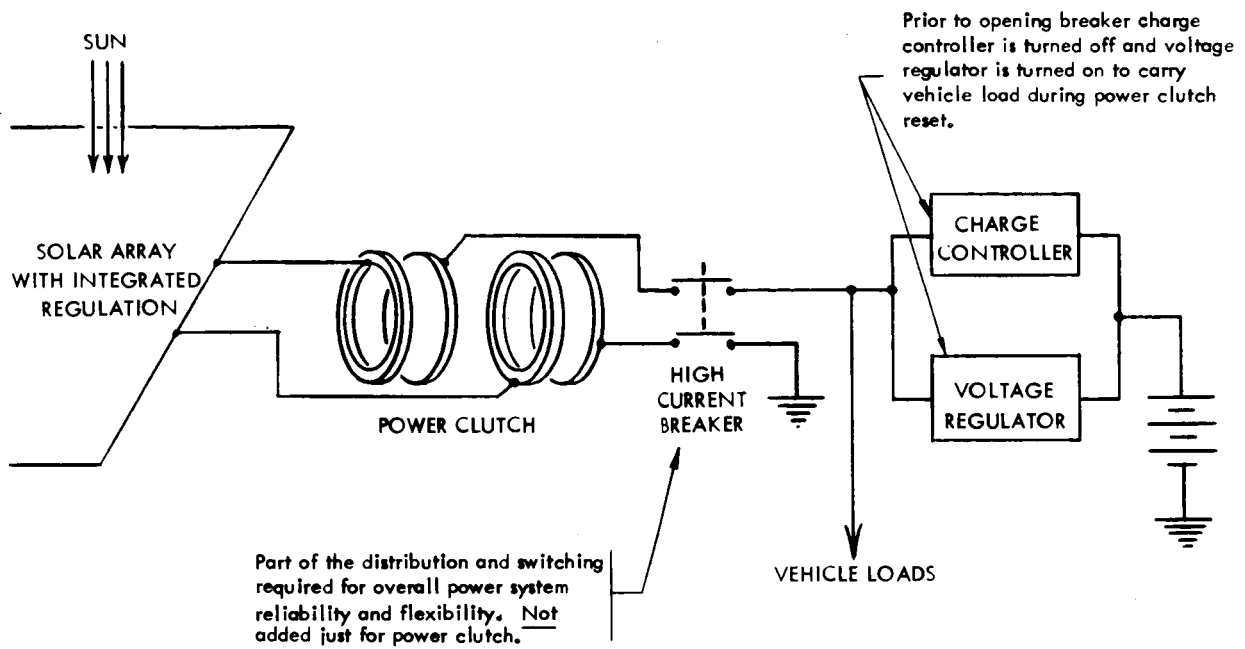


Fig. 3. Power clutch reset during an all sunlit orbit

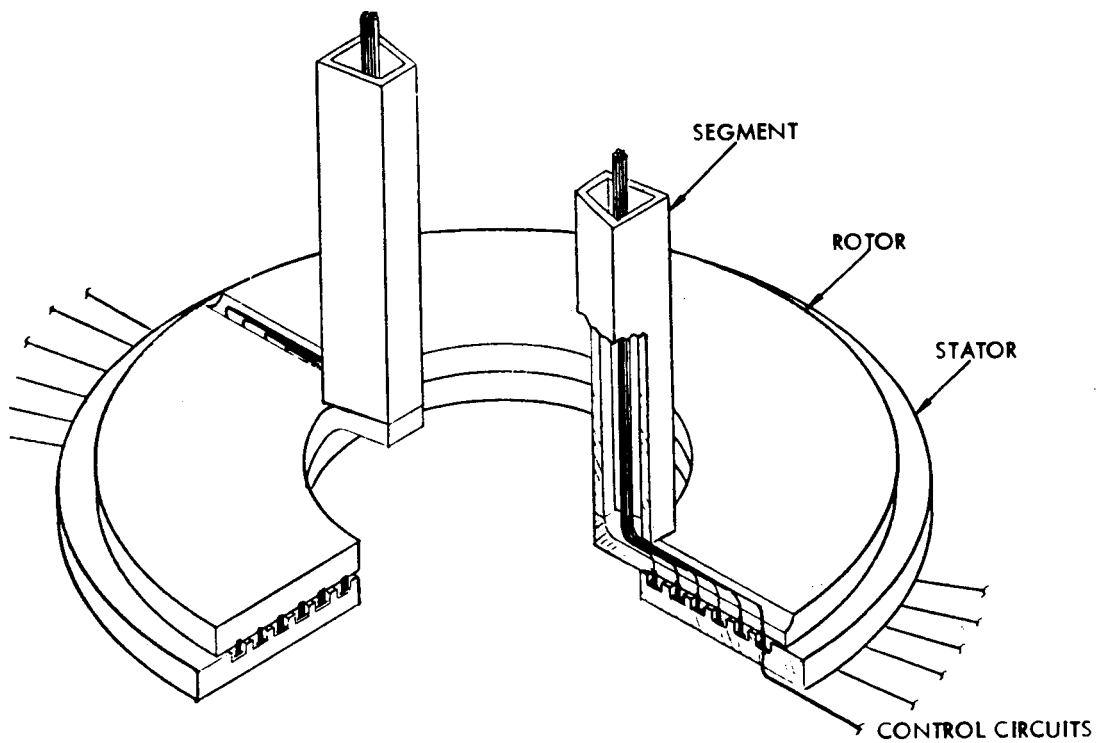


Fig. 4. Low-current housekeeping clutch

other by Teflon insulating bars. Flexible, straight-lay multistrand No. 30 wire (0.010-in. diameter) constitutes the cables bolted to the segments. The umbilical is made of two cables for each rotor assembly.

The operating piston and springs supply the clamping action to maintain the rotors and stators in contact for good electrical conducting properties. Recycle driving torque is supplied by a clock spring. A stepper motor or a gear train can also be used.

Earth satellites and space stations that are required to be earth- or stellar-oriented during orbit will ordinarily be designed to have symmetrical solar panels mounted at the end of a boom. In service, the boom rotates one revolution per orbit to keep the panels pointed toward the sun. One power clutch assembly will be mounted at each boom-to-spacecraft interface, as shown in Fig. 5. The cabling is routed inside and along the axis of the boom. The electrical connections to the spacecraft power bus have sealed pass-through connections in the pressure barrier. A manual override release can be mounted in the pressurized compartment.

The boom is driven by a brushless torque motor controlled by signals from a sun sensor on the solar panel. As the boom rotates, the umbilical twists and the reset spring is wound. When the spacecraft enters the earth's shadow, the linear actuator operates to separate the rotors from the stators. As these separate, the reset spring turns the rotors and untwists the umbilical in preparation for another orbit.

Time in the earth's shadow, hence, recycle time, typically varies from 36 minutes for a 100-mi equatorial orbit to zero for some 200-mi orbits inclined at 55 deg or more. The circuit of Fig. 3 can accommodate a power clutch recycle during an all-daylight orbit.

III. DEMONSTRATION MODEL

The demonstration model, Fig. 6, is a full-size assembly designed to fit within a standard 6-in. pipe. It contains six conductors (three complete circuits), each capable of carrying a 500-A current. To operate the model, one must rotate the handle on the end one full turn clockwise. This winds a clock spring in the

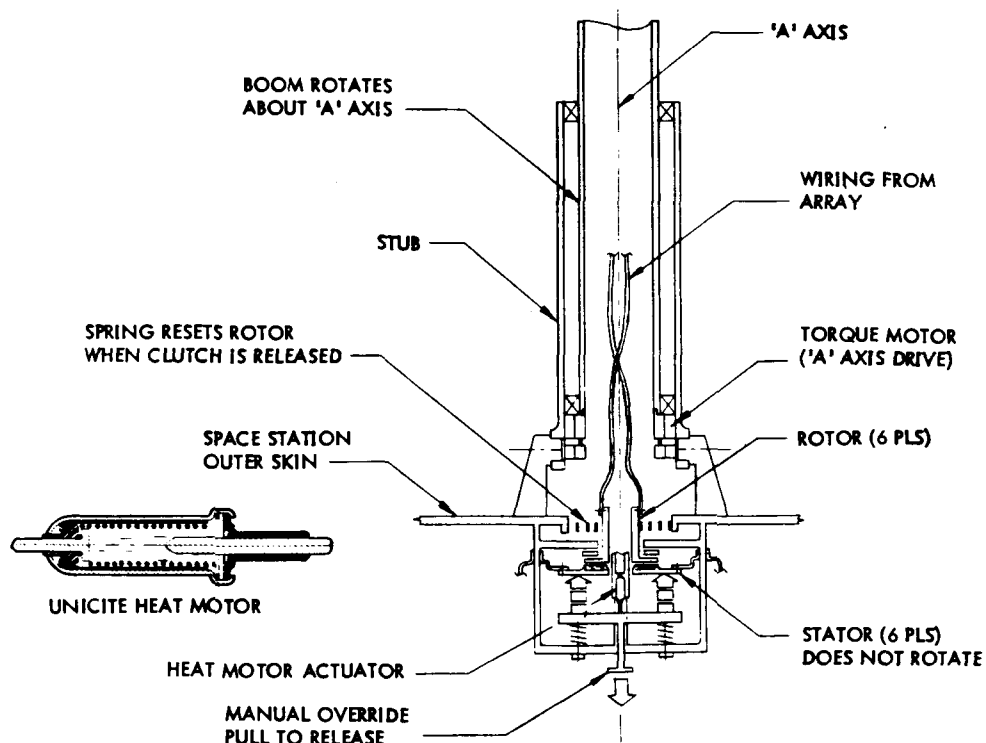


Fig. 5. Power clutch installation

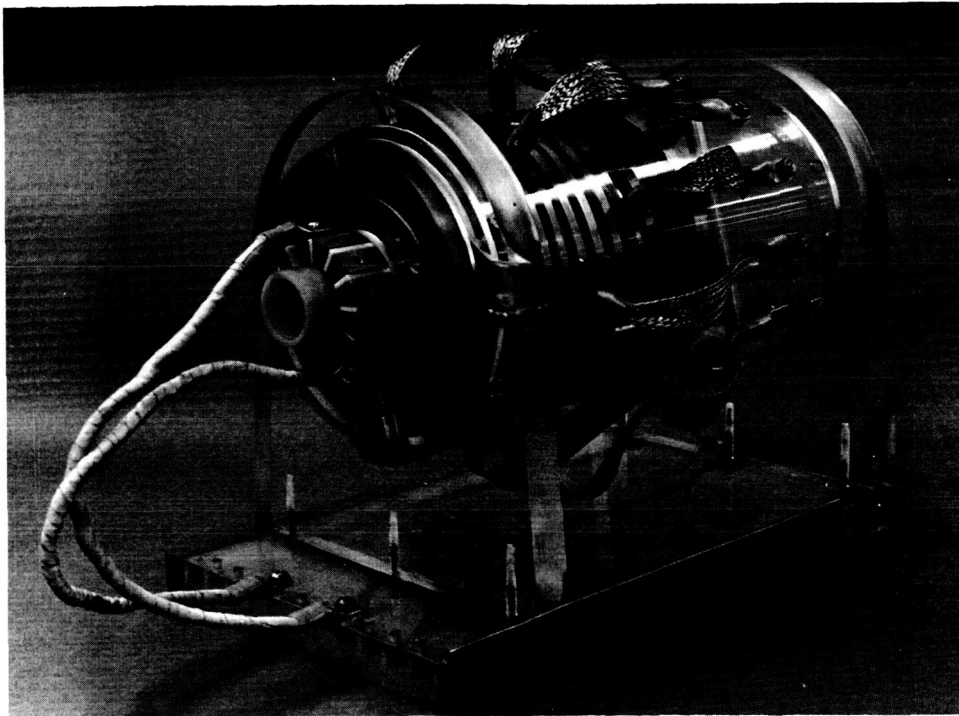


Fig. 6. Demonstration model

mechanism which provides the recycling energy for the system; it also twists the power umbilical cable one revolution. One turn of the handle simulates one orbit.

To recycle the clutch, a 24-V current is applied to a heat motor,¹ which causes a container of wax to melt and expand. The expansion develops a 40-lb force that extends a small piston 1/2 in. The force compresses the four clamping springs until the product of the spring force and the friction coefficient equals the clock spring torque, when the rotor and umbilical recycle in preparation for another orbit. Power is removed from the heat motor, the wax cools, and the power clamp closes.

Although copper was used in the model, 50 percent of the weight can be saved if the material is changed to aluminum. Further weight savings will result from optimization of the design for specific power loads.

¹Manufactured by Unicite, Division of United Carr Co.

IV. APPLICATIONS

Figure 7 shows a futuristic space-station concept that is assumed to require about 50 kW of electrical power from two solar panels. Each panel will be about 2500 ft² in area and weigh about 1250 lb, estimated on the basis of today's folding modular technology. The moment of inertia of both panels is 16,200 slug-ft². The panels rotate about the boom axis once each orbit.

Figure 8 shows a small, earth-oriented experimental satellite where one power clutch is used for each solar panel. Applications are not limited to solar power systems. A space station that is spun for an artificial gravity environment will require a power connection to the despun docking hub.

Two power clutches installed in parallel can be used where the short power interruption during recycle is unacceptable. An interlock will prevent the simultaneous recycling of both clutches.

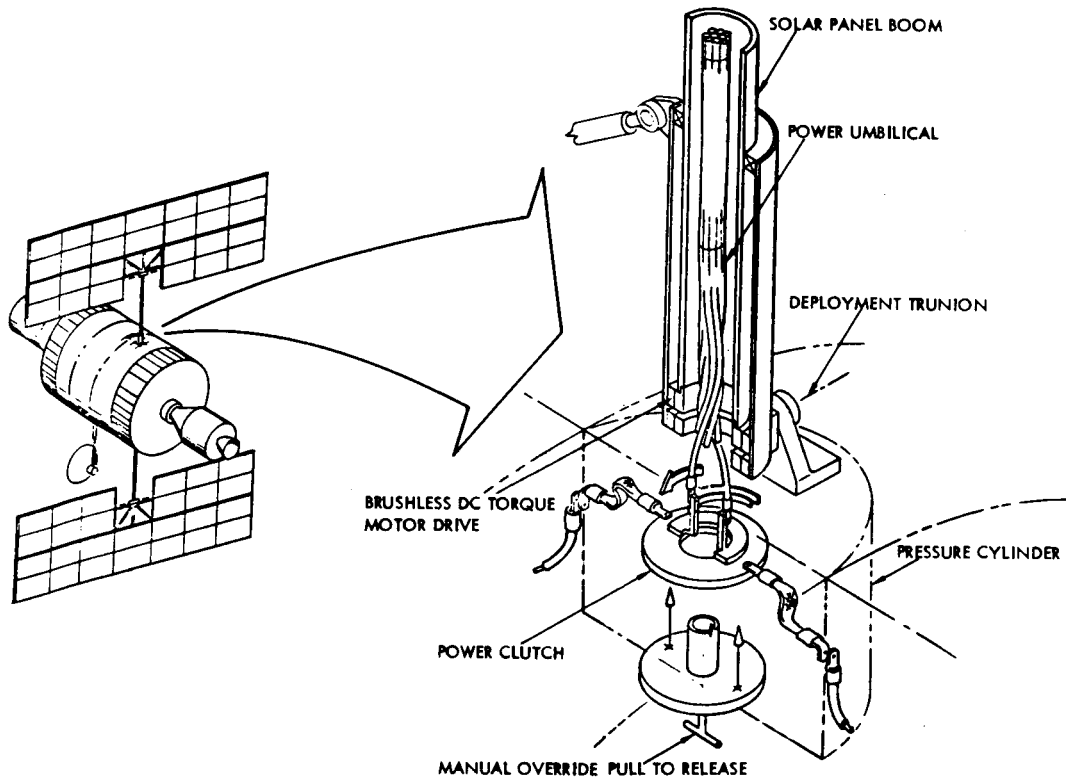


Fig. 7. Space station application

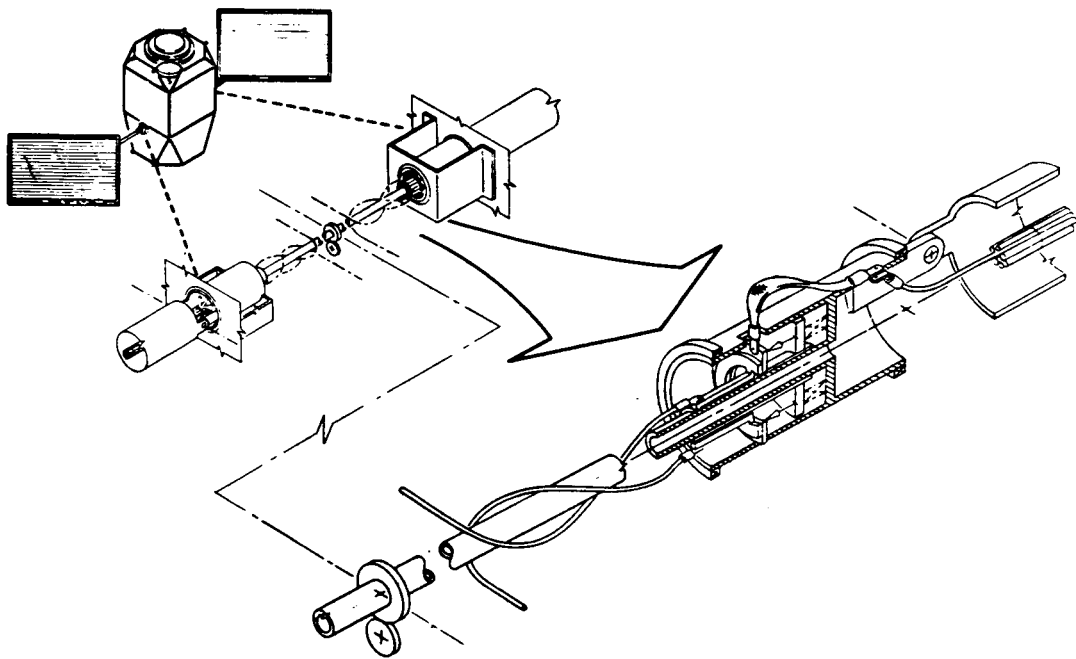


Fig. 8. Earth-oriented satellite

V. CONCLUSION

Tests on the demonstration model have shown that this device can solve the problems associated with

high-current power transfer across slowly rotating joints. The power clutch can transfer either ac or dc and does not require conversion, as does the rotary transformer. There are none of the liquid sealing problems encountered in the liquid slipping system.

DISCUSSION

Barry Tossman:

Why was a heat motor used rather than some kind of a dc motor?

Haynie:

Many drivers can be used to drive the system. All that is needed is $\frac{1}{4}$ inch of linear travel and the heat motor seemed to be the smallest, lightest and easiest to control of all candidates.

Tossman:

Have you checked the reliability of the heat motor thermal vacuum tests?

Haynie:

This program was temporarily shelved before serious design work was completed. Our preliminary design trade study did include other actuating methods. For vacuum service, a bellows sealed heat motor can be used.

Ray Bohling:

Did you run voltage drop tests across the clutches?

Haynie:

Not as yet. All we have built is this demonstration model and it doesn't have the solid lubricant on the clutch faces. This material will be the Boeing Compact lubricant which has been used in many NASA tests as a brush material.

Harry Mannheimer:

Is there any limitation in terms of the amount of power you can transfer through this device?

Haynie:

The contact surface area and reasonably sized umbilical conductors would be the only limitation.

Bill Moyer:

How do you apply heat to the heat motor to melt the wax?

Haynie:

24-volt power is applied to an enclosed nichrome wire that heats and melts the wax.

Harry Van Elkan:

You indicated that the clutch mechanism was pressurized and vented to space. Is the system pressurized in space and does it retain its pressurization or do you depend on a vacuum environment?

Haynie:

I think I am guilty of misinformation. The metal container surrounding the clutch actually serves as a pressure seal between a space station and the clutch mechanism. The clutch is not pressurized.

Rudy Lutwin:

What was the design goal for the torque on this joint for one revolution?

Haynie:

The model contains a retractor spring for an outboard motor as the driving power. In demonstrations I wind it about halfway and develop about 18 inch pounds.

John Matilaine:

Have you investigated what frequencies could be carried through the clutch? Could one put RF power through it?

Haynie:

We have done no investigation in this area but any power carried in an ordinary conductor could go through it. Shielding may be a problem with RF.

RESPONSE CHARACTERISTICS OF A THERMAL-HELIOTROPE SOLAR-ARRAY ORIENTATION DEVICE

Frederick H. Morse
Department of Mechanical Engineering
University of Maryland
College Park, Maryland

The thermal heliotrope is a passive solar-array orientation device containing a bimetallic helix that rotates when activated by solar energy. The rate and extent of the rotation depends upon the properties of the two metals and the temperature of the helix. An energy-balance analysis is performed to determine the temperature distribution in the helix. By initially restricting the analysis, a simplified equation governing the response of the heliotrope is obtained. In order to gain insight into the response of the heliotrope, a series of experiments were performed. The results of these tests and their implications are presented.

I. INTRODUCTION

The electrical energy requirements of many satellites and spacecraft are presently met by the use of large arrays of solar cells. The energy conversion efficiency of a solar cell is directly related to its orientation with respect to the sun. Therefore, it is desirable to maintain a minimum angle between the solar cells and the sun during all portions of the satellite's trajectory for which the sun is visible. At present, this is accomplished by mounting the solar cells on movable supports, activated electromechanically, that track the sun. These systems require electrical power for their operation, are expensive, and tend to have many complex components with inherent reliability problems.

An alternative system has recently been proposed by Byxbee and Lott.¹ In this system, called the thermal heliotrope, solar energy activates a bimetallic helix that serves as the motor element of the device producing torque and causing angular displacement. A control mechanism consisting of one or more shades completes the basic device. In contrast to the electromechanical tracking systems, the heliotrope is electrically passive,

contains relatively few parts, has a low starting inertia with an inherent dynamic stability, and has long-life capabilities.

The essential components of a heliotrope are shown in Fig. 1. The fixed end of the helix is attached to the vehicle, and the other end, the free end, is attached to

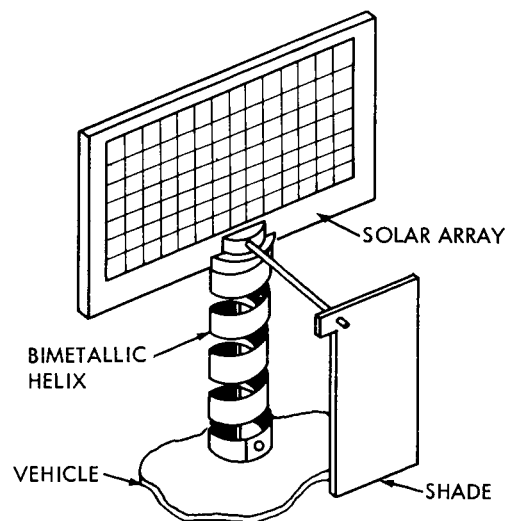


Fig. 1. Schematic of thermal heliotrope

¹Byxbee, R. C., and Lott, D. R., "Thermal Heliotrope: A Passive Sun-Tracker," (Preprint No. 13, Fourth Aerospace Mechanisms Symposium, University of Santa Clara, May 1969.)

the solar array. A shade is fixed to the free end of the helix. The function of the shade is to regulate the amount of solar radiation incident on the helix and thereby cause the rotation to stop when the solar array is aligned with the sun. The principle of operation may be illustrated by first assuming that the sun's rays are initially at an angle θ_0 with respect to the normal to the solar cells, as shown in Fig. 2a. The solar-energy input to the helix causes its temperature to rise, which, in turn, causes the two components of the helix to expand unequally. This nonuniform expansion causes the free end of the helix to rotate, the rate and extent of rotation depending upon the properties of the helix material and the temperature distribution within the helix.

The rotation of the free end is such that the solar array to which it is attached rotates towards the sun, as shown in Fig. 2b. At an angle θ_A , the shade begins to cast a shadow on the helix. Further rotation of the helix causes the shade to shield a greater portion of the helix from the solar radiation. The decreased solar-energy input reduces the rate at which the temperature of the helix is increasing, which, in turn, reduces the angular velocity of the helix. A point is reached at which the net energy input to the helix is zero, and the rotation ceases. At that point the solar array is aligned perpendicular to the sun's rays, as shown in Fig. 2c.

The tracking feature of the thermal heliotrope may be illustrated by considering the situation in which the relative position of the sun changes such that θ_0

increases slightly in a clockwise direction. This change will increase the surface area of the helix illuminated by the sun's rays. The resulting increase in temperature of the helix will cause the shade to rotate in the clockwise direction until the energy balance of the helix is restored. A similar sequence of events would occur should θ_0 decrease. In such a manner, the solar array is able to track the sun continuously. The thermal heliotrope shown in Fig. 1 must be reset whenever the total angular rotation reaches a certain limit. Resetting is accomplished by allowing the helix to cool. Cooling may be achieved during passage behind the Earth or by the use of a second shade.

The thermal heliotrope concept for solar-array orientation and tracking has been verified, and models of four heliotropes have been built and tested in a simulated orbital environment (Ref. 1).

II. THERMAL ANALYSIS

In order to determine the spatial and temporal temperature distribution within the helix, an energy-balance analysis on the control volume shown in Fig. 3 is made. This control volume is taken to be any illuminated segment of the helix when it is in equilibrium. The following energy terms must be included in the energy balance:

- (1) Q_1 solar energy radiated to the helix control volume.

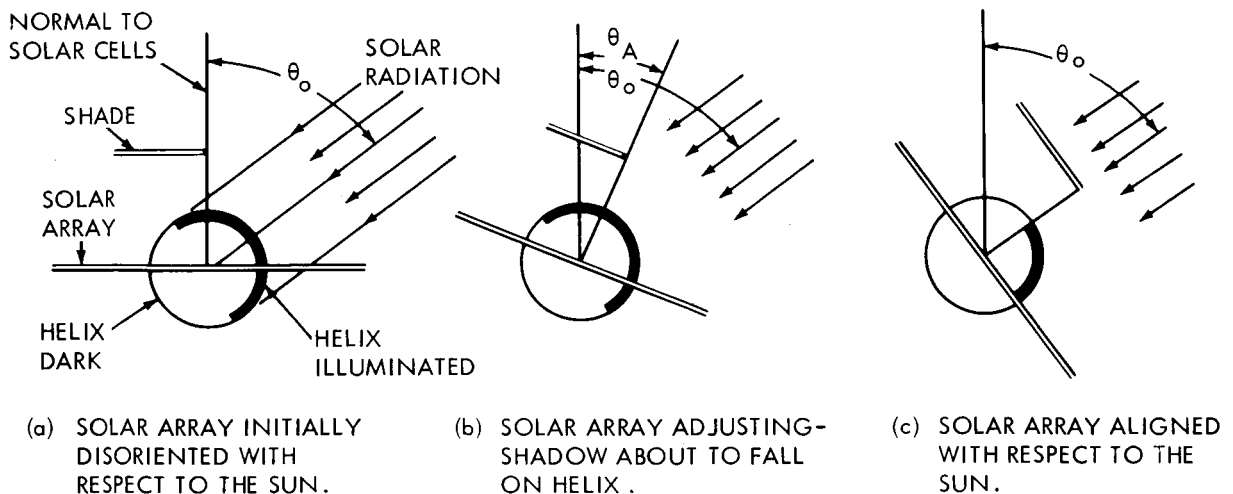


Fig. 2. Thermal heliotrope orientation sequence

- (2) Q_2 thermal energy radiated from the helix control volume to space.
- (3) Q_3 thermal energy radiated to the helix control volume from other parts of the heliotrope, the satellite, or the earth.
- (4) Q_4 thermal energy radiated from the helix control volume to other parts of the satellite.
- (5) Q_5 thermal energy conducted from the helix control volume to adjacent helix material.
- (6) Q_6 energy convected into or out of the helix control volume as a result of the rotational motion of the helix.
- (7) Q_7 work done by the helix material in the control volume on the system to which it is attached.
- (8) Q_8 energy stored within the helix control volume.

For the purposes of illustrating an approach to the task of determining the thermal response of the heliotrope, several terms— Q_3 , Q_4 , Q_6 , and Q_7 —will be neglected. The neglected terms all depend primarily upon the design of the heliotrope and its location on the

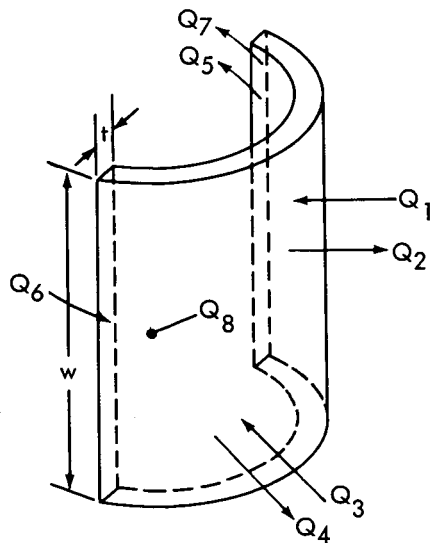


Fig. 3. Control volume for heliotrope thermal analysis

satellite. Therefore, these terms should be included in a complete thermal analysis of a particular system.

Since the solar-energy flux impinges on a cylindrical surface area, the total solar-energy input per unit time \dot{Q}_1 is obtained by integrating the normal component of the solar energy flux \dot{Q}_0 over the illuminated area. The result, expressed in terms of the projected illuminated area A_p , is

$$\dot{Q}_1 = \frac{2}{\pi} \dot{Q}_0 A_p \quad (1)$$

While it is possible for the sun to illuminate portions of the interior of the helix through its gaps, this effect will be neglected in this paper.

The thermal heliotrope has two modes of operation: orienting and tracking. In the orientation mode, the solar-energy input remains constant until the shade begins to cast a shadow on the helix. For all subsequent time, the solar-energy input decreases as a function of the rotation angle θ , becoming zero at an angle θ_B when the helix is completely shaded. The completely shaded condition is not reached in normal operation because the heliotrope rotation stops when an energy balance is achieved, and this occurs close to the position for half illumination. The functional dependence of the solar-energy input on the rotational angle θ may be shown to be

$$\dot{Q}_1 = \frac{\dot{Q}_0}{\pi} A_p \left[1 + \frac{R_S}{R_H} \cos\left(\frac{\pi}{2} - \theta_0 + \theta\right) \right] \quad \theta_A \leq \theta \leq \theta_B \quad (2)$$

where R_S and R_H are the shade and helix radii, respectively, and θ_0 is the initial angle between the solar-cell normal and the sun's rays. The solar-energy input per unit time Q_1 may therefore be written:

$$\dot{Q}_1 = \dot{Q}_0 A_p \frac{f(\theta)}{\pi} \quad (3)$$

where

$$f(\theta) = \begin{cases} 2 & 0 \leq \theta \leq \theta_A \\ 1 + \frac{R_S}{R_H} \cos\left(\frac{\pi}{2} - \theta_0 + \theta\right) & \theta_A \leq \theta \leq \theta_B \\ 0 & \theta \leq \theta_B \end{cases} \quad (4)$$

The function $f(\theta)$ represents the loss of illuminated surface area on the helix when the shade causes a shadow to move across it.

The thermal energy radiated from the helix control volume per unit time is given by

$$\dot{Q}_2 = \sigma F_\epsilon F_A (T_H^4 - T_S^4) \quad (5)$$

where σ is the Stephan-Boltzmann constant, F_ϵ is the emissivity factor, F_A is the shape factor, and T_H and T_S are the helix and space temperatures, respectively.

Thermal energy will be conducted from the higher-temperature illuminated control volume to the adjacent, lower-temperature dark portions of the helix. However, because of the linear relation between the temperature change and the resulting rotation (Ref. 2)

$$\Delta\theta = K\Delta T_H \quad (6)$$

where K is a constant involving the dimensions and properties of the helix, the reduced contribution to the rotation of the helix by the illuminated region is exactly compensated by the increased contribution of the dark region. Therefore, it is possible to eliminate the conduction term Q_5 from the energy balance without altering the angular response of the helix.

Since the internal energy of the bimetallic materials is a function of its temperature only, the energy stored per unit time within the helix control volume Q_8 may be written:

$$\dot{Q}_8 = \rho c V \frac{dT_H}{dt} \quad (7)$$

where ρ and c are the density and specific heat, respectively, of the bimetallic material, V is the control volume, and t is time.

The principle of conservation of energy requires that the difference between the energy input and energy output appears as an increase in the internal energy of the material within the helix control volume. Thus,

$$\dot{Q}_0 A_p \frac{f(\theta)}{\pi} - \sigma F_\epsilon F_A (T_H^4 - T_S^4) = \rho c V \frac{dT_H}{dt} \quad (8)$$

Changing dependent variables from T_H to θ results in a differential equation for the angular rotation of the helix:

$$\dot{Q}_0 A_p \frac{f(\theta)}{\pi} - \sigma F_\epsilon F_A \left[\left(\frac{\theta}{K} + T_0 \right)^4 - T_S^4 \right] = \frac{\rho c V}{K} \frac{d\theta}{dt} \quad (9)$$

This equation is nonlinear in θ , with both exponential and trigonometric terms present. The initial condition is that, at $t = 0, \theta = 0$.

Because the normalized solar-energy input function $f(\theta)$ is constant for all angles less than θ_A , it is convenient to solve Eq. (9) in two steps. The first solution would be for all angles equal to or less than θ_A , i.e., angles for which the solar-energy input is constant. The second solution would be for all angles between θ_A and θ_B , where the solar energy varies. Accordingly, the orientation-mode response would involve both solutions, and the tracking mode would be described by the second solution. Because of the nonlinear nature of this equation, a computer solution is required, and this has not yet been performed.

III. EXPERIMENTS

In order to gain insight into the thermal response of the heliotrope, a series of preliminary experiments was performed. A schematic of the experimental setup is shown in Fig. 4. The response of a single-coil, continuous track and reset heliotrope to illumination from a high-intensity lamp was measured. Only the orientation mode was investigated.

The bimetallic helix was 0.69 in. OD, 0.022 in. thick, and 0.5 in. wide. Its active length was 11.25 in. The helix was sprayed with a flat black paint, and two thermocouples were mounted on the inside surface midway between the free and fixed ends and 180 deg apart. One end of the helix was secured to a fixed, vertical support shaft, and the other was connected to the slide holder of a potentiometer. In that way, rotation of the free end of the helix caused the housing to rotate relative to the slide, thereby changing the resistance of the potentiometer and providing a measure of the rotation. A shade made from a thin aluminum sheet was mounted on a shaft that was fixed to the potentiometer housing. During the tests, the distance between the high-intensity lamp and the helix was varied so that a range of values of \dot{Q}_0 could be obtained.

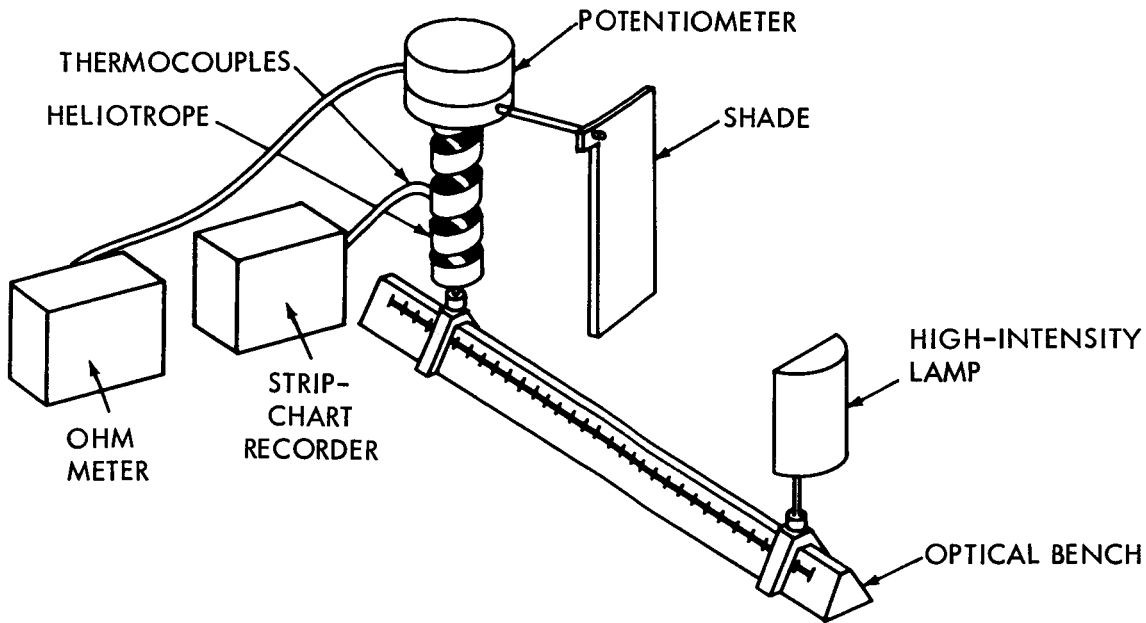


Fig. 4. Schematic of thermal heliotrope experiment setup

Since these preliminary tests were not conducted in a vacuum chamber, the dominant energy loss mechanism was natural convection. Under this condition, the governing equation, Eq. (9), reduces to

$$\dot{Q}_0 A_p \frac{f(\theta)}{\pi} - \frac{h A_c}{K} \theta = \frac{\rho c V}{K} \frac{d\theta}{dt} \quad (10)$$

where the radiation-loss term has been replaced by a convection-loss term. The symbol h represents the natural-convection, heat-transfer coefficient, and A_c is the total surface area of the helix within the control volume. Equation (10) is of the form

$$\frac{d\theta}{dt} + a\theta = b(\theta) \quad (11)$$

where a is a constant representing the ratio of the energy lost per unit time to the energy stored:

$$a = \frac{A_c h}{\rho c V} \quad (12)$$

The quantity $b(\theta)$ is a variable representing the ratio of the energy input per unit time to the energy stored:

$$b = \frac{K \dot{Q}_0}{\pi \rho c V} A_p f(\theta) \quad (13)$$

As previously mentioned, it will be convenient to employ a two-step solution. For all angles $0 \leq \theta_A$, b is a constant, and the solution to Eq. (11) is

$$\theta = \theta_{EQ} (1 - e^{-at}) \quad (14)$$

where

$$\theta_{EQ} = \frac{2}{\pi} \frac{\dot{Q}_0 K A_p}{h A_c} \quad (15)$$

Equation (14) implies that values of the rotation angle θ , when plotted on semilog paper as $(1 - \theta/\theta_{EQ})$ versus time, should fall on a straight line with a negative slope that is proportional to the constant a . Figure 5 shows typical data plotted in this way. For the test presented here, the equilibrium angle θ_{EQ} was such that the helix

remained unshadowed, that is, $\theta_{EQ} < \theta_A$. It is seen that the data do fall on a straight line, and this line has slope a .

Another series of tests were conducted in which the equilibrium angle was such that the helix became shadowed. The differential equation governing this response contains the nonlinear $b(\theta)$ term, making an exact solution difficult. Data from this test are also shown in Fig. 5. It can be seen that the initial response of the helix is the same as that for the previous test. However, at a time corresponding to the appearance of the shadow on the helix, the slope abruptly changes. The linear dependence in variable-energy-input time interval suggests that the governing equation may be linearized.

IV. CONCLUSION

The differential equation governing the response of a heliotrope has been derived, subject to the absence of several design-dependent energy-transfer terms. The experiments conducted under atmospheric conditions confirm the possibility that the governing equations may be linearized under just such conditions. It is anticipated that vacuum-chamber tests will also yield data indicating the possibility of obtaining approximate solutions for the response of a thermal heliotrope. Such approximate solutions would be most useful in the design of a thermal-heliotrope solar-array tracking system.

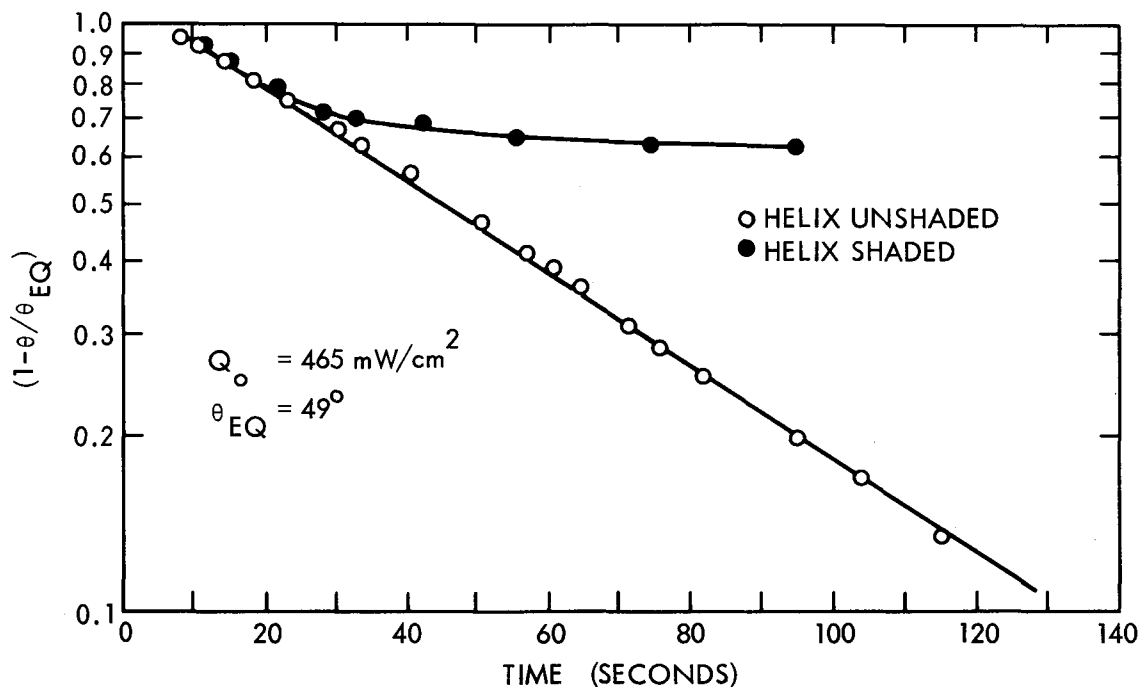


Fig. 5. Time dependence of angular rotation of thermal heliotrope

REFERENCES

1. "Passive Solar Array Orientation System (Thermal Heliotrope)," Final Report, Lockheed Missiles & Space Co., Sunnyvale, Calif., Sept. 1969.
2. Timoshenko, S., "Analysis of Bimetal Thermostat," *J. Am. Opt. Soc.* 2:233, 1925.

DISCUSSION

Richard Pefley:

Would you explain why you left the conductive component of the heat flow out of the picture?

Morse:

The conduction component of the heat flow reduces the temperature distribution in the illuminated portion of the helix while the temperature distribution in the adjacent dark portion increases. If for the moment, another control volume consisting of an illuminated portion and the two adjacent half-portions is considered, it can be seen that the energy conducted out of the illuminated region is, by symmetry, stored within the dark region material. As a result of the linear relationship between the temperature change and the resulting angular displacement, the reduced contribution to the angular rotation of the helix by the illuminated portion is exactly compensated by the increased contribution of the dark portion. It is therefore possible to eliminate the conduction term from the energy balance without altering the angular response of the helix.

Maitland McLarin:

I'm wondering about the vibration characteristics of this coiled spring. Would it only operate in a very quiet area, or could you damp it in some way?

Morse:

Vibrational motion of the helix would be damped by the tracking characteristic of the heliotrope. In fact, a thermal heliotrope solar array orientation system should offer advantages as far as vibrations are concerned. That is, with large panels connected to a spacecraft with these helical elements, motion of the spacecraft would be damped by the tendency of the panels to maintain a fixed orientation with respect to the sun.

McLarin:

I was referring to some commercial use also, possibly as an automobile attachment.

Morse:

It would depend on the particular application, however, the heliotrope does have an inherent damping capability.

Barry Tossman:

What is the sensitivity of the sun-seeking aspect to degradation of the surface of the heliotrope?

Morse:

The response time would be dependent upon the condition of the surface of the heliotrope. Therefore degradation of the surface would have some effect on the performance of the heliotrope. I would expect this effect to be quite small. Lockheed has developed a surface coating designed to withstand this particular degradation effect. Preliminary testing in a vacuum chamber under high intensity arc lamps did not indicate that a surface degradation problem existed.

Harry Montgomery:

You said that you were able to linearize the nonlinear differential equation. Is this because of the presence of the air? Or do you think it would turn out that in, for example, a space environment the fourth power of temperature would be significant?

Morse:

Certainly the radiation term introduces a nonlinear exponential term into the governing equation (see Equation 9). However, because of the relatively small temperature change of the helix, the non-linear radiation loss term could be linearized, resulting in an equation of the form of Equation 10 with, of course, the convective heat transfer coefficient replaced by an appropriate radiation coefficient. I believe the error introduced by such a linearization would not significantly change the nature of the results described in this paper.

Montgomery:

So, it would work either way?

Morse:

I would expect the response of the heliotrope to exhibit the same exponential function with time.

SESSION II

**Session Cochairman
Raymond F. Bohling
NASA—Headquarters**

DOCKING-MECHANISM ATTENUATOR WITH ELECTROMECHANICAL DAMPER

V.S. Syromyatnikov
Institute for Machine Technology
USSR

Theoretical and practical problems involved in the application of electromechanical damping for spacecraft docking-mechanism attenuation are discussed. Some drawbacks of hydraulic dampers used for this purpose are pointed out. The basic scheme of the attenuator with the electromechanical damper is given, and it is noted that similar attenuators were used in the docking mechanisms of the Soyuz spacecraft.

The features of the electromechanical damper and the principal relationships governing it are considered. The dynamic characteristics of the damper are estimated through the use of a time constant of the electromechanical brake which produces a damping force in the attenuator. The brake is described, and its typical mechanical characteristic is given. The dependence of the time constant and other brake characteristics on the brake's basic parameters is analyzed. The possibilities for electrical damping and the characteristics of real brakes are numerically estimated. A basic approach to the choice of the main parameters of the brake and the gear for given parameters of the docking-mechanism attenuator is presented.

In conclusion, problems associated with the heating of the brake rotor during operation and the brake characteristic changes caused by this heating and that due to environmental temperature change are discussed. Problems of measuring the brake's characteristics during ground tests, which are also affected by brake heating, are considered.

I. INTRODUCTION

To absorb the impact energy of docking spacecraft, docking devices are provided with a damping system. This system is designed to absorb the impact energy in all cases of relative spacecraft motion, thus limiting the force produced by the impact.

Since the docking, as a rule, is accompanied by several impacts and the docking device is generally used several times, the attenuator must contain an elastic element to return the system to its starting position. To damp the angular motion of spacecraft after they have coupled and to provide the spacecraft engagement, the attenuator must have an energy absorber, a damper. Thus, the docking-device attenuator is a combination of the elastic element and the damper. Hydraulic dampers

are the most widely used types (e.g., in a car suspension or an aircraft chassis). The docking systems of Gemini and Apollo also include hydraulic dampers.

Although there are apparent advantages in the use of hydraulic dampers (relative simplicity and small dimensions and inertia of moving parts), they have some drawbacks that result mainly from fluid viscosity and volume changes due to temperature change, possible leakage, and a square-law dependence of the damping force on the velocity of the working element's movement with a fixed throttling orifice. These drawbacks can be overcome, but they must be taken into account in the design of docking mechanisms.

Calculations and experiments show that electromechanical damping could be used for docking-device

attenuation, as well as for solving a number of other engineering problems. The design of such a damper has revealed its features and has required solving a number of theoretical and practical problems which are considered in this report.

II. ELECTROMECHANICAL ATTENUATOR

Figure 1 shows a simplified attenuator for the docking mechanism consisting of a longitudinal spring with stiffness C_1 and a damper. The damper is an electromechanical brake whose rotational motion is transformed into the progressive motion of a rod through a gear having a gear ratio t . The basic scheme of the brake and a typical dependence of the braking moment on rotor rotation velocity is given in Fig. 2.

The brake is an electric machine in which the hollow rotor rotates between two magnets. Such attenuators, damped by electromechanical brakes, were used in docking mechanisms of the Soyuz spacecraft.

The attenuator having such a brake provides damping that is approximately proportional to the velocity of its deformation, with the accuracy depending on the choice of the operational range of the brake characteristic. At a certain rotation velocity ω_{cr} , which is called critical, the real brake moment reaches its maximum; the value of the maximum depends mainly on the characteristics of the magnetic system.

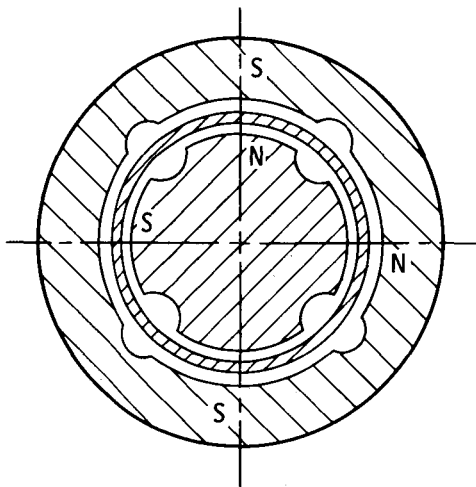


Fig. 2. Dependence of braking moment on rotor rotation velocity

III. MINIMUM MASS OF MOVING PARTS

One of the main problems that must be solved in the development of the electromechanical damper is the provision for the minimum mass of its moving parts.

It is clear by intuition that, at a rational choice of the brake parameters and operational range (from the standpoint of weight and dimensions), the gear ratio t must be comparatively large and the maximum rotor velocities will be equal to several thousands per minute. Then the rotor moment of inertia can considerably increase the mass of the damper moving parts.

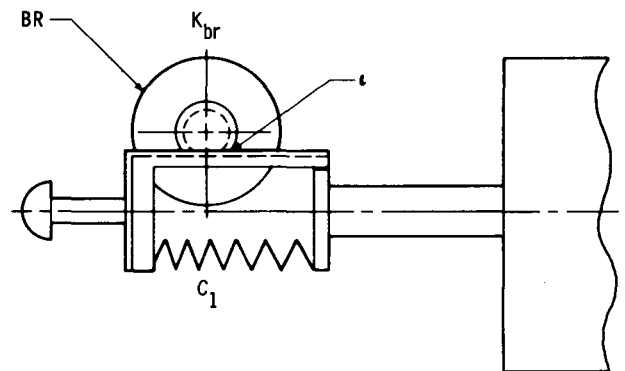
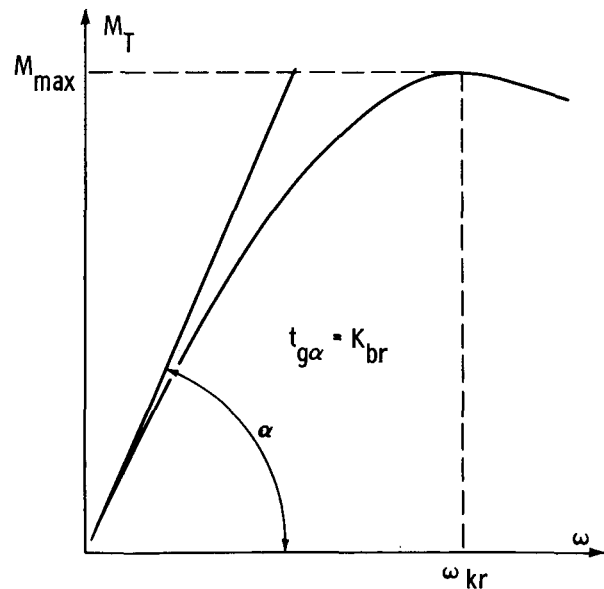


Fig. 1. Docking mechanism attenuator



Let us consider these problems in detail. The damping ratio K_d (N-s/m) is defined by the steepness of the brake characteristic K_{br} (N-m-s) and the gear ratio ι :

$$K_d = \frac{K_{br}}{\iota^2} \tag{1}$$

where the gear ratio ι is given in meters. For example, in a rack-and-gear drive the gear ratio is given by

$$\iota = \frac{mz}{2}$$

where m is the gear modulus and z is the number of teeth in the gear engaged with the rack. In a screw gear

$$\iota = \frac{S}{2\pi}$$

where S is the screw pitch.

The mass of the brake's moving parts m_r reduced to the progressive motion of the rod is given by

$$m_r = \frac{I_r}{\iota^2} \tag{2}$$

The notion of the reduced mass is based on the condition that the inertial force developed at the rod during the rotor acceleration is equal to the inertial force of the reduced mass m_r , the rod acceleration being the same.

However, the mass does not fully characterize the dynamic qualities of the system, just as the dynamic characteristics of an electric drive are not governed by the moment of inertia of the motor rotor only.

IV. TIME CONSTANT

By analogy with the study of motor dynamics, let us introduce the notion of a time constant for the damper T_d which will be suitable for further analysis

$$T_d = \frac{m_0}{K_d} \tag{3}$$

where $m_0 = m_r + m_{rod}$ and m_{rod} is the mass of the attenuator moving parts including the rod and gear-element masses.

The physical meaning of the damper time constant becomes evident when one considers the law of motion for the rod under the application of a constant force F . In this case, the equation of motion for the rod has the form

$$m_0 x'' + K_d x' = F$$

where x is the rod movement.

At zero initial conditions, if the damping ratio K_d is considered to be constant, the solution of the equation is

$$x' = \frac{F}{K_d} \left[1 - \exp\left(-\frac{K_d}{m_0} t\right) \right]$$

hence, the rod velocity x' approaches its set value with the time constant T_d .

It follows from Eqs. (1), (2), and (3) that

$$T_d = \frac{I_r}{K_{br}} + \frac{m_{rod}}{K_{br}} \iota^2 \tag{4}$$

As can be seen from the above equation, if the term defined by the mass of the moving parts of the rod and gear elements is not taken into consideration, the damper time constant is independent of the gear ratio ι and equals the brake time constant T_{br}

$$T_{br} = \frac{I_r}{K_{br}}$$

Let us consider how the brake time constant depends on its parameters. The initial steepness of the brake moment characteristic is defined by

$$K_{br} = \frac{\pi \cdot 10^6 B_0^2 d_r^3 L \cdot \delta \cdot K_\phi}{4\rho K_R} \text{ (N-m-s)}$$

where B_0 (T) is the magnetic induction in an air gap, which is considered constant along the rotor working length L (m) and polar arc width; ρ ($\Omega\text{-mm}^2/\text{m}$) is the resistivity of the hollow cylinder material; K_ϕ is the polar arc coefficient ($K_\phi < 1$); K_R is the coefficient including the resistance of the rotor frontal parts ($K_R > 1$); and δ (m) is the hollow cylinder thickness.

If the moment of inertia of auxiliary elements and frontal parts is taken into consideration, the rotor moment of inertia is defined by

$$I_r = \frac{\pi d_r \delta \gamma L K_I}{4g}$$

where γ (kg/m^3) is the specific density of the hollow cylinder material, $g = 9.81 \text{ m}/\text{s}^2$, and K_I is the coefficient which allows for the increase of the hollow cylinder's moment of inertia at the expense of its frontal parts and auxiliary elements ($K_I > 1$).

Using the last two equations for the brake time constant in an initial portion of the moment characteristic curve, i.e., for the constant steepness of this curve which is equal to its initial steepness, we get a simple relation:

$$T_d = \frac{10^{-6} \gamma \rho}{B_0^2} \cdot \frac{K_R K_I}{K_\phi} \quad (\text{s}) \quad (5)$$

where γ is given in kg/m^3 , ρ is in $\Omega\text{-mm}^2/\text{m}$ and B_0 is in T.

This equation shows that if the coefficients K_ϕ , K_I , and K_R are not taken into account, the brake time constant depends only on the hollow cylinder material of the brake and the induction in the magnetic gap.

V. MATERIAL SELECTION

The product $\gamma\rho$ in Equation (5) is minimum for aluminum. Therefore, this material is best for the hollow cylinder from the standpoint of the minimum brake inertia.

$$(\gamma\rho)_{\text{Al}} = 75.5 \frac{\text{kg}\cdot\Omega\text{-mm}^2}{\text{m}^4}$$

The production is twice as large for copper.

$$(\gamma\rho)_{\text{Cu}} = 155.0 \frac{\text{kg}\cdot\Omega\text{-mm}^2}{\text{m}^4}$$

The resistivity of the material is taken at room temperature.

VI. SAMPLE CALCULATION

Equation (5) allows us to predict a theoretical value for the electromechanical-damper time constant. If the magnetic induction in the gap B_0 is 0.6 T, then, taking the values of the coefficients to be

$$K_\phi = 0.5 \quad K_R = 1.3 \quad K_I = 1.5$$

we shall get

$$T_{br} = 0.85 \cdot 10^{-3} \quad (\text{s})$$

for the aluminum rotor.

When $B_0 = 1.2$ T, T_{br} decreases by a factor of 4.

$$T_{br} \approx 0.21 \cdot 10^{-3} \quad (\text{s})$$

An absolute value for the reduced mass of the brake's moving parts may be found from

$$m_r = T_d \cdot K_d$$

For instance, to have $K_d = 6000 \text{ N}\cdot\text{s}/\text{m}$, then at $B_0 = 0.6\text{T}$, $m_r = 5 \text{ kg}$ for the aluminum rotor and the values of the coefficients K_ϕ , K_R , and K_I as above the mass m_r is commensurate with the attenuator rod and spring masses.

The increase of B_0 permits us to decrease still further the value of the reduced mass. Thus, the theoretical value of the time constant, on the one hand, gives the limit which can be attained and, on the other hand, it shows that, for a rational design, the brake inertia is commensurate with the inertia of other moving parts of the attenuator.

VII. MAGNETIC DESIGN

Figure 3 shows the characteristics of the brakes with permanent magnets made of the IuNDK GOST 9575-60 type alloy with varying thicknesses of the hollow cylinder. The maximum moment of the brake is mainly governed by the magnetic energy in the air gap and depends slightly on the hollow cylinder thickness. Naturally, when the hollow cylinder thicknesses are different and the air gap is the same, this moment is obtained at different rotational velocities.

For fixed magnet volume and configuration, we may choose a definite value of the air gap Δ_{opt} for which the magnetic energy in the gap is maximum. It is expedient to choose the gap value slightly smaller than Δ_{opt} because the initial induction B_0 in the air gap is larger than at the gap equals Δ_{opt} , and the scattering of the magnetic field, which is inherent in a system with permanent magnets, is less than expected.

When choosing the hollow-cylinder thickness δ , we take into account that since the initial steepness is proportional to that thickness and, at a larger thickness,

the maximum moment is obtained at a lower rotational velocity, the maximum braking power increases with decreasing hollow-cylinder thickness. Thus, from the standpoint of the brake's weight and dimensions, a smaller thickness of the hollow cylinder is more beneficial. However, this results in raising the maximum velocity of the brake and the value of the gear ratio ι , as well as in increasing the contribution of auxiliary elements to the rotor moment of inertia and the heating of the hollow cylinder, which will be discussed below.

Therefore, the choice of the hollow cylinder thickness depends practically on a definite construction of the brake and the damper as a whole, permissible maximum rotations of the brake, its rotor construction, the gear type and dimensions, and a requirement for linearity of the brake characteristic.

VIII. MAXIMUM ABSORBED POWER

The maximum power absorbed by the damper at a maximum attenuator deformation velocity is given by

$$W_d = K_d x_{max}'^2$$

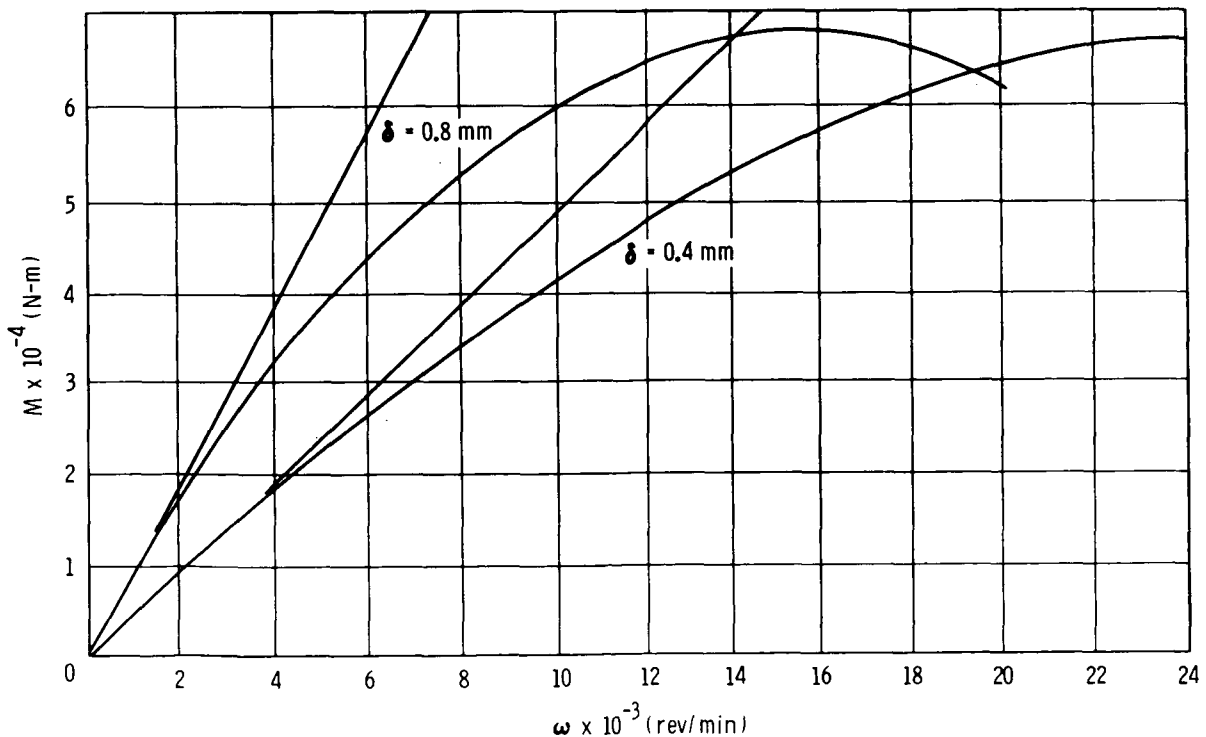


Fig. 3. Characteristics of brakes made of IuNDK GOST 9575-60 alloy

where x'_{max} is the maximum deformation velocity, which may be taken equal to the maximum velocity of the spacecraft rendezvous at the moment of impact. Thus, the power absorbed by the brake depends substantially on the rendezvous velocity. The damping ratio K_d usually depends on the attenuator stroke where the impact energy absorption takes place. The relation between the elastic-element stiffness C_1 and the damping ratio K_d is selected on the condition that a required coefficient of restitution at impact, which governs the engaging process, is provided. On the other hand, the stiffness C_1 must be one order of magnitude lower than that of the rest structural element so that the operation of the attenuator can be effective and govern the coefficient of restitution at impact. It should be noted that the electromechanical damper's weight and dimensions do not depend on its stroke.

IX. THERMAL DESIGN

At impact, the kinetic energy of the spacecraft relative motion goes into heating of the brake rotor. The calculations show that even when the maximum energy is absorbed, this heating is comparatively small. The heating of the rotor having mass m_r is defined by

$$\Delta t(^{\circ}\text{C}) = \frac{W_k}{\alpha m_r}$$

where W_k is the energy in joules, and α is the specific heat of the rotor material.

Since the duration of the impact is relatively small and in real conditions the brake operates in a vacuum, it

is assumed that the heat exchange, in fact, does not occur. If the maximum energy is absorbed, the heating of the brake rotor usually does not exceed several scores of degrees Celsius. For example, upon absorbing 500 N-m of energy, an aluminum rotor of mass 20×10^{-3} kg heats up approximately 50°C .

X. TESTING

More difficulties associated with the rotor heating result from the testing of the brakes at maximum rotation, when the resulting temperature can damage the structure. Therefore, the test bench for checking the brakes must provide for a short-duration operation of the brake and for the measurement of its operating parameters during this period.

When the structure temperature is changed during operation as a result of the heating due to energy absorption, the heat-conduction coefficient of the hollow-cylinder material is changed as well. It is accompanied by appropriate changes of the initial steepness of the brake moment characteristic; although, as indicated above, the brake maximum moment remains, in fact, unchanged.

Varying the temperature by 100°C changes the aluminum's resistance by a factor of about 1.36, and the damping ratio of the electromechanical damper is changed by the same factor. However, as the moment characteristic approaches saturation, this difference decreases with increasing attenuator-deformation velocity.

REFERENCE

1. Tamoyan, G. S., and Khairulin, N. Kh., "Several Questions on the Theory of Dampers," Moscow Energetics Institute, conference materials, 1969.

DISCUSSION: SOVIET SPACECRAFT

George Herzl:

I have some pictures here of the equipment that the Soviet Union displayed in Osaka, Japan. They come from the April 27 issue of *Aviation Week & Space Technology*, and I have their kind permission to present them. Since we are not as familiar with this hardware as our Russian colleagues are, I asked them for their concurrence to present these figures. Vladimir, if you would join me, we can describe these figures together.

Now in Fig. 1, on the left is Soyuz 4 and on the right, Soyuz 5. Here is the docking mechanism that we are discussing. Now, the overall length of Soyuz 4 is 50 ft and the diameter excluding these booms is 12 ft. The combined weight is 30,000 lb.

Each spacecraft consists of three modules. Here is the service module. Next is the command module, and finally the work and rest module. In addition to this, there is the tubular section which is part of the docking mechanism.

Vladimir, would you like to say something in addition?

Syromyatnikov:

Here you can see the solar batteries which you saw in flight. Here there are two antennas which are used when the two spaceships are approaching. You can see another antenna which is used for approaching too.

This is the command module, and in this module the astronauts return to the earth. Are there any questions?

Bill Simpson:

There seems to be a pipe across the docking tunnel section between the two living modules on the spacecraft. Can you tell me what that is? It is about on the centerline, midway between the antennas and external.

Syromyatnikov:

This is where the docking mechanism is located.

Maitland McLarin:

Can you show me where the cosmonauts came out to inspect the coupling?

Syromyatnikov:

You can't see it in this picture, but there is a hatch on the orbital module at another site.

Yuri Yezhov:

It can be seen from another view of the spacecraft. It's the orbital section of the spaceship. There is a hatch in this part from the other side.

Herzl:

Could I ask you about these numbers which you have discussed in your paper. Are these actual numbers applicable to your spacecraft or just assumed examples?

Syromyatnikov:

The brake characteristics which are shown here are very close to the real ones.

Yezhov:

May I ask a question on this one please. Where on the spacecraft are located the sun and star sensors?

Syromyatnikov:

Unfortunately, I am not familiar with this system, and I can't show you these devices.

Herzl:

Okay, Fig. 2 is the end view. That was the view from the left. In other words, this is the view from the Soyuz 4, which is the drogue, the passive device.

Vladimir, will you take it from here?

Syromyatnikov:

This is a radiator of the thermal cooling system. Here you can see the antennas very well, and batteries again. This is the orbital module. This is the work and rest module. The astronauts go to the open space from this module.

Herzl:

Figure 3 shows the end view of the service module. You will notice here in the middle are the four vernier nozzles.

You see next the toroid load structure. You can notice the pressure transducer here. What does this toroidal structure do, for example?

Syromyatnikov:

This is a device module. There are devices not there.

Herzl:

Oh, there is no gas.

Syromyatnikov:

No gas. There are some control devices.

Herzl:

Are these pressure transducers?

Syromyatnikov:

No, they are not.

Herzl:

What are these things here?

Yezhov:

He thinks they are pressure devices or something of that kind. He is not sure what it is.

Herzl:

It's not pressure. Okay, Fig. 4, please.

The next slide just shows another view of the juncture between the service module, command module again and the work-rest module. Notice here the umbilical cord which we saw on the other slides and in the films which they used when they were outside of the spacecraft.

Now this structure is here just to hold up the model in Osaka, Japan. It has nothing to do with the spacecraft. Here is the

cooling system, and here is an interesting thing. This slide is dark, but there is a periscope that is sticking out of the spacecraft. Is that correct? The slide is dark, so I can't see it.

Syromyatnikov:

It's no telescope, because there are no astronauts.

Herzl:

Figure 5, please.

Here we have a nice view of the service module. Again here are the same cooling pipes. Are these holes where the antenna fits in?

Syromyatnikov:

This is the eliminator. No, it's a window.

Herzl:

You can also see the elaborate electrical junction. Figure 6, please.

Here is the docking collar. And you notice here the shape of the shadow, indicating that it is flared.

Syromyatnikov:

It's flared during undocking.

Herzl:

This is for smoother docking?

Syromyatnikov:

This is for smoother docking.

Herzl:

Would you like to add something? Here we have the handles for the cosmonauts.

Syromyatnikov:

Yes, you're right. And here is the hatch for loading the module. It is not seen here, but you can see the antennas and some handles, a window.

Herzl:

Okay, Fig. 7, please.

That's another detail showing the juncture of the work/rest module (on left) and the command module (on right). Now this protrusion here on this side of the work/rest module—is that for the crane to lift up the spacecraft during assembly?

Syromyatnikov:

Yes, you're right. This is for the crane for lifting the spacecraft.

Herzl:

Vladimir, would you care to elaborate a little more on something else?

Syromyatnikov:

I am sorry, but I am not a designer and perhaps I will not satisfy you with my answers.

Herzl:

Well, thank you.

Fig. 1. Full-size mockup of two Soyuz spacecraft linked into what the Soviets describe as "the world's first space station" was put on display at Japan's Expo 70 in Osaka. Model depicts Soyuz 4 and 5, revealing differences between active and passive variants of the basic spacecraft.

Passive spacecraft, Soyuz 4, is at left and active variant, Soyuz 5, is at right. Overall length of model is more than 50 ft and maximum diameter, excluding girder-mounted acquisition and tracking antennas, is about 12 ft. Weight of the combined spacecraft is approximately 30,000 lb.

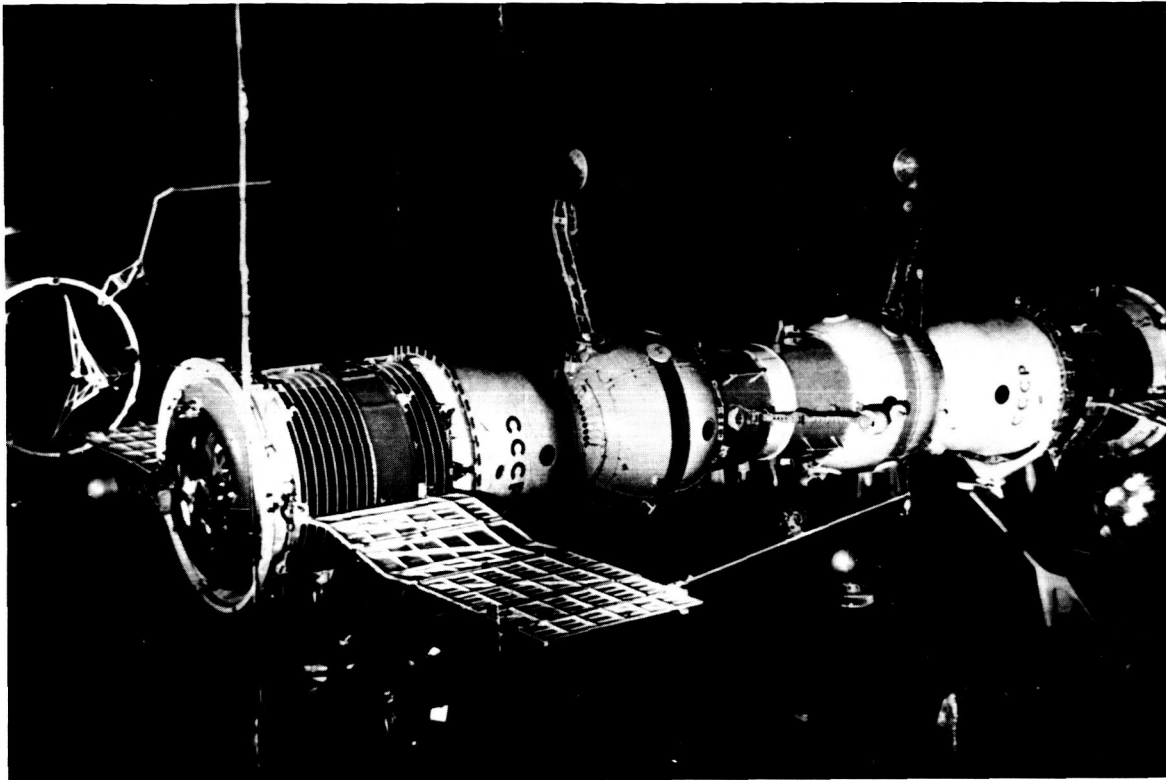
Tri-modular construction of the Soyuz is clearly shown. Service module, on which wing-like solar batteries are mounted, houses main power supply and restartable engine. Note low-pressure toroidal container for gas, probably oxygen, around exhaust nozzle mount.

Solar cells do not gimbal and are active on only one surface, indicating entire space station must be oriented toward sun to receive solar power. Communications with earth are maintained regardless of spacecraft orientation by means of phased array antenna mounted around the extreme forward edge of service module. Antenna consists of about 40 T-shaped units.

Command module is located immediately forward of service module, and contains couches for three cosmonauts. Main control console is located there. Work/rest module, forward of command module, is revealed as slightly larger in size. Command module contains about 143 cu. ft. of interior space while work/rest module has about 175 cu. ft., for a total of 318 cu. ft.

Additional crew space can be contained in tubular portion of structure forward of work/rest module, but in Soyuz 4-5 configuration, drogue and probe mechanism used in docking occupied this portion of spacecraft. Removal of docking mechanism would provide passage from one portion of space station to other, without necessity of extravehicular activity used to transfer crew members of Soyuz 4-5.

Note difference between long-range acquisition and tracking antennas mounted on girders on work/rest modules. Soyuz 4 antenna, left, is gimballed in two directions while Soyuz 5 antenna is stationary. Gimbaling permits passive



spacecraft to acquire signal from oncoming active spacecraft at distances of more than 100 mi. Tower mounting provides for receiving of signals with minimum of interference from spacecraft itself. Antenna on passive spacecraft appears to be transceiver, while separate small dish on active spacecraft antenna tower is for receiving only.

Active and passive roles of spacecraft could be reversed only by major changes in avionics configuration on the ground, prior to flight.

What appears to be Doppler velocity radar antenna is mounted on a smaller girder at 90 deg. angle to main acquisition radar. Radome-covered device appears to be four-horn directional radar. Girder is attached to the spacecraft at drogue tunnel and can be extended forward over the docking collar to come within inches of cone-shaped antenna on the other spacecraft. Opposite side of space station has the same configuration of antennas, but in reverse: radome-covered antenna is on the active spacecraft and cone-shaped antenna is located on the passive one.

Note receptacles for both large and small antennas. Main acquisition tower folds forward toward receptacle in roof of drogue and probe tunnels, while smaller Doppler radars fold backward into different receptacles on same tunnels. Bend in the main radar tower is to accommodate the curve of the work/rest module, over which it lies during launch of the space vehicle.

Radome antennas at rear of each spacecraft appear to be used for close approach of additional spacecraft. At greater distances, the main acquisition antenna of the passive spacecraft can be gimbaled to acquire signals from oncoming third or additional active spacecraft.

For re-entry, the two spacecraft are separated and the crew takes positions in command module after hatch between it and work/rest module is sealed. Work/rest module is separated first, then service module is separated. Bell-shaped command module makes re-entry with flatter portion, containing heat shield, facing forward. (Photo and caption courtesy of *Aviation Week & Space Technology*.)



Fig. 2. Asymmetrical antenna deployment with gimballed passive acquisition radar transceiver antenna of Soyuz 4 in foreground and fixed-position dual-dish active spacecraft antenna in background. Note cone-shaped Doppler radar antenna at left is attached to Soyuz 4 and radome-covered antenna is attached to Soyuz 5, while on right side of joined spacecraft their positions are reversed. (Photo and caption courtesy of *Aviation Week & Space Technology*.)

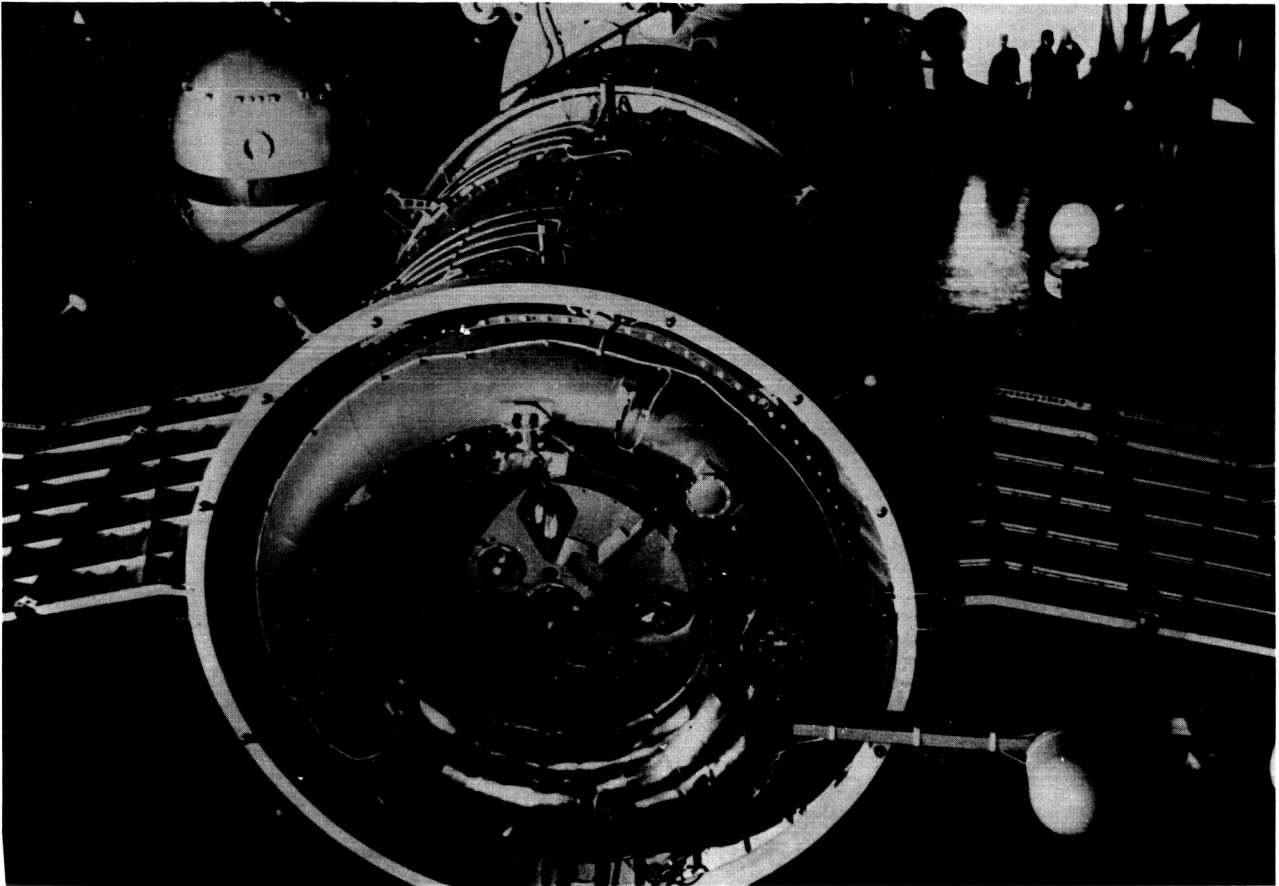


Fig. 3. Nozzle configuration also shows emplacement of the rearward-looking radome. This radome, on the rear of each Soyuz spacecraft, appears designed for use in alignment for formation flying and for control where a third spacecraft is involved. Sump-like depression in nozzle cluster holds radome during launch.

Plate containing radome sump appears to blow away after orbital insertion, revealing main engine bell and four cruciform vernier rockets used in final approach maneuvering. Two clusters of four small pipes, mounted at top and left and protected by small heat shield, appear to be connector guides to main propulsion stage. Third cluster, right side, is missing. Note pressure, temperature transducers on toroid, which is protected by shiny shield. (Photo and caption courtesy of *Aviation Week & Space Technology*.)

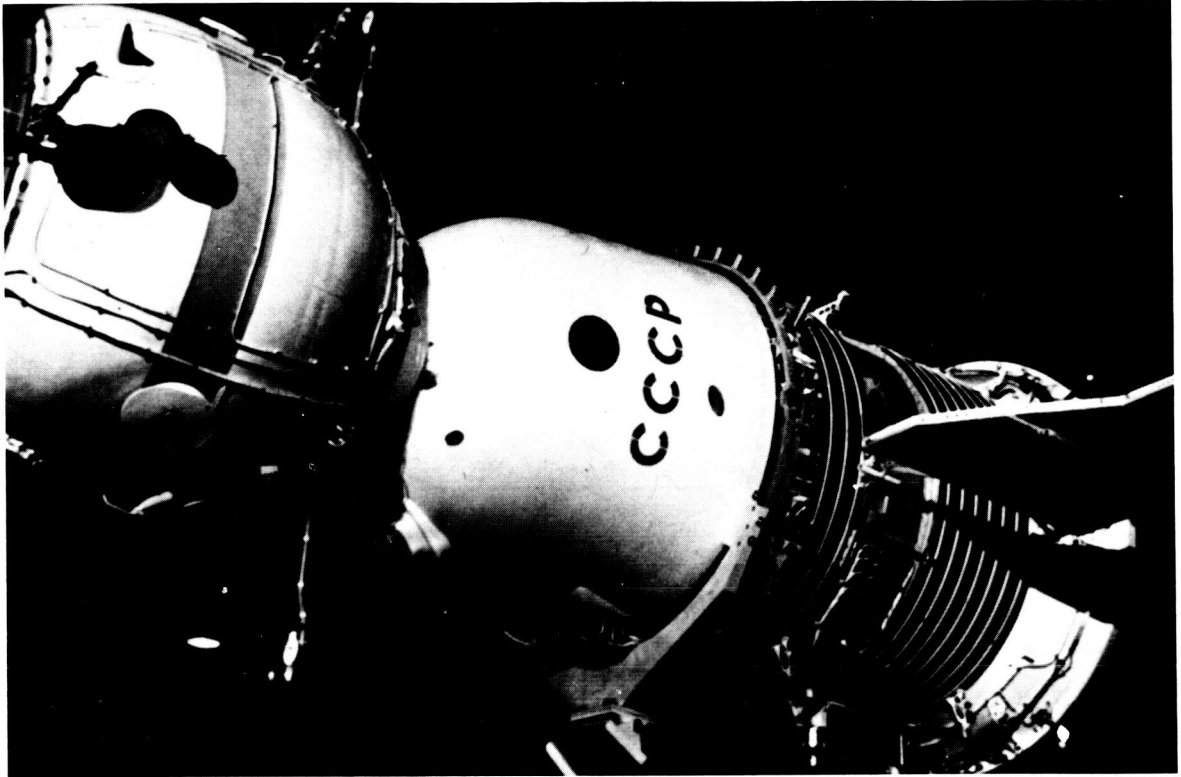


Fig. 4. Umbilical plug-in units are located on opposite sides of the work/rest module supplying oxygen, power and communications lines to cosmonauts during extravehicular activities. Nozzle for venting carbon dioxide is contained in the unit. During EVA, cosmonauts attach a long extension umbilical, permitting them a wide range of movement. Exit hatch is directly in front of umbilical plug-in.

Black tubular structure extending from bottom of the command module is a periscope which can be switched from outward-looking to sideward-looking mode by an electrically actuated servomechanism in the periscope head. Periscope could inspect spacecraft during flight and monitor EVA. It is mounted on a plate which is blasted away prior to re-entry.

Shiny nozzle-like structure extending from bottom of service module is receptacle for main umbilical in prelaunch mode. Small white spheres, attached to rear ring of service module, denote position of fairing which covers spacecraft during launch and orbital insertion. Clamp protruding from forward top of service module has dual purpose of holding spring-loaded folding solar panels and protective fairing before and during launch.

Main body of service module is painted black for heat absorption; white tubing forms a fluid loop which carries heat to other modules. (Photo and caption courtesy of *Aviation Week & Space Technology*.)

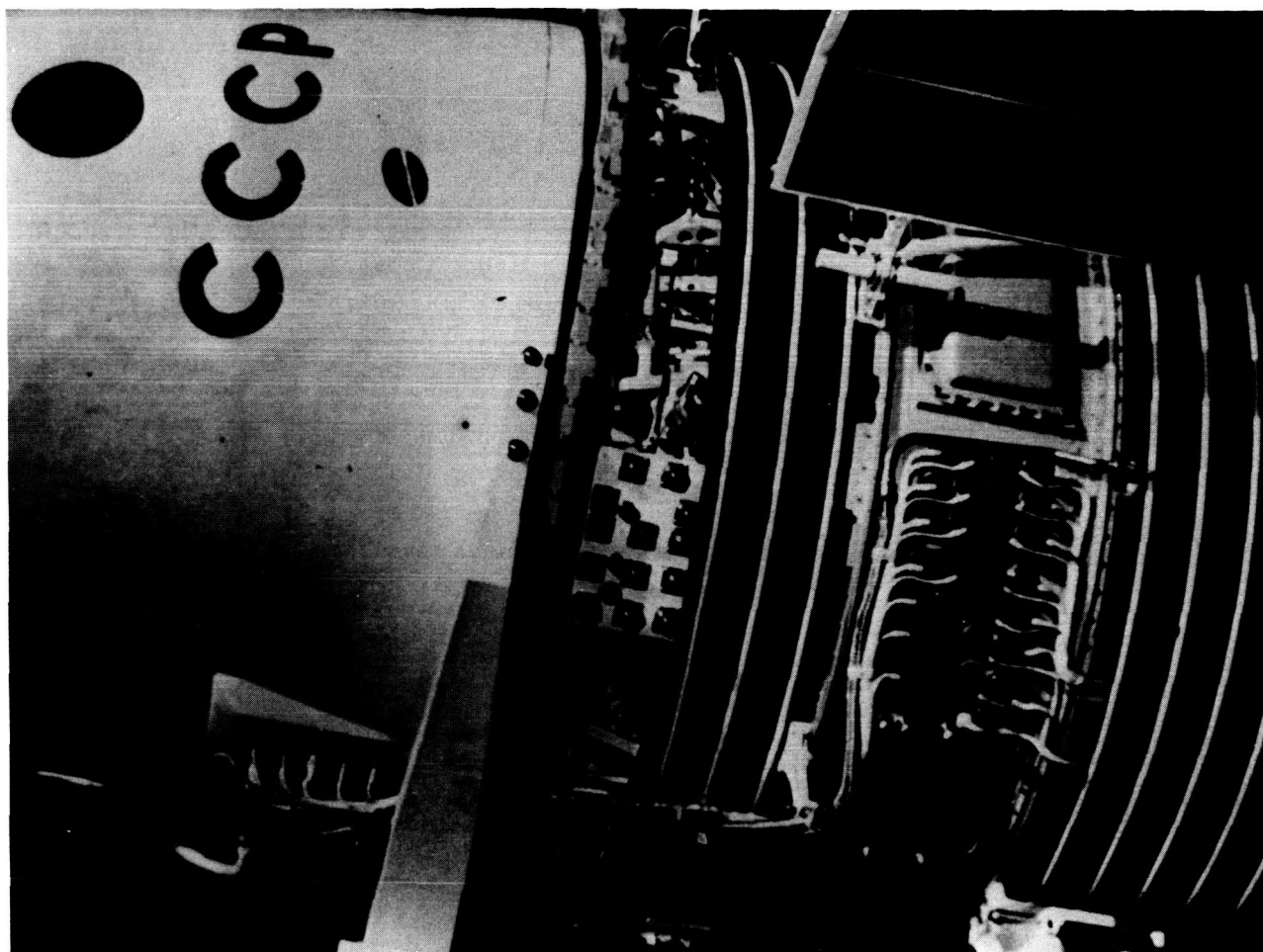


Fig. 5. Junction of command and service modules, is partially obscured by support brace for mockup. Separation of service module leaves clean re-entry surface, containing heat shield, on command module. Heavy conduit between modules is shown. Plate on command module containing hermetic seals for conduit is blasted off at separation of modules. Small pipes, one of which is clearly shown at top of spacecraft, are for venting. They are located at 60-deg. angles around service module.

Note location of active solar batteries on underside of wing-like support structure. Upper side of structure has no batteries. (Photo and caption courtesy of *Aviation Week & Space Technology*.)

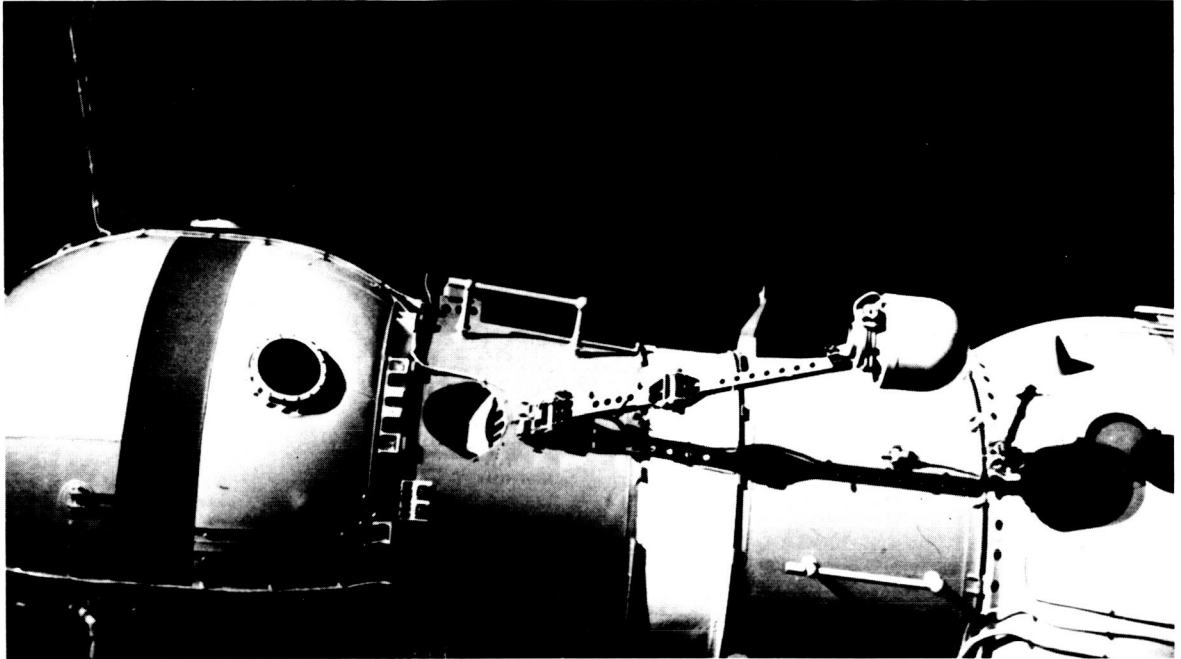


Fig. 6. Junction of two spacecraft is achieved when active Soyuz 5, at right, slips probe into passive Soyuz 4, left. Docking collar is permanently attached to front of drogue tunnel on Soyuz 4. Its forward end is slightly flared, as shown by shadow, permitting a tight fit.

Receptacle for radome is cut to shape of radome, indicating stowage position during launch. Radome is extended to a point where it would be only inches away from point of cone-shaped antenna on other spacecraft. Radome-cone pair on one side of mockup is positioned so that they almost meet, while on side shown the cone antenna is pointed at approximately a 90-deg. angle away from radome.

Object protruding like a thumb at forward edge of active spacecraft, on right, appears to be light source arranged to interact with black tubular photocell mounted at rear of drogue tunnel on left spacecraft. Three such combinations are deployed at 120-deg. intervals around the docking collar and drogue tunnel.

The optical arrangement could serve as backup for Doppler radar during the docking exercise, or could serve as an alignment check prior to "hard docking" or firm latching together of the spacecraft.

Note hand-holds for crew members to use during EVA. Roll control jets are visible in lower left corner, just to the rear of dark ring painted around work/rest module. (Photo and caption courtesy of *Aviation Week & Space Technology*.)

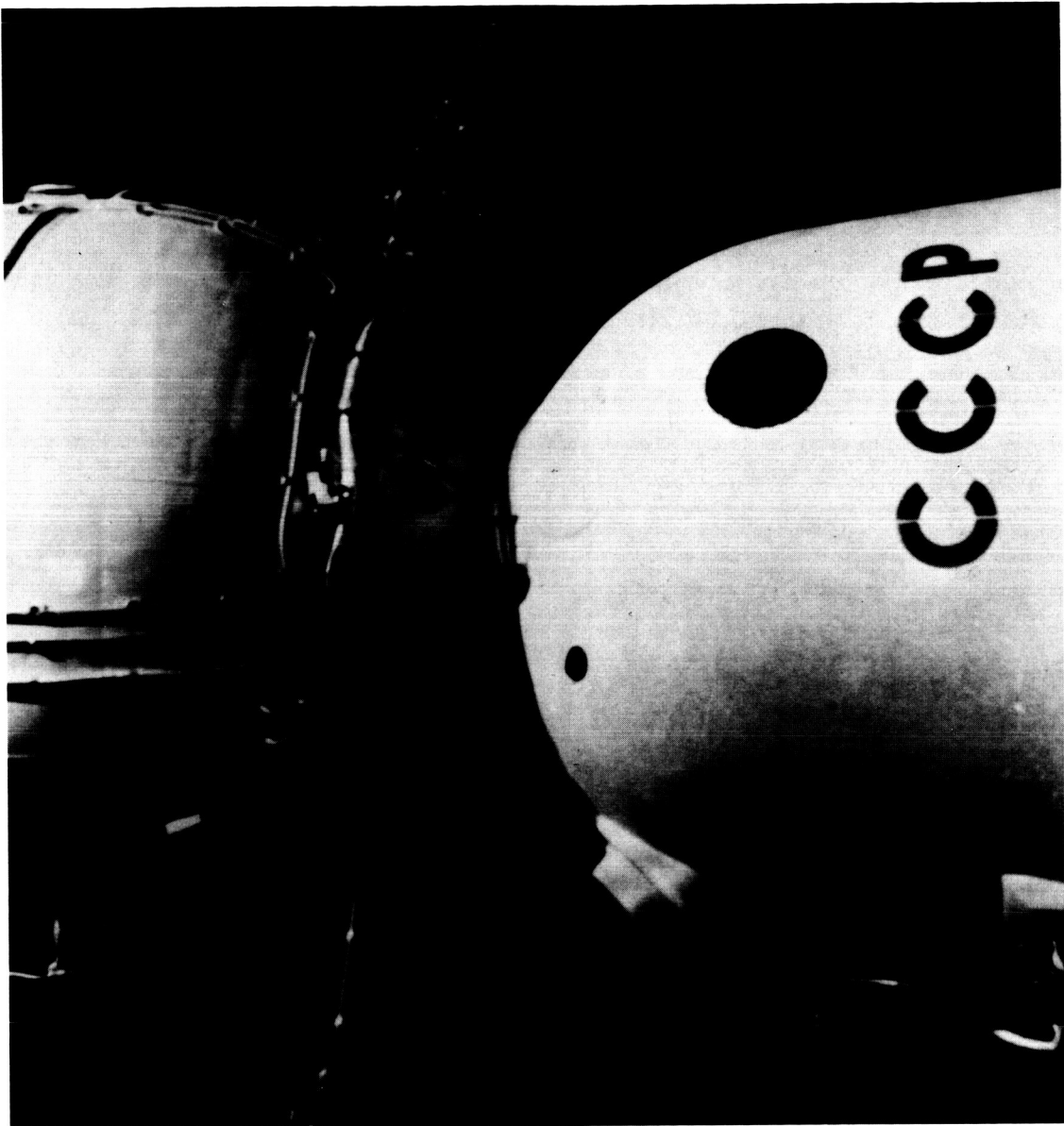


Fig. 7. Umbilical plug-in is movable along one axis. Hermetically sealed lines emerging from work/rest module are clustered into a single cable leading to command module. Sump-like protrusion from command module probably is for crane attachment when spacecraft is on ground. (Photo and caption courtesy of *Aviation Week & Space Technology*.)

DAMPER DESIGN FROM A STRUCTURAL ENGINEER'S POINT OF VIEW*

Jay C. Chen
*Jet Propulsion Laboratory
California Institute of Technology
Pasadena, California*

A nonlinear structural analysis, employing the nonlinear damper characteristics obtained from a damper test, was successfully performed on the Mariner spacecraft's solar-panel system, and the result was compared with results from a system-level spacecraft test in which some solar-panel tip dampers bottomed at a certain frequency. The analysis showed that the damper bottoming was attributable to a "jump phenomenon" that can result when a damper's response is not single-valued at some frequency. The information provided by such an analysis can be very valuable to the structural engineer.

I. INTRODUCTION

The design criteria for a complex structural system, such as a spacecraft, require that its structural elements be able to withstand all design loading conditions without failure, general yielding, excessive deflection, or damage to supported components. The energy of response of a structural element must be dissipated in some manner to prevent excessive deflection due to vibration-induced loading. If the structural damping is not adequate, additional dampers must be introduced to damp out the motion. Then, the structural engineer faces the additional requirement that the functions of these added dampers be properly incorporated into the structural analysis.

Because of the complexity of the structural system, the structural analysis generally employs the finite element method. The continuous structure is idealized to a model of discrete elements, and the dampers are included among these elements. By assuming that the damper is linear (i.e., the damping force is linearly proportional to the velocity), one can calculate the response of the structural system. A typical response curve for the solar-panel system of the Mariner spacecraft is shown in Fig. 1.

*This paper presents the work of one phase of the research carried out at the Jet Propulsion Laboratory, California Institute of Technology, under NASA Contract NAS7-100.

Since the damping provided by the dampers is much greater than the structural damping, the structural response is very sensitive to the dampers. Therefore, the question of whether the damper is properly represented in the structural analysis is constantly asked by the structural engineer. In this paper, the solar-panel tip damper of the Mariner spacecraft is taken as an example

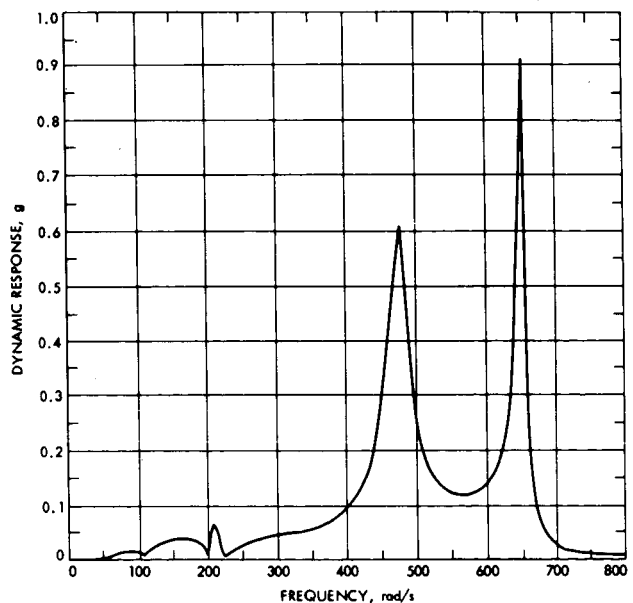


Fig. 1. Solar panel response

for demonstrating that the conventional damper design data are not enough for a proper structural analysis. Also, the discussion indicates what would be desirable damper design data from a structural engineer's point of view.

II. DAMPER DESIGN SPECIFICATION

The Mariner spacecraft's solar-panel tip damper is shown in Fig. 2. The design requirement specifies that when the damper oscillates with a ± 0.025 -in. displacement, the output rms force must be within the limits specified in Fig. 3 over a certain frequency range. The only information on the damper characteristics that a

structural engineer would normally have is of the type contained in Fig. 3. The choice of the mathematical representation of the damper for purposes of structural analysis is left to the individual structural engineer.

In the case of the Mariner spacecraft, the damper design data were considered to be such that the damping force was linearly proportional to the damper velocity (indicating a so-called linear damper). An approximate damping coefficient for the dampers was established from the design data, and a structural analysis was performed on the Mariner spacecraft's structural system. Figure 1 shows a part of the response obtained from that analysis.

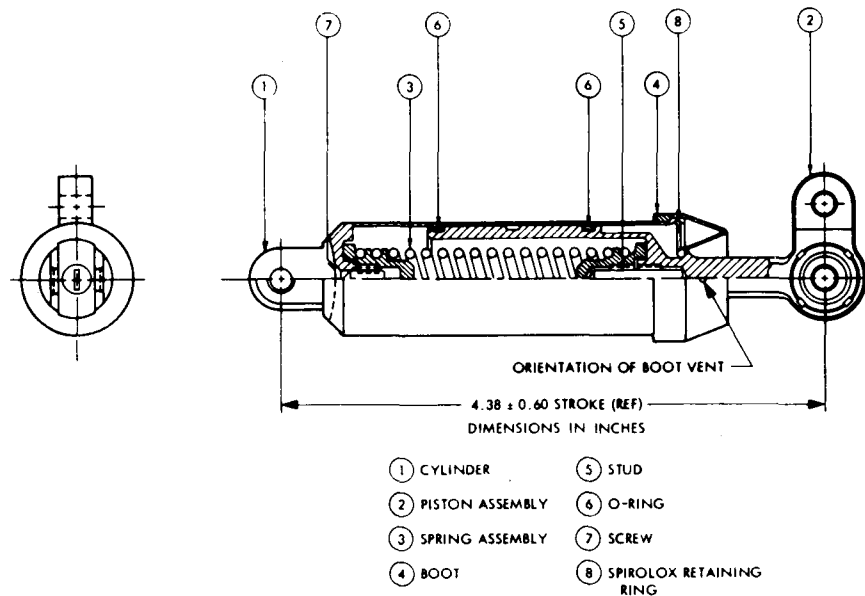


Fig. 2. Solar panel damper

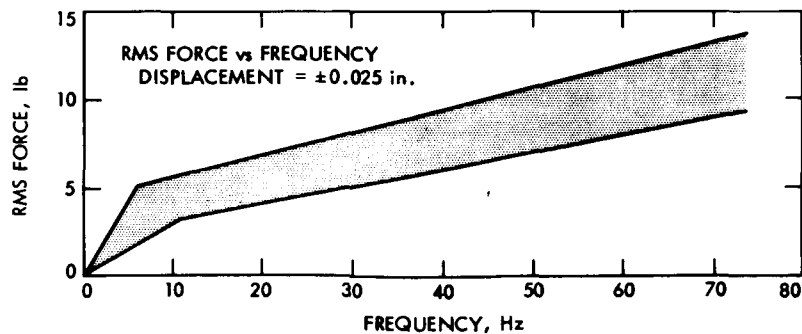


Fig. 3. RMS damping force versus frequency

III. INVESTIGATION OF THE DAMPER CHARACTERISTICS

During a system-level forced-vibration test of the Mariner spacecraft, it was found that some dampers bottomed at a certain frequency. Although no structural damage was found, an investigation of damper characteristics was conducted. A damper-test setup was designed in which the damper was rigidly supported at one end; the other end was connected to two 25-lb-force shakers in series. Each end of the damper was attached to a load cell, and an accelerometer was also mounted on the shaker head to monitor the input signal. (Figure 4 is a schematic drawing of the damper-test setup.) An electronic oscillator and amplifier provided the sinusoidal input to the shakers, and the amplitude and frequency of the shakers were controlled. The force was varied from low amplitude and low frequency to high amplitude and high frequency in small increments. During each test, the shakers were set at a preset frequency, and the amplitude was fixed at a predetermined value and controlled by a servo system.

Figure 5 shows the rms damping force versus damper velocity for different damper displacements. Since a truly linear damper should be represented by a straight line in this plot, these curves are an indication that these dampers are nonlinear (i.e., the damping force is not linearly proportional to the damper velocity). However, the fact that the dampers are nonlinear still does not offer an explanation for the failure that occurred during the structural-system test. A continuous, instantaneous damping force, as a function of damper velocity and displacement, is required not only for the mathematical representation of the damper as an integral part of the structural model but also for the understanding of the damper's characteristics. Figure 6 shows the instantaneous damping force as a function of velocity; Fig. 7 shows the instantaneous damping force as a function of displacement. When the damper oscillates with different maximum amplitudes; different instantaneous values are obtained. With this information, a mathematical model for the dampers can be constructed.

The next step is to incorporate the mathematical model into the structural analysis. A structural system has many natural vibration modes, and the damper is designed to damp the most critical mode—generally the mode with the lowest frequency. Since the modes are

separated, a one-degree-of-freedom system can be studied without the loss of generality. Figure 8a, showing the response-frequency relation of a one-degree-of-freedom linear system, indicates that the damping reduces the response amplitude. More importantly, the response at each frequency and damping coefficient is single-valued. Figure 8b is the response-frequency relation of a one-degree-of-freedom nonlinear system; the nonlinear mathematical model is obtained from the damper-test data. The theory states that when the frequency is increasing, the response will follow the curve a, b, c, d, e, and when it is decreasing, the response will follow e, d, c, f, g, and a. Between b, c and f, g, the response is called the jump phenomenon. This is a special feature existing in nonlinear vibration when the response is not single-valued at a certain frequency. During the jump, although the amplitude of displacement is finite, the rapid change of amplitude generates a large acceleration. It was concluded that this excessive acceleration caused the bottoming of the damper during the structural-system test. A one-degree-of-freedom system was constructed to test the Mariner spacecraft's solar-panel tip damper, and the test clearly demonstrated the jump phenomenon (Fig. 9).

IV. CONCLUSION

A nonlinear structural analysis has been successfully performed on the Mariner spacecraft's solar-panel system using the nonlinear damper characteristics obtained from the damper test. It is an extra effort for the structural engineer to perform a nonlinear structural analysis. Nevertheless, the state of the technology is such that a systematic nonlinear structural analysis can be made (Ref. 1) if the characteristics of nonlinearity are known. From a structural engineer's point of view, the solar-panel tip damper is still a good design despite its nonlinear characteristics because it is simple to manufacture and operate. However, a structural engineer wants to know just how nonlinear a damper is. In other words, merely a design specification, such as that shown in Fig. 3, is not adequate for a proper structural analysis. Complete knowledge of the damping force as a function of velocity and displacement over a wide range becomes necessary. It is not a difficult task to obtain the information indicated by the damper test, and it is the author's belief that it should be provided to the structural engineer by the designer.

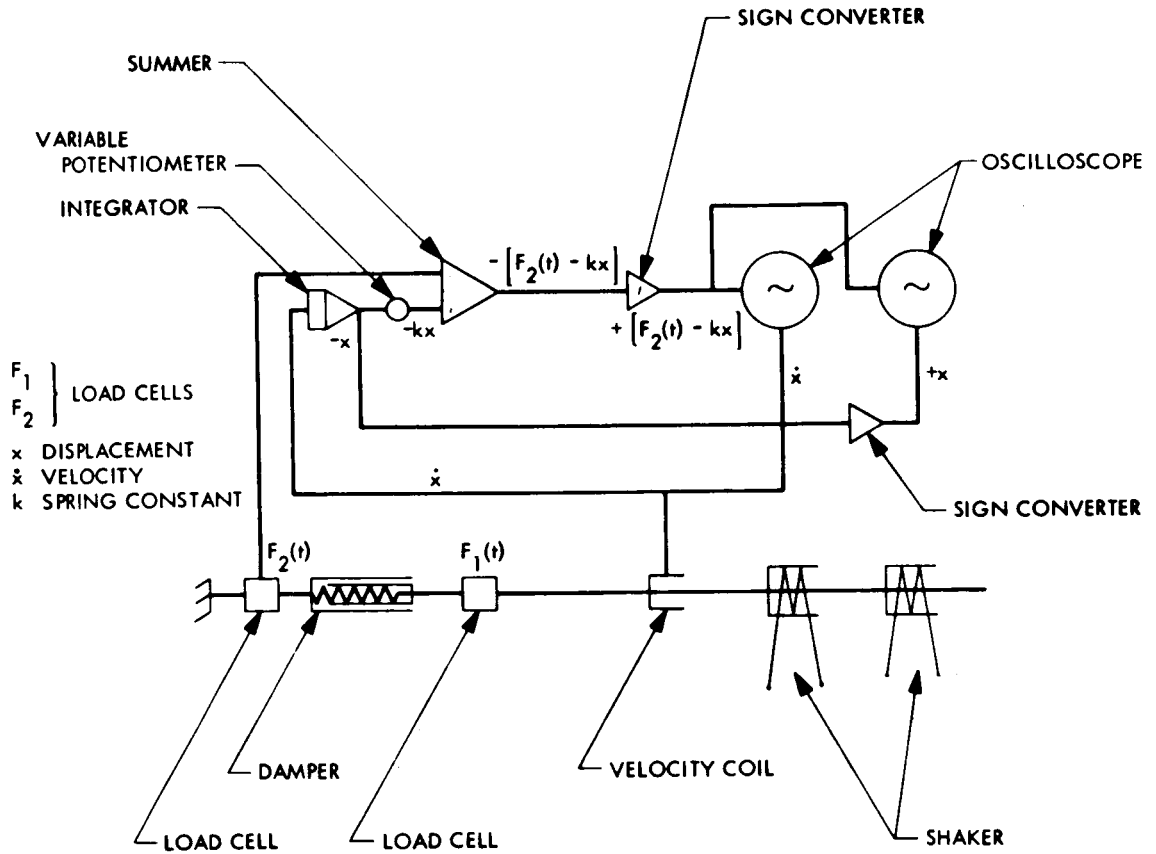


Fig. 4. Damper test setup

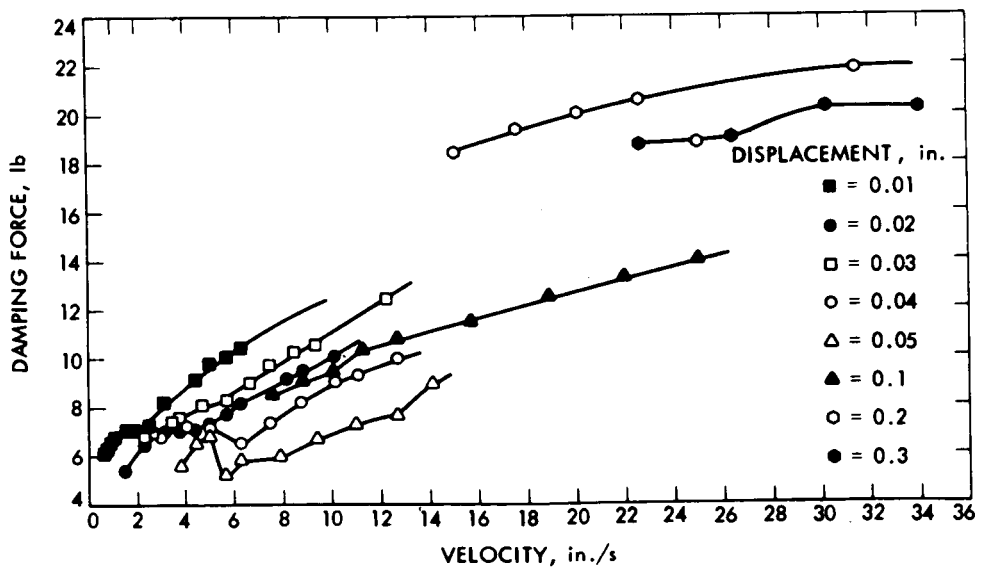


Fig. 5. RMS damping force versus velocity

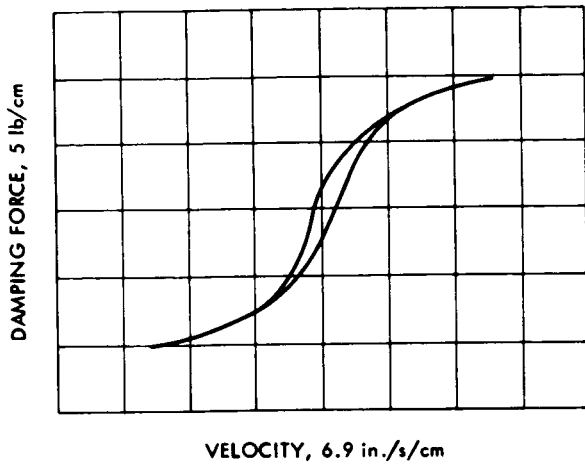


Fig. 6. Instantaneous damping force versus velocity

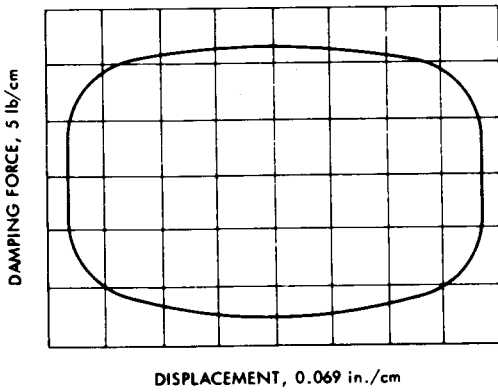


Fig. 7. Instantaneous damping force versus displacement

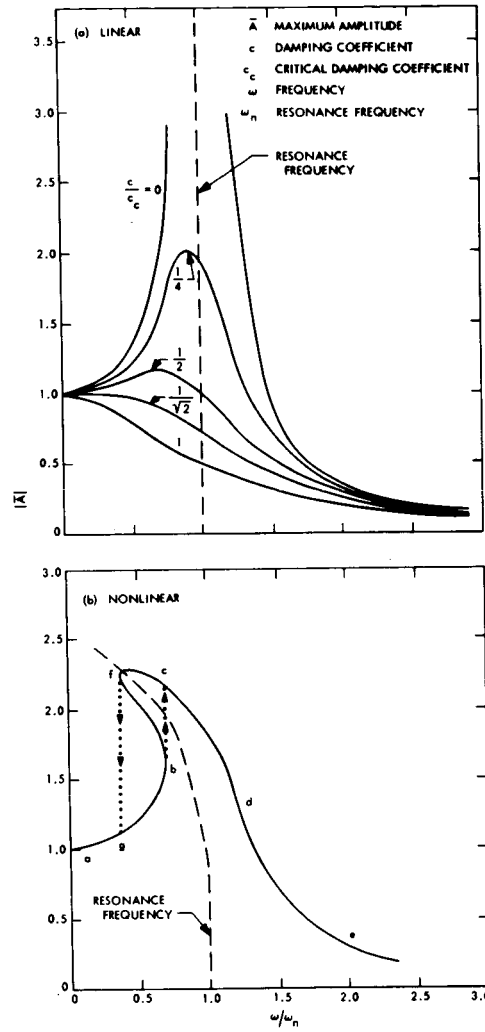


Fig. 8. Response frequencies for linear and nonlinear systems

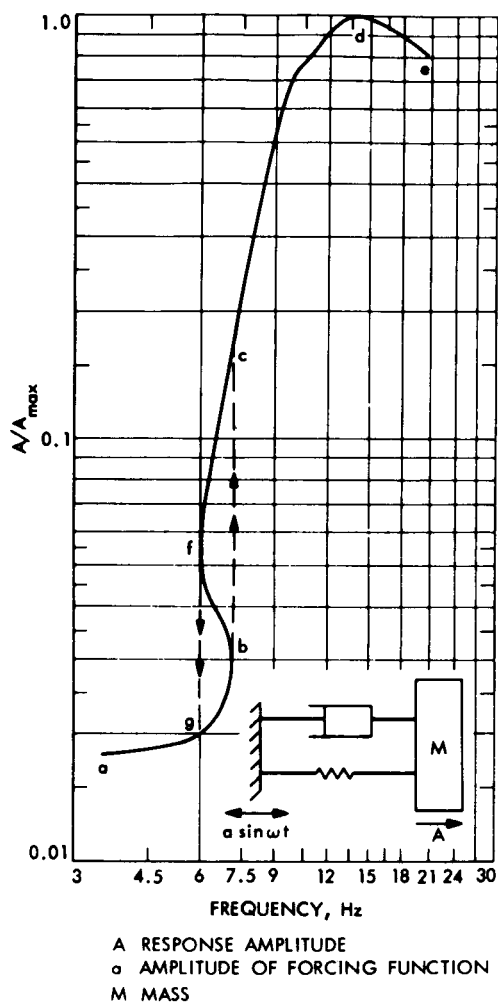


Fig. 9. Jump phenomenon

REFERENCE

1. Chen, J. C., "A Preliminary Study of Nonlinearly Coupled Structural Systems," Space Programs Summary 37-59, 3:158-162, Supporting Research and Advanced Development, Jet Propulsion Laboratory, Pasadena, Calif., 1969.

TERMOMECHANICAL PISTON PUMP DEVELOPMENT*

Eric E. Sabelman
*Jet Propulsion Laboratory
California Institute of Technology
Pasadena, California*

A thermally powered reciprocating pump has been devised to replace or augment an electric pump for the transport of temperature-control fluid on the Thermoelectric Outer Planet Spacecraft (TOPS). The thermally powered pump operates cyclically by extracting heat energy from the fluid by means of a vapor-pressure expansion system and by using the heat to perform the mechanical work of pumping. In essence, the pump is a mechanical analog of the electronic astable multivibrator.

A feasibility test unit has been constructed to provide an output of 7 in.³ during a 10- to 100-second cycle. It operates with a fluid input temperature of 200° F to 300° F and a heat sink temperature of 0° F to 30° F. A second model having improved fluid sealing and cycle period is now being tested.

I. INTRODUCTION

The Thermoelectric Outer Planet Spacecraft (TOPS) project is a JPL advanced system technology activity whose purpose is to develop and demonstrate the capability for performing outer-planet missions such as the proposed Grand Tour. The power source for the spacecraft is a Radioisotope Thermoelectric Generator (RTG) that converts a maximum of 9,000 W of thermal power to 585 W of electrical power. The RTG is mounted on a hinged boom 6 m away from the scientific instrument package in order to minimize the radiation flux at the instruments. Because of the open configuration and extreme distance from the sun, the instrument package would require approximately 125 W of thermal control power in excess of internal dissipation to maintain the desired minimum temperature. The conventional heating method is to install resistance heaters in the instrument. However, only 25 W of electrical power are allocated for temperature control; therefore, alternatives must be sought to make direct use of the RTG thermal output.

One of these alternatives is a fluid loop that would circulate a temperature-control (TC) fluid (such as Coolanol 45, a silicate ester fluid) in a closed tube between heat exchangers at the RTG and science platform. Rotary electric pumps for this task consume 10 to 15 W. The thermomechanical pump is a device intended to replace or back up the electric pump by making use of the 100° C-or-greater temperature differential between the warm, incoming fluid and the instrument platform. A heat sink temperature, the same as the instrument operating temperature, was chosen so that the rejected and waste heat from the pump performed the thermal-control function. The minimum fluid flow required is 1.7 cm³/s, and the thermal pump should be able to operate continuously for 10 years if it is to supplant rather than augment an electric pump.

II. BASIC DESCRIPTION

The design resulting from this study is a two-cylinder piston pump with provision for diverting all or part of the warm TC fluid to operate a heat-to-displacement conversion mechanism that drives the pistons. Each cylinder is equipped with a TC-fluid chamber, a thermally insulating piston, a piston-return spring (which,

*This paper presents the results of one phase of research carried out at the Jet Propulsion Laboratory, California Institute of Technology, under Contract No. NAS7-100.

with the aid of the line static pressure, drives the piston during the downstroke), a chamber containing an evaporable working fluid, such as Freon-12, a copper-tube heat exchanger coupled to the TC fluid input of the other cylinder, and a heat-sink surface (Fig. 1). As vapor in one cylinder condenses, that piston sinks, taking in fluid through the second heat exchanger and causing its piston to rise; the system is a mechanical analog of the electronic astable multivibrator. Each cylinder requires three check valves (Fig. 1) and constricting valves to set the direct-to-diverted fluid input ratios. Since the pump is not self starting, provision must be made to supply warm TC fluid and/or piston displacement until self-powered oscillation begins. This can be accomplished by the installation in one or both cylinders of an electric resistance heater that cycles until warm fluid is available to the heat exchanger.

tially confined by the saturated-vapor portion of the Rankine cycle. The working fluid should be neither subcooled nor superheated, since this would introduce a lag because preheating of the liquid or cooling of the vapor without condensation would be required. Estimated Rankine efficiency is of the order of 2 percent, which is more than sufficient to overcome the frictional losses of pumping the TC fluid through the loop.

The energy-balance equation for one cylinder equates the work output W_p , heat lost to the sink q_{FS} , and change in internal energy of the working fluid U to the sum of the heat input through the heat exchanger q_H and the heat input through the piston q_p :

$$W_p + q_{FS} + U + \text{losses} = q_H + q_p$$

III. THERMODYNAMIC MODEL

The thermodynamics of the thermal pump are essen-

The heat input q_H during the expansion part of the cycle must be sufficient to overcome the continuous q_p

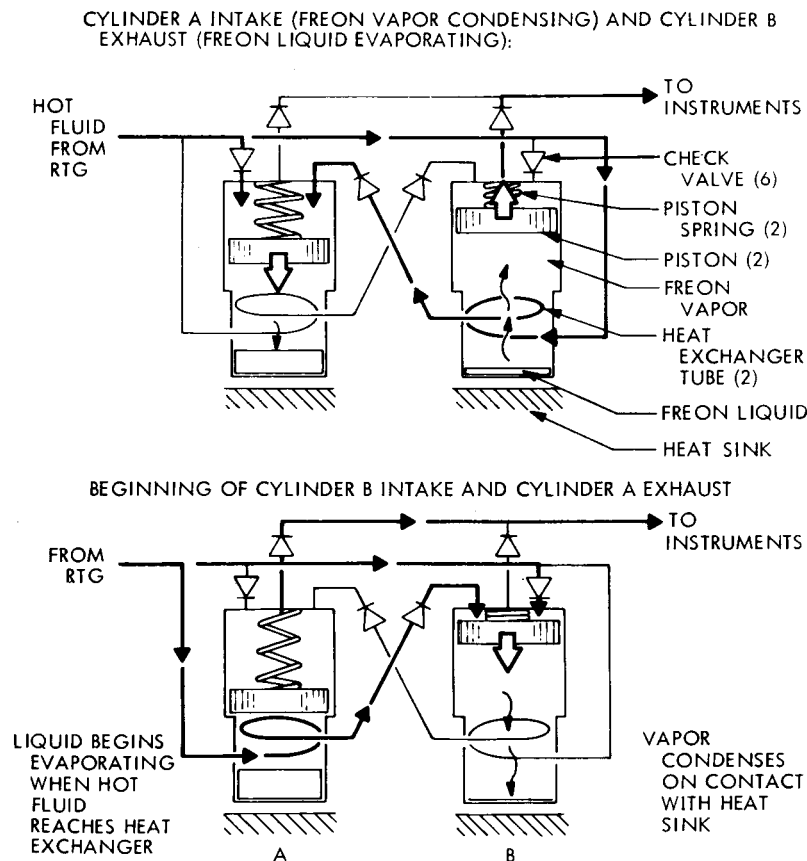


Fig. 1. Thermal pump operating cycle

and q_{FS} . The heat input q_H can be expressed as the heat lost by the TC fluid moving through the exchanger or as the integrated flux through the exchanger-tube wall. The working fluid can be evaporated by nucleate boiling during most of the expansion part of the cycle because of the high thermal gradient attainable with the low conductivity of the Freon liquid. The change in internal energy is the sum of the heat gained by the Freon liquid q_F and that used to vaporize the liquid q_{FV} ; q_{FV} is a function of the mass of Freon vaporized and, hence, proportional to the volume output at the cylinder at a particular operating pressure. The change in internal energy must be zero over a full cycle in order to continue operation at the same conditions.

IV. PROTOTYPE HISTORY

A. Preliminary Model Construction and Testing

In the first physical model of the pump visual observation of the liquid Freon level and mode of evaporation was a basic design criteria; this prompted use of precision-bore glass cylinder walls, which caused

considerable leakage difficulties. This preliminary model had Teflon pistons with circumferential grooves for sealing and series-connected heat exchangers of 1/8-in. copper tubing (Fig. 2).

A test setup was devised: to simulate the RTG and heat sink, to fill and purge the Freon chambers, and to monitor temperatures and pressures during operation (Fig. 3). During the initial phase of testing, it became apparent that cycle periods would be closer to a 100-second limit than to the predicted 10-second limit. Three factors contributed to the lengthening of the cycle: the cooling of the TC fluid in the lines leading to the heat exchanger, the large thermal inertia of the combined heat exchanger tube and enclosed TC fluid during cooling, and the contamination of the heat-sink surface by TC fluid leaking past the pistons.

Despite these difficulties, the pump remained in a near-oscillatory condition, partly because of the increase in loop static pressure caused by the rise of either piston. The longest self-powered oscillation produced by this model was 7 cycles, each averaging 82 seconds, with the model operating at a static pressure of 18 psig, a nominal

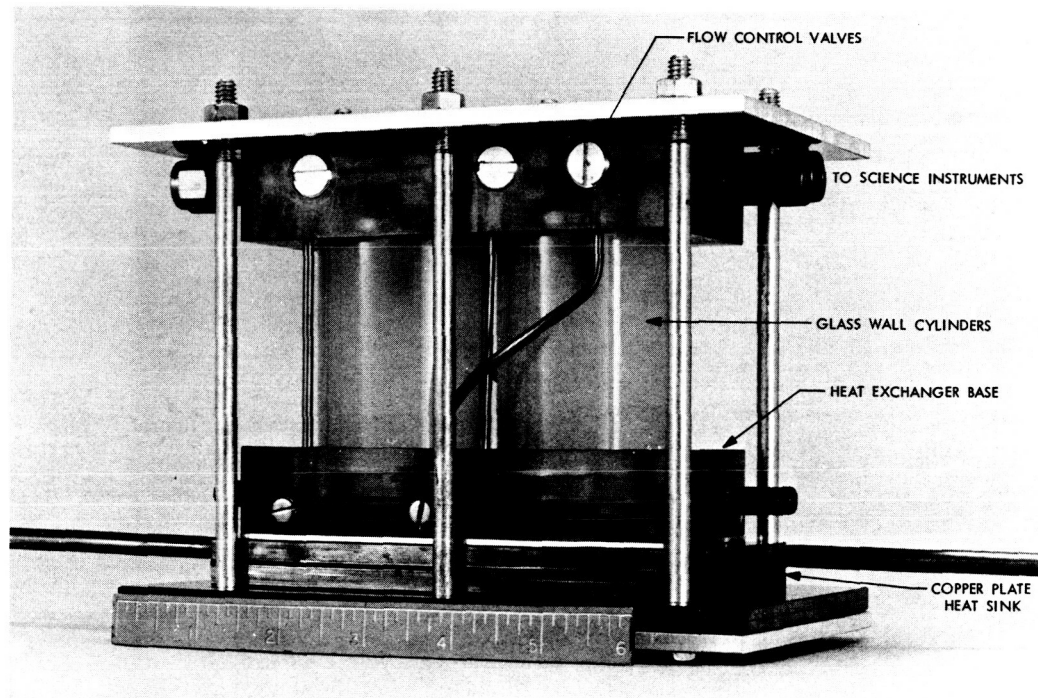


Fig. 2. First prototype thermal pump

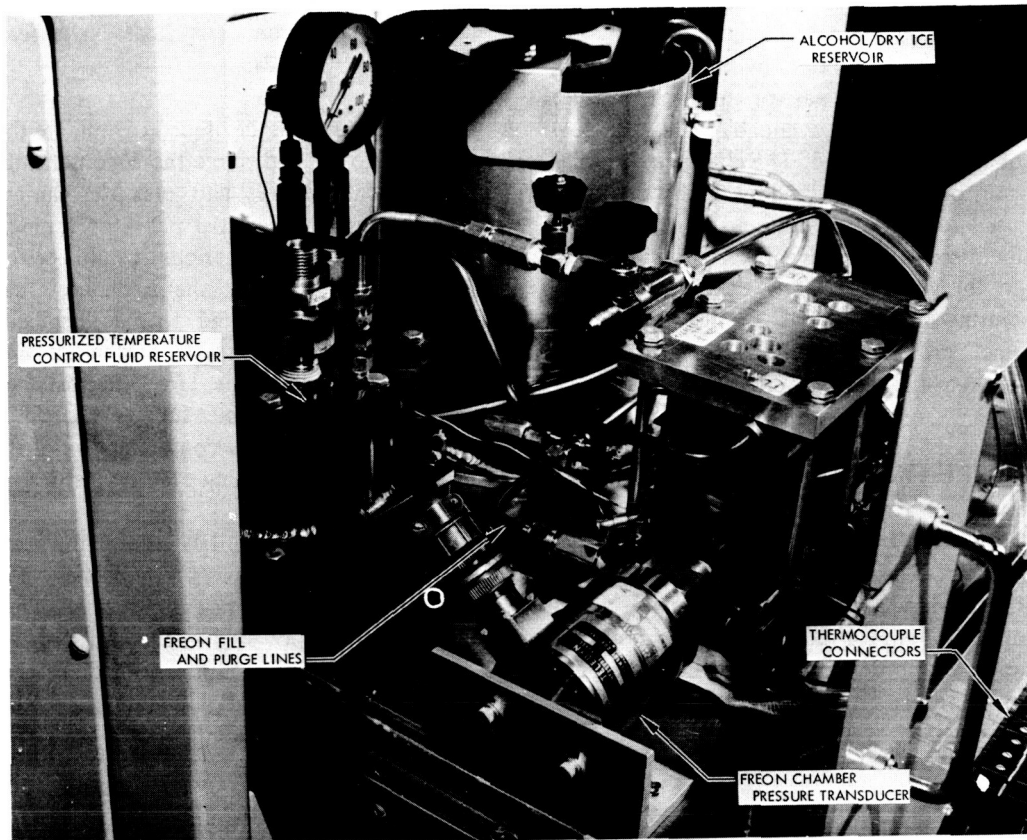


Fig. 3. Thermomechanical pump in operating configuration

TC-fluid temperature of 95°C , a heat sink of -13°C , a Freon temperature change of 2.5°C , and a vapor-pressure range of 5.8 psi. The output recording showed marked differences in the rise times of the two pistons and a lag time of $2/3$ of the cycle for each cylinder.

B. Second Prototype Construction

With the experience gained from the preliminary test model, a second prototype was constructed to correct the deficiencies of the first (Fig. 4). The pump body is a laminate of Micarta sheets with TC fluid passages milled into the laminas. This pump utilizes mechanical rather than visual readout of piston displacement, and leakage is prevented by providing both Freon and TC-fluid chambers with 2-in.-diameter Bellofram rolling diaphragms. The heat exchanger is a set of six, parallel finned tubes whose walls are 0.005-in. thick. This differs

from the thick wall series tube that was previously used. Fins $1/4$ -in. high and $1/16$ -in. wide are cut in the heat-sink surface and are fit into the spaces between the heat exchanger tubes. This arrangement increases the heat loss during evaporation by conduction through the liquid Freon, but it also appreciably decreases the condensing lag time.

Tests with this model have not yet produced multi-cycle oscillations, apparently because of hysteresis losses in the rolling diaphragms. These diaphragms require a gradient of 3 to 6 psi before they begin to move, and they absorb a major portion of the pump's work output in flexing the rubber-fabric sheet during motion.

The combination of finned-tube exchanger and finned heat sink was successful in reducing temperature lag and cycle time. Freon temperature ranges during evaporation were as much as 5°C in 7 seconds, with a

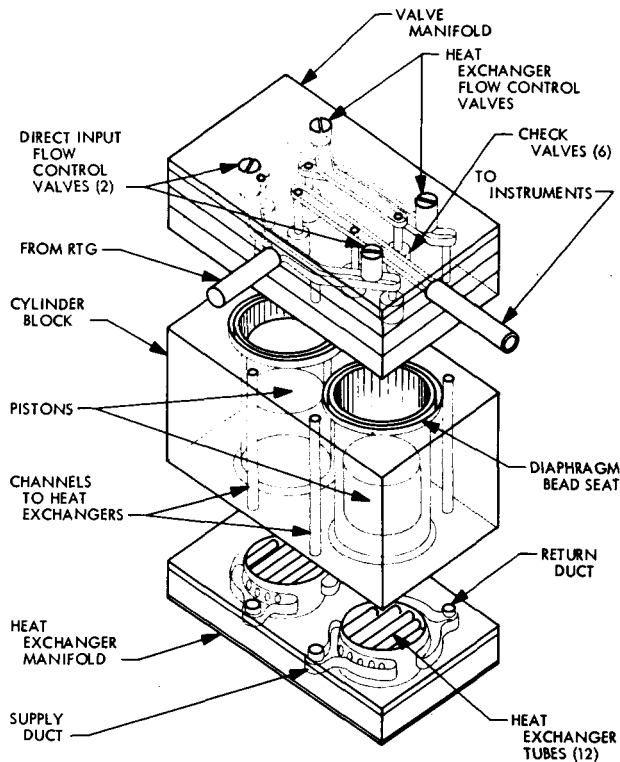


Fig. 4. Components of Model II thermomechanical pump

piston half-cycle of 38 seconds. Ideally, the piston velocity during condensation should be equal to or greater than the upstroke velocity; this has not been the

case, although this model of the pump achieved downstroke/upstroke ratios of 78 percent.

V. CONCLUSION

To date, experimental results indicate that a thermo-mechanical pump for performing the required tasks aboard a TOPS should be physically realizable. The remaining problem is twofold: first, to find a piston or diaphragm with minimum friction and hysteresis, good stroke length, minimum thermal conduction and hermetic sealing; and second, to optimize the tradeoff between maximum heat exchanger and sink areas and minimum vapor volume to achieve a reasonably short cycle time. The requirement for a 10-year operating life is a further limitation, since a 40-million-cycle life without maintenance is exceptional for any reciprocating machine. Such endurance is possible with low-friction diaphragms or bellows, but may be limited by diffusion of Freon vapor through the seals.

Use of a flight-model thermomechanical pump as a backup to an electric pump is a more likely application, with the thermal pump operating at times of peak electrical demand. Even if the performance of the pump is degraded through loss of working fluid or contamination, so that oscillation damps out after a number of cycles, it can be "kicked" with the starter heater to continue operation, providing a power-consumption advantage over the electric pump.

SELECTED BIBLIOGRAPHY

- "Air Conditioning-Refrigerating Data Book," 10th Edition, New York: American Society of Refrigerative Engineers, Chapters 2 and 32, 1957.
- Katz, O. L., and Beatty, I. O., "Condensation of Vapors on Outside of Finned Tubes," *Chem. Eng. Progr.* 44 (1):55-70, 1948.
- McAdams, W. H., "Heat Transmission," 3rd Edition, New York: McGraw-Hill Book Co., Inc., Chapters 9, 13, and 14, 1954.
- Ratiani, G. V., and Agaliani, D. V., "Heat Transfer to Boiling Refrigerants 12 and 22," *ASHRAE J.* 5:53-55, 1963. [Translation from *Kholodil'Naya Tekhnika*, Moscow, No. 1, 1963 (contains an error in data reduction technique, according to McAdams, p. 374).]
- Rohsenow, W. M., "Heat Transfer With Evaporation," Heat Transfer Symposium, University of Michigan, 101-149, 1962.

DISCUSSION

Maitland McLarin:

I have a possible solution for this piston business. Either a bladder should be used to contain the material or the material which is in gaseous state should be the same as the material which is pumped, so that the leakage waste could be utilized.

Sabelman:

This "Bellofram" is essentially a bladder. The working fluid has to be separated from the hot fluid because it is temperature-cycled, so you do need two bladders. And they do have to be rigidly separated to prevent heat leakage directly through them, which was essentially what the "Bellofram" arrangement was

supposed to be. The temperature control fluid is deliberately chosen for a low vapor pressure because of exposure to space and meteorite environment in the rest of the spacecraft.

Member of the audience:

Have you considered using a heat pipe instead of a fluid loop?

Sabelman:

This is certainly an obvious alternative, and it is being considered also. However, the disadvantages are that a heat pipe requires a larger tubing size and must pass through rotating joints.

**PANEL DISCUSSION:
NUTATION DAMPERS**

INTRODUCTION TO PASSIVE NUTATION DAMPERS

George C. Herzl
Lockheed Missiles & Space Company
Palo Alto, California

I. INTRODUCTION

Spin stabilization is the most commonly used method of satellite orientation since it provides an inertially fixed attitude of the spin axis with minimum complexity and weight. The mechanisms associated with launch, separation, spin-up, deployment of booms and solar paddles, orbital maneuvers, and torques due to solar pressure and the earth's magnetic field inevitably cause some coning (also called wobble, nutation, or precession) of the satellite spin axis (Fig. 1). The coning motion can prevent photographic and TV cameras and other oriented spacecraft experiments from maintaining a steady scan, and it can introduce a ripple in the high-gain communication system. Nutation dampers are used to remove this type of spacecraft instability.

Mechanisms that are similar in construction to nutation dampers have been used since the late 1920's for the dynamic balancing of washing machine tubs, automobile crankshafts (e.g., the Pierce-Arrow), and automobile wheels; however, the underlying dynamic principle governing these devices is different from that governing nutation dampers. True nutation dampers were first developed for the stabilization of aircraft gyroscopes. Further work on nutation dampers was done for spin-stabilized rockets that were propelled beyond the earth's atmosphere where fin stabilization becomes ineffective. The first nutation damper flown in a missile was built at the Naval Ordnance Test Station in 1950 for the stabilization of the gyroscope in the Sidewinder missile. This damper consisted of a hollow ring that was partially filled with mercury, and the sloshing of the mercury dissipated the nutational energy. A similar mercury-ring damper was used in the Pioneer 1 lunar probe in 1958 and became the first nutation damper to be used in space. Since then many types of nutation dampers have been designed for spin-stabilized spacecraft ranging in size from small scientific satellites to large space stations.

Nutation dampers were used initially only in disc-shaped satellites since this configuration is inherently stable, i.e., energy dissipation tends to decrease the wobble of the satellite spin axis. This is in accordance with the minimum energy principle since pure spin, i.e., spin without wobble, of disc-shaped satellites corresponds to the minimum energy state. Nutation dampers in prolate, or pencil-shaped, satellites actually increase—instead of decrease—the wobble of the spin axis. The destabilizing effect was even employed advantageously for reorientation of a Naval Research satellite that employed the nutation damper for opening the coning angle.

The use of nutation dampers was extended to prolate satellites with the introduction of the dual-spin concept.

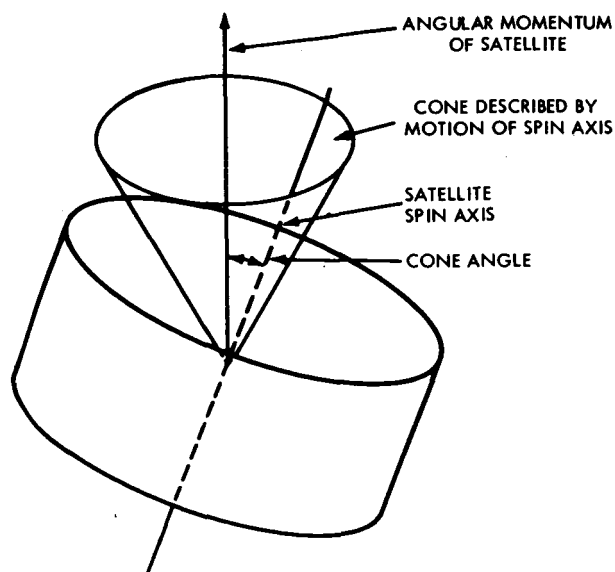


Fig. 1. Cone angle of satellite spin axis

Dual-spin satellites contain a spinning section and a mechanically despun section. The first nutation damper in a dual-spin spacecraft was flown in the OSO 1 satellite in 1962.

II. ACTIVE AND PASSIVE NUTATION DAMPERS

Nutation dampers are either active or passive, depending on whether they use external power for damping or not. Active systems are employed when existing equipment on board satellites can be advantageously used for nutation damping in addition to other control functions. Active nutation systems include pulsed gas jets, single-axis reaction wheels, control moment gyros, and active fluid dampers. The mechanism of these active systems involves problems that are associated with these specialties and will not be discussed here.

Passive nutation damping is most commonly used in satellites because of its reliability, efficiency, and low weight penalty, but it does require a damper that is used for the purpose of nutation damping only.

III. CRITERION FOR DAMPING

The variation of the centrifugal forces in a nutating spacecraft is the key to the possibility of passive dissipation of the nutational energy of spinning spacecraft. By contrast, no energy can be extracted by a passive nutation damper from a body in a state of pure spin since the force field remains constant at every point in the spinning body.

The criterion for nutation damping is that the damper should be located in the spacecraft where the precession rate is higher than the spin rate. If this condition is met, the frictional drag within the damper tends to increase the spin at the expense of the nutation energy. This criterion affords great flexibility in locating nutation dampers in disc-shaped satellites; nutation dampers have even been attached to adjustable mountings and used for the balancing of spacecraft. Dampers in dual-spin spacecraft are located in the despun section.

IV. DYNAMIC CHARACTERISTICS OF NUTATION DAMPERS

All nutation dampers, regardless of the damping principle that is employed, fall into two broad

categories. The more commonly used type of nutation damper is referred to as the "tuned" damper which is, in principle, a dissipative spring-mass system with a natural frequency tuned to or close to the nutation frequency of the combined damper-spacecraft system. This damper operates at peak efficiency when it is sharply tuned to the nutation frequency of the spacecraft. However, in general, it cannot be very sharply tuned because of uncertainties in the spin rate and the mass properties of the spacecraft (due to the design tolerances and thermal deformations) and because of the use of propellant and the dissipation of the spin rate of the spacecraft in orbit. Ordinarily, the resonant frequency should be set to coincide with the final spin rate of the spacecraft, i.e., after all the orbital maneuvers have been completed. The effect of a decrease in tuning sharpness is either a longer time requirement for nutation decay or an increase in the weight and size of the damper.

The second type, referred to here as the "non-resonant" nutation damper, is basically only a damping component of the nutating spacecraft system. The nonresonant damper does not have a spring that provides an energy-storage capacity. The tuned damper has, in general, a higher damping efficiency, but the nonresonant damper is less sensitive to variations in the angular momentum of the spacecraft and affords great flexibility in mounting location within the spacecraft.

V. DESIGN CONSTRAINTS

The nutation damper design is governed by performance requirements imposed by the spacecraft mission and by constraints that are applicable, in general, to all mechanisms in the spacecraft. Each constraint is expressed in terms of numerical values that indicate the relative importance of the constraint. The following are examples of design constraints imposed by the mission requirements:

- (1) Mass properties of the spacecraft.
- (2) Final spin rate.
- (3) Desired time constant.
- (4) Permissible residual nutation.
- (5) Spacecraft deployment sequence.

- (6) Prescribed lifetime.
- (7) Linearity of damper characteristics.

The general constraints imposed by the spacecraft include the following:

- (1) Launch environment.
- (2) Short-term environmental effects.
- (3) Long-term environmental effects.
- (4) Spacecraft integration.
- (5) Reliability.

VI. DESIGN REQUIREMENTS

Nutation damper design consists of the selection of operational principles and characteristics for the basic damper components. The design is primarily governed by a trade-off study among the following desirable features:

- (1) High-damping-to-weight ratio.
- (2) Low threshold of operation.
- (3) Low weight and volume.
- (4) Insensitivity to variation in spin rate and mass distribution of spacecraft.
- (5) Insensitivity to temperature.
- (6) Favorable geometry.
- (7) Flexibility of mounting location and orientation within spacecraft.
- (8) Small effect on spacecraft static and dynamic balance.
- (9) Ease of mathematical modeling.
- (10) Capability of testing on the earth.

VII. ANALYTICAL PREDICTABILITY

The principal methods of nutation damper analysis are outlined in the papers at this panel's presentation. It is shown that most aspects of the performance of nutation dampers are analytically predictable, but some important effects still need to be determined experimentally. These include the following:

- (1) Threshold of performance due to imperfection of damper suspension.
- (2) The effect of structural damping.
- (3) Cumulative effect of spacecraft and damper tolerances due to manufacturing and environmental factors.
- (4) Nonlinear limiting behavior in large amplitude motion of pendulum dampers.
- (5) The behavior of liquid nutation dampers in which large-amplitude surface waves exist in the liquid.

The threshold of performance and the effect of structural damping are discussed under separate headings in this paper, and the last item is discussed in detail by Newkirk and Crout in another paper at this meeting. For the other items, the reader is referred to the extensive bibliography at the end of this paper.

The basic elements of tuned nutation dampers provide—

- (1) Damping.
- (2) Inertial characteristics.
- (3) Constraint for motion of inertial mass.
- (4) Restoring torque.
- (5) Protection from vibrations.

Nonresonant dampers contain the same basic elements except that they do not require restoring torque. The basic nutation damper elements and the design principles that have been implemented for each are shown in Table 1.

The damping modes that are most frequently used in spacecraft nutation dampers are liquid and gas friction. In mechanical dampers inelastic impact and mechanical friction are also employed to provide additional dissipation in certain regimes of operation. The inertial characteristics of the damper are provided by a mass which is either the damping fluid itself or a suitably shaped piece of metal such as a spherical ball or a cantilevered object. The restoring torque is generated by means of centrifugal force, either with or without the aid of mechanical springs. The characteristics of the centrifugal force field are determined by the constraint on the motion of the inertial mass. Mechanical springs are employed when the geometrical constraints in the spacecraft preclude the use of the desired damper shape or in conjunction with mechanical suspensions which inherently provide restoring torque. The constraint for the motion of the inertial mass is provided by various types of bearings and suspensions and by hermetically sealed containers for gas and liquid damping. The damper is either caged or ruggedized to protect it from damage during launch and staging maneuvers. The caging

mechanism temporarily immobilizes the inertial mass and subsequently releases it upon command from the earth. In ruggedized dampers, the inertial mass is permitted to rattle with no permanent damage being done. Adequate dimensioning and appropriate selection of the shape of objects that come in contact with each other provide the necessary protection. Fluid dampers require the least amount of protection. Typical examples of the implementation of the diverse design principles for various satellite applications will be discussed in detail in the papers that follow.

VIII. STRUCTURAL DAMPING

The main sources of structural damping are bending of the spacecraft frame, rubbing of components, and sloshing of liquids and propellants in the spacecraft. These phenomena are complex and not well understood, and are analytically difficult to assess. Structural damping is a particularly important design consideration for single-spin spacecraft that are temporarily in the (nutationally) unstable inertial configuration during

Table 1—Modes of operation for basic nutation damper elements.

Nutation Damper Element	Mode of Operation
Damping	Liquid Gas Mechanical friction Inelastic impact
Inertial mass	Ball Cantilevered mass Fluid
Motion constraint	Suspension Bearing Container
Restoring torque	Centrifugal force Centrifugal force and spring
Protection from vibrations	Caging Ruggedizing

staging and deployment and dual-spin spacecraft, since the energy dissipation of the damper on the despun section must be significantly greater than the structural damping on the rotary section.

The anomalous behavior of several spacecraft is attributed to structural damping, for example, the Explorer 1 satellite which, in less than one orbit, experienced strong nutations that were most likely due to structural damping. This satellite was of prolate shape with flexible whip antennas that exhibited strong structural damping. By contrast, Explorer 3 which was of the same shape as Explorer 1 but without whip antennas, was in orbit for several days before the nutation cone angle reached a significant value. A recent example of damping from a source other than the nutation damper is found in the ATS 5 satellite which went into an unstable spin mode within 8 minutes following spin-up. It is suspected that fluid sloshing in the spacecraft heat pipes was the cause of the rapid increase of the nutation.

IX. RESIDUAL NUTATION

Residual nutation is the limit to which the spacecraft nutation can decay within a reasonable time. This performance limitation is due to the required minimal deflection of the damper necessary for sufficient displacement of the inertial mass to produce effective damping. Below this threshold the damper is inoperable just as a large scale is useless for weighing small objects.

The amount of residual nutation depends primarily on the method of support for the inertial mass in the damper. Nutation dampers using fluid suspension (e.g., fluid contained in a hollow ring) and mechanical suspension (e.g., torsion wire) have very low thresholds of operation, typically of the order of 2 arc-seconds of the cone angle. The threshold of operation of bearing

type dampers, such as the ball-in-tube damper, is typically in the order of $\frac{1}{4}$ deg.

X. CONSEQUENCES OF NUTATION DAMPER FAILURE

The consequences of failure of nutation dampers can range from total failure of the mission to a temporary degradation of performance, depending mainly on the configuration of the spacecraft.

Damper failure in a dual-spin spacecraft can cause increased, instead of decreased, coning until the spacecraft eventually reverts to a spin mode about an incorrect spin axis, and all oriented experiments become inoperable. In the case of a damper failure in a single-spin disc-shaped spacecraft, coning diminishes as a result of structural damping only, and all oriented experiments are either inoperable or are degraded during the long decay time; however, the spacecraft eventually stabilizes in the desired nominal direction. Single-spin prolate spacecraft are dynamically unstable and nutation dampers are certain to cause increased coning.

XI. CONCLUSION

Passive nutation dampers have by now proven their value and firmly established themselves for spacecraft applications. It is noted that nutation dampers are not well-instrumented devices and that there are inadequate data on their performance in space. This is perhaps the best tribute to their success. There is every indication that future spacecraft will continue to have nutation dampers, and that there will be a continuing demand for increased sophistication in their design and efficiency. As in many other spacecraft disciplines, the sophistication of the hardware design lags the progress in the analytical work, and considerable advances in nutation dampers technology can be expected.

BIBLIOGRAPHY

Alper, J. R., "Analysis of Pendulum Damper for Satellite Wobble Damping," *J. Spacecr. Rockets* 2:50-54, Jan.-Feb. 1965.

"An Advanced Study of an Application Technology Satellite (ATS-4) Mission," GE Report No. 66SD4529, General Electric Co., Philadelphia, Pa., Nov. 1966.

- Ashley, H., "Observations on the Dynamic Behavior of Large, Flexible Bodies in Orbit," *AIAA J.* 5:460-469, Mar. 1967.
- Auelmann, R. R., and Lane, P. T., "Design and Analysis of Ball-in-Tube Nutation Dampers," Proceedings: Symposium on Attitude Stabilization and Control of Dual-Spin Spacecraft, Aerospace Corp., El Segundo, Calif., Aug. 1967, AF Report No. SAMSO-TR-68-191, U.S. Air Force, Washington, D.C. Nov. 1967.
- Bauer, A. B., and Du Puis, R. A., "Fluid Drag on a Sphere Rolling in a Tube," *J. Appl. Mech.* Preprint No. 67-APM-18, 1967.
- Bhuta, P. G., and Koval, L. R., "A Viscous Ring Damper for a Freely Precessing Satellite," *Int. Mech. Sci.* 8:383-395, May 1966.
- Bhuta, P. G. and Koval, L. R., "Decay Rates of Passive Precession Dampers and Their Bounds." AIAA Paper No. 64-658 (presented at the AIAA/ION Astrodynamics Guidance and Control Conference, Los Angeles, Calif., Aug. 1964).
- Bracewell, R. N. and Garriott, O. K., "Rotation of Artificial Earth Satellites," *Nature* 182:760-762, Sept. 20, 1958.
- Caggiano, G. J., "Feasibility Study of Fluid Flywheel Techniques to Provide Nutation Damping of Large Spinning Space Vehicles," GE Report No. LMEJ-8116, Light Military Electronics Dept., General Electric Co., Johnson City, N.Y., May 1967.
- Carrier, G. F. and Miles, J. W., "On the Annular Damper for a Freely Precessing Gyroscope," *J. Appl. Mech.* 27:237-240, June 1960.
- Cartwright, W. F., Massingill, E. C. and Trueblood, R. D., "Circular Constraint Nutation Damper," *AIAA J.* 1:1375-1380, June 1963.
- "Comparative Study of Nutation Dampers," Nord-Aviation Report No. 940-030, NASA Technical Translation F-10372, Jan. 1967.
- Connolly, A., "An Active Nutation Control for a Spinning Spacecraft," Proceedings: the Symposium on Attitude Stabilization and Control of Dual-Spin Spacecraft, Aerospace Corp., El Segundo, Calif., Aug. 1967, AF Report No. SAMSO-TR-68-191, U.S. Air Force, Washington, D.C. Nov. 1967.
- Craig, B. D., "Nutation Damper for OSO," *Astronaut. Aerosp. Engr.* 1:50-55, Dec. 1963.
- Crout, P. D., "Theoretical Investigation of the Dynamic Behavior of the Mercury Damper," NAVWEPS Report 8611, NOTS TP3635, U.S. Naval Ordnance Test Station, China Lake, Calif., Nov. 1964.
- Dolder, F. P., Bartoe, O. E., Mercure, R. C., Jr., Gablehouse, R. H., and Lindsay, J. C., "The Orbiting Solar Observatory Spacecraft," Proceedings of the Third International Space Science Symposium, Washington, D.C., May 1964.

"Effects of Structural Flexibility on Spacecraft Control Systems," NASA Special Publication 8016, Dec. 1968.

Evans, W. R., "Control System Dynamics," New York: McGraw-Hill Co., 1954, Ch. 7.

"Feasibility Study and Design of Passive Dampers for a Manned Rotating Space Station," NASA Contractor Report 163, Mar. 1965, pp. 70-81.

"Flywheel Stabilized, Magnetically Torqued Attitude Control System for Meteorological Satellites," NASA Contractor Report 232, May 1965.

Fuller, A. T. and MacMillan, R. H., "Expressions for the Damping and Natural Frequency of Linear Systems," *Quart. J. Mech. Appl. Math.* 9:345-359. Aug. 1956.

Hazeltine, W. R., "Nutation Damping Rates for a Spinning Satellite," *Aerosp. Engr.* 21:10-17, Mar. 1962.

Hazeltine, W. R., "Passive Damping of Wobbling Satellites," NOTS Report No. 6579, pts. 1 and 2, U.S. Naval Ordnance Test Station, China Lake, Calif., Sept. 1959. (also in *J. Aerosp. Sci.* 29:543-549, 1962.)

Herzl, G. G., (Ed.), "Aerospace Mechanisms, Part A: General Applications," Aerospace Mechanisms Series, Palo Alto, Calif.: J. W. Stacey, Inc., 1970. (76-108023).

Herzl, G. G., (Ed.), "Aerospace Mechanisms, Part B: Bearings and Suspensions," Aerospace Mechanisms Series, Palo Alto, Calif.: J. W. Stacey, Inc., 1970. (76-108023).

Herzl, G. G., "Mechanical Suspensions for Space Applications," Proceedings of the 3rd Aerospace Mechanisms Symposium, NASA Technical Memorandum 33-382, Oct. 1968.

Iorillo, A. J., "Nutation Damping Dynamics of Axisymmetric Rotor Stabilized Satellites," (Paper presented at the ASME Winter Meeting, Chicago, Ill., Nov. 1965.)

Landon, V. D., and Stewart, B., "Nutation Stability of an Axisymmetric Body Containing a Rotor," *J. Spacecr. Rockets* 1:682-684, Nov.-Dec. 1964.

Leiss, F., et al., "Technical Possibilities of Active Magnetic Attitude Control for Spin-Stabilized Satellites," APL/JHU Translation No. 2173, Applied Physics Laboratory, The Johns Hopkins University, Silver Spring, Md., Aug. 1968.

Likins, P. W., and Gale, A. H., "Attitude Stability Criteria for Dual-Spin Spacecraft," *J. Spacecr. Rockets* 7:1049-1056, Sept. 1970.

Likins, P. W., "Dynamics and Control of Flexible Space Vehicles," NASA Technical Report 32-1329, Revision 1, Jan. 1970.

Lindorfer, W. J., and Muhlfelder, L., "Attitude and Spin Control for TIROS Wheel," Proceedings of the AIAA/JACC Guidance and Control Conference, Aug. 1966, p. 448.

- Manger, W. P., "Attitude Control for the TIROS Weather Satellites." (Paper presented at the IFAC Symposium on Automatic Control in the Peaceful Uses of Space, Stavanger, Norway, June 21, 1965.)
- Miles, J. W., "On the Annular Damper for a Freely Precessing Gyroscope II," *J. Appl. Mech.* 30:189-192, June 1963.
- Mobley, F. F., Teener, J. W., Tossman, B. E., and Brown, R. D., "Performance of the Spin Control System of the DME-A Satellite," APL/JHU Report No. TG-929, Applied Physics Laboratory, The Johns Hopkins University, Silver Spring, Md. June 1967.
- Newkirk, H. L., Hazeltine, W. R., and Pratt, A. V., "Stability of Rotating Space Vehicles," *Proceedings of the IRE* 48:743-750, Apr. 1960.
- Newkirk, H. L., "Pendulum-Type Nutation Damper Used in the NASA Atmospheric Structure Satellite, S-6," NOTS TP3520, U.S. Naval Ordnance Test Station, China Lake, Calif., Mar. 1965.
- Nuffer, H. D., "Space Vehicle Attitude Control with a Modified Viscous Lanchester Damper," NOTS TP4034, U.S. Naval Ordnance Test Station, China Lake, Calif. June 1966.
- "Orbiting Solar Observatory Satellite," NASA Special Publication 57, 1965.
- Perkel, H., "Space Vehicle Attitude Problems," in "Advances in the Astronautical Sciences," Vol. 4, New York: Plenum Press, 1959, pp. 173-192.
- Perkel, H., "Stabilite—A Three-Axis Attitude Control System Using a Single Reaction Wheel," in "Progr. Astronaut. Aeronaut.," ed. by R. B. Marsten, New York: Academic Press, Inc., 1966, p. 375.
- Perkel, H., "TIROS I Spin Stabilization," *Astronautics* 5:38-39, June 1960.
- Pilkington, W. C., "Vehicle Motions as Inferred from Radio Signal Strength Records," External Publication No. 551, Jet Propulsion Laboratory, California Institute of Technology, Pasadena, Calif., Sept. 5, 1958.
- Reiter, G., "Theory and Design of Nutation Dampers," Proceedings: Symposium on Attitude Stabilization and Control of Dual-Spin Spacecraft, AF Report No. SAMSO-TR-68-191, U.S. Air Force, Washington, D. C., Nov. 1967.
- Scheele, P. F., and Sewell, B. H., "S-17 OSO Communications Systems," National Telemetry Conference, Albuquerque, N. M., May 1963.
- Shvetzoff, A. D., "An Electromechanical Coning Damper, Rebound Project, Model DSV-5," Douglas Report No. SM-41393, Douglas Aircraft Co., Santa Monica, Calif., Jan. 1962.
- Spencer, T. M., "Cantilevered-Mass Nutation Damper for a Dual-Spin Spacecraft," Proceedings: Symposium on Attitude Stabilization and Control of Dual-Spin Space-

- craft, AF Report No. SAMSO-TR-68-191, U.S. Air Force, Washington, D.C., Nov. 1967.
- Spencer, T. M., "Digital Computer Simulation of the Attitude Dynamics of a Spin-Stabilized Spacecraft." (Presented at the AAS Rocky Mountain Resources for Aerospace Science and Technology Symposium, Denver, Colo., July, 1967.)
- Spencer, T. M., "Interactions Between a Pointing Control System and the Nutational Motion of a Dual-Spin Spacecraft," Proceedings of the Symposium in Attitude Stabilization and Control of Dual-Spin Spacecraft, AF Report No. SAMSO-TR-68-191, U.S. Air Force, Washington, D.C., Nov. 1967.
- Spencer, T. M., "Nutation Damping for Dual-Spin Spacecraft." (Presented at the AAS Rocky Mountain Resources for Aerospace Science and Technology Symposium, Denver, Colo., July 1967.)
- Stewart, D. J., "Nutation Damper," U.S. Naval Ordnance Test Station, China Lake, Calif., U.S. Patent No. 2,734,384, Feb. 14, 1956.
- Taylor, R. S., "A Passive Pendulum Wobble Damping System for a Manned Rotating Space Station," *J. Spacecr. Rockets* 3:1221-1228, Aug. 1966.
- Thomson, W. T., and Reiter, G. S., "Attitude Drift of Space Vehicles," *J. Astronaut. Sci.* 7:29-34, Nov. 1960.
- Tossman, B. E., Mobley, F. F., and Fischell, R. E., U.S. Patent No. 3,363,856, Jan. 1968.
- Tossman, B. E., "Nutation Damping Rates of a Z-Axis Coil," APL/JHU Internal Memorandum S2P-5-078, Applied Physics Laboratory, The Johns Hopkins University, Jan. 1967.
- Total, N. I., and Rollins, R., "A Nutation Damper for a Spinning Satellite," Proceedings of the 4th Aerospace Mechanisms Symposium, NASA Technical Memorandum 33-425, 1969.
- Velman, J. R., "Attitude Dynamics of Dual-Spin Satellites," SSD Report No. 60419R, Hughes Aircraft Co., Culver City, Calif., Sept. 1966.
- Wadleigh, K. H., et al., "Spinning Vehicle Nutation Damper," *J. Spacecr. Rockets* 1:588-592, Nov.-Dec. 1964.
- Williams, D. D., "Torques and Attitude Sensing in Spin-Stabilized Synchronous Satellites," in "Torques and Attitude Sensing in Earth Satellites," ed. by S. F. Singer, New York: Academic Press, 1964, pp. 159-174. (Also presented at the Goddard Memorial Symposium of the AAS in Washington, D.C., Mar. 16-17, 1962.)
- Yu, E. Y., "Spin Decay, Spin-Precession Damping, and Spin Axis Drift of the Telstar Satellite," *Bell Sys. Tech. J.* 42:2169-2193, Sept. 1963.
- Zaroodny, S. J., and Bradley, J. W., "Nutation Damper—A Simple Two-Body Gyroscopic System," Report No. 1128, Aberdeen Exterior Ballistics Laboratory, Aberdeen, Md.,

NUTATION DAMPERS FOR SINGLE-SPIN SATELLITES

J. V. Fedor
*NASA-Goddard Space Flight Center
Greenbelt, Maryland*

This paper discusses the physical principles, analysis, and some of the design considerations of passive nutation dampers for single-spin satellites.

I. INTRODUCTION

Basically, nutation dampers eliminate cone angle or undesirable transverse angular rates from spinning spacecraft. There are many types of dampers, and some of them can be quite complex. The dampers that will be discussed and compared in this paper are the linear spring-mass-dashpot type of damper (a fluid-slug impact damper is a special case with zero spring constant) and the completely filled fluid-ring damper (also called a viscous-ring damper). Figure 1 shows a spring-mass-dashpot damper. When assembled, the cylinder is filled with a silicone oil. The coning motion of the spacecraft drives the damper mass through the oil in a sinusoidal fashion, dissipating energy and reducing the cone angle. This type of damper was flown on Explorer 26.

Figure 2 shows a fluid-ring damper that was flown on Explorer 35. Essentially, it is a ring approximately 11 in. in diameter and filled with a silicone oil. Not visible is a reservoir that permits thermal expansion of the fluid. Again, spacecraft coning motion drives the fluid in a circular sinusoidal manner, dissipating energy and causing damper action.

II. ANALYSIS

The mechanical nature of these dampers is simple, but their analysis can be quite complex and difficult because two or more bodies are interacting while performing three-dimensional motion. A rigorous dynamic analysis of the dampers invariably requires sophisticated mathematics and a computer solution. One method of analysis that circumvents much of this difficulty is the energy-sink approach. Essentially, this method assumes the spacecraft to be in a torque-free

environment and equates the rate of change of the kinetic energy of the spacecraft with the average rate of energy dissipation of the damper. In writing this

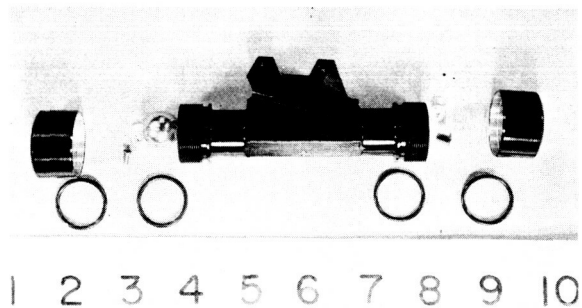


Fig. 1. Spring-mass-dashpot damper

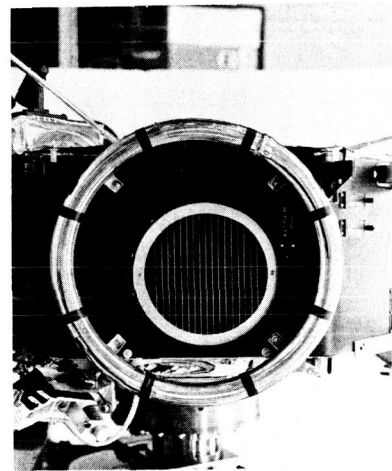


Fig. 2. Fluid-ring damper

“conservation” equation, the torque-free motion of the spacecraft is considered to be the damper driver. This method leads to a first-order differential equation for the cone angle, and a time constant can easily be determined. Although this method of analysis is approximate, it leads to simple, useful equations in preliminary design. The following equations for the kinetic energy and the time rate of change of the energy for symmetrical spacecraft are used in the energy-sink approach:

$$T = \frac{H^2}{2C} [1 + (C/A - 1)\sin^2\theta] \quad (1)$$

$$T = \frac{H^2}{C} (C/A - 1)\sin\theta \cos\theta \dot{\theta} \quad (2)$$

where

H = angular momentum (a constant)

A = transverse principal moment of inertia

C = roll moment of inertia

θ = cone angle

To complete the energy-sink approach, Eq. (2) is equated with the damper’s energy-sink dissipation rate, which is a negative quantity.

Equation (2) indicates that, for the cone angle to decrease (θ negative), $C > A$. This is the maximum-moment-of-inertia principle for stable spin of a satellite.

The question may arise as to where to put or align the sensitive axis of the damper. Figure 3 shows possible locations for the spring-mass-dashpot damper. Spin is about the z -axis. Positions 2 or 3 are preferred and

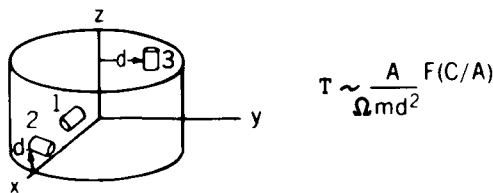


Fig. 3. Possible locations for spring-mass-dashpot damper

position 3 is more frequently used. Position 1 should be avoided because there is a possibility of damper resonance with the spin period. Large, static damper-mass displacement will occur, and the damper will bottom out and become ineffective. Note the form of the time constant for position 3. It is proportional to the spacecraft transverse moment of inertia and inversely proportional to the moving mass of the damper, the spin rate, and the square of the distance from the spin axis. The most efficient way to reduce the time constant is to increase the distance from the spin axis.

Figure 4 shows the two positions at which the viscous ring damper can be placed. Position 2 is preferred because the amplitude of the sinusoidal body angular rates are higher about the y -axis than about the z -axis. Note also the form of the time constant for position 2 (R is the radius of the ring). The most efficient way to reduce the time constant is to increase the radius of the damper.

III. DAMPER TUNING

Dampers are usually tuned, or optimized, so that the energy dissipated per cycle is a maximum at some nutation rate, and for the spring-mass type of damper, this usually requires that the amplitude of the sinusoidal motion of the damper be a maximum. This results in a sharply tuned system. Damper performance is excellent at the nominal spin rate and parameters. However, deviations from the nominal quantities result in significantly reduced performance. For the ring-type damper, tuning requires that a Reynolds-type dimensionless quantity $(\Omega_n a^2)/\nu$ have a certain value where Ω_n is the nutation frequency, a is the radius of the tube, and ν is the kinematic viscosity. This results in a broadly tuned system. Damper performance is good at the nominal spin

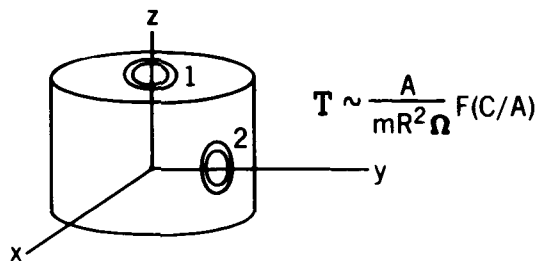


Fig. 4. Possible positions for the ring damper

rate and parameters. Deviations from the nominal quantities do not appreciably reduce performance.

IV. TESTING

A desirable characteristic of a nutation damper is that one can experimentally determine the damping time constant quite easily. The ring damper is an excellent example of a device having this characteristic. One can test the damper by putting it on a simple torsion pendulum and observing the following modeling constraints—

- (1) The damper-fluid Reynolds number should be the same ($\Omega_n a^2 / \nu$) in both the pendulum and the spacecraft systems. Since the actual damper is to be tested, this requires that the pendulum natural frequency be the same as the nutation frequency: $\Omega(C/A - 1)$.
- (2) By invoking the requirement that the equation governing the rate of energy dissipation be the same in both the pendulum and the spacecraft systems, the following scaling equation for the time constant is obtained:

$$\tau = \tau_p \frac{A}{I_p} \left(\frac{C - A}{C} \right)$$

where

τ = spacecraft time constant

τ_p = time constant determined from pendulum tests

I_p = pendulum moment of inertia

A = spacecraft transverse moment of inertia

C = spacecraft roll moment of inertia

Thus, a simple pendulum test can be devised to test any type of viscous "ring" damper. (The quotes indicate that the damper ring need not be circular.)

V. CONCLUSION

It is of value to point out that if a high-performance nutation damper is not required (one whose time constant is of the order of a nutation period), the ring damper is the proper choice because of its design simplicity, ease of fabrication and testing, and predictability. Furthermore, the ring damper requires essentially no threshold cone angle before it will operate; a mechanical damper usually has a threshold value.

NUTATION-DAMPER DESIGN FOR DUAL-SPIN SPACECRAFT

T. M. Spencer
Ball Brothers Research Corporation
Boulder, Colorado

A dual-spin spacecraft is a spin-stabilized spacecraft consisting of two major structures. Momentum is stored in the spinning "wheel," while the "sail," or "platform," can be despun at various rates about the spacecraft axis. Factors that affect the design of nutation-control systems for single- and dual-spin spacecraft are discussed. The nutation-control system of the Orbiting Solar Observatory spacecraft is described.

I. INTRODUCTION

The physical differences between single- and dual-spin spacecraft are illustrated in Fig. 1, which shows a number of examples of spin-stabilized spacecraft. At the upper left are two of the first United States satellites, Explorers 1 and 3. Both were inertially rod-shaped and were nutationally unstable about the desired axis. The Tiros "wheel" satellite is an example of the many inertially disk-shaped spacecraft that have been successfully stabilized by passive mechanical dampers. The Orbiting Solar Observatory (OSO) was the first example of a dual-spin spacecraft; OSO's have always been inertially disk-shaped. The last satellite shown in Fig. 1 is a proposed rod-shaped spacecraft that is actually a "tri-spin" configuration. The wheel spins while the solar array is aimed at the sun and the sensor packages are aimed at some other earth- or space-fixed object.

Important considerations that affect the design of nutation control systems for dual-spin spacecraft are—

- (1) Both rod- and disk-shaped dual-spin spacecraft can be stabilized by a platform-mounted passive damper, if platform and wheel energy dissipation rates are suitable.
- (2) The centrifugal-force fields of the wheel and platform are different.
- (3) Dual-spin spacecraft are usually subject to more severe and frequent nutation disturbances than are single-spin spacecraft.

- (4) The despin controller affects the nutational stability of a dual-spin spacecraft.
- (5) Smaller residual nutation and wobble levels are usually required on dual-spin spacecraft than on single-spin spacecraft.
- (6) Passive nutation dampers can attenuate wobble (caused by principal-axis misalignments) on dual-spin spacecraft.

These factors are illustrated by a description of the nutation control system of the OSO spacecraft.

II. OSO NUTATION CONTROL

Figure 2 shows the three major structures of the OSO spacecraft: the wheel (with ballast arms), the sail (mounting the solar array), and the solar pointed-instrument assembly (PIA). The OSO control axes are shown in Fig. 3. Both the azimuth and elevation control systems interact with nutation, especially when the PIA is mechanically rastered to map the solar disk. This kind of nutation disturbance is not often present on single-spin spacecraft. Also, nutation causes roll-axis (about the sun line) pointing errors, which make residual nutation more critical than for a single-spin spacecraft. The design goal on OSO spacecraft is to reduce the nutation half-angle to approximately a minute of arc. This is accomplished by the use of a passive, platform-mounted damper.

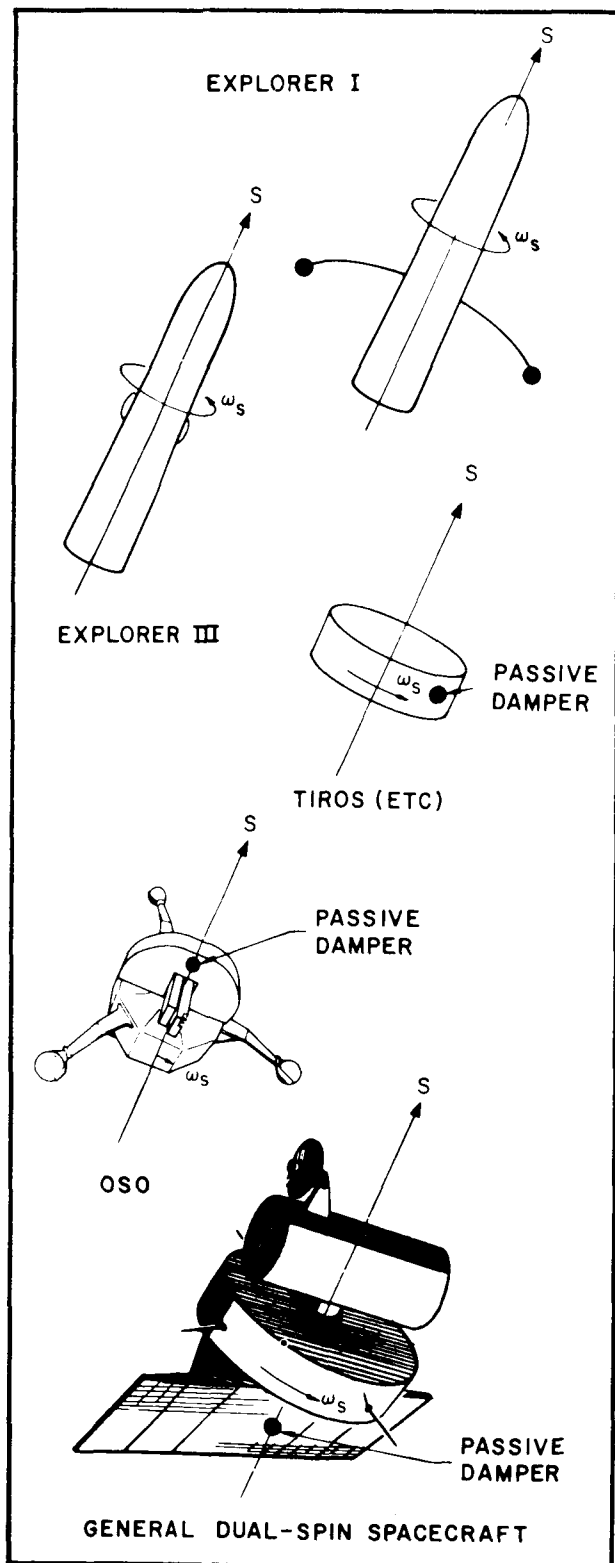


Fig. 1. Spin-stabilized spacecraft

A. Nutation-Damper Location

For a dual-spin spacecraft, the designer has the choice of mounting the nutation-damping mechanism on either the wheel or the platform. Figure 4 is a schematic representation of spacecraft nutation. Equations are given for the "space-fixed" and "wheel-fixed" nutation frequencies. A damper mounted on the wheel obviously "sees" the wheel-fixed nutation frequency. If mounted on a despun platform, the damper "sees" the space-fixed nutation frequency. Since the rate of energy dissipation increases with frequency for most dampers, damper location is important.

For a disk-shaped spacecraft, the space-fixed nutation frequency is higher than the wheel-fixed frequency, and a lighter damper can usually be used if it is platform-mounted (assuming that the sail-mounted damper can be mounted as far from the spacecraft center of mass as can the wheel-mounted alternative). In addition, a passive, platform-mounted damper tends to compensate for wheel-mass imbalances, while a wheel-mounted damper does not. On the other hand, a wheel-mounted damper can be designed to "retune" with wheel spin-rate variations. For a rod-shaped spacecraft, stability dictates that the damper must be located on the despun platform unless it is a fairly sophisticated active damper. The advantages of the platform-mounted damper usually outweigh those of a wheel-mounted damper.

B. Passive Nutation Dampers

Passive mechanical devices are preferred as nutation dampers because they are simpler and more reliable than the active alternatives. Many devices have been successfully used. Figure 5 shows some examples. The non-pendulous devices (such as a fully filled ring damper) do not attenuate wobble as do the pendulous dampers. A ring damper is usually more broadly tuned than a spring-mass damper, and more mass is required to get the same damping performance at resonance. A "point-mass" damper is usually lighter than one with a distributed mass "hinged" near its center because the former has a larger moment of inertia about its center of motion (the spacecraft center of mass). A two-degree-of-freedom spring-mass damper is usually lighter than a single-degree-of-freedom damper because its bob need weigh only half as much. Some of the devices are easier to adapt for zero-g operation on a despun platform, and some are easier to test in the laboratory.

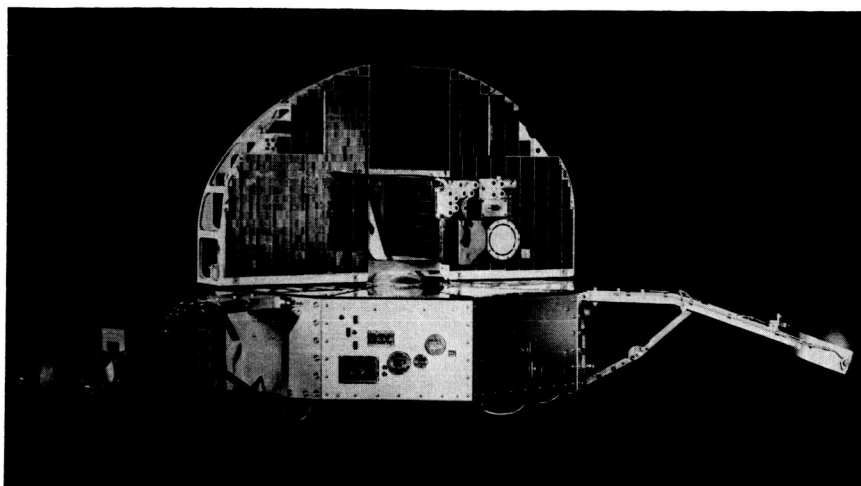


Fig. 2. Orbiting Solar Observatory (a "dual-spin" spacecraft)

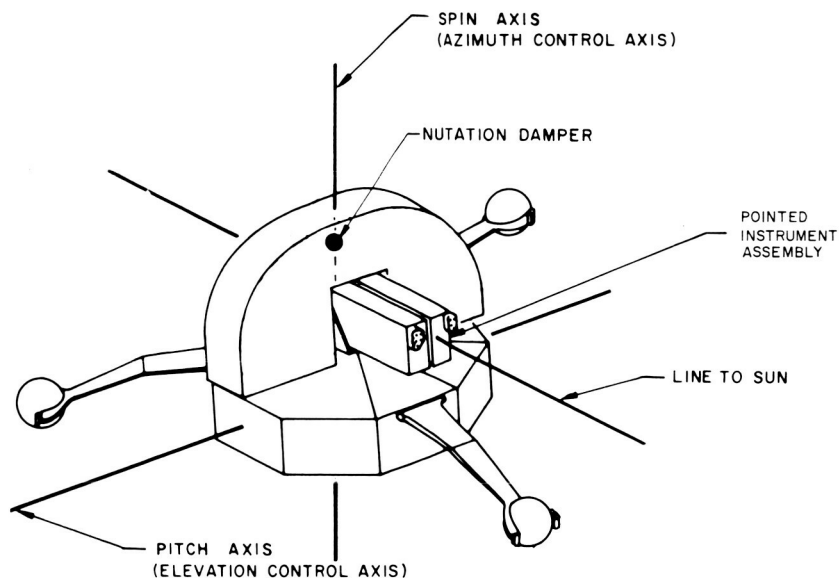


Fig. 3. Control axes of the OSO spacecraft

C. The OSO Nutation Damper

The OSO nutation damper is a two-degree-of-freedom cantilevered mass. Figure 6 shows two versions of this damper. The music-wire cantilever provides the spring; viscous fluid in the case provides the damping. The damper shown at the top weighs 6 lb and has a 1-lb bob. This damper has enjoyed an unblemished record on past OSO's. The damper shown at the bottom is a more efficient design in which the total damper weight is less than twice the bob weight.

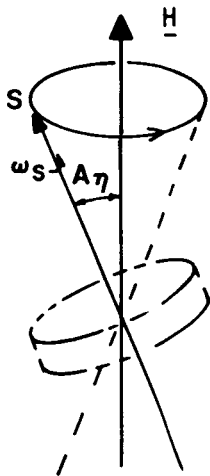
Advantages of the OSO damper are—

- (1) It works well in zero *g*.
- (2) It is very efficient within its linear range.
- (3) It does not "hang up" at small nutation amplitudes.
- (4) It is relatively easy to cage during launch.

- (5) The unit is compact (easy to mount and handle).
- (6) It is easy to retune in the laboratory.
- (7) It can be modeled for physical tests in the laboratory.

Disadvantages are—

- (1) It has a limited linear range.
- (2) For low nutation frequencies (below about 0.1 Hz), the suspension wire must be long (more than 1 ft in length) and the damper is less compact. Also, laboratory tests are difficult at low frequencies.



$$\omega_{\eta} = \frac{l_s}{l_1} \omega_s$$

$$\Omega_{\eta} = \left(\frac{l_1 - l_s}{l_1} \right) \omega_s$$

ω_s = spin rate

ω_{η} = space-fixed nutation frequency

Ω_{η} = wheel-fixed nutation frequency

l_s = wheel spin moment of inertia

l_1 = spacecraft transverse moment of inertia

A_{η} = nutation half-angle

\underline{H} = angular momentum vector

S = spin axis

Fig. 4. Spacecraft nutation

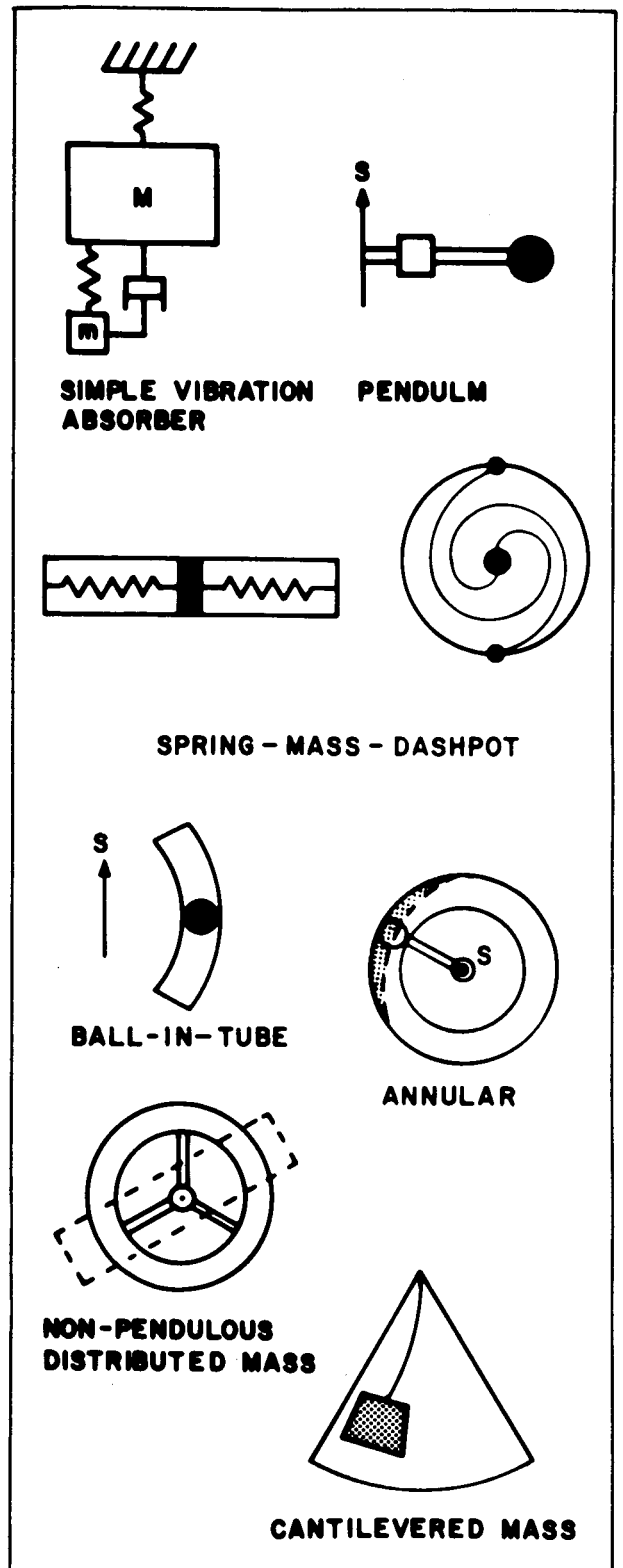


Fig. 5. Passive nutation dampers

- (3) The viscosity of the damping fluid varies with temperature, and the case must be carefully sealed to avoid leaks.

Figure 7 shows how nutation drives the damper bob. Simple reaction-torque and "energy-sink" arguments can be made to show that this motion damps nutation.¹ For a despun platform, wobble drives the bob in much the same way as nutation does. The damper attenuates wobble because the offset bob tips the spacecraft principal axis in the direction of the desired spin axis.

Some simple equations for damper performance at resonance are

$$\tau_{\eta} = \frac{1}{\delta \beta \omega_{\eta}}$$

for the sail-mounted damper and

$$\tau'_{\eta} = \frac{1}{\delta \left(1 - \frac{I_l}{I_s}\right)^2 \beta' \omega_{\eta}}$$

for the wheel-mounted damper, where

$\tau_{\eta}, \tau'_{\eta}$ = time constants

$$\delta = \frac{md^2}{I_l}$$

The equations show that performance is better for higher nutation frequencies, for bigger bobs mounted farther from the spacecraft center of mass, and for higher damper-magnification factors. However, these simple equations do not tell the complete story. For example, higher magnification factors reduce the linear range of the damper and can cause poorer performance at the extremes of the allowable nutation-frequency range.

The OSO damper is tuned by selection of the optimum natural frequency and magnification factor.

¹Spencer, T. M., "Cantilevered-Mass Nutation Damper for a Dual-Spin Spacecraft," Proceedings: Symposium on Attitude Stabilization and Control of Dual-Spin Spacecraft, AF Report No. SAMSO-TR-68-191, U.S. Air Force, Washington, D.C., Nov. 1967.

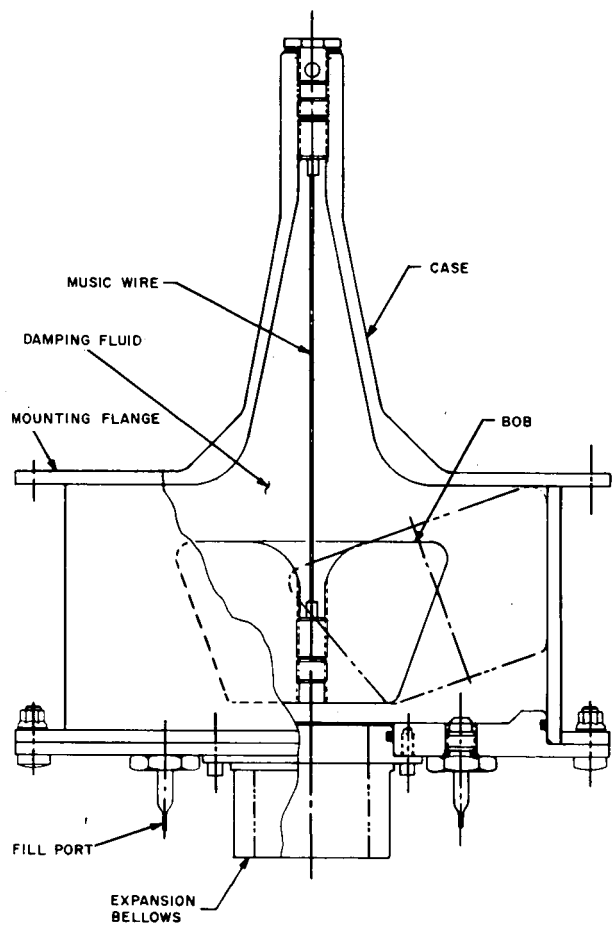
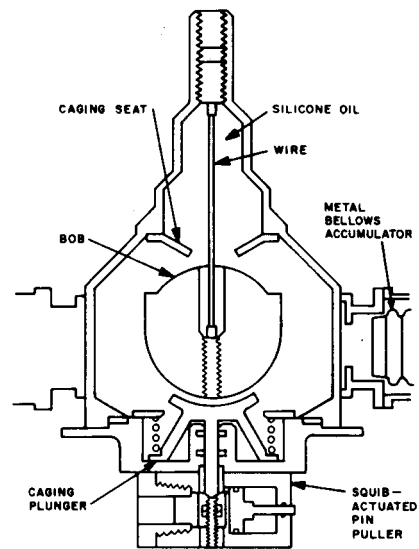
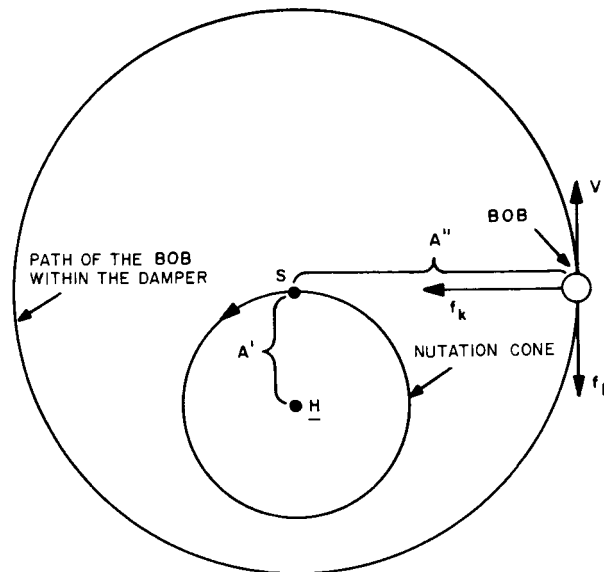


Fig. 6. Cantilevered-mass nutation dampers

The natural frequency is varied by changes in the suspension-wire length or diameter. The magnification factor is varied by changes in the damping-fluid viscosity. Figure 8 shows how damping performance is affected by the choice of natural frequency. Figure 9 shows how performance is affected by the choice of magnification factor.

The efficiency of the OSO damper is illustrated by the fact that an 8-lb damper can give a 1-min nutation-decay time constant on a 1500-lb observatory for a wheel spin rate as low as 10 rpm. By comparison, a fluid-ring damper with the same performance would weigh nearly 100 lb.



\underline{H} = angular momentum vector

S = spin axis

A' = nutation cone angle

A'' = damper bob amplitude

V = damper bob velocity

f_D = drag force on damper bob

f_k = spring restraint on damper bob

Fig. 7. Damper bob motion

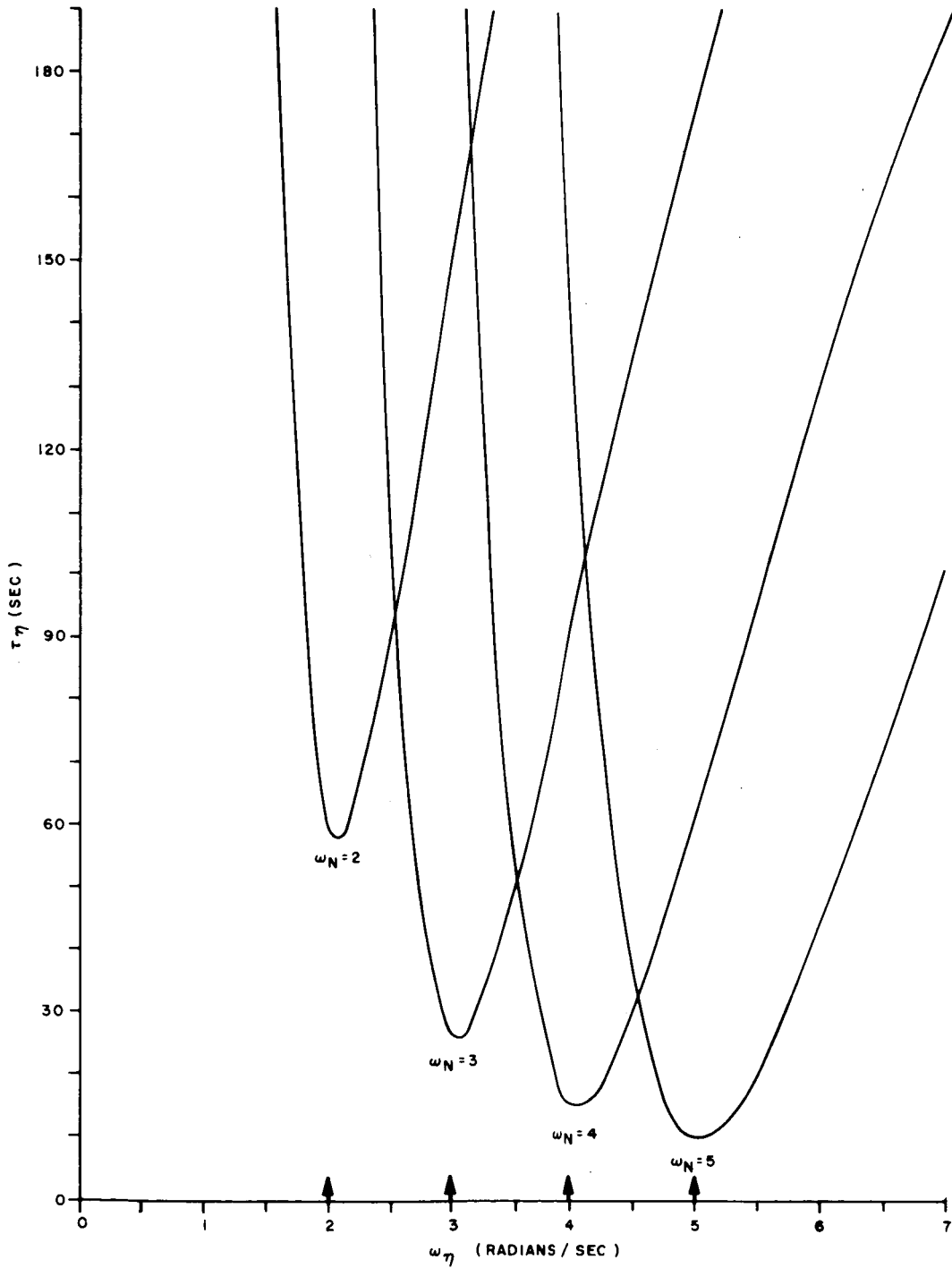


Fig. 8. Effect of damper tuning on performance

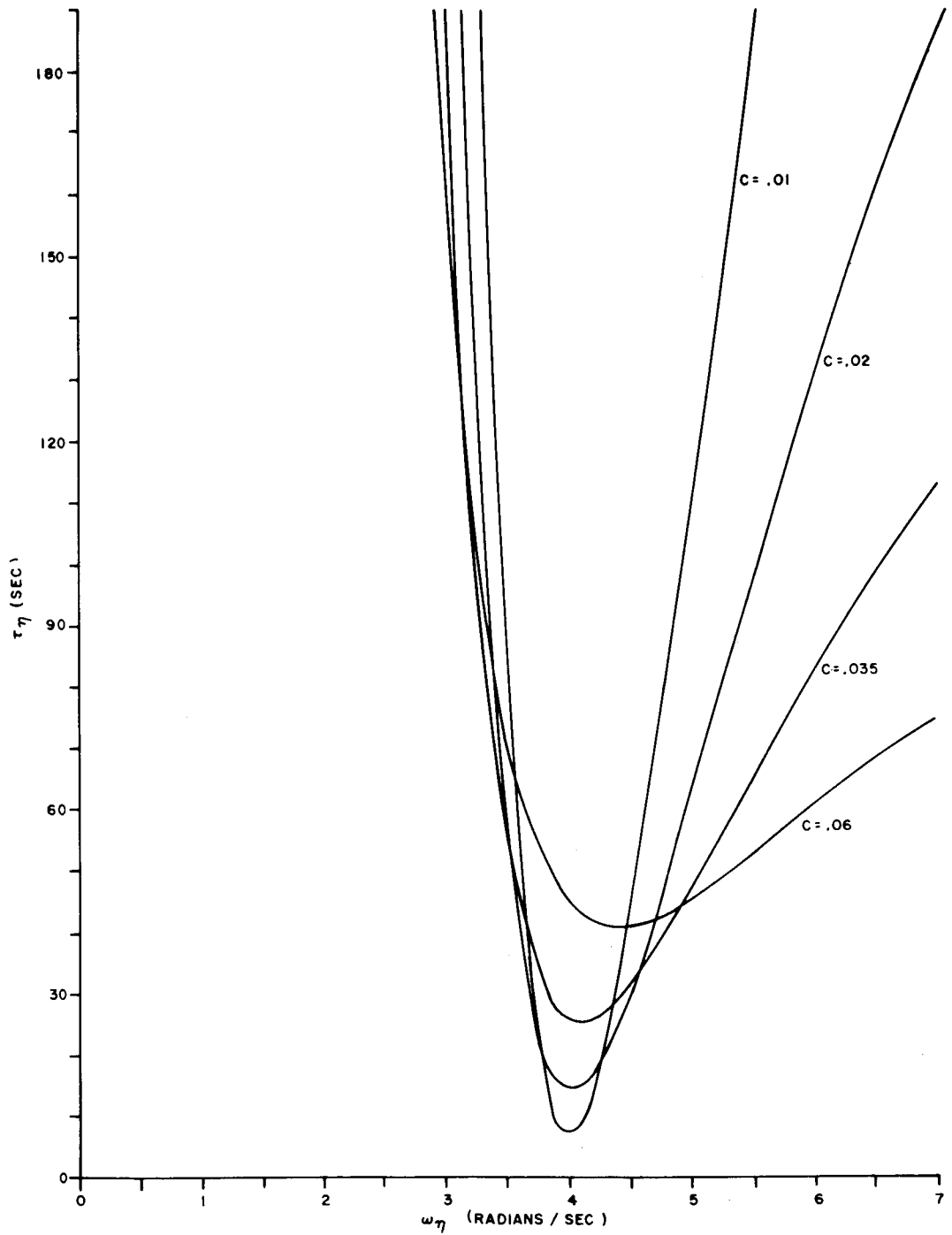


Fig. 9. Effect of damper-fluid viscosity on performance

DISCUSSION

Robert Campbell:

Could you give us some idea of how much penalty one might pay in weight to go to a ring damper of noncircular design, such as say a rectangular shaped design which might conveniently fit into a spacecraft?

Spencer:

I don't know the exact answer to your question, but the fluid-filled ring damper used on the improved Tiros has a rectangular shape.¹ The main thing you wish to achieve is as large an "effective" moment of inertia as possible because of the fluid in the ring. This moment of inertia is about the center of the damper (that is the center of fluid motion) and what you want to maximize is the projected inertia at right angles to a line from the center of the damper.

The Ayache and Lynch paper explains why a circle gives the biggest effective moment of inertia for a given area. A square or rectangle of the same area weighs more for the same damping because the viscous damping forces work less efficiently. In addition, there are peculiar flow characteristics at the corners and you have to round them a bit.

George Herzl:

We would like to stress the failure aspects of nutation dampers. I think maybe we could briefly discuss the aspect that in a single-spin spacecraft in the stable configuration of the types shown here in the beginning, like the Tiros or disc-shaped types, if the nutation damper fails, it will just take much longer to damp out the nutations.

On the other hand, in the dual-spin spacecraft you may want to discuss what happens in the dual spin spacecraft if the nutation damper fails.

Spencer:

Okay, in the case that the dual-spin spacecraft is inertially disc-shaped, that is, that the spin moment of inertia of the wheel of the spacecraft is larger than the transverse inertia the same principle applies as for the single spin spacecraft—no chance for instability caused by energy dissipation. That's been the configuration for past OSO spacecraft.

For the rod-shaped variety (for example, one of the space bases that Peter Kurzhals showed might well have been inertially rod-shaped), if the damper was not designed with sufficient damping ability or if it failed in orbit, then you might lose stability and go into a propeller type tumbling mode. Energy

dissipation on the rapidly spinning body tends to cause this. It is very important for the designer to estimate the potentially destabilizing energy dissipation rates and to make sure the damper will overpower them.

I believe the space lab concept had four independent pendulums. They are mechanically very simple, so the chance of failure is very low, and of course three out of four would probably do the job.

Harry Van Elkan:

I would just like to make one point on the tube type of nutation damper that I've been somewhat familiar with. The most critical thing in a tube type damper is a complete evacuation of all the entrapped air in the fluid. To that effect we completely evacuate the oil of all entrapped air and in addition to that put a spring damper, or rather a spring bellows mechanism, into the system that always provides a positive force on the oil in order to prevent any possible inclusion of bubbles within the tube. It has been a very critical development to get the air completely out of the system to get maximum efficiency out of the damping mechanism. I believe Mr. Spencer probably is aware of this requirement.

Spencer:

Yes, I'm aware that you need to evacuate. But I believe Ayache and Lynch studied the effect of a bubble in the tube, and in going through that analysis they found that in fact you can make these fluid rings so that they are tuned in much the same way. That is, if they are on the spinning part of the satellite so they are subject to a centrifugal force field, you can make them so they are a tuned damper. Thus, you might intentionally build such a fluid damper with a bubble.

Instead of having a vibrating mass, which in the case of the OSO damper is obtained by cantilevering the mass, the fluid is actually in a C-shaped tube of some kind with voids at the end. Then you actually get a tuned fluid ring damper. It has no moving parts except for the fluid.

By the way, the OSO damper has a moving part in a sense, but it is like the tuning fork in an Accutron watch. Friction can't cause it to hang up or stick. There is theoretically no residual nutation that can excite the damper and get damped out. When you have the suspension wire concept on either the OSO damper or the one Barry Tossman discussed, you have no friction threshold problems.

¹Ayache, K., and Lynch, R., "Analyses of the Performance of Liquid Dampers for Nutation in Spacecraft," *J. Spacecr. Rockets* 6:1385-1389, Dec. 1969.

LOW NUTATION-RATE DAMPERS

Barry E. Tossman
The Johns Hopkins University
Applied Physics Laboratory
Silver Spring, Maryland

I. INTRODUCTION

Mission requirements plus spacecraft weight and power constraints often reduce the excitation frequency of a nutation damper below 1 cpm. Since attitude stability is determined by damper performance, maximum effectiveness at low rates is demanded. This paper presents design considerations that low-frequency dampers require, along with descriptions of two low-frequency systems: the Direct Measurement Explorer 1 (DME 1) (Ref. 1) and the Small Astronomy Satellite A (SAS A) (Ref. 2).

II. LOW-FREQUENCY SYSTEM DEFINITION

Two frequencies that are associated with axisymmetric spin-axis-stabilized spacecraft are the space-observed coning rate of the vehicle spin axis

$$\omega_n = \frac{H}{I} \quad (1)$$

and the excitation frequency of a nutation damper

$$\Omega = \omega_n - \omega_z \quad (2)$$

where

- H = total spin-axis angular momentum,
- I = total transverse spacecraft moment of inertia,
- ω_z = absolute spin-axis angular velocity of the spacecraft portion containing the damper.

Low- Ω systems derive from requirements for spin-rate and spin-axis stability plus constraints on spacecraft geometry, weight, and power. For example, consider a dual-spin system where I_z is the total spin-axis moment of inertia and H_r is the angular momentum of a

high-speed wheel relative to the main body. The driving frequency of a damper placed on the main body is, from Eqs. (1) and (2),

$$\Omega = \left(\frac{I_z}{I} - 1 \right) \omega_z + \frac{H_r}{I} \quad (3)$$

Three satellite-system factors influence the parameters of Eq. (3) in a manner that generates a low Ω :

- (1) Weight and power limitations; Ω is reduced if the rotor size and speed are small relative to the spacecraft inertia.
- (2) Slow experiment scan rates; the attitude mission requires a specific spin rate (in the case of astronomical Explorers, it is generally well below 1 rpm).
- (3) Spin-axis stability; the ratio of moments of inertia may be 1.10 or lower in order to minimize gravity-gradient perturbations.

As examples, the excitation frequencies for DME 1 and SAS A were low for all three reasons mentioned above—0.16 cpm for DME 1, and 0.8 and 0.016 cpm for the SAS A primary and backup experiment modes, respectively.

III. DESIGN CONSIDERATIONS

Numerous dynamical aspects of a satellite influence the selection and design of a nutation damper. The following paragraphs consider system dynamic stability and the design of nutation dampers having maximum effectiveness.

A. Satellite-System Parameters

Perhaps of prime governing influence on the attitude system and damper are H and the nutation frequencies ω_n and Ω , each of which should be reasonably large. The overall spin-axis stability is dependent on H , which should be large in order to maintain gyrostaticity in the presence of perturbing torques. The effectiveness of the nutation damper is dependent on ω_n ; it is described by the nutation-damping time constant τ , which generally varies as $1/\omega_n$ (Ref. 2). Finally if Ω is large, the damper will be easier to tune, and it will generally be smaller and less sensitive to variations in the damping constant and to hysteresis in the support mechanism.

B. Stability

The location of the damper in one or the other portion of a dual-spin system will affect attitude stability. If energy dissipation occurs in both the main body and the rotor, a necessary and sufficient condition for stability (Ref. 3) is

$$\left(\frac{P}{\Omega}\right)_{\text{body}} + \left(\frac{P}{\Omega}\right)_{\text{rotor}} < 0 \quad (4)$$

where P is the average energy dissipation rate within either body ($P < 0$). To satisfy Eq. (4), the damper is placed on the despun portion of the spacecraft and is designed to dissipate considerably more energy than that dissipated within the rotor.

Additional conditions of stability depend upon damper geometry and pertain to its weight, size, location, and spacecraft mass properties. Specifically, these conditions derive from the Routh-Horwitz stability criteria applied to the damper and spacecraft coupled equations of motion.

C. Design for Rapid Nutation Damping

After stability considerations, nutation-damper selection is based upon a device's ability to provide rapid nutation damping. The type of damper that achieves this for a particular mission is strongly governed by the excitation frequency Ω . Generally, fluid-ring dampers are used on high- Ω systems, about 30 cpm and above. Here, high fluid-velocity gradients can be established in relatively short and narrow tubes. Ball-in-tube and stiff cantilevered bobs are used effectively in systems with $\Omega \geq 5$ cpm.

For low- Ω systems, ball-in-tube or pendulous dampers on weak springs appear most effective. To examine the design trade-offs inherent with these dampers, consider a mass constrained to move in a circular arc that is in a plane normal to the spin axis. The energy-sink solution for the nutation-damping time constant is

$$\tau = \frac{2H_d}{mcl^2 \omega_n^3 \Omega} \left[\left(\frac{c\Omega}{I_d} \right)^2 + \left(\Omega^2 - \kappa^2 \right)^2 \right] \quad (5)$$

where

$$\kappa = \left(\frac{k}{I_d} + \frac{r_o}{r_1} \omega_z^2 \right)^{1/2} = \text{damper natural frequency,}$$

$$\omega_n = H/I = \text{space observed coning frequency,}$$

$$I_d = \text{damper moment of inertia,}$$

$$m = \text{damper mass,}$$

$$k = \text{torsional spring constant,}$$

$$c = \text{torsional damping constant,}$$

$$r_o = \text{torsion wire offset from spin axis,}$$

$$r_1 = \text{damper arm length,}$$

$$l = \text{elevation of damper plane above satellite-mass center.}$$

Design goals indicated by Equation 5 are that τ is minimized if l and ω_n are large, $\kappa = \omega$ (i.e., the damper natural frequency matches the driving frequency), and c is relatively low. The importance of tuning is demonstrated in Fig. 1, which plots the time constant as a function of the pendulum spring constant k for the SAS A damper. It is seen that minimum time constants are achieved at resonance, with relatively low values of the damping constant.

For very-low-driving-frequency systems, such as the SAS A backup mode, a tuning condition is almost impossible to achieve without destroying one of the conditions for stability. Figure 2 shows the effect of the spring constant on τ for the SAS A backup mode and

indicates that the desirable operating point is a near zero spring constant with larger values of damping. Larger values of the spring constant increase τ , while smaller values hazard instability.

SAS-A PRIMARY MODE TIME CONSTANTS

SPIN INERTIA - $28.5 \text{ kg} \cdot \text{m}^2$
 SPIN RATE - 1/12 RPM
 ROTOR MOMENTUM $2.4 \text{ kg} \cdot \text{m}^2 \text{ rad/s}$
 DAMPER INERTIA - $7.93 \times 10^{-3} \text{ kg} \cdot \text{m}^2$

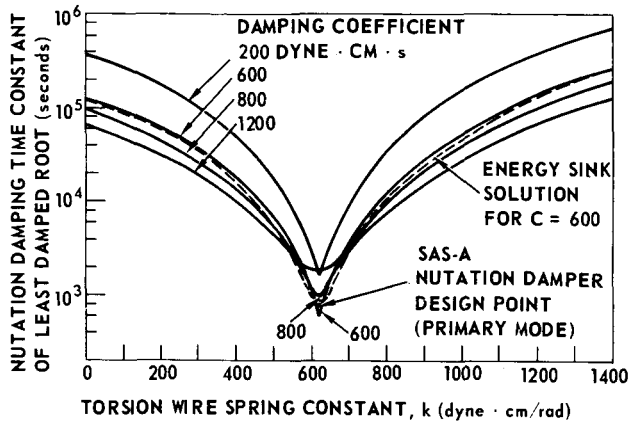


Fig. 1. SAS A nutation damper performance—primary mode

SAS-A BACK-UP MODE TIME CONSTANTS

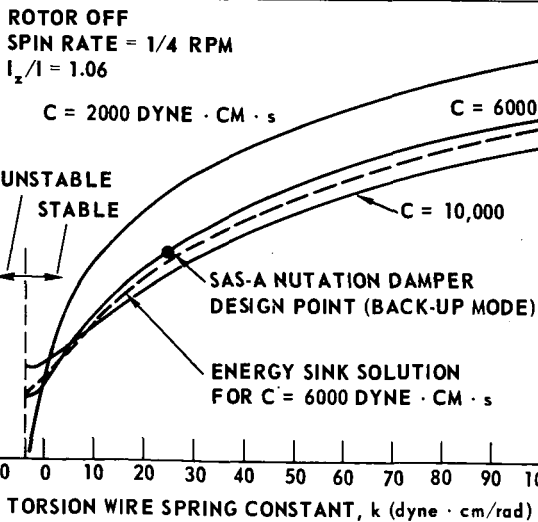


Fig. 2. SAS A nutation damper performance—backup mode

IV. DESIGN EXAMPLES

This section considers the DME 1 and SAS A nutation dampers, the designs of which were strongly influenced by the low excitation frequencies.

A. DME 1 Nutation Damper

The DME 1 was a single-spin system launched in November 1965. Its nominal rotation rate was 3 rpm, and its damper excitation frequency was 0.16 cpm.

The damper was of the ball-in-tube design (see Fig. 3). It consisted of a pair of curved aluminum tubes in a plane normal to the spin axis, each tube containing a polished copper sphere. Permanent magnets attached to the tubes created a high, local magnetic field. Eddy currents generated in the rolling copper balls effected dissipation of nutation energy. The damper provided a small-angle nutation-damping time constant of 8.7 min. The total weight of the nutation damper was 3.24 lb.

Almost all aspects of the DME 1 design were influenced by the low spin rate and excitation frequency. Ball-and-tube smoothness was paramount in ensuring ball motion for small nutations. A nonmagnetic ball was required to preclude attraction to magnetic materials within the spacecraft. Although a ball rolling in a gas-filled tube might have worked just as well, this design was discarded because of the problems associated with ensuring tube smoothness and a positive seal for a sharply curved tube. Magnetically induced eddy currents appeared to be ideally suited for the damping mechanism.

The DME 1 flight performance was of particular interest in as much as the system had a low spin rate of 3 rpm and a moment-of-inertia ratio of 1.04. These values were the lowest recorded for a spin-stabilized satellite. Also unique was the use of eddy-current coupling as the energy-loss mechanism. The nutation-damper performance, as evidenced by telemetered nutation decay, was quite close to the values predicted by computer simulation. The observed time constant was approximately 9.2 min for a spin rate of 3 rpm. The attitude performance was degraded at spin rates below 1 rpm, where the nutation-damping time constant was significantly increased and ball motion was impaired because of an imperfect rolling surface.

B. SAS A Nutation Damper

The SAS A spacecraft, launched in December 1970, is spin-axis stabilized by a high-speed momentum wheel while the main body rotates at 1/12 rpm. The nutation damper consists of a pendulum, mounted on a torsion wire, which swings in a plane normal to the spin axis. The damper has the capability of changing, by command, its mechanical resonance to match a dual-spin excitation frequency of 0.8 cpm for the primary experiment mode and, if the spacecraft momentum wheel fails, of closely matching a single-spin frequency of 0.016 cpm for a backup capability. The damping coefficient of this damper can be varied from 700 to 6700 dyne-cm-s in order to achieve minimum nutation-damping time constants for the primary and backup modes as well as an acquisition mode. In the acquisition mode, the spacecraft spin rate is being gradually diminished from the value established by yo-yo despin of the Scout fourth stage, ~ 5 rpm, to the primary spin mode of 1/12 rpm.

The SAS A nutation damper is shown in Fig. 4. The assembled natural frequency of the pendulum and

torsion wire matches the spacecraft nutation frequency in the primary mode (momentum wheel on). The mechanism for varying the effective torsion-wire spring constant consists of a magnet, a coil, and a constant current source. A permanent magnet is attached to the pendulum pivot which has its magnetization directed along the pendulum centerline. The coil produces a magnetic field that normally opposes the permanent magnet. The net effect is that the pendulum torque caused by the torsion wire is nearly negated by magnetic torque.

Damping is achieved by eddy currents induced in the copper vane as it swings between the pole faces of a chargeable "C" magnet. The damping coefficient is varied by changing the magnetization within the chargeable-magnet circuit. The low flux state provides a damping constant of 700 dyne-cm-s, which is nearly optimal for the primary dynamical mode. The high flux state provides 6700 dyne-cm-s damping constant.

The pendulum assembly consists of a copper end mass, an optical mask, pendulum arms, and torsion wire. The pendulum, except for the parameter change magnet,

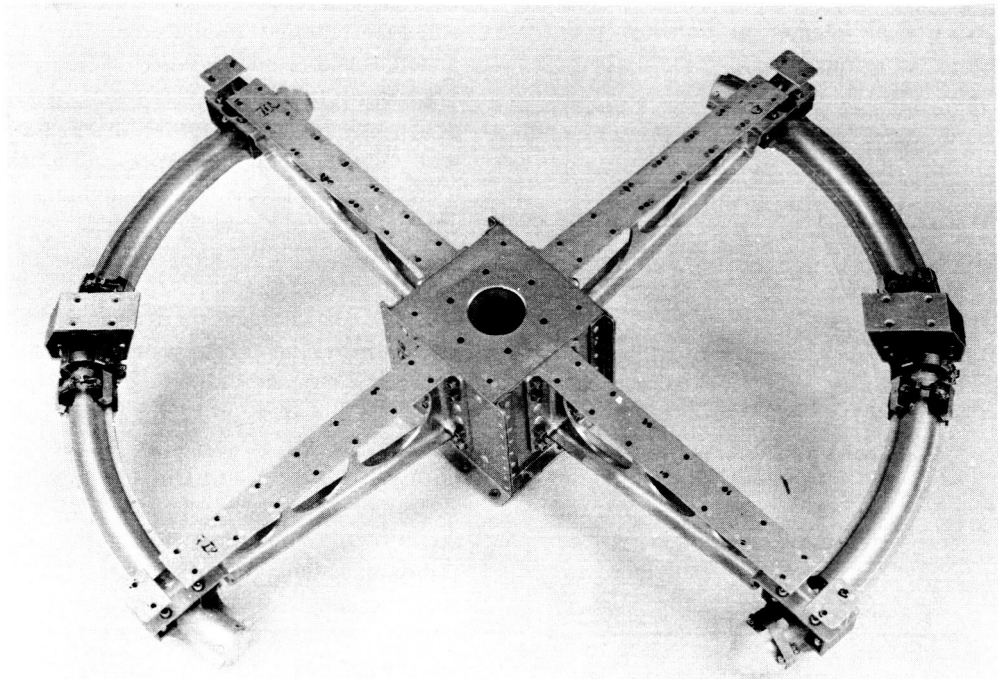


Fig. 3. DME 1 nutation damper

is composed of nonmagnetic alloys so that magnetic forces will not affect damper motion. The end mass is constructed of high-purity copper and provides damper inertia and damping via magnetically induced eddy-currents. The torsion wire is a 10 percent Ni/Pt ribbon of the type used in taut-band meter movements. BeCu springs position the torsion wire and provide a constant tension that restrains the pendulum from moving either vertically or radially.

The pendulum is restrained by a motor-driven clamp throughout spacecraft testing, shipping, and launching.

The damper weighs 2.6 lb and draws 20 mW power when operating in the primary mode for dual-spin conditions. The nutation-damping time constant in this mode is 20 min, and, according to comprehensive digital simulation, steady-state spin-axis pointing accuracies on the order of 0.1 deg have been achieved.

Most aspects of the SAS A damper design were dictated by the low frequencies involved. The near-zero spin rate precluded the use of a centrifugal force field for centering a ball, and no degree of tube smoothness

would have assured us that a ball would respond to low-level nutations. The low driving frequency also precluded tube-filled devices, as insufficient velocity gradients could be established in even moderately sized tubes. The torsion wire of rectangular cross section appeared to provide a zero-threshold suspension that was weak in torsion but relatively strong in tension. A pendulum mounted on such a torsion wire could be built to match resonance with the low excitation frequency. The pendulum itself had to be completely nonmagnetic so that it would not be biased by magnetic elements within the spacecraft.

The real achievement for a low-frequency damper is in the backup mode, where the torsion-wire spring constant is nearly negated by a magnetic circuit. Here, the pendulum is suspended by a relatively strong wire with almost zero torsional compliance and zero threshold.

V. CONCLUSION

This paper has presented some of the more salient aspects of nutation-damper design, with emphasis on

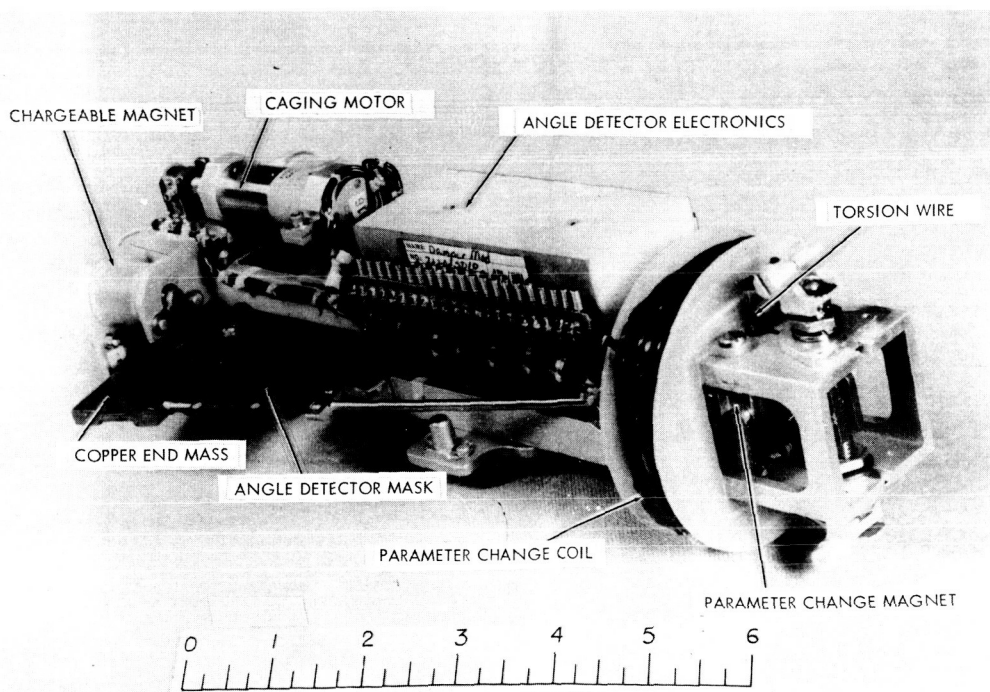


Fig. 4. SAS A nutation damper

systems with low nutation frequencies. Aspects of stability, optimization of the time-constant equation, and design have been discussed.

It is clear that there is strong need for low-frequency devices with which to stabilize spacecraft that have

limitations on spin rate, power, weight, and attitude perturbations. It is also clear from the experience of the DME 1 and the SAS A that these devices are realizable, and that their stabilizing performances are quite acceptable.

REFERENCES

1. Mobley, F. F. et al., "Performance of the Spin Control System of the DME-A Satellite," Proceedings of the AIAA/JACC Guidance Control and Flight Mechanics Conference, August 1966.
2. Tossman, B. E., "Variable Parameter Nutation Damper for SAS-A," AIAA Paper No. 70-972, presented at AIAA Guidance, Control, and Flight Mechanics Conference, Santa Barbara, Calif., August 1970.
3. Likins, P. W., "Attitude Stability Criteria for Dual Spin Spacecraft," *J. Spacecr. Rockets* 4(1967): 1638-1643.

DISCUSSION

Mark Scher:

Mr. Tossman, can you test this magnetic damper that you described in the 1-g field?

Tossman:

Not as a complete unit. There are tests that we can perform

to establish that the torsion wire has exactly the right compliance that we want. We can measure independently and very accurately the moment of inertia of the pendulum. And we can measure the damping established by the pendulum in the magnetic field fairly accurately. But testing the entire unit is impossible in a 1-g environment.

NUTATION DAMPERS FOR MANNED SPACECRAFT

Peter R. Kurzhals
NASA-Langley Research Center
Hampton, Virginia

Nutation dampers are examined from the standpoint of application to manned space stations with artificial gravity. Typical spacecraft concepts and associated control requirements are considered, and examples of the dampers proposed for these spacecraft are discussed.

I. INTRODUCTION

To visualize the problems and design techniques associated with nutation control for manned, rotating spacecraft, we must first review possible manned-spacecraft configurations and then investigate examples of the damper designs for these spacecraft. Figures 1 through 4 illustrate the range of spacecraft configurations that have been considered for artificial-gravity operations.

Figure 1 shows one of the earliest space-station concepts, circa 1960. It is a hexagonal, 150-ft-diameter space station capable of housing 21 men in earth orbit and has a spin momentum of about 5 million ft-lb-s. Figure 2 depicts a rotating space station that was in vogue around 1965—the manned orbital research laboratory. This near-cylinder spacecraft consisted of a manned module and a counterweight connected by cables or struts and is similar to manned space-station configurations with artificial gravity that are now under study. Finally, Figs. 3 and 4 show two proposed concepts for space stations capable of accommodating 50 or more astronauts each. The station in Fig. 3 has a zero-gravity laboratory with nuclear power modules and a symmetrical spinning section which serves as living quarters for the crew. The concept depicted in Fig. 4 has similar zero-gravity laboratory and power modules, but uses two, near-cylinder, counterrotating sections as artificial-gravity quarters.

II. BASIC REQUIREMENTS

The basic characteristics of the manned missions under study are indicated in Fig. 5. The spacecraft have near-cylinder or near-disk inertia distributions, and generally spin at a rate of from 2 to 4 rpm about a maximum axis of inertia. Artificial gravity is provided by either single-spin or multi-spin operation, with spin momenta ranging from 5 million to 100 million ft-lb-s. Disturbances acting upon these spacecraft arise from both internal and external sources. Perhaps the most critical of these, in terms of nutation damping, are docking and crew-motion effects, which can produce maximum wobble angles on the order of several degrees. Since crew motion in particular will occur continuously, and the resultant errors in spacecraft motion in particular will occur continuously, and the resultant errors in spacecraft motion may be cumulative, some form of energy dissipation or nutation damping is required.

Although the requirements for such a damping system have not been firmly established to date, preliminary guidelines for the system do exist, and have been used in a number of trade-off and design studies. Basically, these requirements call for a system weighing less than 2 percent of the rotating spacecraft configuration, with minimal interference with the configuration and experimental mission. In terms of performance, three elements that contribute to errors in

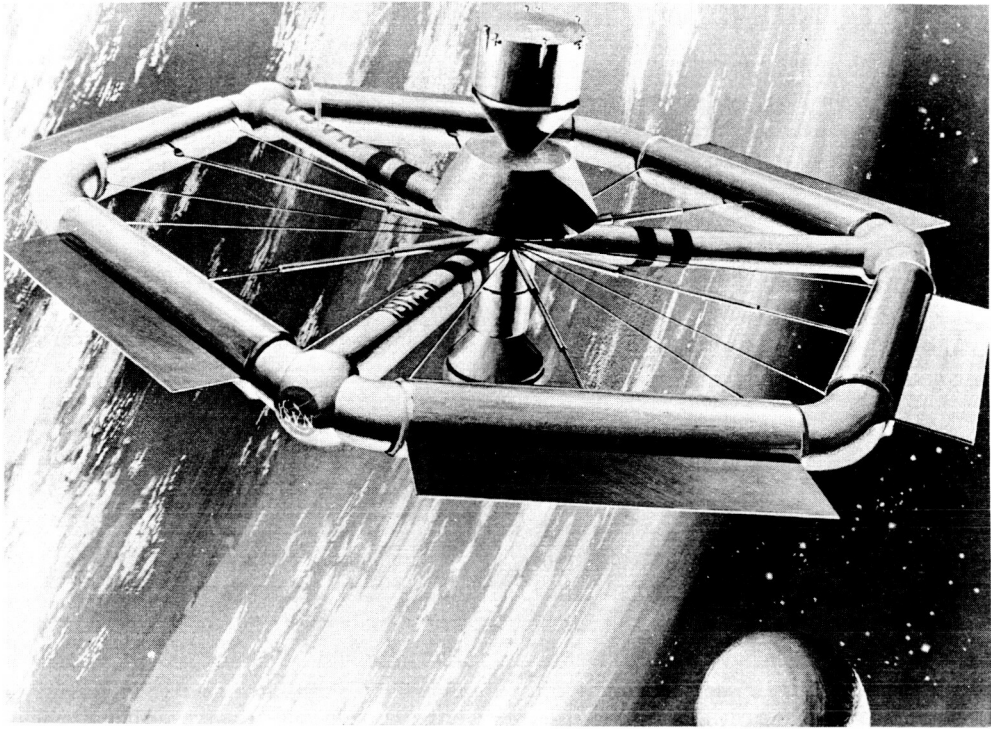


Fig. 1. Early rotating space station concept

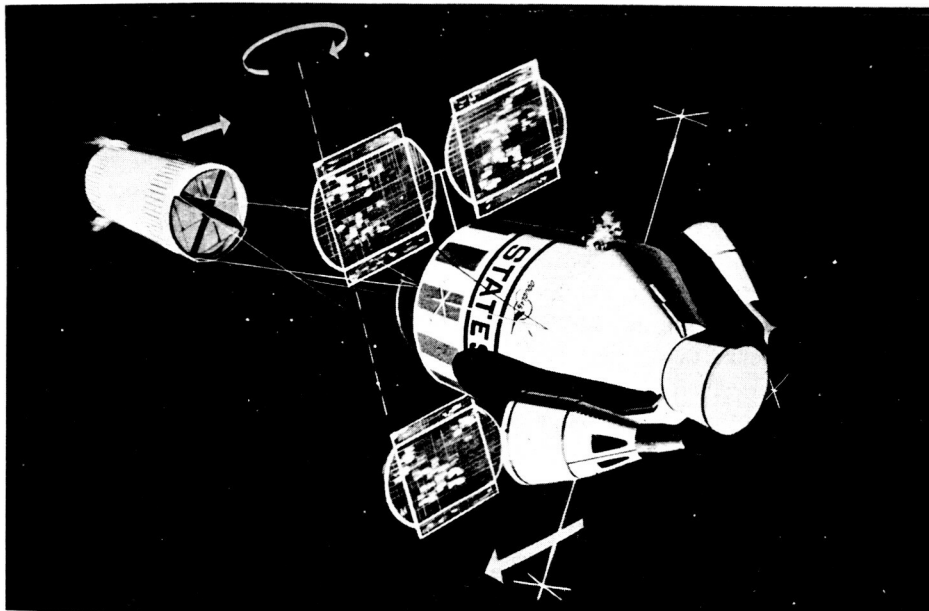


Fig. 2. Manned orbital research laboratory concept

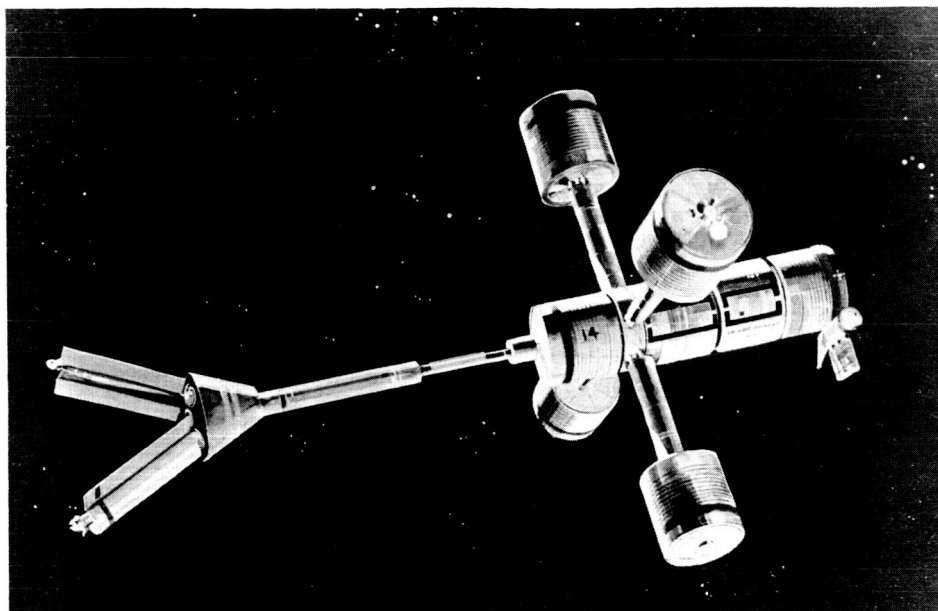


Fig. 3. Single-rotor space-base concept

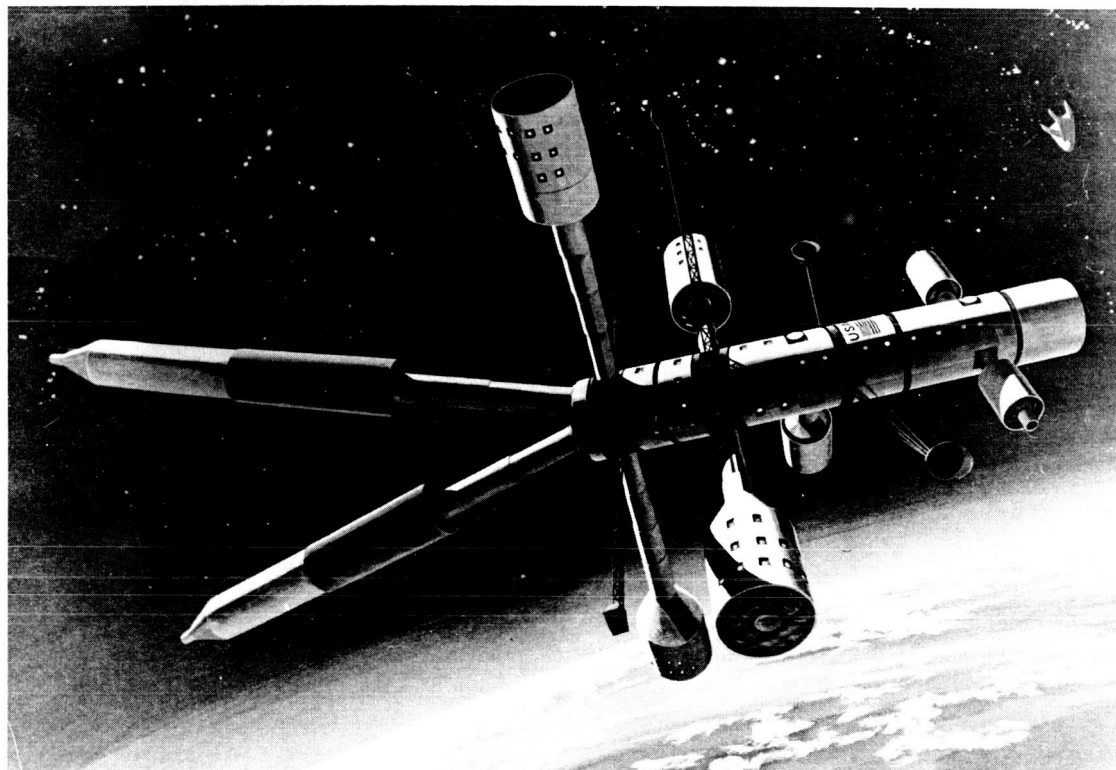


Fig. 4. Dual-rotor space-base concept

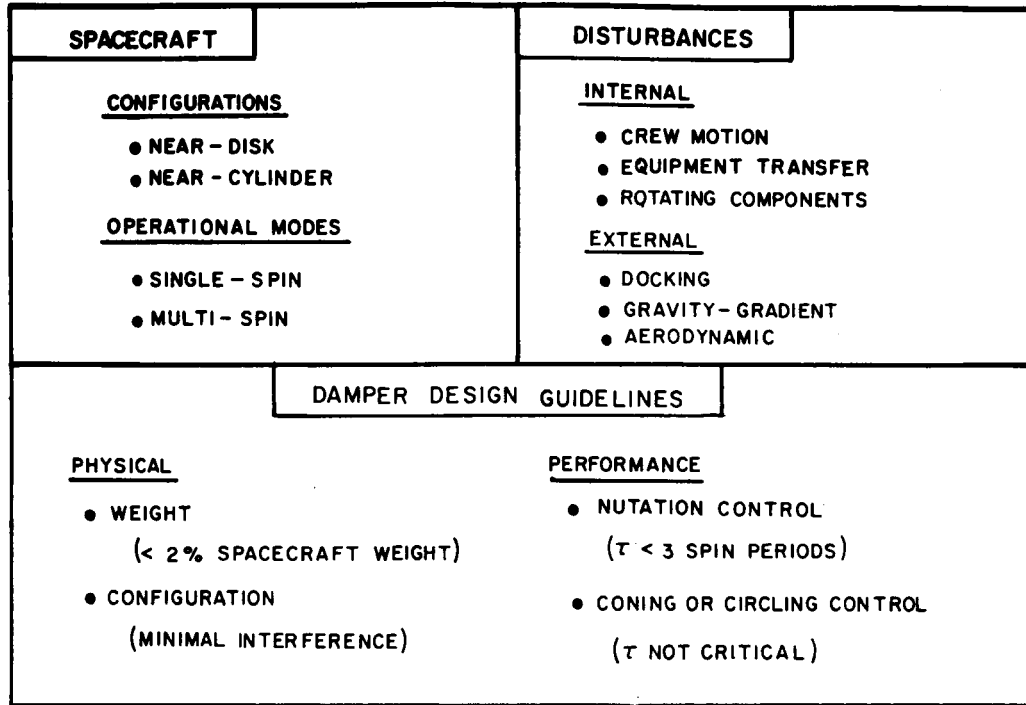


Fig. 5. Basic mission requirements

spacecraft motion must be considered—circling, coning, and nutation. Circling, defined as translation of the maximum principal inertia axis relative to the spin-reference axis, produces a change in the nominal gravity level. Coning, defined as spin about a maximum principal inertia axis that is rotated relative to the spin reference axis, appears primarily as a tilt in the station floor. Nutation, defined as periodic motion of the spin vector about the maximum inertia axis, results in a rolling motion of the station floor. For a multi-spin configuration, all of these errors may also interfere with zero-gravity experiments in the nonspinning, attached modules.

In general, circling and coning errors are small and noncumulative. Control of these errors, when necessary for accomplishment of the spacecraft mission, can probably be obtained with a low-response system with a time constant on the order of 30 spin cycles. By comparison, nutation errors can be cumulative, and they should be damped more rapidly to maintain spacecraft control. A typical time constant for nutation control, one that is used in many of our design studies, is on the order of three spin cycles.

III. DAMPER CONCEPTS

A. Nutation Control

With these requirements in mind, let us now consider some specific nutation dampers. Figure 6 shows an example of an active damper—the control-moment gyro (CMG). The CMG is a constant-speed flywheel mounted on either single or double gimbals. Precession of the flywheel momentum vector H by gimbal torque motors produces a reaction torque M which can be used to provide spacecraft damping. For example, if H is initially aligned with the spacecraft spin axis, then a control torque can be produced by driving H through an angle α . A characteristic control technique (Refs. 1 and 2) is to command CMG gimbal angles α_1 and α_2 proportional to the transverse spacecraft rates ω_1 and ω_2 along the initial gimbal axes. Either a single gimbal (corresponding to α_1) or a double gimbal (corresponding to α_1 and α_2) could be used. The resulting linear time constant τ is inversely proportional to the number N of CMG's, the momentum H of each CMG, and the gimbal angle gains K_1 and K_2 . Note that control is much more effective for near-cylinder configurations ($A \ll B$) than for near-disk

configurations ($A \approx B$). For equal spin inertia C and time constant, the near-cylinder configurations spinning about a maximum moment of inertia permit reductions in damper momentum and weight of one to two orders of magnitude.

The maximum control moment, M_L , which sizes the gimbal torquers, is a direct function of the CMG momentum H and the CMG excursion α_L . For fixed H and M_L , optimal response for double-gimbal and single-gimbal CMG's can be described in terms of the ratio R of the maximum expected body rates ω_{1L}/ω_{2L} . Since R here varies from one to infinity, a CMG with a single gimbal along the minimum inertia axis is preferable to a double-gimbal CMG for this particular control law.

The CMG can provide control for both nonspinning and spinning spacecraft with response independent of damper location in the spacecraft. For fixed maximum control moment, the CMG response can be improved by increasing the working gimbal angles through larger gains or through added rate-integral feedback.

As an indication of the relative performance of the CMG and passive nutation dampers, consider Fig. 7, which summarizes the results of contractor studies (Ref. 3) of a 150-foot-diameter near-disk space station with a spin rate of 3 rpm and an allowable damper weight of 2,000 lb. The CMG used here was a 10,000-ft-lb-s double-gimbal unit with rate plus rate-integral control. The passive dampers considered a spring-mass-dashpot with three pendulums pointed inward and mounted 120 degrees apart on the outer modules, and fluid rings mounted parallel or transverse to the spin plane. The pendulums were considered to have either constant damping or controlled damping, which kept the working amplitude of pendulum oscillation near its maximum value. For this application, the CMG time constant was several times better than that for the passive dampers. However, the station launch configuration here did impose rather severe restrictions on the passive dampers, and passive dampers could be made competitive with active dampers, particularly for very large spacecraft where part of the onboard fluids or components could be used as damper mass.

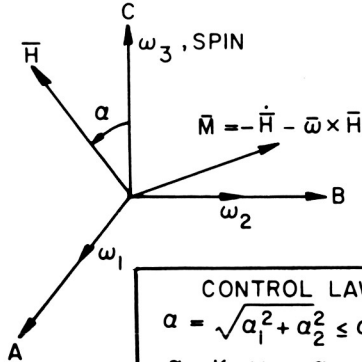
<p>CONCEPT</p>  <p>$A \leq B \leq C$</p>  <p>$\vec{M} = -\dot{\vec{H}} - \vec{\omega} \times \vec{H}$</p> <p>CONTROL LAW</p> $\alpha = \sqrt{\alpha_1^2 + \alpha_2^2} \leq \alpha_L$ $\alpha_1 = K_1 \omega_1 \leq \alpha_{1L}$ $\alpha_2 = K_2 \omega_2 \leq \alpha_{2L}$	<p>PERFORMANCE OPTIMIZATION</p> $R = \frac{\omega_{2L}}{\omega_{1L}} \approx \sqrt{\frac{A(C-A)}{B(C-B)}}$ <p>DOUBLE-GIMBALED CMG</p> $\alpha_{1L} = R \alpha_{2L} = \alpha_L \sqrt{\frac{R^2}{R^2+1}}$ $K_1 = R^2 K_2$ <p>SINGLE-GIMBALED CMG</p> $\alpha_{1L} = \alpha_L$ $\tau_S = \tau_D \sqrt{\frac{R^2}{R^2+1}}$
<p>DESIGN CRITERIA ($\alpha_1, \alpha_2, \omega_1, \omega_2$ SMALL)</p> $\tau \approx \frac{AB}{\pi CNH (K_1 + K_2)} \text{ IN SPIN PERIODS}$ $M_L = M_{1L} = M_{2L} \approx \omega_3 NH \alpha_L$	<p>FEATURES</p> <ul style="list-style-type: none"> • USABLE FOR ZERO-G AND ARTIFICIAL-G SPACECRAFT • RESPONSE INDEPENDENT OF DAMPER LOCATION • WITH M_L FIXED, RESPONSE MAY BE IMPROVED BY <ol style="list-style-type: none"> 1. INCREASED ($K_1 + K_2$) 2. RATE INTEGRAL CROSSFEED $\alpha_1 = K_1 \omega_1 - K_3 \int \omega_2 dt$ $\alpha_2 = K_2 \omega_2 + K_4 \int \omega_1 dt$

Fig. 6. Control moment gyro nutation dampers

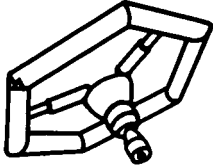
	<p> $A = 10,500,000 \text{ SLUG FT}^2$ $B = 10,500,000 \text{ SLUG FT}^2$ $C = 15,000,000 \text{ SLUG FT}^2$ $\omega_3 = 3 \text{ RPM}$ DAMPER WEIGHT = 2000 LB </p>		
	DAMPER TYPE	CONFIGURATION	TIME CONSTANT, SPIN PERIODS
CMG	DOUBLE-GIMBALED CMG, RATE + RATE-INTEGRAL CONTROL	< 3	
SPRING-MASS-DASHPOT	3 PENDULUMS, 120° APART	CONSTANT DAMPING	15.9
		CONTROLLED DAMPING	12.9
SPIN-PLANE FLUID RING	SINGLE RING ABOVE SPIN PLANE	> 36	
TRANSVERSE-PLANE FLUID RING	6 HALF-RINGS	14.1	

Fig. 7. Relative performance of active and passive nutation dampers

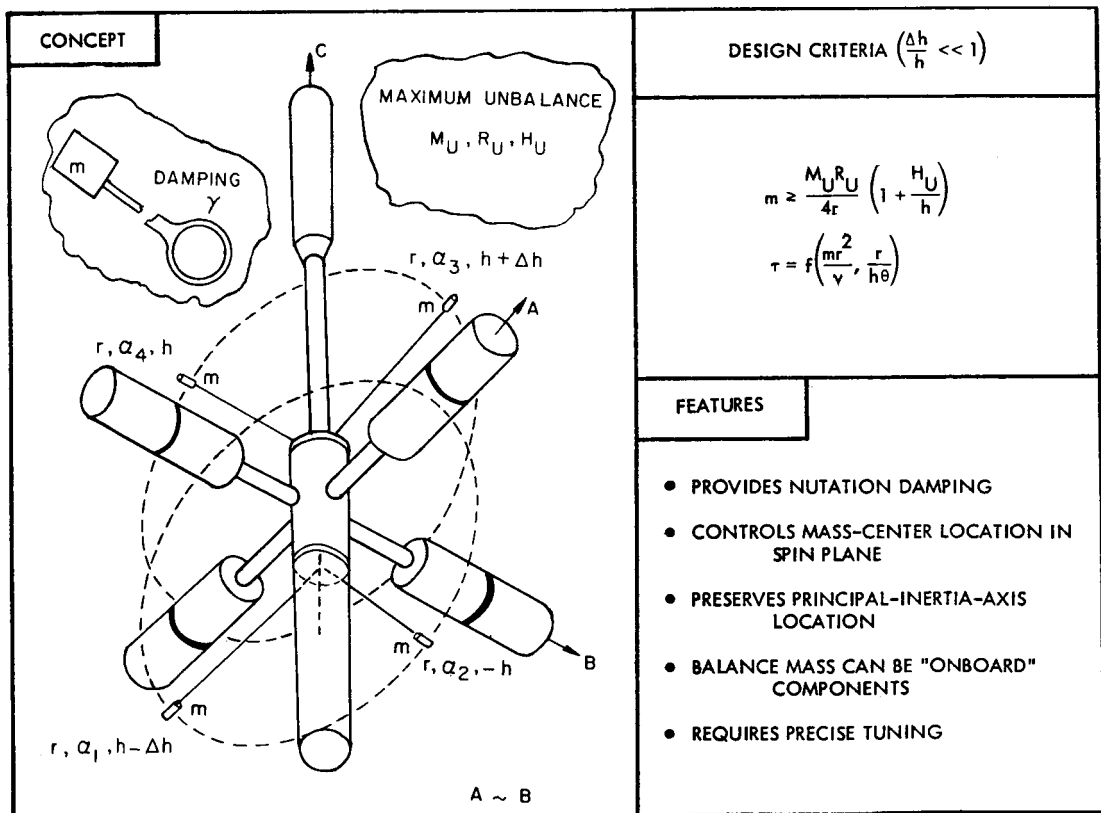


Fig. 8. Mass-balance damper concept

Many other damper approaches, e.g., reaction wheel (Ref. 4) or reaction jet systems, are feasible. However, the higher power or fuel required for these techniques makes CMG or passive dampers preferable for nutation control during the long-duration missions generally associated with future manned spacecraft.

B. Principal Axis of Inertia Control

If these spacecraft require coning and circling control as well as nutation damping, a promising candidate is an active or passive mass balance system. Figure 8 shows one such concept applied to a possible space-base configuration. As indicated earlier, this configuration consists of an artificial-gravity section spinning on bearings relative to two zero-gravity modules. A passive mass-balance damper for this configuration (under study at NASA's Langley Research Center) could use four pendulums of radius r and damping γ moving in planes below and above the spin plane. Theoretically, these pendulums could provide both nutation damping and coning and circling control. For a maximum mass unbalance M_u at a radius R_u and height H_u , the required pendulum mass would be defined as a function of the pendulum radius r and height h .

For a linearized analysis, the motion of each pendulum can be reduced to pendulum motion in a viscous

medium with a nonlinear restoring torque proportional to the wobble angle θ and with constant and periodic forcing functions. The time constant τ can be defined in terms of mr^2/γ and $r/h\theta$, with the best nutation damping obtained in a steady-state where each pendulum rotates at approximately the nutation frequency relative to the spacecraft. Combined mass balancing and nutation control are more complex, but time constants on the order of 10 spin cycles have been obtained during our initial simulations. These preliminary results indicate that nutation and mass-center control are feasible, but may require active control of the pendulum damping or position.

IV. CONCLUSION

This discussion has touched on some of the characteristics of typical nutation dampers for manned spacecraft. Of course, many other damper concepts are possible, and may have application to specific manned missions. However, current design studies on the manned space station/base indicate that CMG's or mass-balance systems are preferable for the long-duration missions requiring artificial gravity. Near-term applications, such as Skylab or a near-cylinder space station, would use CMG's for nutation control, whereas later and larger spacecraft, such as a space base, would rely on active or passive mass balancing and nutation damping.

REFERENCES

1. Adams, J. J., "Study of an Active Control System for a Spinning Body," NASA Technical Note D-905, 1961.
2. Zetkow, G., "Study of Control Moment Gyro Applications to Space Base Wobble Damping and Attitude Control Systems," Grumman GCR-70-2, 1970.
3. Taylor, R. S., "Feasibility Study and Design of Passive Dampers for a Manned Rotating Space Station," TRW Report 4134-6003-RV000, Contract NAS1-3400, 1964.
4. Caggiano, G. J., "Feasibility Study of Fluid Flywheel Techniques to Provide Nutation Damping of Large Spinning Space Vehicles," AFFDL-TR-67-3, 1967.

SESSION III

**Session Cochairman
Bernard A. Kulp
Eglin Air Force Base**

A SCANNING MIRROR SYSTEM FOR THE APOLLO TELESCOPE MOUNT ULTRAVIOLET SPECTROHELIOMETER*

C. O. Highman
Ball Brothers Research Corporation
Boulder, Colorado

The scanning mirror system described in this paper is being developed as the primary mirror in the Spectroheliometer. The system consists of a gimbale mirror mount that is rotated through extremely small angles by the use of frictionless pivots and a closed-loop servo system. Design, fabrication, and test experience are discussed.

I. INTRODUCTION

The Harvard College Observatory Ultraviolet Spectroheliometer is one of four solar astronomy instruments being developed for the Apollo Telescope Mount to be launched with the Skylab in 1972. The Spectroheliometer measures the spectral intensity of selected regions of the sun. The scanning mirror system is a two-axis gimbale mount for a 13-lb, 8.5- by 9.5-in. mirror. The mirror focuses an image of the sun on the entrance slit of a spectrometer. The mirror is gimbale through very small angles in a precisely controlled sequence to scan a raster pattern of a small area of the sun (5×5 arc-min) across the slit. Each axis of rotation uses a pair of pivots, a torque motor, and a transducer—all identical parts.

Four systems have been manufactured: development, engineering, prototype, and flight models. Although all operating tests have been successful, problems encountered during vibration testing required design modifications, as will be discussed.

II. DESIGN CRITERIA

Some significant design requirements of the mirror system (Fig. 1) are—

- (1) Size of raster pattern: 5 arc-min ± 5 arc-s square.
- (2) Lines in raster pattern: 60 lines, spaced 5 arc-s ± 1 arc-sec apart.
- (3) Scan velocity: 1 ± 0.01 arc-min/s.
- (4) Turnaround time: 0.5 sec maximum.
- (5) Scan time: 5.5 min.
- (6) Accumulative error in lines over entire raster pattern: ± 10 arc-s maximum.
- (7) Power-off null-position repeatability: Within 5 arc-s diameter circle at center of line 30.
- (8) Modes of operation:
 - a. Continuous raster.
 - b. Three raster.
 - c. Scan of selected line.

Although they are not firm design requirements, the following are of interest:

Weight of assembly:	
Mirror and mechanism (lb)	67.23
Drive electronics (lb)	3.94
Total (lb)	71.17

*This paper presents the results of research carried out at Ball Brothers Research Corp. under Contract No. B-9651 from Harvard College Observatory, sponsored by NASA Contract NAS5-3949.

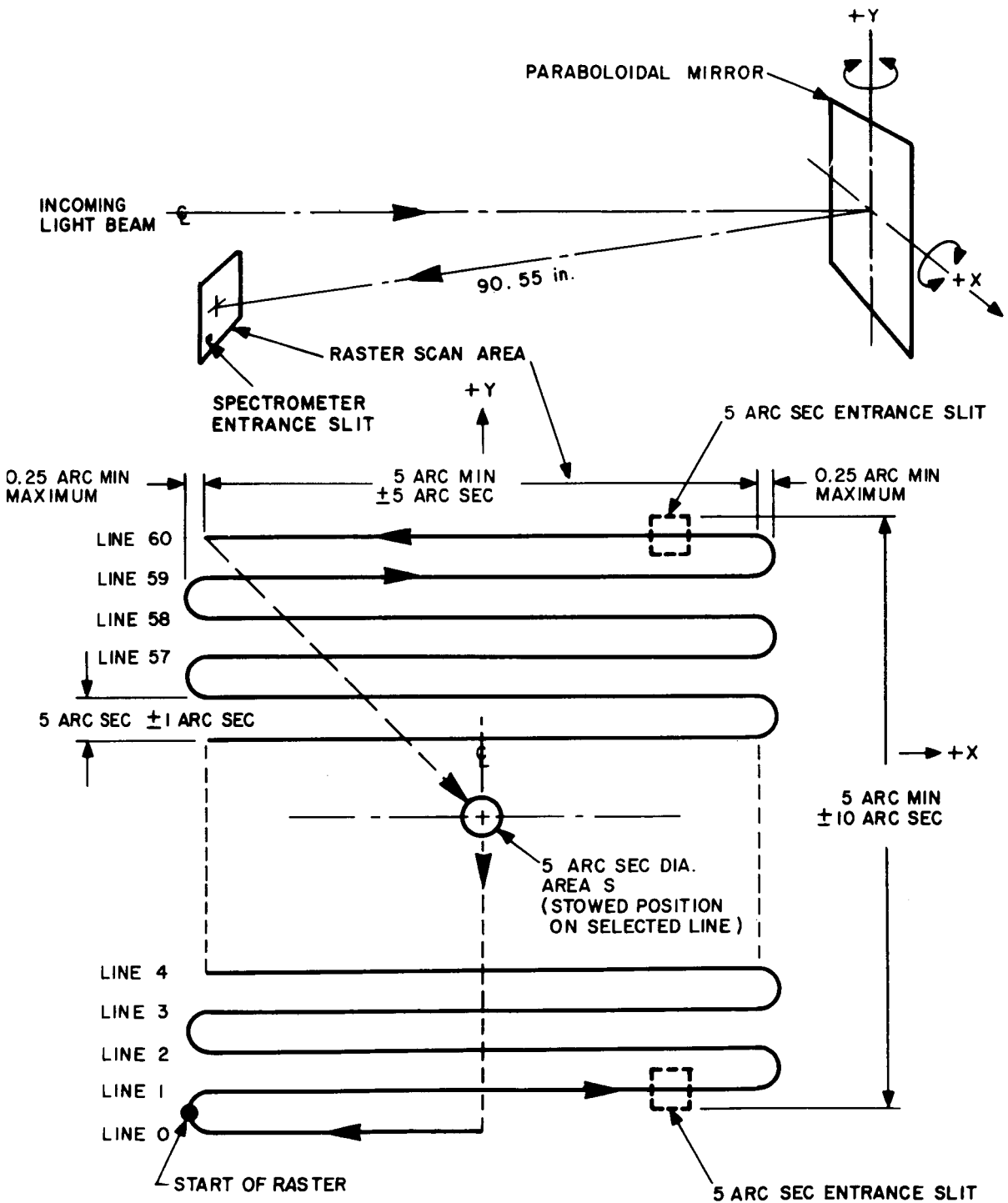


Fig. 1. Mirror raster scan pattern

Overall dimensions:

Mirror and mechanism (in.)	10.2 by 13.8 by 17.8
Drive electronics (in.)	3.9 by 6.5 by 6.0

III. DESCRIPTION**A. General**

To fulfill design requirements, a mechanism was designed to rotate the mirror about two mutually perpendicular axes, each moving through an angle of ± 1.375 arc-min (Fig. 2). The resulting gimbal system is supported in each axis by a pair of unique flexure pivots developed specifically for this application. Since the pivots are essentially torsion springs, the result is an undamped spring-mass system. Although such an undamped system was dictated by the accuracy required, it was necessary to develop a positive-feedback closed-loop servo system to control the two brushless dc torque motors that rotate the gimbals (Ref. 1). The servo system eliminates the effects of the undamped springs, driving the torque motors in response to precisely generated reference waveforms. Each gimbal position is sensed by a linear variable differential transformer (LVDT), which feeds this information into the control system. To avoid effects of gravitational changes on the system and damage from oscillations during launch, each spring-mass system is dynamically balanced to within 0.5 oz-in.

Mounting the mirror within the inner gimbal frame was complicated by the mirror's size and weight, the severe launch environment, thermal cycling during operation, and the need to not distort the mirror. Since the mirror, an off-axis paraboloid, is polished to a figure tolerance of $\pm 1/10 \lambda$ at $\lambda = 5641 \text{ \AA}$, allowable distortion becomes a very small number. In addition, the precise requirements listed in II above do not allow any permanent displacement of the mirror within its mount. To meet all these requirements, a modified kinematic approach was used with success.

Although all operating requirements were met and initial vibration tests were passed, a weight-reduction program eventually led to a vibration failure. As a result considerable analysis and retesting dictated the addition of a remote-controlled mechanism to lock the gimbals during launch. Every effort had been made to avoid doing so to preserve the simplicity of the system.

B. Structure

The outer frame (the primary load-carrying structure) is machined from a handforged billet of 2014 aluminum alloy. To minimize internal stresses within the material and develop required mechanical properties, the frame is stress relieved and heat-treated prior to finish machining. Other major parts, such as the gimbal frames, are fabricated in a similar manner. For effective control and distribution of solar heat absorbed by the mirror, black anodize and chromate conversion coatings are used where required. Chromate conversion coatings are also used as electrically conductive protective coatings on faying surfaces used for EMI bonding.

C. Flexure Pivots

The usual choice of a precision support for a rotating member is a bearing (ball, roller, needle, or other type). However, bearings were not used in this application for several reasons:

- (1) Rotation is limited to an angle of ± 1.375 arc-min. Under such limited rotation, all contact loads between balls and races are concentrated into such small areas that unacceptable radial and axial play results from wear or brinelling.
- (2) Static and dynamic friction torques must be equal and repeatable for the servo system to operate as required. These torques can never be equal with any type of bearing. In addition, the concentrated loads described in (1) lead to gradual changes such that the torques are not even repeatable.
- (3) Vibration loads during launch are severe. It is doubtful that ball, roller, or needle bearings could survive the launch environment in a non-rotating mode, particularly because space availability limits bearing sizes.
- (4) The mirror is required to return to the center of the raster pattern in a power-off condition. This return would have necessitated return springs.

For the reasons listed, a rotating support that will be referred to as a "flexure pivot" was developed (Fig. 3). The flexure pivot has no friction, static or dynamic; it has no hysteresis, requires no lubrication, and has a low

torsional spring rate (0.05 oz-in./arc-s) with high axial and radial stiffness.

The flexure pivot may be thought of as a bicycle wheel with only four spokes, spaced 90 degrees apart. If the rim of the wheel is held fixed while the hub is rotated about its axis through a very small angle, no significant tension is created in the spokes, and the spokes bend essentially as fixed-end beams. The analysis is complicated because the fixed ends do not remain parallel, but a good approximation has been developed.

By substitution of flat springs for round "spokes," the desired relationship between torsional spring rate and axial stiffness may be obtained by variation of the cross-sectional proportions.

Although the basic principle is not unique, several innovations were developed to simplify manufacture, improve operation, and fit into the space available. These innovations are—

- (1) Choice of materials and development of a

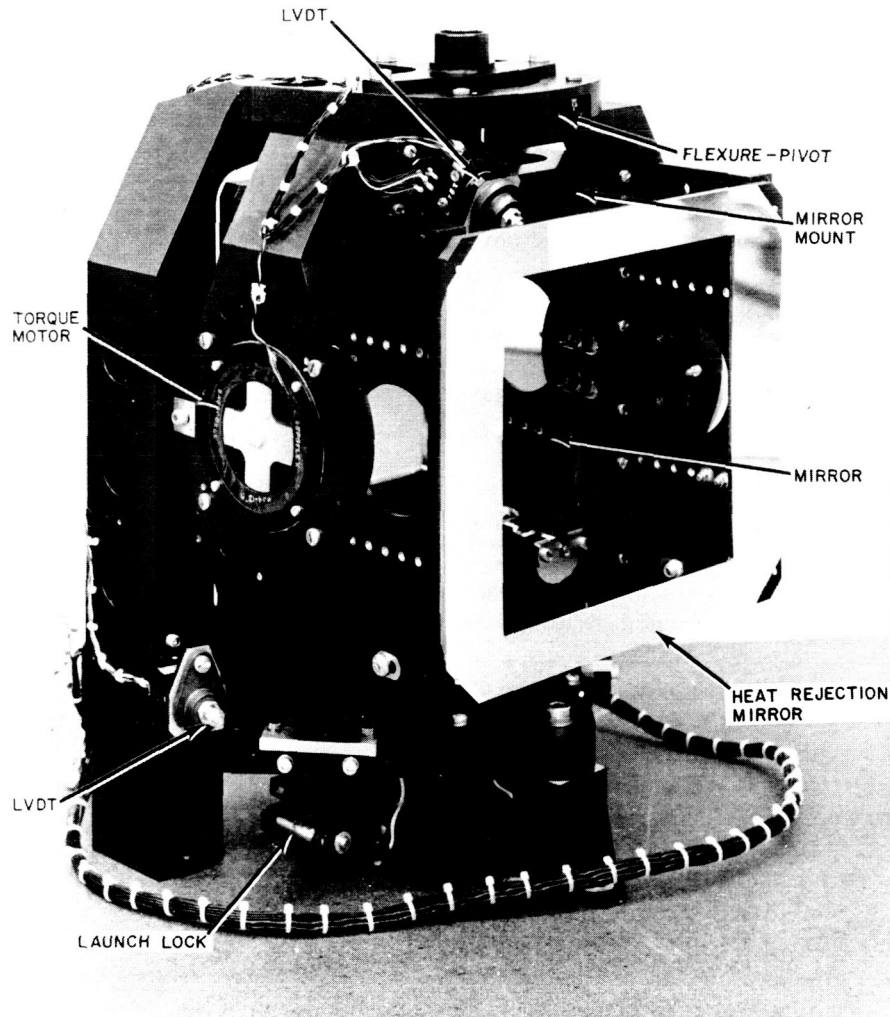


Fig. 2. Scanning mirror system

- (3) A "pancake" shape, which requires minimum thickness.

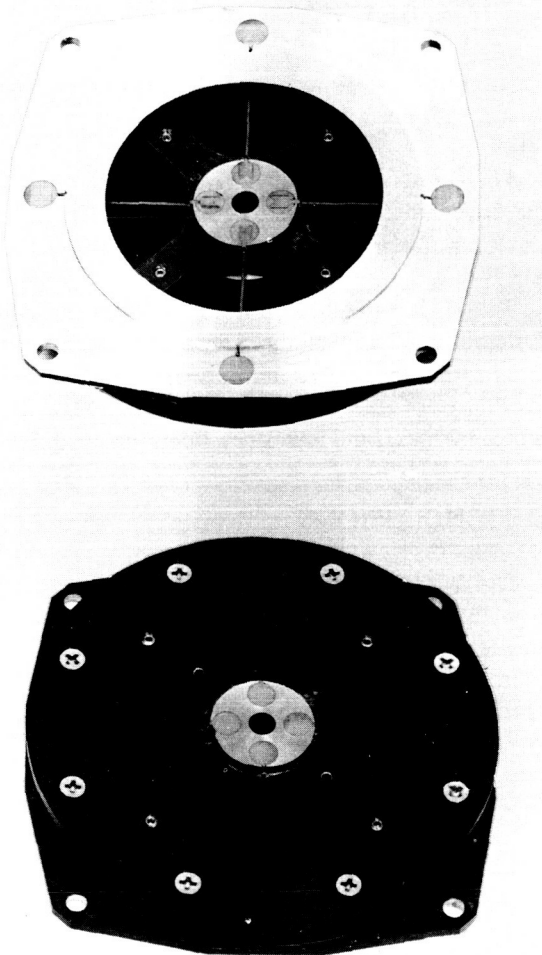


Fig. 3. Flexure pivot

method of construction that prevent built-in tensile or compressive stresses in the flexing elements. Such stresses would cause a form of mechanical hysteresis,¹ introducing error into the servo.

- (2) Internal limit stops to prevent excessive axial or torsional movement.

¹Mechanical hysteresis "is revealed graphically by failure of the descending and ascending branches of the stress-strain diagram to coincide" (Ref. 2).

D. Torque Motors

A brushless dc torque motor similar to Aeroflex Laboratories² Model TQ34 drives each of the two gimbals. This type of motor was chosen because there is no mechanical contact between rotor and stator to create friction and require lubrication. Support of the rotor is provided by the flexure pivot.

E. Linear Variable Differential Transformer (LVDT)

The LVDT³ is an electromechanical transducer that produces an ac output voltage directly proportional to the displacement of the movable core. The scale factor is 50 mV minimum per 0.001 in. when the output is loaded with 100 k Ω . Linearity is 0.2 percent of full scale.

F. Mirror Mount

The mirror mounting system (Fig. 4) is a kinematic⁴ mount that uses swivel pads faced with Vespel SP-3⁵ in contact with the mirror. Beryllium copper flat springs apply predetermined loads to the spring-loaded pads, holding the mirror in contact with the fixed pads. To restrict movement of the mirror under vibratory resonance conditions, limit stops are adjusted to allow approximately 0.005 in. of mirror movement. Thus, buildup of kinetic energy in the system is minimized.

G. Launch Lock

The launch lock applies loads to the gimbals to provide support for the sprung masses during exposure to the launch environment.

²Aeroflex Laboratories, Inc., Plainview, Long Island, N.Y.

³Manufactured by Tresco, Inc., Philadelphia, Pa.

⁴A kinematic mount constrains the optical element singly in each of its six degrees of freedom (translation along each of its three rectangular coordinate axes and rotation about each axis). More or less constraint deforms the element or allows it to move. (Paraphrased from Ref. 3).

⁵Vespel SP-3 is a DuPont trade name for a polyimide plastic impregnated with molybdenum disulfide to provide a reduced coefficient of friction.

A linear solenoid rotates an eccentric shaft to force a pair of spring-loaded plungers into contact with pads on the gimbal frame. To prevent unlocking of the over-center linkages because of launch vibration acting on the heavy solenoid plungers, a rotary solenoid is used as a latch.

A mechanism of this type locks each of the two gimbals.

IV. TESTING

Tests performed as of February 1970 during development, evaluation, and qualification phases include the following:

- (1) Flexure pivot performance and structural tests.
- (2) Breadboard servo electronics tests.
- (3) Development-model mirror-system vibration and servo tests.
- (4) Engineering-model mirror-system vibration and servo tests.

- (5) Engineering-model mirror-system vibration tests with simulated launch locks (installed in the spectroheliometer case). (Preliminary qualification test.)
- (6) Engineering-model mirror-system vibration tests with operational launch locks.

These tests successfully demonstrated operation of the drive and control system. All parameters listed in II above have been met. (Figure 5 is a typical X-Y plot.)

The engineering-model vibration tests indicated the desirability of adding the previously described launch locks to the mirror system. Subsequent tests proved the feasibility of the launch locks: initial tests involved simulated locks, and later ones, operational hardware.

V. CONCLUSIONS

The feasibility of developing a mechanism to gimbal a large, highly figured mirror to produce a small, ultra-precise raster pattern has been demonstrated. Several unusual features of the design have proved to be of significant benefit in such a system.

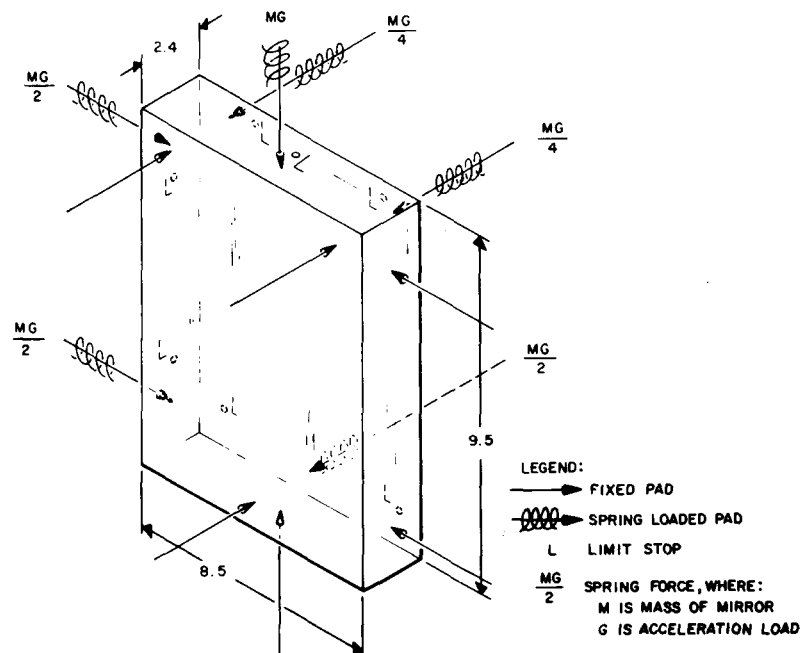


Fig. 4. Mirror mounting system

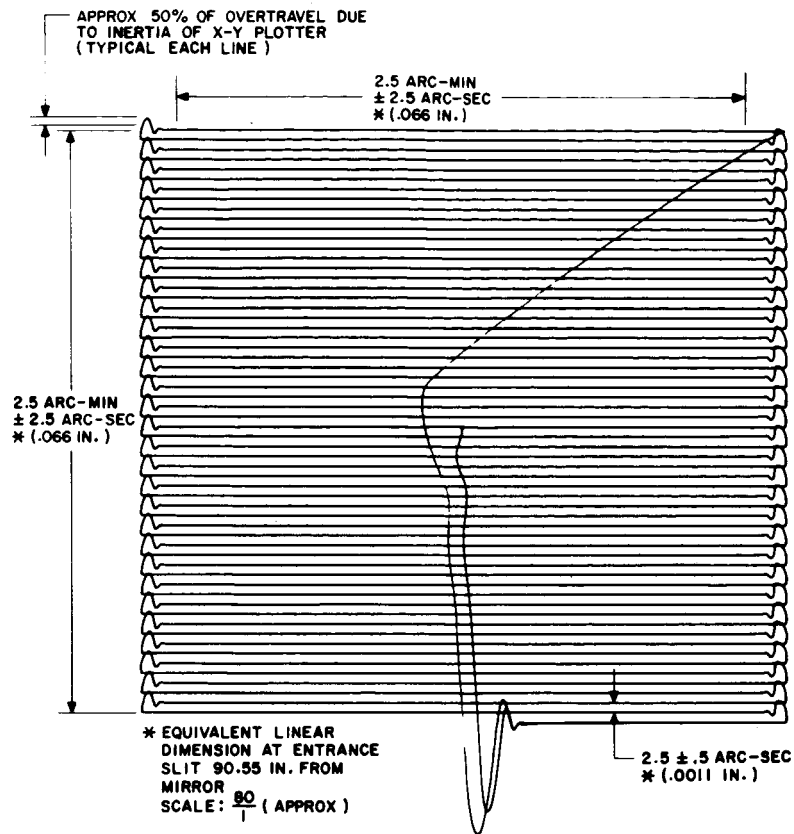


Fig. 5. Typical X-Y plot of raster pattern

REFERENCES

1. Culver, R. C., "The Use of Positive Feedback to Control Spring Mass Systems" Report No. M68-03, Ball Brothers Research Corp., Boulder, Colo. (Presented to American Astronautical Society Symposium, Denver, Colo., July 1968).
2. Roark, R. J., "Formulas for Stress and Strain," New York: McGraw-Hill Book Co., Inc., 1965.
3. Smith, W. J., "Modern Optical Engineering," New York: McGraw-Hill Book Co., Inc., 1966.

DISCUSSION

Member of the audience:

Do you have any more information about the zero-parabola coefficient expansion material? What design change, in addition to the material change, did you make in the bracket to increase its natural frequency?

Highman:

I don't have any additional information with me. I could direct you to Owens-Illinois Co., which could give you plenty of information. The material is Cer-Vit. We used a particular grade, the premium grade, I believe it is called C-101.

Member of the audience:

Is it glass?

Highman:

It is not really a glass. They call it a combination between a ceramic and a glass. And on the bracket, the only change we made was in the material. This change increased the natural frequency enough to get us out of the problem range.

Member of the audience:

If the ratio of stiffness to density in the two materials mentioned stays the same, I don't really understand, unless this bracket was loaded in some fashion, how it changes the frequency.

Highman:

As I recall, it wasn't loaded. It is possible I could be wrong on that. But it seems to me that just the difference in damping

characteristics was enough to take care of it. I could be mistaken on that.

Member of the audience:

How is the five-minute pattern moved about on the sun?

Highman:

The sun size is about thirty minutes of arc. We are really looking at a five-arc-minute square area of the sun at any one time. The whole ATM is pointed so that we can look at any particular region. To keep the resolution down within limits, we only look at a five-arc-minute square area at any one time and move the entire ATM around to look at other areas.

Member of the audience:

What are the power requirements of the system?

Highman:

As I recall, I mentioned the motors were driven well below their rated torque. I believe the power requirements are only on the order of about three-tenths of a watt for these 28-volt type motors.

Nat Kramer:

What type of brushless dc motor did you use on the mechanism?

Highman:

That is a modified Aeroflex unit, which changes the potting materials to materials that were acceptable as far as the out-gassing, etc., is concerned.

A RELEASE MECHANISM WITH MECHANICAL REDUNDANCY*

John J. Paradise
Lockheed Missiles & Space Company
Sunnyvale, California

This paper describes a simple release mechanism that achieves high reliability through active mechanical redundancy on the SERT 2 satellite. Principle of operation, design details, and the test program are discussed. Examples of developmental and proposed alternate configurations also are included.

I. INTRODUCTION

Pinpuller-operated release systems, whether they be actuated pyrotechnically, pneumatically, or by a solenoid, typically achieve reliability through the use of backup commands, dual squibs, or redundant wiring of squib, valve, and switch components. When properly implemented, redundant wiring almost certainly precludes malfunction from electrical causes. It cannot, however, overcome a mechanical failure of the pinpuller device. This deficiency now has been overcome through the development of a release system that uses a simple clevis fitting in combination with two pinpullers to achieve active mechanical redundancy.

The mechanism described successfully released two extendable solar arrays of the Space Electric Rocket Test (SERT 2) satellite launched in February of 1970. Reliability was of paramount importance, since the failure of either array to deploy would compromise the entire mission.

II. PRINCIPLE OF OPERATION

The solar-array assembly for which this release system was developed is shown in Fig. 1. A tension element (tie rod) restrains two spring-loaded arms, which clamp the folded solar array against its mounting bed. The tie rod is permanently attached to the right-hand clamp assembly. As shown in the detail view, a clevis device (swivel fitting) at the other end of the tie rod is entrapped behind the extended shafts of two pinpullers which are

mounted in a staggered manner on either side of the left-hand clamp assembly. The pinpullers utilize dual squibs and are qualified for single-squib operation for the cross-pin shear loads associated with this application. The turnbuckle is used to develop the desired tension preload. The solar-array deployment sequence is initiated by tie-rod release.

In the locked condition depicted in Fig. 2a, the swivel fitting distributes tie-rod tension equally to each of the pinpuller shafts in double shear. The swivel fitting automatically compensates for small angular misalignment between the tie rod and the pinpuller shafts.

In normal operation, simultaneous retraction of both shafts releases the tie rod, as indicated in Fig. 2b. This figure also describes certain squib failure modes. Since the pinpullers are qualified for single-squib operation, failure of one squib in either pinpuller or in both pinpullers still allows this simultaneous retraction.

In the failure modes depicted in Figs. 2c and 2d, the failure of either shaft to retract causes eccentric loading of the swivel fitting, and it simply rotates and rides over the extended shaft.

III. DESIGN CONSIDERATIONS

The primary design goals and constraints that influenced the development of this release mechanism are described in the following paragraphs.

*Developed under contract to NASA (LeRC).

A. Functional Considerations

The critical relationship of solar-array deployment to mission success dictated that reliability be given the highest priority. A system reliability of >0.98 was established, the system consisting of two separate solar-array assemblies with individual release systems. Since the system reliability goal exceeded the 0.97 reliability estimate assigned to a single pinpuller, mechanical redundancy became a design requirement. The reliability analysis is discussed in VI. Each mechanism was required to function in a 1-g field during preflight acceptance testing and to function once in orbit.

B. Physical Considerations

The solar arrays are housed within a booster-adaptor structure during ascent. The clearance envelope is very limited and imposes severe volumetric restrictions on the release system.

System weight was a design consideration, although the space limitations obviated the need for a weight-savings campaign.

As often as possible, existing qualified components were used to maintain cost and schedule effectiveness.

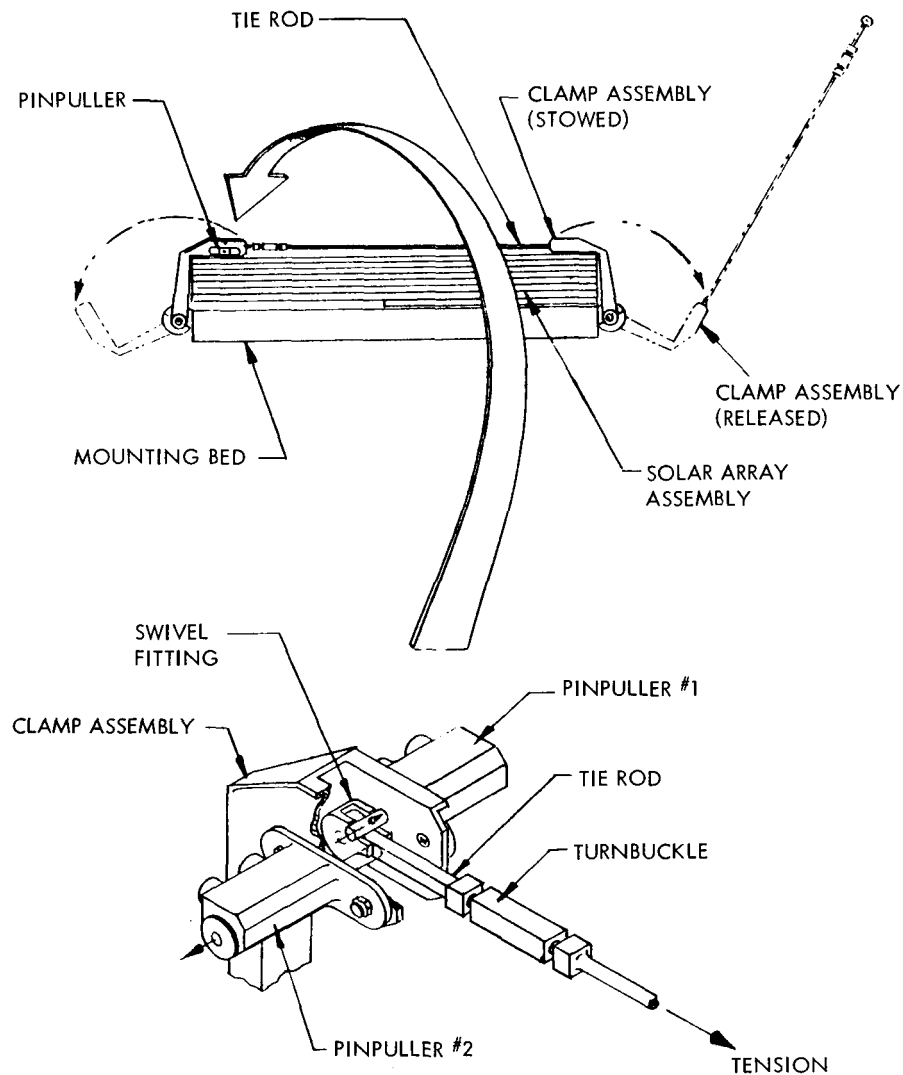


Fig. 1. Solar-array release mechanism

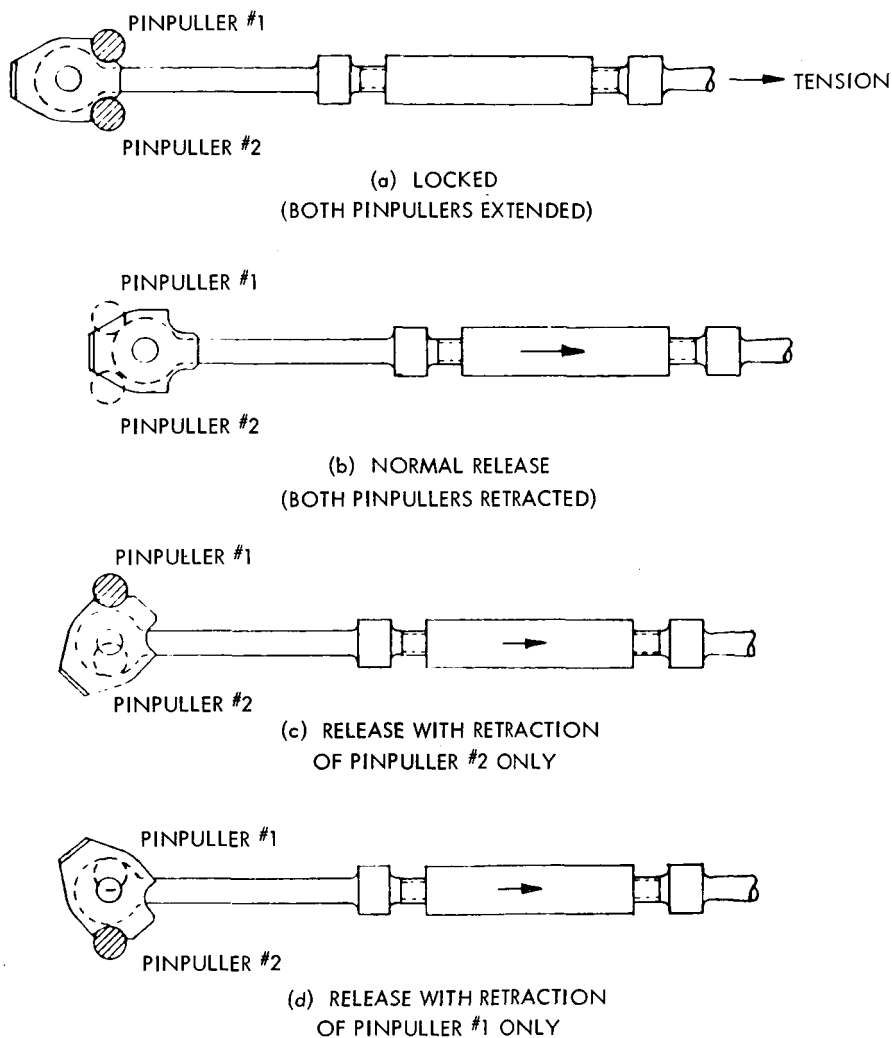


Fig. 2. Release—normal and failure modes

C. Environmental Considerations

Solar-array deployment occurs less than two hours after launch. Since the release system is a one-shot device, sustained life and operation in a vacuum were not significant design problems.

Primary consideration was given to the vibrational and thermodynamic environment that would be experienced by the solar arrays before release and deployment.

tie-rod tension preload of about 400 lb, and thermodynamic effects tend to increase this tension before deployment. Titanium alloy (6AL-4V) is used for the tie rod, turnbuckle, and swivel fitting. This material was selected for its combined properties of high strength, light weight, and low coefficient of expansion.

Cross-pin shear forces and space limitations indicated the need for a small, high-energy, one-shot device. Previous experience and development effort led to the selection of the pyrotechnic pinpuller.

IV. DESIGN FEATURES

Restraint of the solar array during ascent requires

Locating the pinpullers on opposite sides of the clamp assembly minimizes their stacked height. This arrangement also serves to prevent coupling of pyrotech-

nic shocks when the pinpullers are actuated simultaneously.

The designs of the tie rod and the mechanism elements have minimum cross sections to conform to loads criteria. The clevis-pin material is CRES (303SE), the clamp assembly is aluminum alloy (7075-T6), and pinpuller shafts are steel (4130).

For this application, the relationship of the clevis pin to the pinpuller shafts is important. The tie rod is near to the solar-array surface and the throw of the swivel fitting must be minimal to prevent it from impacting the array. The throw is minimized by placement of the clevis pin as near to the pinpuller shafts as is practicable.

Shear distribution to the pinpuller shafts is optimized when the swivel fitting is designed to a maximum width within the confines of the clamp assembly. The clevis pin is press fit to the swivel fitting and has a slip fit with the tie rod; all other means of mechanical fastening are eliminated. After assembly, the pin ends are ground flush with the fitting. No lubricant is used.

V. TESTING

The test program was established to verify the following:

- (1) The release system will adequately restrain the stowed array assembly through the ascent vibration environment.
- (2) After surviving the vibration environment, the mechanism will function in the normal and failure modes.

A. Vibration Testing

A solar-array assembly was subjected to sinusoidal vibration testing in each of three mutually perpendicular axes. Input excitation was applied from 0 to 400 Hz at amplitudes ranging from 0.3 g to 5.0 g (0 to peak). This testing had no adverse effect on the release mechanism.

B. Functional Testing

After vibration testing, the solar array was oriented and supported so as to simulate closely zero-g conditions for release and deployment.

Live pyrotechnics were used for all release tests, which were performed in the following order:

- (1) Fire two pinpullers (four squibs) simultaneously.
- (2) Fire two pinpullers (four squibs) with a 100-msec time delay between pinpullers.
- (3) Fire No.1 pinpuller only (two squibs).
- (4) Fire No.2 pinpuller only (two squibs).
- (5) Fire No.1 pinpuller only (one squib).
- (6) Fire No.2 pinpuller only (one squib).

No release-mechanism anomalies were encountered, and high-speed film data showed no difference in release-time histories among the normal- and failure-mode tests.

VI. RELIABILITY ANALYSIS

The dramatic increase in the probability of success (P_s) of the mechanically redundant system as compared with the single-pinpuller mechanism is illustrated by the reliability block diagrams and analyses in Fig. 3. Figure 3b depicts the release mechanism for one solar array. The system reliability estimate for two arrays is expressed

$$P_s = \left(\left[1 - (1 - R_s)^2 \right]^2 \left[1 - (1 - R_p)^2 \right] \right)^2 = .998$$

thus satisfying the reliability goal of $>.98$.

VII. ALTERNATE CONFIGURATIONS

The basic principle of this system is being adapted for other applications and has assumed a variety of configurations, as shown in Fig. 4.

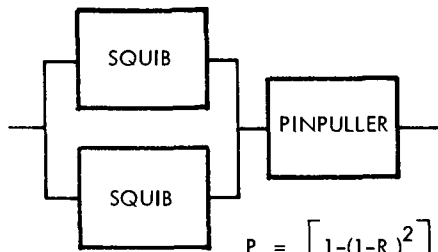
Concept A utilizes a long swivel fitting, with the clevis pin comparatively distant from the pinpullers. This design offers the advantage of allowing the pinpullers to be mounted within a small volume.

Concept B is a simplified system in which reduced tension loads permit the use of a flexible cable, greatly reducing complexity and the cost of fabrication.

Concept C is adapted from the design above and is proposed to release the spring-loaded latches on two extendable antenna booms through use of one mechanically redundant release system.

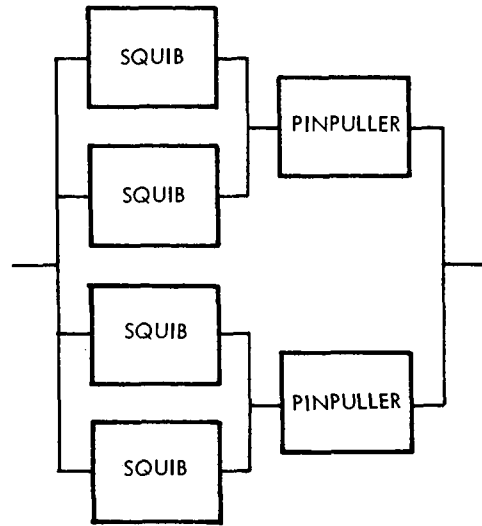
VIII. CONCLUSION

The release system described here is simple, inexpensive, and effective; it has performed successfully to release two solar arrays while in orbit. The mechanical designer can readily adapt the principle of mechanical redundancy to other release-system applications by using a variety of pinpuller devices.



$$P_s = [1 - (1 - R_s)^2] R_p = .9699$$

(a) SINGLE PINPULLER



$$P_s = [1 - (1 - R_s)^2]^2 [1 - (1 - R_p)^2] = .999$$

(b) REDUNDANT PINPULLERS

SQUIB RELIABILITY (R_s) = 0.998
 PINPULLER RELIABILITY (R_p) = 0.97

Fig. 3. Reliability block diagram

DISCUSSION

Member of the audience:

Would you consider getting rid of the dual bridge wires of the squibs?

Paradise:

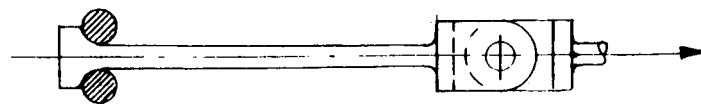
The reason we used both sets of bridge wires was because this was based upon an existing design.

Member of the audience:

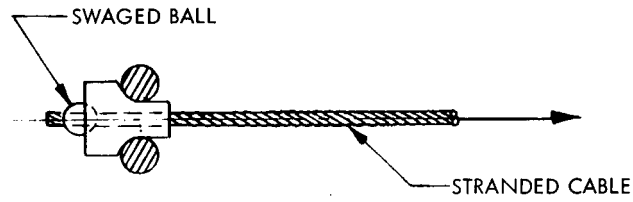
If you had started from scratch, though, would you have gotten rid of them?

Paradise:

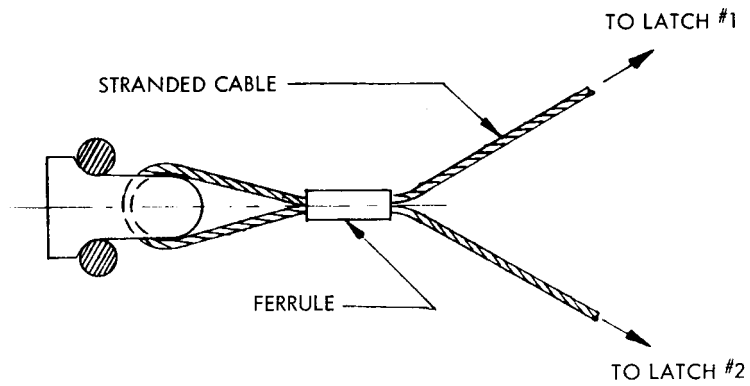
Yes.



CONCEPT (A)



CONCEPT (B)



CONCEPT (C)

Fig. 4. Alternate configurations

ACCELERATED VACUUM TESTING OF LONG LIFE BALL BEARINGS AND SLIPRINGS

C. R. Meeks
R. I. Christy
A. C. Cunningham
*Space Systems Division
Hughes Aircraft Company
El Segundo, California*

Extensive analytical studies and testing have been conducted on bearings and sliprings in vacuum at temperatures from +30° F to +130° F. Thirty-six bearings lubricated with two types of oil were tested in vacuum of $<10^{-8}$ torr at speeds from 55 to 180 rpm. Temperatures, load, speed, and oil viscosity were varied to evaluate the effects on life and wear. All bearings performed successfully during a 7-month test, and the potential merits of the two oils were compared.

Over 25 different, dry-lubricated brush/slipring material combinations have been tested, with variations of brush and ring design and surface speed. Test results indicate the probability of 10 years or more of slipring and brush lifetime with properly designed brushes for 1-in.-diameter rings rotating at 60 rpm.

I. INTRODUCTION

Increases in operating life requirements of spacecraft, communication satellites and manned space stations have created a need for long-lived bearings and sliprings for gyroscopically stabilized spacecraft with despun antennae, for zero-gravity cells in space stations with artificial gravity sections, and for various positioning mechanisms capable of multi-year operation without servicing. Program delivery schedules often preclude real-time life testing to demonstrate confidence in such bearing and slipring systems; therefore, test methods that permit acceleration of testing and development of methods of extrapolating bearing and slipring life based upon less than full lifetime tests are needed. The analytical studies and tests discussed herein were directed primarily toward the development of technology for long-lived bearings and sliprings for despun joints in gyroscopically stabilized communications satellites with spin rates of 40 to 100 rpm, temperatures from 30° F to 130° F, and life requirements up to 10 years. The bearings in such systems must perform reliably, with low running torques and very small dynamic variations in torque to optimize antenna-pointing system accuracy.

Sliprings must conduct up to 1000 W of dc power with efficiencies better than 99 percent, and signal sliprings are required with less than 0.5 mV/mA noise for lifetimes up to 10 years at 60 rpm (3.0×10^8 revolutions).

II. BEARING-LIFE TESTS

A. Considerations in Accelerated Testing

Any attempt at accelerated testing of ball bearings must consider the probable failure modes and attempt to isolate the effects of any acceleration factors introduced and to relate the results to actual performance at design conditions. The three most likely modes of failure of lightly preloaded, well designed, satellite despun bearing systems during a 10-year operating period are (1) lubrication degradation due to chemical contamination, polymerization, decomposition, and/or catalytic effects of bearing component materials; (2) loss of lubricant due to evaporation or surface migration; and (3) cage, ball, and race wear or damage.

Lubrication breakdown due to causes such as temperature effects, catalytic effects of wear particles, or contamination is very difficult to evaluate except by real-time testing. However, a combination of laboratory chemical analysis and bearing testing can yield valuable insight into long-term performance that might be expected.

Lubrication loss by evaporation and/or surface migration can be predicted analytically by molecular-flow theory and estimated by surface-physics theory. Localized effects of small thermal gradients, bearing and housing geometry, and surface barrier coatings can appreciably affect performance, however, and attention must be given in design, and results confirmed by test, to achieve optimum oil supply control system performance. Bearing test temperatures can be raised to accelerate lubricant losses; however, the results must be interpreted in light of thermodynamic flow loss, and surface-physics loss theory. The lowering of viscosity by elevated temperature also reduces bearing hydrodynamic oil film thickness unless the rotation speed is changed to produce a compensating effect.

Wear is significantly affected by lubrication film thickness, and any attempt at accelerating life testing should maintain film thickness representative of the actual application. Film thickness can be varied by increasing preload and rpm, which will accelerate bearing wear but in a manner less predictable than the lubricant evaporation because the wear rate is affected in a complex way by preload, which affects the amounts of sliding and of fatigue wear. Many other variables must be considered, such as microscopic asperity temperatures, oil viscosity pressure coefficients, ball-cage dynamics, oil distribution and transfer dynamics, and time-dependent lubricant chemical changes. A detailed discussion of these effects is not possible in this brief report.

B. Bearing-Life Tests

One group of tests was run with the test apparatus shown in Fig. 1a. The bearing test consisted of three such test shaft assemblies, each mounting six test modules. Each test module (see Fig. 1b) contained a preloaded bearing pair, labyrinth seals, and an oil reservoir representative of a despin assembly design. Barrier coatings (low-surface-energy films) were used to control surface migration of oil. Half the test modules were lubricated with General Electric's Versilube F-50 (modified and applied per a Hughes process) and the

other half with a hydrocarbon oil having a high-pressure additive. The two end modules on each shaft are used as support modules for the shaft and are not instrumented for making measurements during the test. The bearings, test parts, and lubricants were thoroughly cleaned and the lubricant vacuum-impregnated into the bearing parts to achieve optimum performance.

The three test shafts were driven at test speeds of 55, 120, and 180 rpm. The test bearings in the modules on a single shaft are set at three preload levels, 10, 20, and 40 lb. The test was conducted at 130° F to control the oil-film thickness to boundary lubrication levels (i.e., no significant elasto-hydrodynamic film load support) that occur in typical satellite despin bearings.

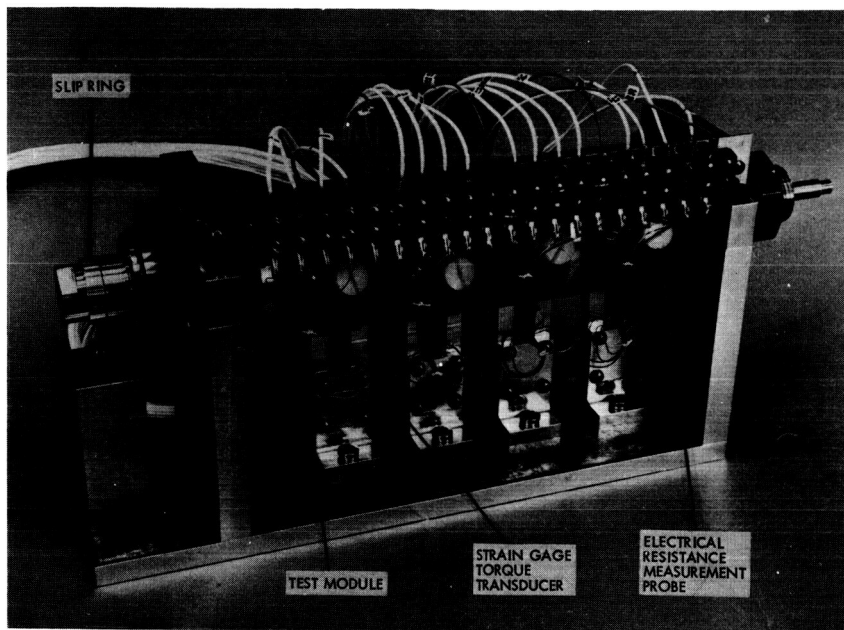
The measurements recorded during the test (Fig. 2) were (1) bearing torque, (2) temperature of the outer race of one bearing in each module, and (3) electrical resistance through one of the bearings in each module. The electrical resistance was measured at periodic intervals by an electrical contact attached to one outer race, of each bearing pair. The current path was from the outer race, through the bearing balls, to the inner race, and thence to a common shaft and slipring. The test current used for this measurement was 100 μ A. This measurement is used to establish the percent metal-to-metal contact occurring, i.e., detect the extent of boundary lubrication operation.

The bearing samples used for this test were angular contact bearings, of 440C stainless steel, 1.312-in.-diameter bore (MPB 3 TACR 25-32U) ABEC7P with special, high-porosity cotton-phenolic ball cages and special, grade-5 balls.

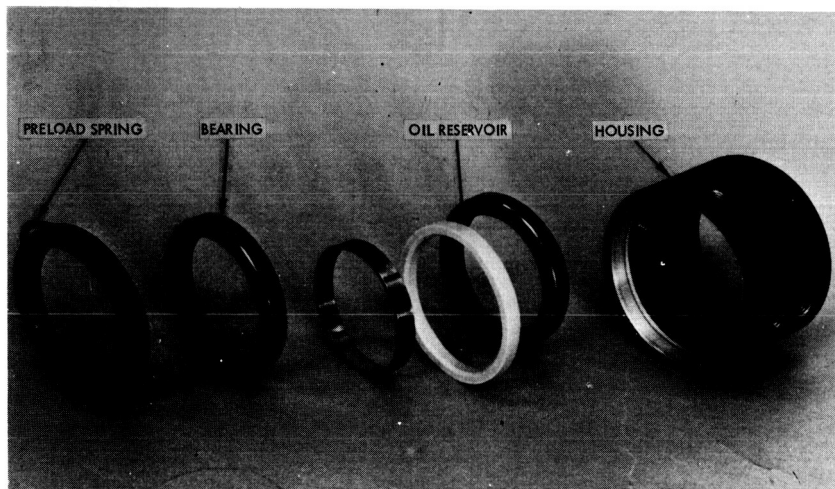
C. Bearing-Life Test Results

The running torques of all bearings were relatively constant during the 220-day test at 6×10^{-9} torr in a cold trapped oil diffusion pumped system, except for the 55-rpm F-50 lubricated modules. The peak torques ran as high as four times the average (see Fig. 2); however, during the period from about 150 to 186 days, the shaft speeds drifted upward, and, when corrected for this, the worst peak torque would be about two times the average.

Analysis of the ball-to-race contact resistance data demonstrated that the 55-rpm bearings were operating entirely in the boundary lubrication regime, and the



(a) ACCELERATED LIFE TEST FIXTURE



(b) TYPICAL LIFE TEST MODULE

Fig. 1. Accelerated life test equipment

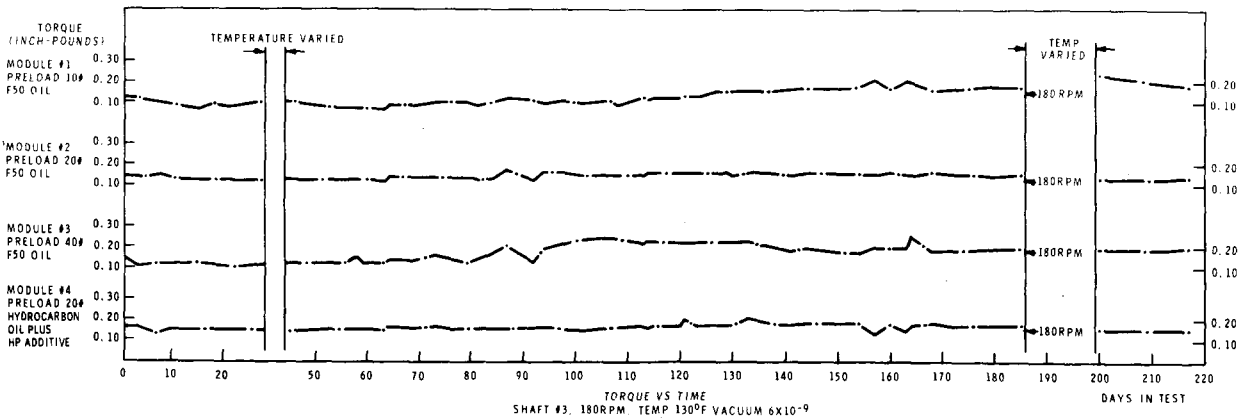
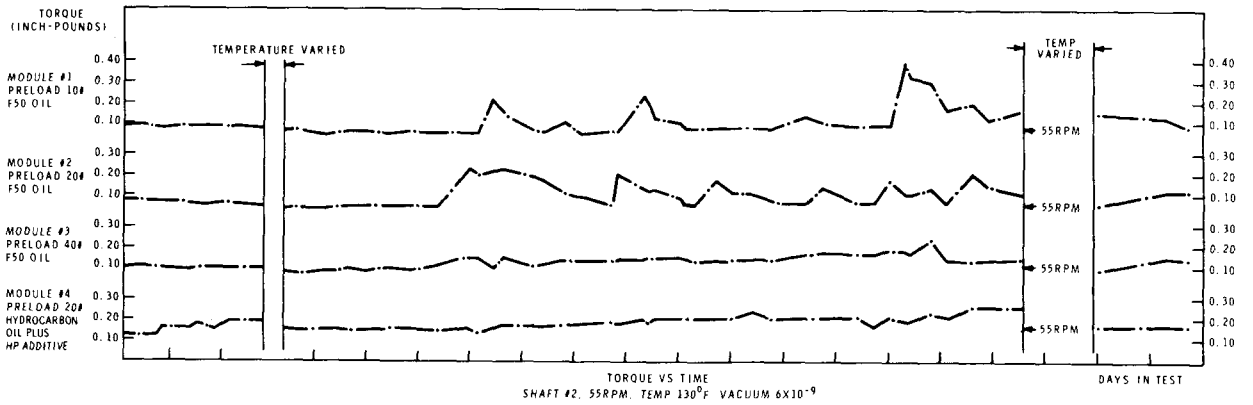
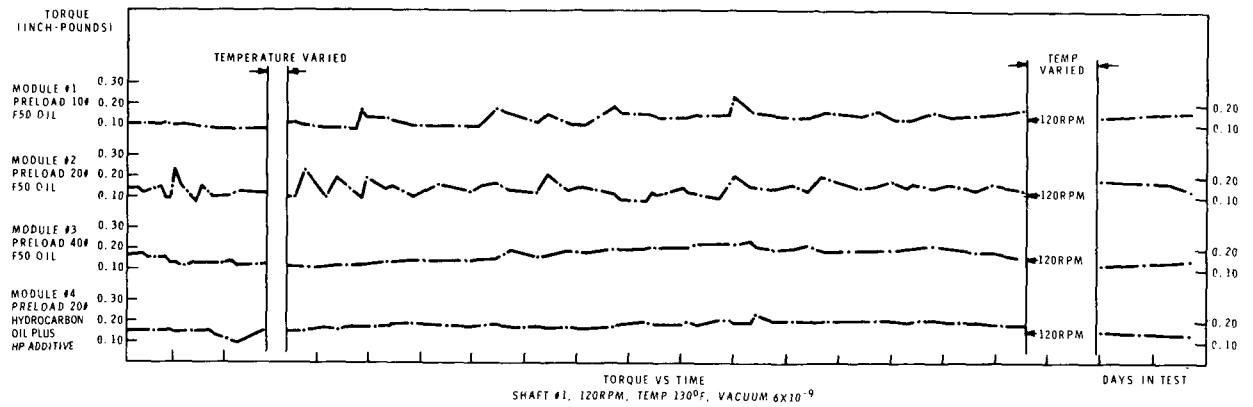


Fig. 2. Test results

120- and 180-rpm bearings were in the transition regime between boundary and hydrodynamic lubrication.

The oil losses from the modules showed an average rate of approximately 25 mg/year, which is within the range of predicted rates and is easily tolerated because several hundred milligrams of oil can be stored in a bearing system of this size.

Post-test examination of the bearings revealed no perceptible wear. The actual wear is being measured by radiographic methods. The oil in the F-50 lubricated bearings had polymerized extensively in the low-speed and high-preload modules and less so in the high-speed modules. An excellent inverse correlation between theoretical oil-film thickness and amount of polymer was observed. The reason for this is believed to be the very high temperatures—hundreds of degrees Fahrenheit¹—produced at the microscopic asperity contact points occurring with very thin oil films, which produced polymerization of the F-50. F-50 oil polymerizes or cross-links at approximately 600° F.

D. Conclusion

From these tests and careful consideration of bearing theory, it is possible to extrapolate the effects observed and make an estimate of probable bearing/lubrication system life. The estimated life of F-50 lubricated, small-size bearings at 55 rpm before significant torque fluctuations (greater than two times average) occur is less than 1 year, due to thermally induced chemical changes in the oil. The ultimate failure life of such bearings lubricated with F-50 can be conservatively predicted to be probably less than 2 years. The hydrocarbon-lubricated bearings could be expected to last considerably longer than 2 years with uniform torques. The oil supply losses were low enough for up to 10 years life in either lubricant. Quantitative measurements of wear showed that wear is inversely proportional to oil-film thickness.

From the analysis of the data from these tests, several factors offer encouraging support for the validity of carefully controlled accelerated bearing tests. Very good correlation was observed between predicted film thickness in the boundary regime for the 55-rpm bearings and the transition regime (between boundary and elasto-hydrodynamic) for the 120- and 180-rpm bearings, and the ball/race electrical contact resistance data. Also, the amount of oil polymerization and wear in the 55-rpm

bearings with F-50 lubrication, which operated entirely in the boundary lubrication regime, are much higher than the amounts in the 120- and 180-rpm bearings, which were in the transition lubrication regime. This agrees well with prior bearing testing which shows that high microscopic-asperity temperatures¹ occur in pure boundary conditions, becoming progressively less as hydrodynamic conditions are approached.

Obviously though, more work must be done before highly accurate correlations of accelerated test results and real-time conditions can be attained.

III. SLIPRING LIFE TESTS

A. Spectrum of Tests

Nine separate dry-lubricated slipring fixtures have been tested in ion-pumped vacuum chambers, encompassing a broad range of brush/ring material combinations, brush mount geometry, and ring surface speeds, as shown in Table 1. All brushes tested are sintered composites, with the dry lubricant contained in the brushes. The performance parameters of brush wear, contact resistance, and electrical noise (variations in contact resistance) were monitored during each test to determine the rate of change of each parameter. Results show that the brush/ring material combination and brush mount design can radically affect the magnitude and rate of change of the performance parameters, while for properly mounted brushes, the ring surface speed variations in the range from design speed (60-rpm 1-in.-diameter rings) to 35 times design speed have much smaller effects on performance.

B. Typical Performance Parameters

Despite a large variation in performance through variation in materials and brush mounting design, all dry-lubricated sliprings tested exhibited generally similar dynamic characteristics. Typical wear and contact resistance values are plotted against the number of ring revolutions in Fig. 3, for coin-silver rings and brush material A. Note that neither the wear rate (slope of the wear curve) nor the contact resistance are constant. Electrical noise (variation in contact resistance) shows an increase comparable to the contact resistance, with an

¹Bowden and Tabor, "The Friction and Lubrication of Solids, Part I," New York: Oxford University Press, Inc., 1964.

Table 1. Spectrum of dry lubricated slipping vacuum tests

Ring material
Coin silver
Electrodeposited silver (3 types)
Copper
Nickel-plated copper with rhodium overplate
Brush material
(A) 85% Ag, 3% C, 12% MoS ₂
(B) 82.5% Ag, 2.5% Cu, 15% MoS ₂
(C) 85% Ag, 15% MoS ₂
(D) 85% Ag, 15% NbSe ₂
(E) 16.5% Ag, 12.5% Mo, 4% Ta, 67% MoS ₂
(F) 15% Mo, 5% Ta, 80% MoS ₂
Characteristics
Ring diameter: 1, 2, 4-3/4, 10 in.
Rotation rate: 60, 200, 500, 1000 rpm
Brush force: 10 to 120 g
Brush pressure: 1.8 to 9.7 psi
Current density: 15 and 75 A/in. ²
Ring surface speed: 10,000 to 350,000 in./h

initial value of approximately 0.002 mV/mA. Initial wear rate for the 80-g brush was approximately 10^{-9} in. of brush wear per in. of ring travel, but reduced to 2×10^{-10} in./in. after 2 million revolutions, and to 2×10^{-11} in./in. after 8 million revolutions. This remarkable reduction in wear rate (a factor of 50) during the 3-month test demonstrates the importance of both long-term vacuum tests and in-test monitoring of brush wear. For example, if the test had been terminated after 1 month (2.6 million revolutions), and if only total brush wear were known (0.007 in.), wear rate would appear to be 5×10^{-10} in./in., or 25 times higher than that actually obtainable.

C. Extrapolation of Test Results

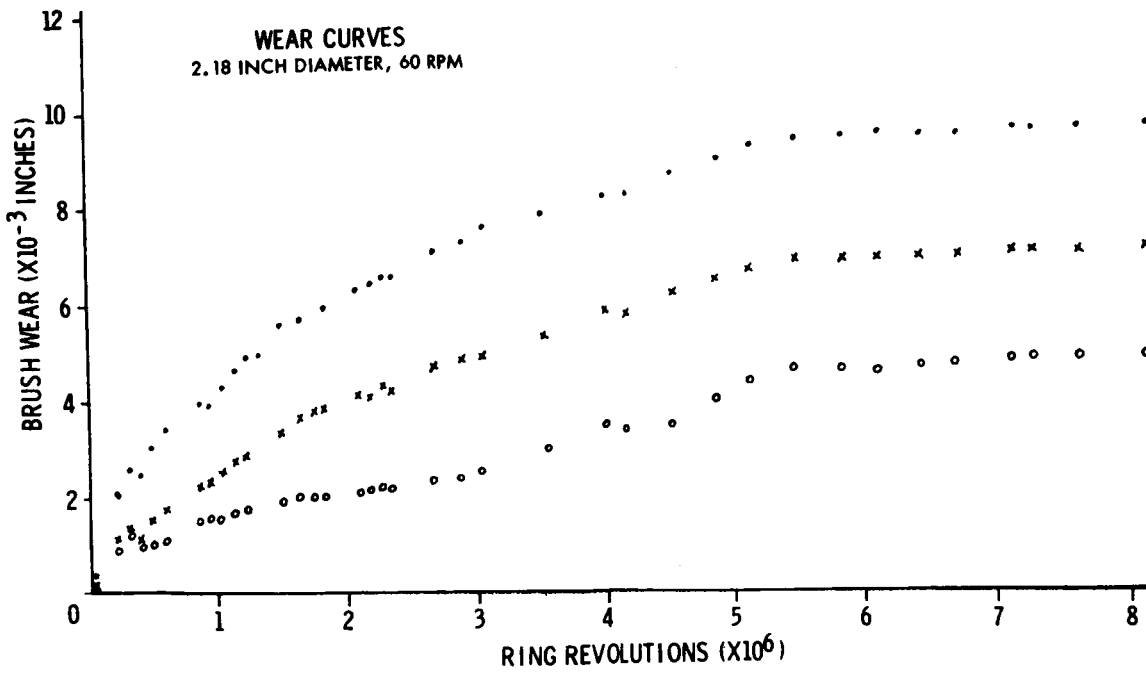
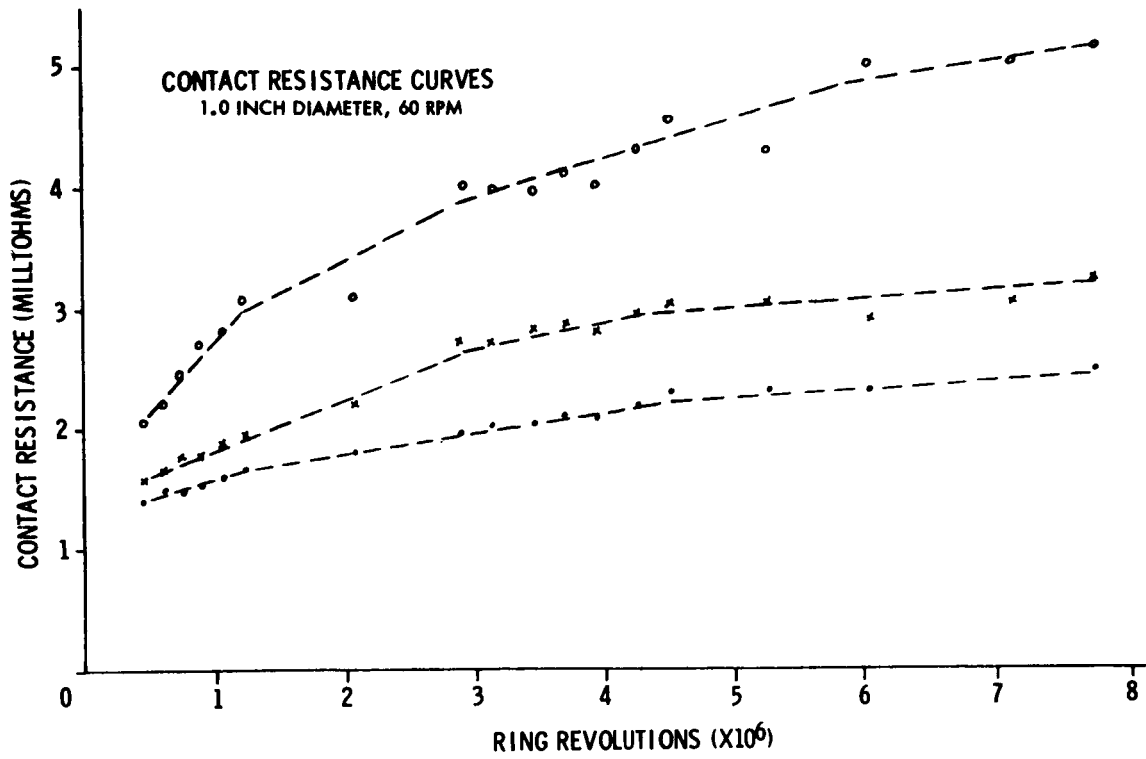
Extrapolation of these test results to longer duration is complicated by the fact that the performance param-

eters are not constant. Since the wear rate reduces as additional revolutions occur, straight-line extrapolation should be conservative. With a rate of 2×10^{-11} as recorded at 8 million revolutions, straight-line extrapolation results in over 50 years of brush lifetime. Results from other tests indicate that even lower wear rates can be produced. Another test on the same brush/ring material combination, run at accelerated speeds, showed comparable wear rates for the first 8 million revolutions, but the rate continued to reduce and reached 1×10^{-12} in./in. at 36 million revolutions. Straight-line extrapolation of this wear rate results in over 1000 years of brush lifetime. Unfortunately, consideration must be given to the contact resistance and electrical noise, whose values increase with time. The importance of these parameters in determining the ultimate life of a slipping is not well established, since good mechanical designs of the material combination shown have never been tested to failure. A simple theoretical model of the slipping dynamics is presented to show what might happen.

D. Theoretical Model

Initially, the brush contacts a clean metal ring, so that an intimate metal-to-metal contact exists and contact resistance is low. As the ring begins to rotate, the brush begins to wear. Initially, the wear rate should be high, since there is no lubricant between the metal brush and metal ring. However, as the brush wears, the lubricant contained in the brush is fed to the ring at the brush/ring interface, and is smeared onto the ring as the brush passes. Subsequent passes over the same spot on the ring deposit more and more lubricant, so that a film is gradually burnished into the ring. As this occurs, the rate of brush wear is reduced, since the film provides better and better lubrication properties as it builds up in average thickness and surface coverage. The lubricant generally used is MoS₂, which is nonconductive, causing the contact resistance to increase as the film thickness or surface coverage increases. If this process were to continue without reaching equilibrium, the film could eventually become too thick in some places, so that contact resistance would exceed some critical value, with excessive noise or open circuits resulting. If this occurred, arcing and pitting of the ring could result, followed by rapid deterioration and brush failure due to wear. This type of failure mode has been observed in some tests. There are two ways to avoid this disastrous performance:

- (1) Since the wear rate reduces as the film grows, the



RING MATERIAL: COIN SILVER
 BRUSH MATERIAL: 85% Ag, 3% C, 12% MoS₂
 BRUSH FORCE:
 ● = 80 GRAMS
 X = 60 GRAMS
 O = 40 GRAMS

Fig. 3. Typical performance curves

rate at which the film grows also reduces. Thus, it is possible that the contact resistance and electrical noise will never grow to the critical value.

- (2) Some equilibrium value may exist where the film thickness stabilizes so that contact resistance and wear rate are constant. This would occur if the rate of removal of the film (due to passage of the brush pushing it aside or by abrasive action of smaller percentage constituents of the brush, such as graphite) were equal to the rate at which the film is deposited. This equilibrium film thickness could be less than the critical thickness which leads to eventual failure. Thus, if dry-lubricated sliprings are to last the required 10 years (300 million revolutions at 60 rpm), the contact resistance must either stabilize and remain constant, or grow at such a slow rate that the critical value is never reached. A 1-year vacuum-life test on five brush/ring material combinations is presently underway, with the goal of obtaining 300 million revolutions to determine

whether or not the buildup in contact resistance and electrical noise will become critical.

E. Recommendations for Life Testing

To obtain confidence in the ability of each slipping design to meet its required lifetime, two tests should be conducted. One test should be run at design speed for at least 3 months to establish design speed performance. A second test of an identical unit run at accelerated speed and long enough to obtain the total number of revolutions required by the mission should also be conducted. In both tests the brush wear and contact resistance must be monitored in situ without disturbing the test, to determine the rate of change of performance. Comparison of design speed data with accelerated speed data will show little or no difference for properly mounted brushes and a good brush/ring material combination. Extrapolation of design speed data along the route traced by the accelerated test can thus be made with increased confidence.

DISCUSSION

Member of the audience:

Were those tests carried out under an electrical load? In other words, were you putting current through the rings at the time?

Cunningham:

Yes, in the two test fixtures I showed you. For example, in the materials evaluation fixture, the brushes were operating at 75 amps per square inch current density. For those size brushes, that is 3.6 amps per brush. Power is passed continuously during the test.

Also, I meant to mention that those fixtures which I showed have now accumulated nine months of continuous operation.

Member of the audience:

Is there any change in the performance depending on what kind of current is flowing through?

Cunningham:

No. We have run some with no current and we can't detect any performance change.

Member of the audience:

What was the vacuum chamber pressure for your tests?

Cunningham:

Most tests were conducted at less than the 10^{-7} -torr range. Some were in the 10^{-8} - and upper 10^{-9} -torr range.

Member of the audience:

Were the bearings run in prior to the vacuum test?

Christy:

No, these bearings were not run in prior to test. They were very carefully handled prior to the application of the lubricants to avoid rotation. They were not run in after lubrication except for what little rotation they may have received in mounting of the test fixture.

Member of the audience:

Did you give any consideration to a dry lubricant in the bearings?

Christy:

We are currently investigating dry lubricants of several varieties in our lubricating systems in our bearings. We do not have a system that we have enough confidence in to consider for a spacecraft application at this time. We have several promising candidates that are under test right now.

Member of the audience:

Would you recommend brush material A for use on dc motor commutator bars? And what is your recommended material for brushes for long life?

Cunningham:

I will answer your second question first—Brush materials A, B, or C in combination with ring materials 1 or 2 of Table 1 are all good brush/ring combinations, and all are nearly identical in performance. However, the best choice today would be brush material A on coin silver rings, since this material combination has the largest background of development testing and space history.

As for the first question, no, I wouldn't necessarily recommend the same brush material for slip rings as for commutators. I believe the higher percentage molybdenum disulphide brushes, such as brush E or F, would be better for commutation.

Member of the audience:

Was the ball-bearing retainer material phenolic?

Christy:

Yes, I forgot to mention that. We used a special high porosity phenolic retainer material on these tests which was impregnated with the lubricant as an added reservoir of lubricant during the vacuum tests.

Member of the audience:

Was some of the polymer in the phenolic a silicone?

Christy:

We ran infrared spectrometer tests as well as emission spectrometer tests, and we went through quite a bit of analysis and concluded that it was all silicone. We also duplicated the silicone polymerization in vacuum only with just temperature. We found that the amount of polymer formed in a silicone oil lubricated bearing was roughly proportional to the degree of boundary lubrication, as opposed to hydrodynamic lubrication.

I know there have been quite a few very successful applications of the silicone lubricant in space technology which were closer to the hydrodynamic regime, or when longer lifetimes were not required so that the rate of polymer formation was low enough to not interfere with the application requirements.

A MOTOR CANISTER DESIGNED FOR PROLONGED OPERATION IN SPACE*

A. Wells

*Spar Aerospace Products, Ltd.
Malton, Ontario, Canada*

A special canister was designed to protect the dc motors used on the ISIS 1 antenna unit. The canister is provided with a pressure-monitoring device and has a special shaft seal that imparts minimum load to the motor output shaft. The development and flight testing of the canister are discussed. Problems that were encountered during fabrication and inspection and the problems caused by material/lubricant incompatibility and low temperature are also discussed.

I. INTRODUCTION

In January 1969, the ISIS 1 satellite was launched into polar orbit to continue a series of studies of the ionosphere that had started in 1962, with the launch of the Alouette 1 satellite. Of all the experiments carried on ISIS 1, the sounder system was the prime experiment.

A set of four motor-driven STEM¹ antennas were designed as part of the sounder system, but, because of commutation problems experienced when dc motors are run in a vacuum, it was decided to protect the motors by enclosing them in airtight canisters. This paper describes how a lightweight canister was designed to provide protection for a size-8 dc motor without appreciably reducing its performance.

Various methods were considered for transmitting the drive from the inside to the outside of the canister. The three methods found to be worthy of further consideration were a bellows drive, a magnetic drive (both using hermetically sealed enclosures), and a sealed-shaft system. The bellows drive was used in the sealed drive system for the primary boom system of the Applications Technology Satellite (ATS), but it was discounted for the ISIS application because of its relative inefficiency, size, and weight. The magnetic drive was also considered

to be rather heavy, and it also introduced an unacceptable amount of magnetic material into the antenna. It was concluded that a sealed-shaft canister offered the best combination of size and weight that was consistent with reliable and efficient operation.

This paper traces the history of design, testing, and retesting that went into producing motor canisters for the ISIS 1 satellite and then explains how the canister's sealing capability was further improved for use in the ISIS B satellite.

II. PRELIMINARY DESIGN

A. Basic Design Requirements

The motor that had been selected to drive the antennas was a Clifton size-8 dc motor, which, for purposes of reliability had to be fitted with a lightweight canister that would prevent the motor from being exposed to a hard vacuum until after the antennas had been fully extended. The flight plan called for the antennas to be extended after a maximum period of four days in orbit, and it was required that the antennas operate within specification over the temperature range of -50° C to $+55^{\circ}$ C. In addition, a pressure-sensing device was required to monitor the internal canister pressure during ground testing.

*This work was carried out under Contract No. TP-1164 with RCA Ltd., Montreal, Canada.

¹Registered trademark—Storable Tubular Extendible Member.

B. Original Design

Consideration of the RF field inside the antenna indicated that a metallic canister should be used, and an aluminum alloy was selected because of its low weight and nonmagnetic properties.

The cylindrical canister (Fig. 1) was split into two parts in order to facilitate assembly, with the motor being secured to the front end cap by means of three clamping plates located in a clamping groove around the gearhead housing. Two leads from the back of the motor were brought forward to the end cap where they were soldered to feed-through terminals. The terminals were secured into the end cap in a plug of Stycast epoxy resin. This design facilitated easy assembly and wiring and permitted the canister/motor assembly to be rigidly

mounted to the antenna side-plate with three screws threaded directly into the end cap.

The canister was completed by the addition of a cylindrical canister body that carried a pressure transducer in its end. Viton O-rings lubricated with G300 silicone grease were used to seal the interface between the two halves of the canister and between the canister body and the transducer.

A plain O-ring seal was also considered for use in sealing the motor output shaft but was rejected in favor of a roto-seal because the former absorbed too much power. In the roto-seal principle, the bore diameter of the O-ring is larger than the shaft diameter, and it is compressed in its groove to provide a small interference fit around the shaft. By loading a ring in this way, a

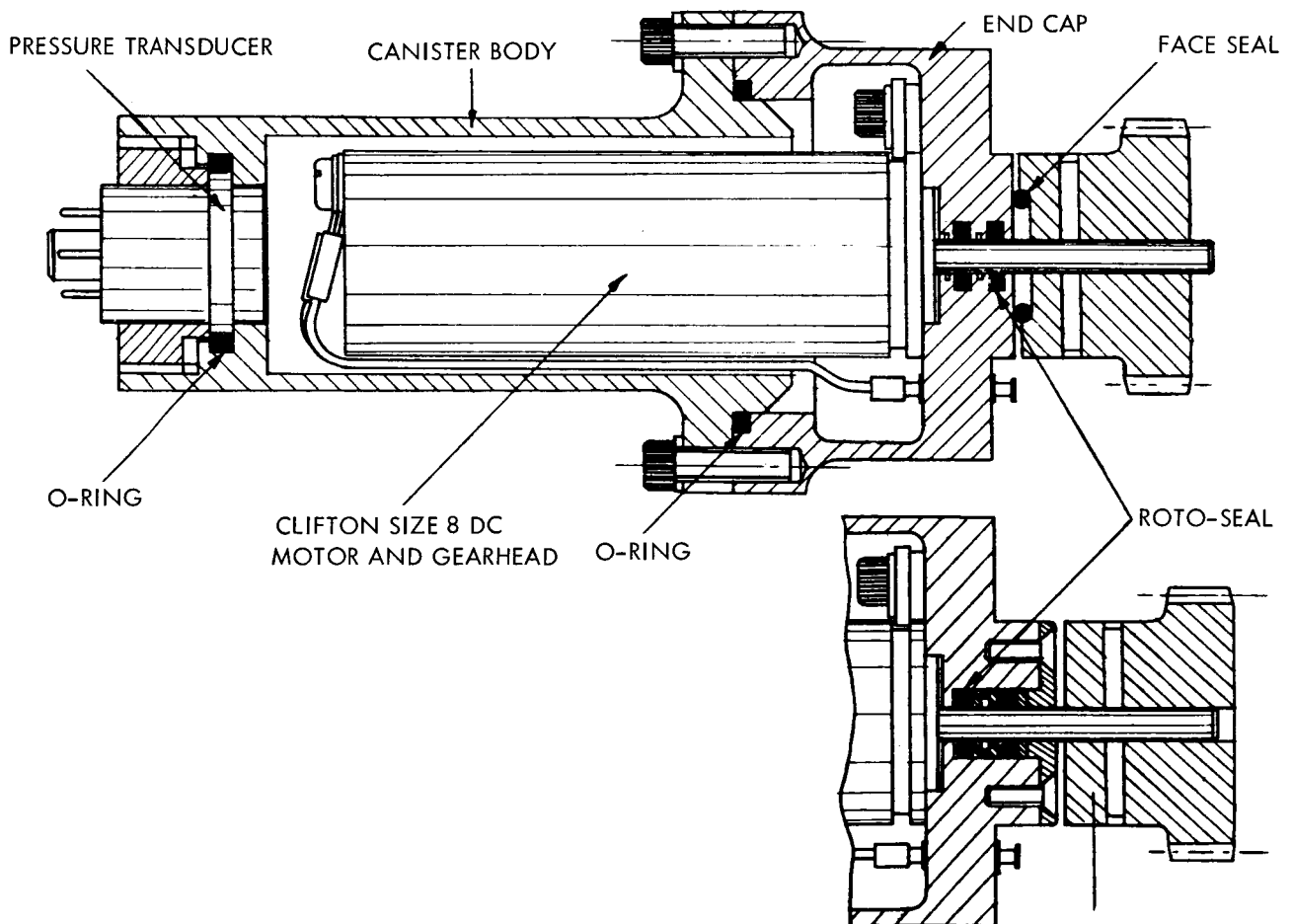


Fig. 1. Design of ISIS motor canister showing original design (top) with face seal in position between the end cap and the drive gear and (bottom) the modified rotor-seal

minimum of loading of the shaft is provided, and continuous heat buildup is prevented. Tests have shown that, when the shaft rotates, there is an initial increase in O-ring temperature which quickly levels off with continued running. Two roto-seals were fitted in the canister end cap to seal the motor output shaft; the groove dimensions and tolerances were taken directly from the O-ring data sheet from the manufacturer.

C. Sensing of Canister Pressure

Because of its small size and weight, a C.E.C. pressure transducer (No. 4-312) was selected for use in the motor canister. It used an unbonded strain-gauge bridge displaced by proportional displacement of a thin, stainless steel diaphragm. The transducer used in the ISIS canisters was capable of measuring absolute pressures in the range 0 to 20 psi and required a minimum of equipment for the continuous monitoring of canister pressure. Testing showed that in general, for a 5-V input, an output of 1 mV was equivalent to a pressure of 1 psi.

III. DEVELOPMENT TESTING—DETERMINATION OF THE LEAKAGE-RATE/TIME RELATIONSHIP

For these tests, a canister assembly was manufactured, but for convenience at this stage, it was fitted with a pressure gauge instead of a transducer. A number of 10-day tests were performed on the assembly with the canister soaked in a 1×10^{-5} -torr vacuum at ambient temperature. The motor was run for 40 minutes each day, first clockwise then counterclockwise, and records of motor current, breakaway voltage, and canister pressure were made.

Initially, there were leakage problems at the terminals, and it was necessary to change the detailed design of the feed-through and add RTV-502 around the terminals inside the end cap. When this problem had been resolved, further testing demonstrated that the roto-seal provided an effective seal whether the motor was operating or not. The leakage rate was shown to be 0.1 psi per 24 hours of soak. The motor-current increase was negligible, and the maximum breakaway voltage was 4.5 V. This showed that the basic canister design was sufficient to meet the design leakage rate of 1 psi per 24-hour period, and as evidenced by the breakaway voltage having increased only slightly from 3 to 4.5 V, the frictional torque was still very low. On the basis of

these results, the basic design was accepted, and qualification hardware went into production.

IV. ACCEPTANCE TESTING

A. Acceptance Testing of Canister

It was planned to do acceptance tests on the canister immediately after assembly and then again after installation in the antenna module to see if its installation and the addition of a gear to the motor shaft would cause any sealing problems.

The problems actually started before any canisters were tested. Difficulty was experienced in the turning of the end-cap grooves, and, once cut, they could not be inspected. Eventually, it became necessary to make special tooling to cut the grooves, and inspection was done by sectioning samples of the end caps taken from the production batch. Analysis of the roto-seal assembly showed that, because of the relatively high tolerances on O-ring diameter and section, it was essential to use a selective assembly approach.

After these problems were resolved, a batch of 11 canisters was acceptance tested. Testing consisted essentially of soaking the canister in vacuum for 24 hours, then running the motor for 10 minutes, and then checking that the canister pressure did not drop by more than 1 psi during the test. All canisters were eventually tested, accepted, and installed in antenna modules.

B. Acceptance Testing of Canister in Antenna Mechanism

The tests performed with the canister in the antenna mechanism were identical to the earlier acceptance tests except that the units could not be operated because of space restrictions. Acceptance criteria were identical. Again, with the exception of two units that failed initially because of insufficient lubricant on the roto-seals, testing was successful. All 11 antennas were accepted, and 10 were stored. The remaining one was completed for qualification testing.

V. QUALIFICATION TESTING

A. Testing Resulting in Canister Leakage

Qualification testing began with sinusoidal, and random vibration of the antenna, post-vibration functional

tests, and then thermal vacuum tests. After a 96-hour vacuum soak at ambient temperature, the canister pressure dropped from 14 to 12 psi, and then continued to leak during high- and low-temperature vacuum testing until the pressure was down to zero. Leakage only occurred when the motor was running.

B. Analysis of Qualification Failure

It was concluded that failure had been caused by disruption of the lubricant film on the roto-seal during vibration. The manufacturer recommends that the roto-seal should be well lubricated, and it was thought that the two grease grooves might not have provided sufficient lubrication. The addition of a face seal between the front of the end cap and the motor gear was recommended in order to overcome this problem (Fig. 1). This seal would add a further sealing stage and would also provide a grease reservoir to improve the lubrication of the seals.

C. Face-Seal Development

A series of tests were undertaken to determine the best face-seal configuration (O-ring compound, compression, lubrication, and operating temperature range). The first tests were done with a size 007 Viton O-ring with G-300 grease. These materials were selected because they had already been used successfully in other parts of the canister design. In the face seal however, it was found that low-temperature embrittlement of the Viton caused excessive wearing on the front face of the aluminum end cap at temperatures below -35°C .

Testing continued with silicone-rubber O-rings until it was found that, after the canister had been assembled for some time, the silicone rubber absorbed the silicone grease causing the O-ring to swell and seize the motor shaft.

At this stage, the mission requirements were reviewed, and it was concluded that it was unrealistic to test the canister down to -50°C because the lowest temperature to which it would be exposed in flight was estimated as -5°C . The low-temperature specification was eased to -25°C , and testing began again, this time using the Viton O-ring and G300 grease.

Testing of canisters fitted with face seals showed the effectiveness of the improved seal configuration over the full operating-temperature range. Supplementary testing

proved that the .004-in. compression applied to the face seal did not overload the motor shaft. Finally, before starting requalification of the antenna, a modified canister was pressurized to 28 psi and vibrated to test the adequacy of the lubrication in the new design. The seal remained intact throughout this vibration test and subsequent running tests.

VI. REQUALIFICATION TESTING

A. Acceptance Testing

The modified qualification motor canister was successfully tested out of the antenna mechanism and then again in the complete antenna assembly.

B. Qualification Testing

The antenna was again subjected to vibration and thermal vacuum testing, and again the shaft seal failed when the motor was operated. A failure analysis compared the test conditions during the development and the qualification of the canister, and it was noted that the only significant difference was in the method of loading the motor shaft. During the development tests, the shaft was loaded with a dynamometer that imparted a pure torque to the shaft, but, in the mechanism, the motor drive was transmitted through a gear-train from the motor shaft, applying a side load to the shaft. Even for the relatively low torque of 4 oz-in., there was a significant side load, and it was thought that this side load was the cause of the problem. For this reason it was decided that a side load would have to be applied to the motor output shaft for all tests, and test plans were modified accordingly. All canisters were successfully tested in accordance with the new test plan.

Prior to a repetition of the qualification testing, three elements of the canister program were reviewed: the qualification status of the canister, what had been achieved with the current design, and the actual mission requirements. The canister design had always maintained 100 percent seal under static conditions. On most occasions when it leaked dynamically, it took some 4 to 6 minutes to completely evacuate. This performance would ensure that the motor would always be protected from launch until the moment of switch-on, and, in most instances, the motor would never be exposed to hard vacuum even after switch-on. The combination of a low air-leakage rate and material outgassing would

provide a usable canister environment until long after the antennas had fully extended.

Additional tests had also been performed on uncanistered motors to determine their reliability in a hard-vacuum environment. These tests showed that, in the event of a canister failure at launch, the motor would still operate within specifications after a 4-day soak in hard vacuum (1×10^{-6} torr). After consideration of all the test results, the canister was accepted as giving adequate protection to the motor, thus ensuring reliable antenna operation for the ISIS 1 mission.

VII. FLIGHT OF THE ISIS 1 SATELLITE

After acceptance of the design, the antennas were installed in the satellite, and they passed through vibration and thermal vacuum tests on the spacecraft without failure.

On January 29, 1969, the ISIS 1 satellite was launched, and the antennas extended normally. Unfortunately, the canister pressure is not monitored in flight, so the history of the ISIS 1 canisters virtually ends at launch.

VIII. CANISTER TESTING FOR THE ISIS B SATELLITE

A. Acceptance Testing

Even before the ISIS 1 satellite was launched, work was progressing on the antennas for the ISIS B satellite. Canisters were manufactured to the same specifications used for the ISIS 1 canisters. They were tested with the same procedures, and every one failed.

All the previous problem areas were investigated without success, and it was decided to go back to the beginning and check the basic design of the roto-seal. It was thought that perhaps the wide tolerances on the size of the O-ring might be responsible for the failures, so a series of tests was performed to determine a relationship between the outside diameter and the inside diameter of a size 007 O-ring in peripheral compression. While these tests were being conducted, it was noted that it was almost impossible to compress a size 007 O-ring to a .125-in. bore without severely distorting it laterally. Because of this problem, it became necessary to add lateral restraint to the compressed O-ring in order to

simulate the grooved sides. However, with the lateral clearance recommended by the manufacturer, it was impossible to prevent the O-ring from twisting in the groove, and it was found that twisting within the groove resulted in clearance being generated between the O-ring and the shaft.

This realization led to a review of the canister development and the conclusion that perhaps this had been the problem all along. The twisted O-ring would seal effectively as long as there was a continuous film of grease to fill the void between the O-ring and the shaft, but, if the grease seal was broken during vibration or running, the seal would fail. This conclusion led to the further modification of the shaft seal.

B. Seal Design Modification

The modified seal still used the roto-seal principle, but the O-ring stack was assembled from O-rings, spacers, shims, and an end washer so that, by selective assembly, there was no lateral clearance in the O-ring groove (Fig. 1). From a manufacturing point of view, the modified design was considerably easier to make and inspect.

C. Acceptance Testing of Modified Canisters

Testing of the modified canisters was performed with side load applied, and the tests were so successful that the face seal could be omitted without reducing the canister's sealing capability. The canisters were installed in antenna mechanisms where they underwent further testing, and these mechanisms have been installed in the ISIS B satellite where the canisters are still functioning perfectly.

IX. CONCLUSION

Despite the many problems encountered during development, the final design of the motor canister has demonstrated its ability to protect the motor from the effects of temperature and vibration. The only real problem was found in sealing the motor shaft, and only after a long development period was an effective seal obtained.

It was found that the geometry of the O-rings being used in the roto-seal should be such that the peripheral compression of the ring does not cause the ring to twist

in the groove. If the shaft is of such a diameter that a standard O-ring will not give the required compression, a custom-designed ring should be considered. If, as in the case discussed here, program constraints necessitate the use of a standard ring, it should be adequately restrained laterally to prevent twisting. In either case, the design should take account of the tolerances on the O-ring

dimensions and should facilitate manufacture and inspection of the ring-groove profile.

Finally, this program showed the importance of performing complete functional tests on any newly designed component to ensure that operation, loading, temperature, and pressure conditions are reproduced as accurately as possible.

DISCUSSION

Edward Mundy:

I believe you stated that on the four antennas on the ISIS-1 that you maintained pressure up to deployment?

Wells:

Yes.

Mundy:

Now, what happened to the pressure upon deployment? Did it maintain or did you lose pressure as you deployed the antenna?

Wells:

It leaked out during deployment.

Mundy:

Do you have any idea of the rate?

Wells:

Over a period of about five minutes, it leaked out, as near as we could determine, to a vacuum level. The sensitivity of the pressure transducer here is 1 mV per psi approximately, so it is not very sensitive and we couldn't appreciate whether it was down to hard vacuum or whether it was just down to 0.5 psi.

Mundy:

But you did lose pressure.

Wells:

We lost pressure on those units.

Mundy:

Thank you.

Member of the audience:

Did you communicate this information that you learned from your testing to the manufacturers from whom you had received the bad advice initially?

Wells:

On the O-rings, no, I don't believe we did.

Member of the audience:

I recommend that you do that so he doesn't give this recommendation to some of us.

Wells:

No, I think perhaps the fault was two-fold: Perhaps recommending the specific size of the O-ring for sealing the shaft of 1/8-in. diameter was incompatible with what they had stated in another part of their data, that the peripheral compression should be limited to between 5 and 10 percent.

This is a comment I make lackadaisically. You should consider perhaps the selection of custom-made O-rings to achieve this. When you get down to the small sizes of shaft, particularly, you may be left with no alternative but to select an O-ring which is going to give you something like 30 or 40 percent compression. This was indeed the fault here.

We selected the manufacturer's recommended O-ring, but it gave this high compression and was at variance with his recommendation.

Member of the audience:

Is it really necessary to design a pressure canister to protect a motor for only four days? It is my impression that dc motors could run for as much as a week or longer without protection.

Wells:

Oh, yes. I think we have people here today that have had experience in flying dc motors for periods of ten or twelve months without any protection whatsoever. We realize now that this was a belt-and-brace approach, and indeed the tests that we did on the bare uncanistered motors luckily proved without a shadow of doubt that the motor would operate for much longer than four days without any sealing. But it was a belt-and-brace approach put upon us by our customers.

EFFECTS OF ENERGY DISSIPATION IN THE BEARING ASSEMBLIES OF DUAL-SPIN SPACECRAFT

M. P. Scher
TRW Systems Group
Redondo Beach, California

Proper evaluation of the effects of bearing assembly flexibility on the attitude stability of dual-spin spacecraft may explain the observed anomalies in the motion of a recently launched satellite. A convenient, but approximate, expression with which to gauge these effects is presented, as is an example of a possible application of this expression in a design role.

I. INTRODUCTION

A. Background

Those who design mechanisms for spacecraft are aware of the many constraints that must be placed on design alternatives to guarantee the survival of the mechanism and the feasibility of the mission. Often such constraints are imposed to insure the stability of the attitude motions of the spacecraft; but attitude instabilities still are occasionally encountered, frequently as a result of oversights on the part of the attitude dynamicist. The classic case of this nature occurred in 1958 with the Explorer 1, a slender satellite whose symmetry axis was to be spin stabilized in inertial space. Shortly after insertion in orbit, the symmetry axis was observed to be "coning," and the spacecraft finally settled into a stable spin about an axis perpendicular to the intended one. Several analyses (Refs. 1 and 2) confirmed that energy dissipation caused by structural damping in the antennae affected stability, and it is now widely accepted that a single-body, spinning spacecraft can achieve stable motion only when spinning about its centroidal principal axis of maximum inertia.

Within the past year, a similar phenomenon occurred, and this event raises important questions about a specific class of spacecraft mechanisms: the bearing assemblies of dual-spin spacecraft. The name "dual-spin" arises because spacecraft of this category are composed of two sections that can rotate relative to one another about a

common axis. Typically, one section of the spacecraft, called the rotor, is symmetric about this axis and rotates rapidly relative to the other section, termed the platform, which is rotationally at rest in inertial space. The two sections are separated by the bearing assembly, which consists of an axle, bearings, and a motor that cancels the frictional torques between the rotor and the platform, thereby keeping the platform at rest (Fig. 1).

B. Dual-Spin Stability

The stability of attitude motions of these spacecraft has been the subject of numerous recent investigations (e.g., Refs. 3-6). Although a detailed review of this material is beyond the scope of this paper, the conclusions are of great importance. Analyses have demonstrated that dual-spin spacecraft may perform a stable motion in which the rotor spins about its symmetry axis, whose orientation remains fixed in inertial space. This motion is possible even when the moment of inertia of the entire spacecraft about a line through its mass center and perpendicular to the spin axis is greater than the moment of inertia of the rotor about its symmetry axis, provided that the rate of energy dissipation on the platform exceeds that on the rotor by a sufficient amount. As indicated previously, this conclusion is not true for single-body satellites and is important because it permits dual-spin spacecraft to be rod-shaped rather than disk-shaped, thereby making better use of the available space on present launch vehicles.

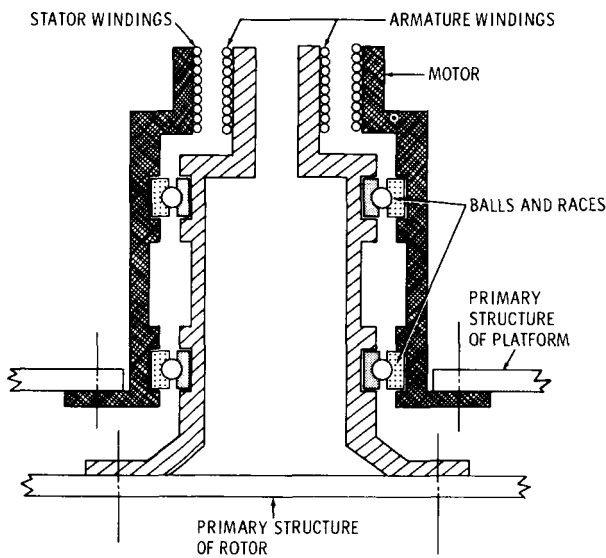


Fig. 1. Schematic of bearing assembly

C. Recent History

Unfortunately, the first dual-spin spacecraft to which these principles were applied exhibited unexpected instability in the motion of the rotor symmetry axis. Because of the stabilizing influence of the spacecraft's platform-mounted energy dissipator and sophisticated control system, this instability did not manifest itself in large angular motions of the symmetry axis; rather, the symmetry axis "coned" about an inertially fixed line with a small cone angle. Extensive investigations were launched to explain this instability, and nonrigidity in the bearing assembly has been identified as a possible cause. Flexibility in lateral bending may have permitted energy to be dissipated through some means such as hysteresis or viscous damping. This eventuality was not adequately assessed before launch.

II. DISCUSSION

A. Obstacles to Analysis

Bearing assemblies are complex devices¹ exhibiting nonlinearities in their moment-deflection characteristics during bending and in the ensuing viscous flow of the

¹Meeks, C. R., "A Despin Assembly for the Tacomsat Communications Satellite," Fourth Aerospace Mechanisms Symposium, The University of Santa Clara, Santa Clara, Calif., May 22-23, 1969.

lubricant among the bearings and races. Consequently, positive identification of an exact source of energy dissipation is difficult, even by experimental means. Moreover, analysis of this phenomenon is difficult for two reasons: first, since the actual dissipation mechanism is undefined, it cannot be analytically modeled; and second, the aforementioned stability investigations deal only with idealized spacecraft having rigid bearings and provide no method for apportioning energy dissipation between the rotor and platform, even if the magnitude of the dissipation could be estimated.

B. An Analytical Approach

An approach circumventing these obstacles is to consider the simplest relevant model of a dual-spin spacecraft with a compliant bearing assembly. Assume (1) that the entire spacecraft in its unflexed state is symmetric about the rotor's spin axis, (2) that the bending occurs at only one point, and (3) that the restoring and damping forces in the assembly are proportional to the deflection and rate of deflection, respectively. The question of apportioning energy is avoided by modeling a system in which the dissipating mechanism is tied neither to the rotor nor to the platform. This is accomplished by considering a spacecraft whose rotor and platform are separated by a massless, viscoelastic bushing that rotates at constant rates relative to both sections. The system is shown in Fig. 2, in which A and B are rigid bodies representing the platform and rotor and having mass centers A^* and B^* , respectively. The bushing is composed of two symmetric, massless annuli, C and D , connected by idealized springs and dashpots that resist bending of C relative to D about a line passing through point O and normal to the plane defined by the symmetry axes of C and D . (Axial rotation of C relative to D is prohibited.)

Typically, it might be desired that the system remain unflexed and that the symmetry axis remain fixed in space while A spins at a rate s (in inertial space) about this axis and while B rotates relative to A with rate Ω . (One may require the platform to be rotationally at rest by setting $s = 0$.) C and D , as a unit, may also be allowed to rotate relative to A about the symmetry axis with a rate $r\Omega$. Thus, if r is zero, C and D are fixed relative to A ; and, if r is unity, they are fixed in B . Values of r between zero and one are meaningful as long as the bushing is being considered. However, if C and D are to represent, say, a ball-bearing assembly, then an appropriate value for r is not immediately apparent. Now, if

the spacecraft is coning about an inertially fixed line (parallel to the spacecraft's angular momentum vector), the bushing assembly must transmit torques applied by *B* to *A*. These torques cause bending, which, in turn, leads to viscous dissipation in the bushing. If the spacecraft is "stable," the lateral bending will diminish and the coning will be reduced until the symmetry axes of *A* and *B* and the direction of the angular motion vector coincide. On the other hand, "instability" is manifested by increased bending and coning.

C. The Time Constant

A major objective of this paper is to present a time constant *T* for the growth or decay of the coning angle. A positive time constant is defined as the time required for the cone angle to decrease by a factor of $1/e$. This time constant has been estimated by using "energy sink" arguments in which a certain amount of rigor is sacrificed to obtain a simple closed-form expression for *T*. An outline of these techniques is presented in Ref. 7, and for now it will suffice to indicate that the crux of the energy sink argument lies in (1) the recognition that

the bushing is excited in a periodic fashion, (2) the computation of the energy dissipated per excitation cycle, and (3) the relation of energy changes to attitude changes. The principal assumptions involved in this process are (1) that the cone angle is small, (2) that the energy dissipated per cycle of excitation is small, (3) that no external torques act on the spacecraft, and (4) that the natural frequency of the system in lateral bending (when not spinning) is much greater than the excitation frequency. The outcome of this energy sink analysis can be presented in terms of the following parameters, which characterize the system:

- I* moment of inertia of the entire system about the symmetry axis (when unflexed)
- J* moment of inertia of the entire system about any line through the system mass center and normal to the symmetry axis (when unflexed)
- B*₁ moment of inertia of *B* about its symmetry axis
- B*₂ moment of inertia of *B* about a line normal to its symmetry axis and passing through *B**
- m*_{*A*} mass of *A*
- m*_{*B*} mass of *B*
- a* distance from *A** to *O*
- b* distance from *B** to *O*
- k* spring constant for lateral bending about *O*
- c* damping coefficient for lateral bending about *O*
- s* nominal spin rate of *A* in inertial space
- Ω nominal spin rate of *B* relative to *A*
- r* ratio of spin rate of *C* in *A* to nominal spin rate of *B* in *A*

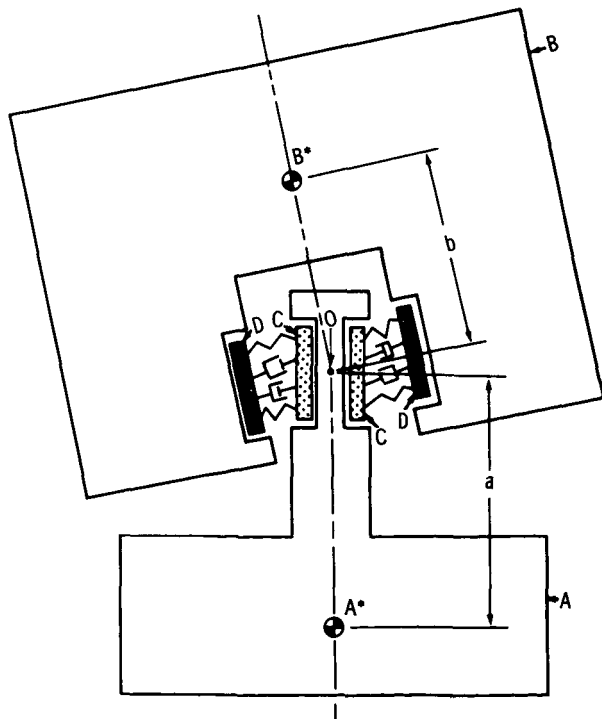


Fig. 2. Model of symmetric dual-spin spacecraft with flexible bushing

If one defines

$$\left. \begin{aligned}
 M &= \frac{m_A m_B}{m_A + m_B} & \alpha &= I/J \\
 \rho &= s/\Omega & \beta_1 &= B_1/I \\
 \eta &= c/I\Omega & \beta_2 &= \frac{B_2 + Mb(a+b)}{I} \\
 \Lambda &= \beta_1(\rho + 1) - \alpha\beta_2(\rho + \beta_1)
 \end{aligned} \right\} (1)$$

$$\sigma = k/I\Omega^2 \tag{2}$$

and

$$\lambda_r = \rho(\alpha - 1) + \beta_1\alpha - r \tag{3}$$

then T may be estimated as

$$T = \frac{1}{\Omega} \left[\frac{\sigma^2 + \lambda_r^2 \eta^2}{\alpha^2 (\rho + \beta_1) \Lambda^2 \lambda_r \eta} \right] \quad (4)$$

All the terms of importance in the model appear in this expression; e.g., the spring and damping coefficients enter via σ and η . The rate of rotation of the bushing is introduced through λ_r (of Eq. 3), which plays an important role in the analysis. In particular, $\Omega \lambda_r$ is the frequency with which the dissipator is excited.

D. Stability

In using Eq. (4), it usually is convenient to choose $\Omega > 0$, in which case $\eta > 0$. Then stability is assured if

$$(\rho + \beta_1) \lambda_r > 0 \quad (5)$$

a criterion that depends only on the inertia properties and spin rates of the rotor and platform.² For a spacecraft having its platform at rest in inertial space, $s = \rho = 0$ and Eq. (5) may be replaced by

$$\beta_1 \alpha - r > 0 \quad \text{or} \quad B_1/J - r > 0 \quad (6)$$

Note from Eq. (6) that if the dissipator is fixed relative to the platform ($r = 0$), stability is always assured, whereas if the dissipator is fixed in B ($r = 1$), then the moment of inertia of the rotor about its symmetry axis must exceed the entire transverse centroidal moment of inertia.

E. Bounding Analyses

In many circumstances, it is sufficient simply to determine whether or not bearing flexibility will be beneficial, in which case Eqs. (5) or (6) suffice. In other cases it may be necessary to ascertain $|T|$, and thus, values of k and c must be available. Routinely, k is determined from static deflection tests; however, only more complicated experiments can furnish a value for c . In lieu of this value, one can determine from Eq. (4) that

²When $r = 0$, Eq. (5) reduces to the stability criterion presented in the introduction of Ref. 6, and Eq. (5) can also be used with r equal to 0 and 1 to generate the stability chart presented in Fig. 2 of Ref. 4.

value of η that minimizes $|T|$; and substitution into Eq. (4) produces

$$|T|_{\min} = \frac{2\sigma}{\alpha^2 \Lambda^2} \left| \frac{1}{\Omega(\rho + \beta_1)} \right| \quad (7)$$

From Eq. (4), it is clear also that the maximum possible value of T is infinite (i.e., when $\eta = 0, \infty$). Thus, $|T|$ can be bounded without any knowledge of c , and incidentally, these bounds are independent of r .

F: Sample Calculation

As an example, suppose that a spacecraft were being designed with the following parameters:

$$\begin{aligned} \alpha &= .9 & \rho &= 0 \\ \beta_1 &= .8 & \beta_2 &= .7 \\ I &= 250 \text{ slg-ft}^2 & \Omega &= 60 \text{ rpm} \end{aligned}$$

The problem is to determine what shaft stiffness k is required to guarantee that in no case can there exist a destabilizing time constant T_0 of less than 15 minutes. Inspection of Eq. (6) reveals that instability is indeed possible if $r > .72$; and solution of Eq. (7) for σ leads to the minimum permissible value of σ :

$$\sigma_{\min} = \frac{1}{2} \alpha^2 \Lambda^2 \left| \Omega T_0 (\rho + \beta_1) \right| \quad (8)$$

Finally, the minimum acceptable shaft stiffness for the worst-case dissipator location and damping coefficient is found from Eqs. (2) and (8), i.e.,

$$k_{\min} = I \Omega^2 \sigma_{\min} = 1.6 \times 10^6 \text{ ft-lb/rad}$$

Stiffnesses predicted in this manner may be overly conservative, perhaps by one or more orders of magnitude, depending on the values of c and r that are bypassed in this bounding analysis. If weight limitations prohibit such conservative stiffnesses, laboratory tests may be run to determine suitable values of c and r ; Eq. (4) may then be solved for σ_{\min} , and k_{\min} again follows from Eq. (2).

III. CONCLUSION

In summary, insufficient attention has thus far been paid to the effects of bearing assembly flexibility on dual-spin spacecraft. It has been shown that the time constant for the growth or decay of wobble induced by compliance in the bearing assembly can be estimated, even in the absence of precise data regarding the dissipation mechanism. The qualitative effect of the

bearing assembly on spacecraft stability can be even more readily ascertained. In practice, the dynamicist must also consider the effects on stability of numerous other dissipation sources, such as fuel slosh and structural damping. The time constant expressions for these phenomena can be compared to determine which effects are negligible and which are not. The important phenomena should be included in more rigorous stability analyses or in simulations.

REFERENCES

1. Pilkington, W. C., "Vehicle Motions as Inferred from Radio Strength Records," External Publication 551, Jet Propulsion Laboratory, Pasadena, Calif., Sept. 1958.
2. Bracewell, R. N., and Garriott, O. K., "Rotation of Artificial Earth Satellites," *Nature* 182: 760-762, 1958.
3. Likins, P. W., "Attitude Stability Criteria for Dual Spin Spacecraft," *J. Spacecr. Rockets* 4 (12): 1638-1643, 1967.
4. Mingori, D. L., "Effects of Energy Dissipation on the Attitude Stability of Dual-Spin Satellites," *AIAA J.* 7 (1): 20-27, 1969.
5. Likins, P. W., and Mingori, D. L., "Liapunov Stability Analysis of Freely Spinning Systems," in the Proceedings of the Eighteenth Congress of the International Astronautical Federation, Belgrade, Yugoslavia, 1967.
6. Pringle, R., "Stability of the Force-Free Motions of a Dual-Spin Spacecraft," *AIAA J.* 7 (6): 1054-1063, 1969.
7. Scher, M. P., and Gebhardt, L., "Simulation and Nutation Damping of Dual-Spin Spacecraft," Report No. 9994-6047-T0-00, TRW Systems Group, Redondo Beach, Calif., Dec. 1969.

DISCUSSION

Member of the audience:

Have you given any thought to how you measure these parameters such as the damping of the bushings of a real unit?

Scher:

Yes, I have. I haven't proven this, but I think actually if you just took the assembly and twanged it and watched the decay, you could get an idea of the damping effect. But, more importantly, a recent paper by Charles Johnson, of Hughes Aircraft Company, described tests that were performed on a bearing assembly on TACSAT which showed this peculiar behavior. And the testing assembly, I think, can be used directly to determine these parameters, although he himself could not do it since he didn't have the formulation with him at the time.

Member of the audience:

Please explain in a little more detail what the most convenient energy relation is.

Scher:

You mean the time-constant expression?

Member of the audience:

Yes.

Scher:

What one does is assume the spacecraft to be rigid so far as bearing flexibility goes and assume that it is coning. Then, simply by using rigid-body equations the moment applied by the rotor to the platform is computed. One can then solve a second problem in which these moments are applied to the bushings and the rate at which energy is dissipated is computed. One can then solve a third problem relating the rate at which that energy is dissipated to the changes in the spacecraft attitude motion. It is admittedly an informal analysis, but I have had occasion to run computer simulations which show that it is in quite excellent agreement when the bearing stiffnesses are high. And when they get low, so that the natural frequencies of bending of the spacecraft are of the same order as the excitation frequency of the bushing, it breaks down.

METAL-SILICATE FRICTION IN ULTRAHIGH VACUUM

E. I. Ofodile

*E. I. DuPont de Nemours and Company
Wilmington, Delaware*

J. Frisch

*University of California at Berkeley
Berkeley, California*

Results of the analysis and experiments on the frictional behavior of materials under conditions of ultrahigh vacuum, as related to kinematic problems in a lunar environment, are presented. Experiments have been performed under varying conditions of cleanliness to determine frictional characteristics at 10^{-7} to 10^{-8} torr between flat basalt and spherical 7075-T6 aluminum surfaces. A quantitative analysis has been made of the factors influencing frictional behavior of these materials. The proposed mathematical model incorporated parameters of surface cleanliness, surface roughness, and surface energy.

I. INTRODUCTION

The results of a study of the frictional behavior between hard silicate rock (basalt) and 7075-T6 aluminum alloy in a 10^{-7} to 10^{-8} torr ultrahigh vacuum are presented. Friction forces F and the coefficient of friction μ were compared under different environmental conditions and degrees of surface cleanliness: some samples were chemically cleaned with acetone, some degassed at high temperature, and some ion bombarded. The results compared favorably with values of μ and F obtained from equations based on the work of Tabor (Ref. 1), Archard (Ref. 2), and Rabinowicz (Ref. 3). The complete derivation of the equations (Ref. 4) takes into account the elastic and plastic behavior of the dissimilar materials, the surface energies, the state of surface cleanliness α , and the environment. Considering the properties of the flat 1/2-in.-wide basalt surface in contact with the spherical 7075-T6 aluminum rider of 5-in. radius under a normal force N , the following equation for the coefficient of friction μ can be written:

$$\mu = \frac{2.31}{\lambda N^{1/2} + qN^{1/3}}$$

where λ and q are coefficients that depend on the test conditions, as shown in Table 1. The factor α denotes the extent of surface contamination at the contacting regions. The numerical values for μ from the above equation, as well as the friction forces, are shown in Table 2. The theoretical model for μ , which includes surface cleanliness, roughness, and surface energy as pertinent factors, is valid when compared with the experimental results.

II. EXPERIMENTAL TECHNIQUE

The ultrahigh vacuum system and friction test apparatus has been described in detail (Ref. 5). It consists essentially of a vacuum chamber with a 200 l/s vac-ion pump, a titanium sublimation pump, a nude Bayard-Alpert ionization gauge, and a residual-gas analyzer. A typical record of the partial pressures of gases present in the chamber during test conditions is shown in Fig. 1. An auxiliary pumping system consisting of a 75 l/s vac-ion pump and sorption pump is used for removal of argon after ion bombardment. A hydraulic system is used to pull the basalt and aluminum specimens relative to each other, and a force dynamometer measures the

Table 1. Values of λ , q , and α for different conditions

Conditions	λ	q	α
Air tests	3.0	1.0	$1.5N^{1/6}$
Vacuum tests	0.8	1.0	$0.4N^{1/6}$
Sputtered specimens (ion bombarded)	1.0	0	0

Table 2. Test results and theoretical values for the coefficient of friction μ and the friction force F

Test	Environment	Experimental results				Theoretical values	
		N (lb)	Average frictional force F (lb)	Average coeff. of friction F/N	α	μ	$F = \mu N$ (lb)
Air						$\mu = \frac{2.31}{3N^{1/2} + N^{1/3}}$	
1	Air	2.47	1.02	0.42	$1.5N^{1/6}$	0.381	0.942
2	Air	8.30	1.91	0.23	$1.5N^{1/6}$	0.216	1.783
3	Air	1.33	0.44	0.31	$1.5N^{1/6}$	0.507	0.675
4	Air	2.49	1.03	0.40	$1.5N^{1/6}$	0.379	0.945
5	Air	5.68	1.43	0.26	$1.5N^{1/6}$	0.258	1.465
Vacuum						$\mu = \frac{2.31}{0.8N^{1/2} + N^{1/3}}$	
1	3.5×10^{-8} torr	10.01	3.76	0.38	$0.4N^{1/6}$	0.482	4.830
2	1×10^{-7} torr	1.76	2.37	1.35	$0.4N^{1/6}$	1.018	1.793
3	4.5×10^{-8} torr	5.21	4.34	0.84	$0.4N^{1/6}$	0.649	3.380
4	1.3×10^{-7} torr	5.32	4.26	0.83	$0.4N^{1/6}$	0.643	3.420
5	2.8×10^{-7} torr	3.06	2.24	0.73	$0.4N^{1/6}$	0.809	2.470
Vacuum and sputtered specimens						$\mu = 2.31N^{-1/2}$	
1	7×10^{-8} torr	6.15	5.03	0.82	0	0.932	5.73
2	9×10^{-8} torr	1.36	3.00	2.36	0	1.985	2.70
3	1.4×10^{-7} torr	4.48	4.58	1.08	0	1.090	4.88
4	5×10^{-8} torr	1.43	2.52	2.06	0	1.932	2.76
5	3×10^{-7} torr	4.27	3.98	0.93	0	1.115	4.76

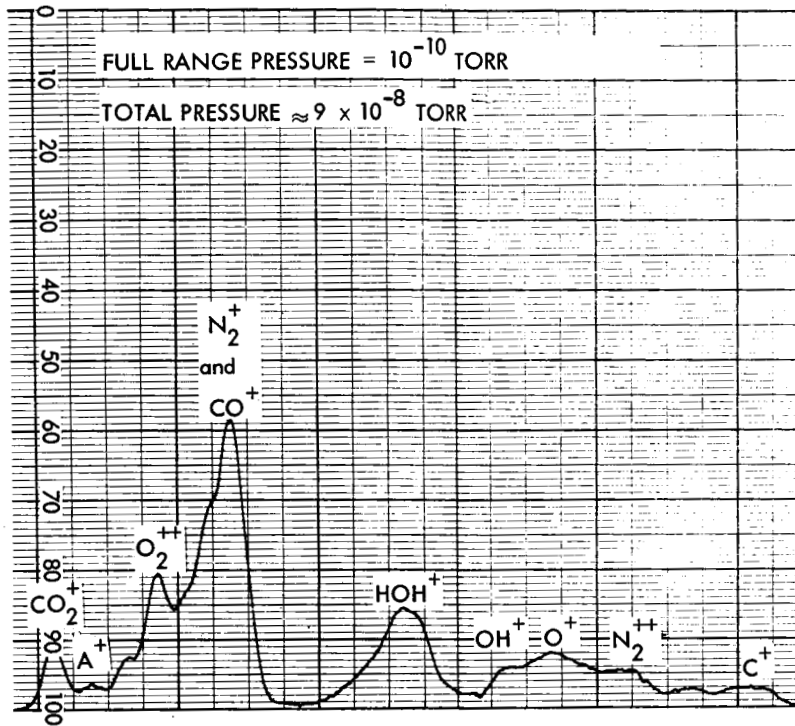


Fig. 1. Mass spectrometer reading of partial pressures during a vacuum test

normal and tangential forces. The recording equipment shows the normal force N , the friction force F , and coefficient of friction μ . Argon gas is used for ion bombardment. The sputtering equipment has been described previously (Ref. 6). After ion bombardment, electron bombardment of the basalt specimen was carried out to neutralize the charged surface.

The flat basalt specimens measured 1/2 by 1/2 by 2 in. The chemical composition of the rock material is shown in Table 3. On the basis of Surveyor data, basalt was selected as a material comparable to lunar surface material. Table 4 shows the chemical analysis of lunar surface materials from four landing sites. The companion specimen, with a 5-in.-radius spherical surface, was made from 7075-T6 aluminum (a representative lightweight material with a favorable strength-to-weight ratio). The specimens were rigidly mounted in a specially designed combination of pulling fixture and force dynamometer within the vacuum chamber. As shown in Table 2, three sets of tests were performed. All specimens were cleaned with acetone, and in the case of vacuum tests, bake-out

procedures and sputtering also were employed. The aluminum and basalt specimens had an average surface roughness of 25 μ in.

III. RESULTS AND CONCLUSIONS

As can be seen in Table 2, the experimental results agree well with the theoretical predictions. Figures 2 and 3 show the coefficient of friction μ and the friction force F plotted against the normal force N , respectively.

The ratio of tangential friction force to normal force (coefficient of friction) is strongly influenced by the normal load in the 1- to 10-lb range, particularly at small loads. However, for all normal loads, the ion-bombarded surfaces exhibited higher coefficients of friction (up to 2.5) than did chemically cleaned surfaces in either vacuum or air. In the vacuum environment, the coefficient of friction increased by a factor of two. Adhesive and surface-energy properties, as well as surface roughness, were found to be important parameters in the frictional behavior of the surfaces.

Table 3. Chemical composition of basalt specimens

Compound	Approximate percent composition	Compound	Approximate percent composition
SiO ₂	47.4	CaO	8.8
TiO ₂	2.1	Na ₂ O	3.7
Al ₂ O ₃	15.8	K ₂ O	1.7
Fe ₂ O ₃	2.2	P ₂ O ₅	0.6
FeO	7.9	H ₂ O	0.9
MnO	0.2		

Table 4. Chemical compositions of the lunar surface at Surveyor 5-1, 5-2, 6, and 7-1 landing sites (preliminary results)^a

Element	Percent of atoms			
	Mare sites			Highland site
	5-1	5-2	6	7-1
C	< 3	< 3	< 2	< 2
O	58 ± 5	56 ± 5	57 ± 5	58 ± 5
Na	< 2	< 2	< 2	< 2
Mg	3 ± 3	3 ± 3	3 ± 3	4 ± 3
Al	6.5 ± 2	6.5 ± 2	6.5 ± 2	9 ± 3
Si	18.5 ± 3	19 ± 3	22 ± 4	18 ± 4
"Ca"	13 ± 3	13 ± 3	6 ± 2	6 ± 2
"Fe"			5 ± 2	2 ± 1

Notes: "Ca" represents elements with atomic weights approximately between 30 and 47
"Fe" represents elements with atomic weights approximately between 47 and 65

^aTurkevich, A. L., Patterson, J. H., and Franzgrote, E. J., "The Chemical Analysis of the Lunar Surface," *Amer. Sci.*, 55(4): 312-343, 1968.

Strong welding of the junctions has not been observed. In Figs. 4 and 5, stereoscan microscope observations (from 200X to 2000X) show that there is a definite adhesion of aluminum specimen fragments on the basalt surfaces after the tests are completed. In some tests, basalt specimen fragments adhered to the deformed aluminum surfaces. The softer aluminum left clearly visible deposits of plastically deformed material on the harder basalt surface and, at the same time, showed evidence of severe deformation and galling in high vacuum and mild deformation in air. Plastic deformations of both the ductile and the brittle

materials were observed, although some elastic deformation on the brittle surface throughout contact produced ploughing on the softer surface. The apparent area of contact increased as sliding progressed, thereby increasing the number of asperity contacts; but after sliding, the real area of contact did not appear to have increased significantly.

The agreement between the theoretical model and the experimental results indicates that the frictional factors used for surface cleanliness, surface roughness, and surface energy were valid.

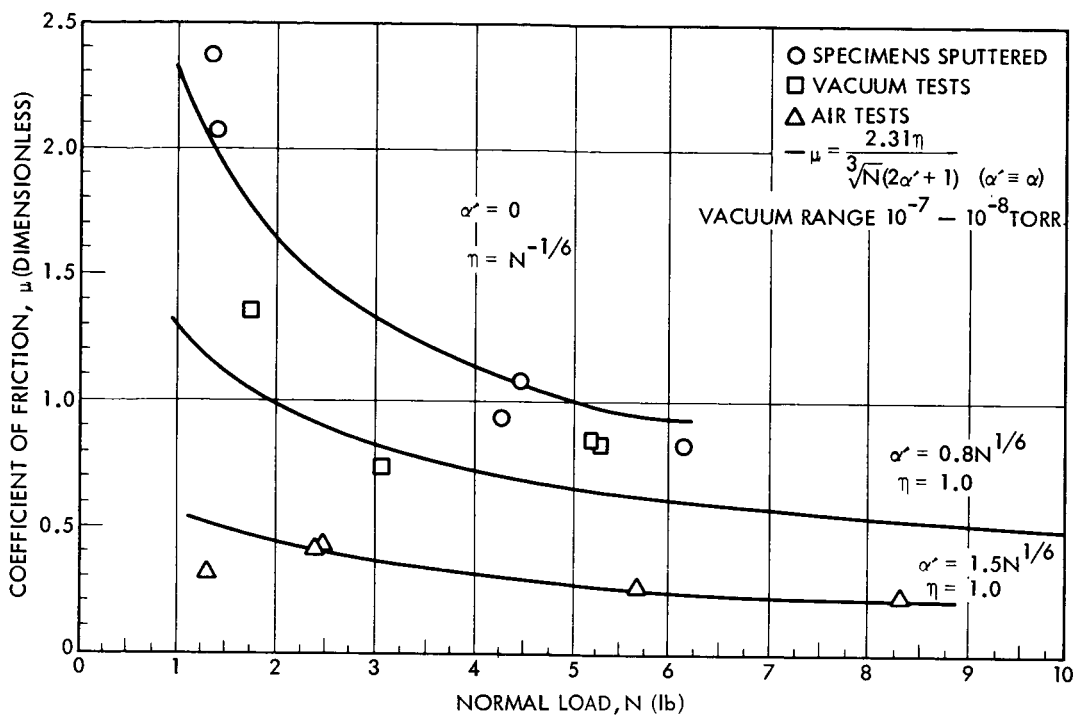


Fig. 2. Comparison of experimental and theoretical values of μ

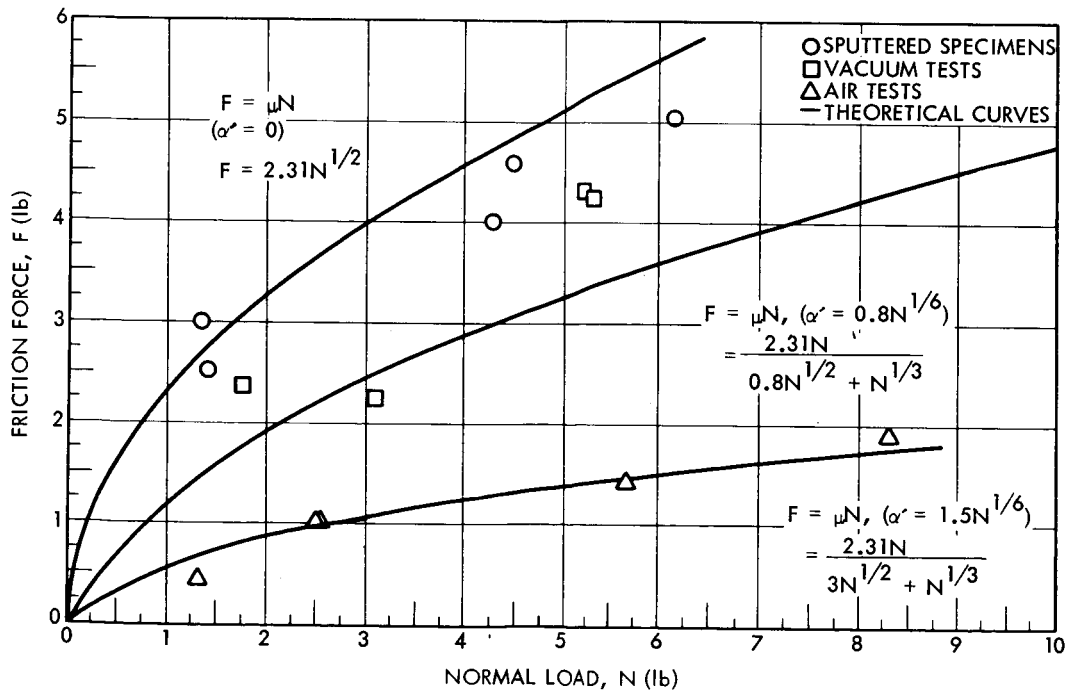


Fig. 3. Comparison of experimental and theoretical values of the frictional force

ARROWS INDICATE DIRECTION OF ALUMINUM SPECIMEN TRAVEL

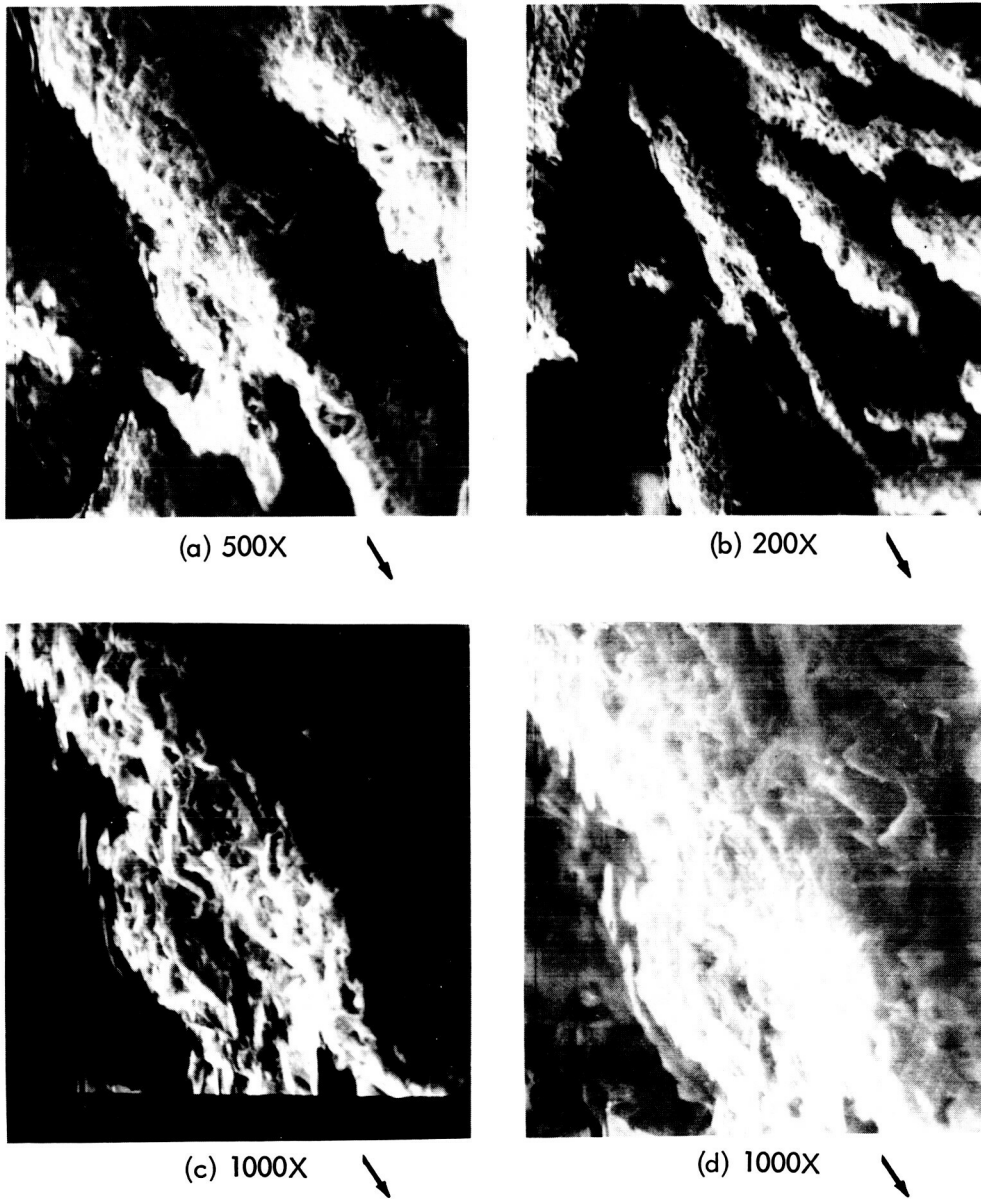


Fig. 4. Stereo-scan photograph of basalt surface showing imbedded aluminum fragments after a vacuum test ($N = 6.1$ lb; $\mu = 0.82$; 7×10^{-8} -torr vacuum)

ARROWS INDICATE DIRECTION OF ALUMINUM SPECIMEN TRAVEL

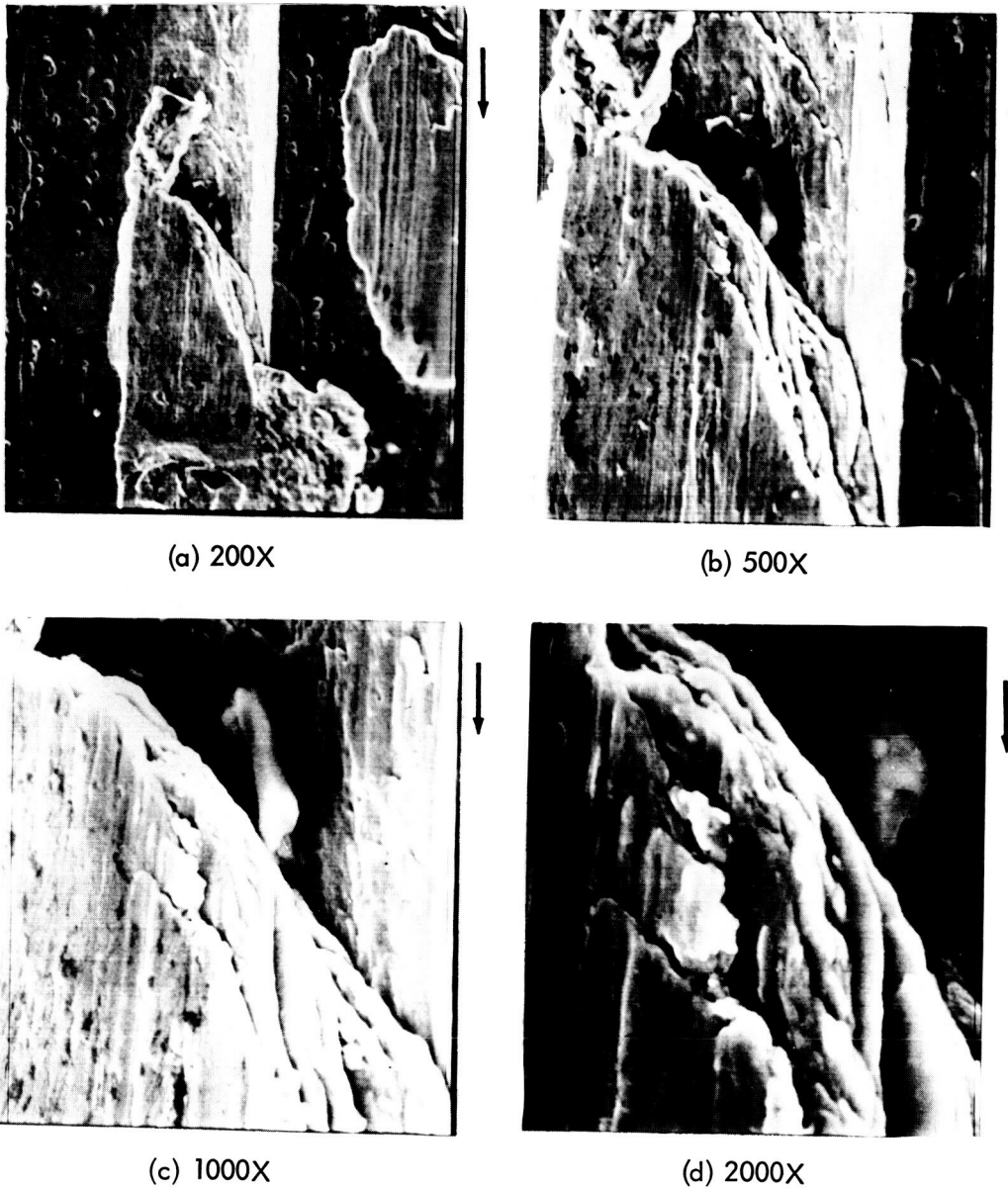


Fig. 5. Stereo-scan photograph of deformed aluminum surface after a vacuum test ($N = 6.1 \text{ lb}$; $\mu = 0.82$; 7×10^{-8} -torr vacuum)

REFERENCES

1. Bowden, F. P., and Tabor, D., "The Friction and Lubrication of Solids," New York: Oxford University Press, Inc., 1954.
2. Archard, J. F., "Elastic Deformation and the Laws of Friction," *Proc. Roy. Soc.*, A243: 190-205, 1957.
3. Rabinowicz, E., "Friction and Wear of Materials," New York: John Wiley & Sons, Inc., 1965.
4. Ofodile, E. I., "Experimental Investigation of Frictional Behavior Between Metallic and Silicate Solids in Ultrahigh Vacuum," doctoral thesis, Engineering Library, University of California, Berkeley, 1969.
5. Frisch, J., and Nelson, R. D., "Anisotropic Friction Between Aluminum Single Crystals in Ultrahigh Vacuum," Engineering Report No. MD-68-1, College of Engineering, University of California, 1968.
6. Frisch, J., and Ozawa, K., "Micrographic Study of the Effect on Silica Minerals Induced by Argon Ion Sputtering in Vacuum," NSF Summer Research Program Report, University of California, Aug. 1968.

SESSION IV

**Session Cochairman
F. R. E. Crossley
University of Massachusetts**

MEETING THE CHALLENGE OF A 50,000-HOUR-LIFETIME REQUIREMENT

Charles E. Vest
Philip A. Studer
*NASA—Goddard Space Flight Center
Greenbelt, Maryland*

Space mission requirements for the 70's have established a 50,000-hour-lifetime challenge for the mechanisms designer. This challenge may be met by two approaches: (1) development of new materials for wear-prone elements and (2) design innovation of new electromechanical devices that do not include mechanical wear-prone components. Present state-of-the-art materials require restricted operation regarding load, speed, and power for gears, bearings, and brush-slipping components. These restrictions are discussed, and methods of improvement are suggested. The design-innovations approach is discussed and is illustrated by the design of an experimental magnetically suspended motor.

I. INTRODUCTION

A unique challenge of the space program of the 70's faces the mechanisms designer: system operating lifetimes must be upwards of 50,000 hours—5 years of continuous operation. Interplanetary missions, operational communications systems, and the space station make several years of operation a practical necessity. The wear life of a component is a fundamental design consideration in very long missions. We are faced with a situation in which operational lifetimes exceed the available development test time.

In our area of work, we have concentrated on the wear-prone elements (electrical sliprings, commutators, and brushes) and on gear and bearing materials and lubricants. We have used two approaches in design:

- (1) Materials—to improve the wear life of state-of-the-art materials or develop new materials using the materials scientist's approach.
- (2) Noncontacting elements—to find innovations in which the wear-prone elements are eliminated or their numbers reduced.

II. MATERIALS APPROACH

In this effort, we have used an "engineering judgment" evaluation followed by limited test evaluation on state-of-the-art materials.

Table 1 shows typical conditions applicable for the listed materials. These data were collected from Refs. 1 through 5 and an unpublished source.¹

For gears and bearings, the indicated conditions are in a practical range for several applications. The typical load-speed conditions for brushes, however, are extremely limited. The wear limit assigned to the brushes results from the associated wear-debris contamination. If operation is not continuous, these load-speed factors can be increased in proportion to the total brush-contact travel.

To meet the 50,000 hour criterion with a more usable load-speed factor, wet lubricants (low-vapor-pressure oils

¹"Sliding Electrical Contacts in Vacuum and Space," (Proceedings of a seminar, Virginia Polytechnic Institute, Sept. 30-Oct. 1, 1969.)

Table 1. Materials, component size, loads, and speeds applicable for 50,000-hour lifetime

Component and size	Material	Load	Speed (rpm)	Remarks
Slipring 0.3-in. diam	Coin silver	80 g	1	No wear
Brush 1/8 in. X 1/8 in.	85% Ag, 3% Cu, 12% MoS ₂	8 psi	0.084 in. of wear	Wear rate 3 X 10 ⁻⁸ in./in. ^a
Commutator 0.3-in. diam	Cu + Rh plate	80 g	1	No wear
Brush 1/8 in. X 1/8 in.	88% Ag, 12% S ₂	8 psi	0.084 in. of wear	Wear rate 3 X 10 ⁻⁸ in./in. ^a
Gears, instrument	Nitrided Nitalloy M Hard Anodized Al 7075 Hardened 440 CSS	20 oz-in. torque 20 oz-in. torque 20 oz-in. torque	25	Less than 4% tooth wear, unlubricated b
Ball bearings R2-6 R8-24 B524	440 CSS and Duroid retainers	1#axial 1#axial 1#axial	120 30 5	c

^aThese brushes are operated without liquid lubricants and are the best engineering judgment materials.
^bHard anodized Al gears in air failed under our test loads but performed as well as the other two materials in vacuum.
^cData based on our in-flight and laboratory bearing lubricant testers.

or greases) can be applied. For instance, Clauss (Ref. 6) applied low-vapor pressure oil to a brush slipring arrangement, and the wear rate decreased significantly. Appropriate seals or labyrinth shields and barrier films, with enough oil to allow for loss by evaporation and creep, must be provided. Wet lubricants also may contaminate optical components. The only sure method of prevention of liquid-lubricant contamination is hermetic sealing.

To approach a more usable load-speed factor with the use of dry films, we feel that a thin, more adherent film (for example, a sputtered and diffusion-bonded film) must be more fully developed. To decrease the contamination problem in using wet lubricants, we feel

that lower vapor-pressure materials must be developed and the use of very thin liquid films evaluated.

III. THE NONCONTACTING APPROACH

This approach consists of eliminating wear-prone elements from the system.

A. Commutator Design

We first studied the sliding-contact-commutator dc motor, which had been virtually abandoned by the aircraft industry in favor of ac motors. This approach is less acceptable in spacecraft because of dc power

systems and more demanding motor weight and efficiency in spacecraft.

We separated the dual functions of the carbon-brush versus copper-bar commutator. A noncontacting photo-optical position sensor was combined with a transistorized switching network to accomplish the task. A wear-prone element still is used: a tungsten-filament lamp. Its life is limited by the evaporation of the filament, a process that is predictable and susceptible to accelerated-life testing. Derating to a 50,000-hour design life was considered more than adequate in 1963. A motor of this type (Ref. 7) has been operating for over 50,000 hours in the Mechanical Systems Branch (of GSFC) thermal vacuum chambers at 3000 rpm. Figure 1 is an exploded view showing its construction. Five motors of this type have successfully powered our in-flight friction and wear and bearing lubricant

experiment, as well as other NASA flight applications, such as the lifepacks used by the astronauts in the Apollo program. Currently, we are investigating integrated-circuit Hall-effect sensors to replace the photo-optical sensor assembly without introducing additional complexity into the commutator circuitry.

B. Gearing

In many mechanisms, the need for gearing can be completely eliminated by matching the motor characteristic to the load. This "direct drive" approach generally calls for a torque motor. The torque motor or "torquer" provides higher torque at lower speeds than do conventional motors. Typically of large diameter and "pancake" construction, they take advantage of the fact that the torque is directly proportional to the air-gap radius. The same weight savings associated with gear

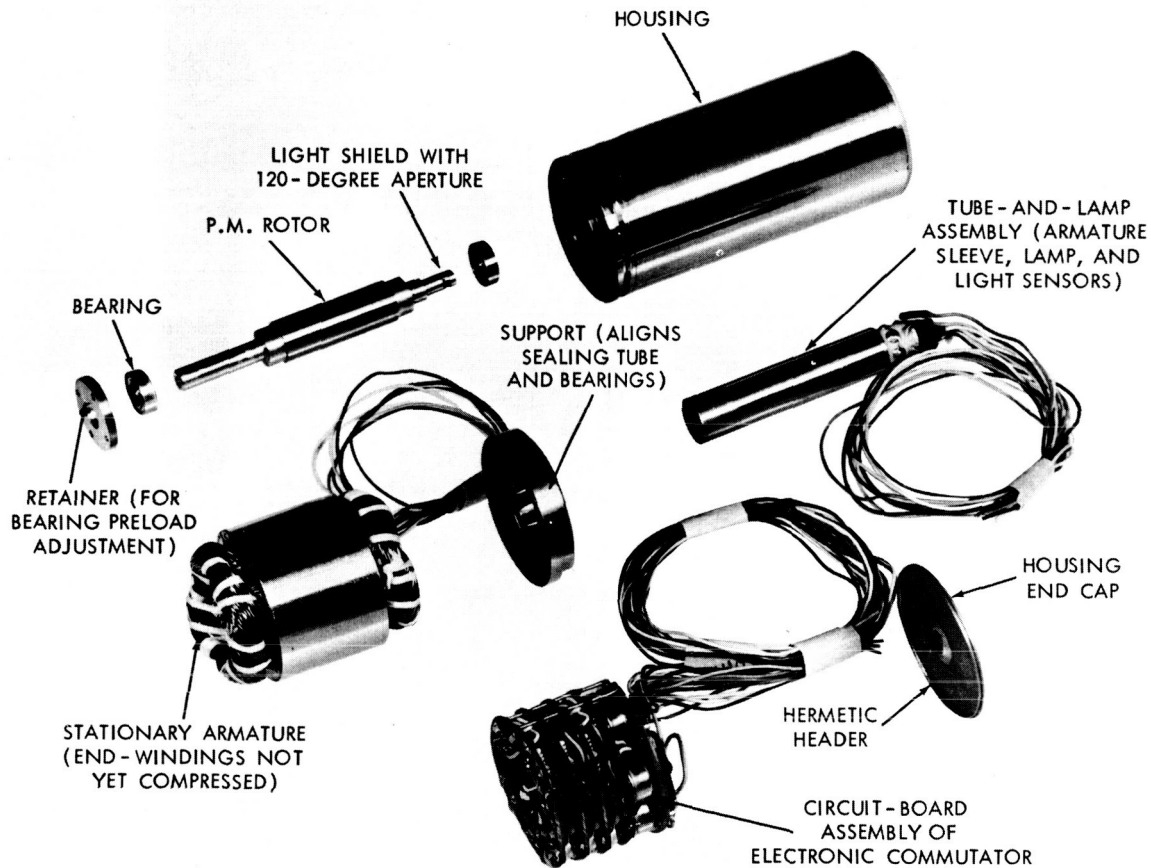


Fig. 1. Sealed brushless dc motor

reduction are available through an increase in the diameter of the motor, and the difficult lubrication problem and backlash associated with gearing are eliminated. The designer should employ the largest-diameter motor possible within the space available (Table 2).

C. Bearings

In a direct-drive mechanism, the only remaining point of contact between surfaces in relative motion is at the bearings. Although these are rolling contacts, they do have a finite life. The speed of a device that must operate for several years may be constrained by wearout considerations. In general, all electromechanical systems can be made lighter and smaller by operating at higher speeds. This principle is obviously true in the case of momentum-storage devices such as are used in the attitude control of spacecraft.

The noncontacting approach has recently been applied to bearings. An experimental device (Fig. 2) using magnetic suspension techniques is in operation at GSFC. A radial load capacity of 10 lb and an axial load capacity of 50 lb, with stiffnesses of 1000 and 10,000 lb/in., respectively, have been achieved. A 6-lb rotor is actively servoed in the axial direction by electromagnets and has passive radial support.

The price in weight and power for these desirable life characteristics is high. Approximately 4 lb and 15 W of power per bearing are currently needed to replace a ball bearing weighing a fraction of an ounce. In addition, the change cannot be tolerated where magnetic field measurements are to be made. However, considerable reductions of weight and power are expected from designs now on the drawing boards, and continued development is expected to yield flight-weight devices with no known mechanical wearout characteristics.

Active electromechanical mechanisms whose lives exceed that of the electronic control system and sensors can be envisioned.

IV. INDIRECT RESULTS

Some unexpected benefits generally can be derived from exploring new approaches to old problems. In the case of electronic brushless commutation, an exceptionally fast mechanical time constant was achieved because the permanent-magnet rotor is smaller in diameter than is the equivalent wound rotor. Another benefit of this arrangement is that no heat is generated on a permanent-magnet rotor, in contrast to the rotating wound armature of a conventional dc motor. In a vacuum, the only thermally conductive path for heat transfer from the rotor is through the bearings; thus, stationary armature windings are a valuable asset.

In the case of the brushless torquer (Ref. 8), the indirect benefit was the fact that the electronic commutator, with its inherent power amplification, can eliminate the need for a separate power amplifier and reversing bridge, again reducing system complexity and enhancing reliability.

V. CONCLUSION

A review of progress in mechanisms shows that continuous operation under vacuum for 50,000 hours restricts mechanisms to low speeds and light loads. The prospects are considerably brighter for intermittently operating devices in these long-term applications.

Advanced materials and lubrication developments and elimination of physically contacting surfaces, where necessary, establish a basis for new mechanisms design.

Table 2. Typical "brushless" torque motor characteristics

Torque (lb-ft)	Speed (rpm)	Weight (lb)	Power (W)	Diameter (air gap) (in.)
0.1	75	1	4	3
0.4	250	3	40	4

Incorporation of these advances into new designs will permit mechanical systems to keep pace with the requirements of future space ventures.

A new development that may provide an electromechanical device whose life is not a function of

speed or total number of revolutions is the magnetically suspended motor. This motor may make possible mechanisms in which the electronic control system, instead of wear, may be the limiting element in reliability calculations.

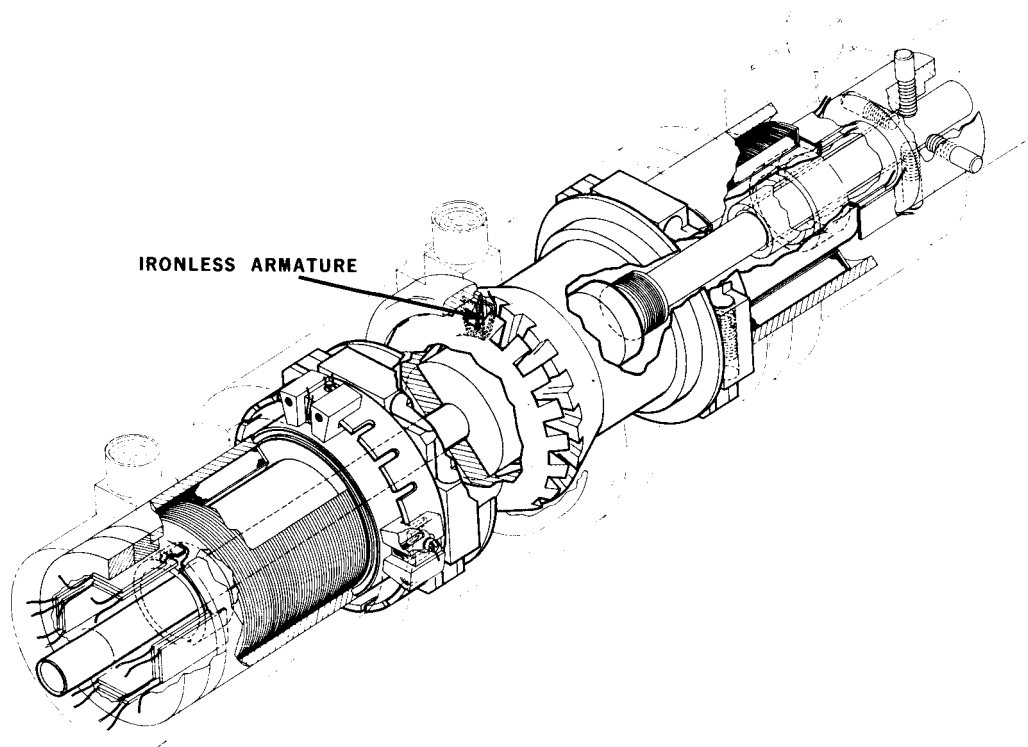


Fig. 2. Magnetically suspended motor

REFERENCES

1. "Interdisciplinary Approach to Lubrication of Concentrated Contracts," NASA Symposium, Rensselaer Polytechnic Institute, July 1969.
2. Federline, M. F., and Vest, C. E., "Operating Gears in Simulated Space Vacuum: The Vacuum Facility and Several Techniques," *Lubric. Eng.* 23 (4), 1967.
3. Vest, C. E., Courtney, W. J., and Farrell, J. J., "Evaluation of Gear Materials for Space Applications," *Lubric. Eng.* 26 (2): 46, 1970.
4. Vest, C. E., and Ward, B. W., Jr., "Evaluation of Space Lubricants Under Oscillatory and Slow Speed Rotary Motion," *Lubric. Eng.* 24 (4), 1968.

5. Devine, E. J., Evans, H. E., and Leasure, W. A., "Instrument Bearing Performance in Space and Laboratory Vacuum," NASA Technical Note D-6035, Jan. 1970.
6. Clauss, F. J., and Young, W. C., "Space Materials Handbook," 1st ed., Lockheed Missiles & Space Co., Contract AF 33(657)-10107, ML-TDR-64-40, (12):209, Jan. 1965.
7. Studer, P. A., "Development of a Sealed Brushless D. C. Motor," NASA Technical Note D-2819, May 1965.
8. Fulcher, R., "A Brushless D. C. Torquer-Driven Reaction Wheel for Spacecraft Attitude Control," NASA Technical Note D-5265, July 1969.

DISCUSSION

Member of the audience:

You seem to be concentrating on dry lubricants and the paper earlier this morning concentrated on wet lubricants. I would like to understand why this divergence. Can wet lubricants really be used for long life?

Vest:

I say they can, if you take care of the seals and the shields

and don't worry too much about contamination. The big advantage to using wet lubricants is lower frictional losses. Your big advantage to solid films is no contamination and reduced weight as seals and shields are not required. But, the lifetime of a solid lubricant is much shorter than that of the wet lubricant, if you have enough wet lubricant to last your predicted time. But our concern is contamination. We feel that the selection of the best hermetically sealed unit is not the best approach, as a great number seem to leak.

A LIGHTWEIGHT BIMETALLIC ACTUATOR FOR SPACECRAFT THERMAL CONTROL

Keith L. Schilling
RCA Astro-Electronics Division
Princeton, New Jersey

This paper describes the design, development, and construction of two types of active thermal-control systems. These designs are based on the controlled angular deflections of spiral-wound bimetallic actuators. The use of these actuators and lightweight louvers results in a frictionless system that is low in weight yet simple in design and low in cost. Both designs exhibit high reliability, good performance repeatability, and do not require power from the spacecraft. Design philosophy and implementation, design tradeoffs, and materials selection are reviewed. The test program is described, and results are presented.

I. INTRODUCTION

Control of the thermal environment is important for the reliable operation of the various equipment and components of any spacecraft. Thermal control can be achieved either by active or by passive means. Reliable passive techniques, such as the proper use of surface finishes, the optimum location of critical spacecraft components, and the choice of the orbit, are commonly used for spacecraft. However, passive designs require larger tolerances in the spacecraft's nominal heat loads. Therefore, it is often desirable to have an active thermal-control (ATC) system where narrower temperature ranges are required. ATC systems regulate spacecraft temperatures by means of a louver or series of louvers that open or close in response to temperature changes and vary the effective area of a designated radiating surface on the spacecraft (Fig. 1).

The thermal actuators described in this paper (Figs. 2 and 3) use spiral-wound bimetallic elements as thermal sensors and prime movers for the systems.

II. ACTUATOR DESIGN CONSTRAINTS

The thermal actuators designed for the ATC systems shown in Figs. 2 and 3 had to meet the following requirements:

- (1) Operating temperature range of $10^{\circ}\text{C} \pm 1^{\circ}\text{C}$.
- (2) Range selection from 12°C to 22°C .
- (3) Over-temperature relief from 0°C to 40°C .
- (4) Minimum weight.
- (5) Reliable operation in space for 18 months (equivalent to 8000 cycles).
- (6) Linearity of system over the operating temperature range of ± 10 percent.
- (7) Short development time.
- (8) Design simplicity.

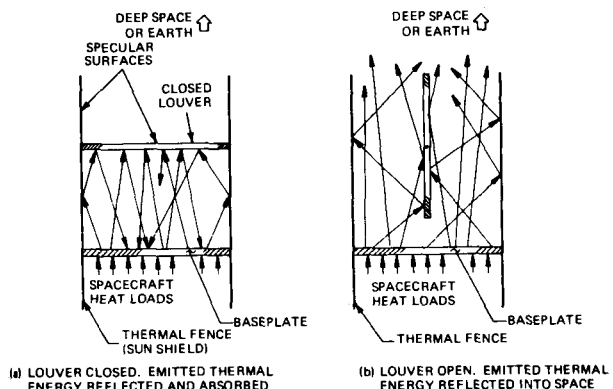


Fig. 1. Principle of operation of the ATC system

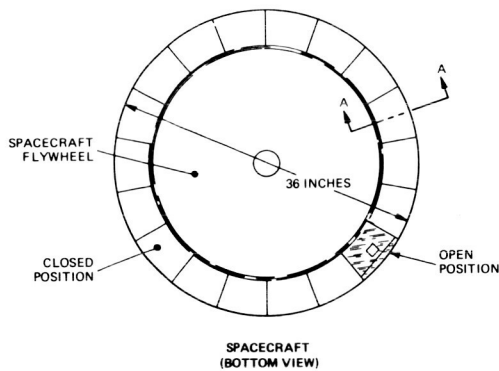
III. DESIGN ALTERNATIVES

Other ATC design techniques or systems that have been considered include the following:

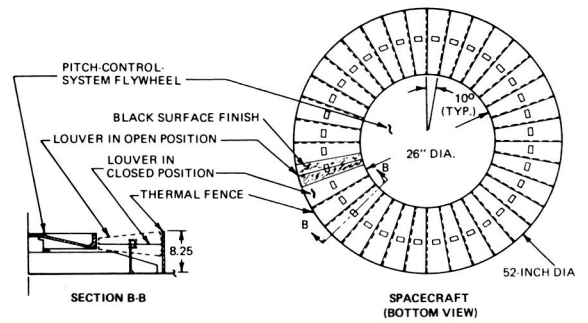
- (1) Electrical heaters with thermostatic control.
- (2) Fluid actuators.
- (3) Two-phase actuators for louver operation.
- (4) Electromechanically operated louvers.
- (5) A thermal switch.

The heater system was eliminated owing to a lack of available power, the electromechanical system was eliminated because of its unnecessary complexity, and the

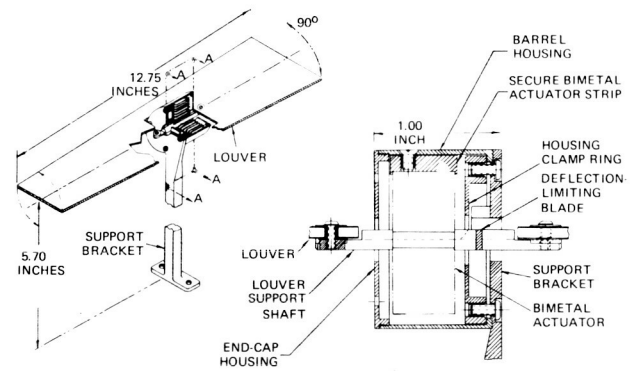
fluid and two-phase actuators were eliminated because of their complexity, lack of redundancy, and cost. Although the thermal switch was considered to be very attractive, it was eliminated because of the development leadtime required.



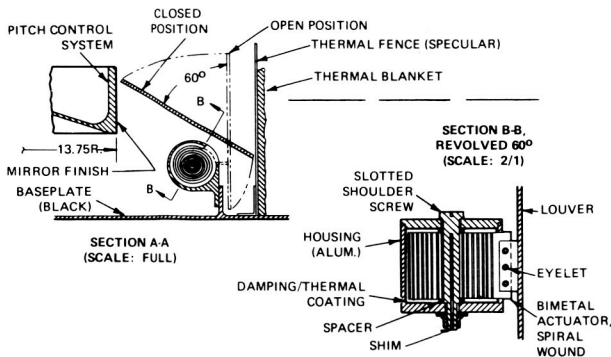
(a) ARRANGEMENT OF LOUVER MODULES



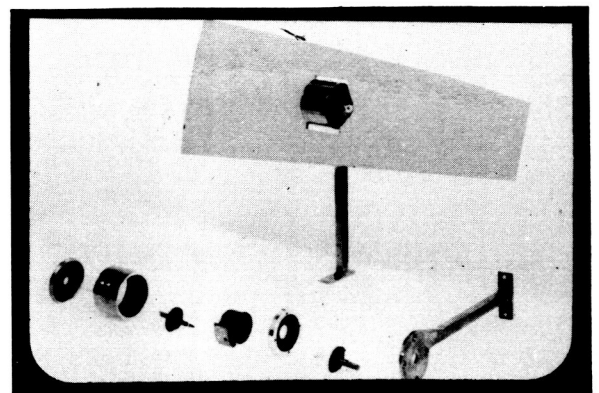
(a) ARRANGEMENT OF LOUVERS



(b) CONTROL MECHANISM



(b) CONTROL MECHANISM



(c) CONTROL COMPONENTS

Fig. 2. Petal arrangement

A tradeoff study of the aforementioned systems established that a design utilizing the bimetallic-actuated louver concept offered several advantages:

- (1) Local temperature sensing provided.
- (2) No external power source required.
- (3) Virtually frictionless.
- (4) High reliability.
- (5) Simplicity of design and analysis.
- (6) Short development and qualification time.
- (7) Low weight.

IV. FUNDAMENTAL DESIGN EQUATIONS

The equation used to describe the angular deflection of a spiral-wound bimetallic coil (Fig. 4) is

$$A = \frac{K_{DC}(\Delta T)Lm}{t}$$

where $m = 1$ when $P = 0$.¹

Since the bimetallic actuator is designed to operate in zero gravity, the load P imposed on the actuator by the louver is for all practical purposes negligible. "The specific deflection m is the ratio of the actual deflection, corresponding to a particular force and temperature change, to the free deflection for the same temperature change. This dimensionless ratio varies from 0.0, for the case of complete restraint, to 1.0 for free deflection, which is the case in this design."²

The basic equation for stress is³ (see Fig. 4)

$$S = \frac{3P(r+z)}{8bt^2}$$

¹"Design Catalog," (unabridged), W. M. Chace Co., p. 28.

²"Design Catalog," (abridged), W. M. Chace Co., p. 10.

³"Design Catalog," (unabridged), W. M. Chace Co., p. 37.

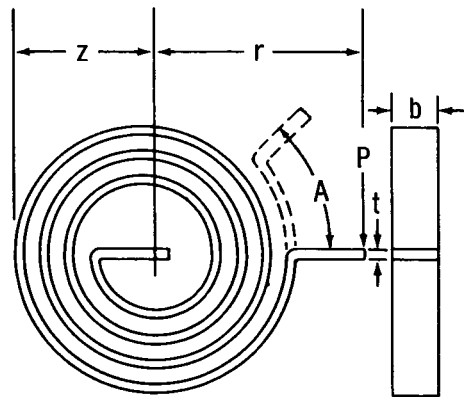


Fig. 4. Spiral coil

V. ATC CONFIGURATION AND OPERATION

The ATC's shown in Figs. 2 and 3 consist of groups of modules having rotating flaps that cover the spacecraft's radiating area. They are driven by spiral-wound bimetallic actuators that are thermally coupled to the spacecraft. In the closed position, each flap will inhibit the thermal radiation from a desired region of the spacecraft; in the open position, the flap will allow maximum radiation from that region (Fig. 1). The spacecraft temperatures are thus controlled by varying the " $A\epsilon$ " (area \times thermal emissivity) of the designated radiating area of the spacecraft as a function of temperature. The bimetallic actuators are essentially thermally decoupled from the louvers and the space environment. Thus, they respond only to a specific spacecraft reference temperature.

The ATC employs a direct drive having no moving parts other than the actuator, which responds to temperature variations. The bimetallic element is encased in a lightweight aluminum housing that thermally grounds the actuator to the spacecraft's radiating surface and limits the actuator excursions during vibratory exposures.

For the ATC shown in Fig. 2, calibration is accomplished by adjustment of the support shaft to the appropriate louver-temperature orientation. The support shaft is then secured. For the ATC shown in Fig. 3, calibration is accomplished by loosening the clamp ring that secures the actuator barrel to the support bracket and then rotating the barrel to obtain the appropriate

louver/shaft orientation for the desired temperature level. For both designs, over-temperature relief is accomplished by the actuator's absorption of the winding-up or unwinding energy, since both designs incorporate deflection-limiting stops. Internal stresses sustained are negligible.

VI. DESIGN CONSIDERATIONS AND MATERIALS SELECTION

A. Cold Welding

For the design concept shown in Fig. 2, metal-to-metal contact was prevented by the use of adequate clearance between the bimetallic actuator and its housing. Careful control of the bimetallic element's dimensions and the use of RTV on the housing's deflection-limiting stops also precluded the possibility of metal-to-metal contact. The ATC shown in Fig. 3 is designed to insure that the louver support shaft will not touch the housing in a zero gravity environment and to avoid any operational metal-to-metal contact. Control of tolerances also assures that the deflection-limiting blade of the louver support shaft will make contact only with the mechanical stops.

B. Selection of Bimetallic Actuators⁴

The performance of a bimetallic element depends upon the following factors:

- (1) Type of bimetals.
- (2) Length of strip.
- (3) Width of strip.
- (4) Thickness of strip.
- (5) Temperature change.
- (6) Magnitude of load.
- (7) Type of element used.
- (8) Electrical resistivity.

The design equation given previously involves several variable factors so that it is necessary in the calculations to assume values that are selected from the specifications and the nature of the application, as far as possible, in order to solve for the thickness, the width, or the length of the strip. When the calculations indicate that the length of a straight strip would be too great to meet the requirements for mounting and containment, then a U-shaped strip or coil would be employed, the choice depending upon the available space for containment. In both cases, a very active coil (large deflection per unit temperature change) was required. Consequently, a bimetallic material with the highest possible coil deflection constant K_{DC} was chosen (Chace Mfg. #6650). The temperature change ΔT was 10°C (18°F) for both ATC's. Because of the zero-gravity environment, the load is negligible for both designs. With zero load on the bimetal, the width of the element b is not related to the angular deflection A . Therefore, the width is chosen primarily on the basis of design convenience, stress requirements, and stability.

C. Actuator-Housing Material

Aluminum was chosen as the basic housing material for both ATC's because of its strength, low weight, and heat-conduction properties. The ATC design shown in Fig. 2 was very closely thermally coupled to the spacecraft, and, since the housing was completely shielded from space on the cold end (louver closed), the surface finish on the outside of the housing was left as bare aluminum with a polished finish. The resulting low emissivity does not cause any thermal imbalance on the hot end (louver open). Also, the portion of the bimetal that is exposed to space is finished with gold. The ATC design shown in Fig. 3 did not require such a rigid thermal coupling with the spacecraft. Also, the housing of this design is exposed to space all of the time, whether the louvers are open or closed. To help compensate for the thermal coupling, the support bracket was made from 6101-T6 aluminum because of its high thermal conductivity. In addition, all exterior surfaces of the bracket and actuator housing were polished to a specular finish and coated by a gold-vapor deposit to produce a very low thermal emissivity that would reduce radiation heat losses.

D. Louver (Flap) Material

The ATC louver has been designed to minimize weight and for ease of fabrication. This low-mass louver

⁴"Design Catalog," (unabridged), W. M. Chace Co., p. 24.

concept minimizes the dynamic actuator loading and reduces the testing complication of static deflection of the actuator in a 1-g field. The basic louver is a sandwich structure composed of two 0.5-mil-Kapton (aluminized H film) skins that are separated by a core spacer of low density polyurethane foam (1.7 lb/ft^3) and held together by Bondmaster M773 adhesive. The typical louver shown in Fig. 2 weighs approximately 3 to 4 g, and the louver from the design shown in Fig. 3 weighs approximately 4 to 5 g.

The polyurethane louver core is made from Scott Industrial Foam, which is a fully open-pore (reticulated), flexible, polyester material with a 97-percent-void volume and high permeability. The foam has a density of 100 pores/in. It also has high chemical resistance, resistance to moisture, and unusual memory. (When a sheet of this foam is crushed into a tight ball and then released, it returns to its original shape with no apparent damage, even after repeated exposures to this treatment.) Also, because it is an open-pore foam, it easily releases any trapped air in a vacuum environment. Exposure to vibration has virtually no deleterious effect upon the integrity of the louver.

VII. TESTING AND RESULTS

Thermal testing was performed in vacuum chambers or bell jars. Electrical heaters simulated spacecraft heat loads, thermocouples monitored spacecraft and ATC temperatures, and electrical sensors verified the open and closed louver positions. Thermal tests verified that the louvers went from full open to full closed over the required temperature range and monitored thermal gradients between louver, actuator, actuator-support housing, and the spacecraft's radiating surface. The thermal tests established that the required change in " A_e " as a function of spacecraft temperature was obtained.

A bimetallic-actuator life test was performed on an actuator of the type shown in Fig. 2. The actuator was thermally cycled between 28.5°C and 46°C for a total

of 8000 cycles representing 18.5 months of mission time. This temperature span is 7.5°C greater than the normal operating range of the ATC system. The actuator's angular movement was constrained to 60 deg, which is the same as that of the flight configuration. No detectable change was noted in the actuator characteristics or in the calibration and angular position of the actuator throughout this test.

Breadboard models were subjected to vibration exposures of 15 g, sine 7 to 2000 Hz at 2 octaves/min, and random vibration exposures of 35.9 g (rms), flat spectrum within $\pm 3 \text{ dB}$ (2 minutes) from 20 to 200 Hz, for three axes of testing. The units tested successfully withstood all of the vibration tests and were in operating condition at the completion of tests; no change in thermal calibration occurred. Magnetic and antenna testing indicated no significant problems with either of the design configurations.

VIII. CONCLUSIONS

The results of the development effort were the bimetallic-ATC designs shown in Figs. 2 and 3.

Basically, the development effort produced a practical flight-hardware design (refer to Figs. 2 and 3) that proved, through rigorous testing, the feasibility of employing spiral-wound bimetallic actuators as thermal sensors and prime movers for thermal control systems. Such devices are particularly suited to applications where low weight, low cost, and high reliability are required and where the consumption of electrical power is not permitted. Also, future growth is easily achieved by—

- (1) Increasing the size of the area to be controlled.
- (2) Minimizing the weight, size, and quantity of actuators.
- (3) Maximizing louver area.

ACKNOWLEDGMENT

The author acknowledges the contributions of Mr. David Nelson, of Aerospace Corporation, who is responsible for the original concept of employing bimetallic elements for the support and activation of lightweight louvers for spacecraft thermal control.

NOMENCLATURE

S	stress (psi)	m	specific deflection
A	angular deflection (deg)	t	thickness of element (in.)
K_{DC}	coil deflection constant	P	load or force (oz)
ΔT	temperature change (F°)	b	width of element (in.)
L	active length of element (in.)	r	radius to point of load application (in.)
		z	mean radius of outer turn of spiral

DISCUSSION

Member of the audience:

I notice the design that you have put forward here was only for use in cooling off the spacecraft, and therefore I assume that when the louver opened it didn't have the sun shining on the black surface.

Schilling:

No, these louver-actuator assemblies were designed to see either space or earth. They will never see the sun. There is a thermal fence running around the outside of the spacecraft which acts as a sun shield, and naturally shields the louvers, so they never do see the sun. The actuators are mounted on the far side of the baseplate and there are a lot of black boxes mounted on the inside of the spacecraft. So essentially there is a heat load, and the actuators just sense the baseplate temperature and open and close the louvers accordingly.

Member of the audience:

Would it be, do you think, feasible to reverse the motion of the heat sensors to actually heat up the spacecraft so that the colder it got, the wider the louver would open and then they could be put on the sun side of the spacecraft?

Schilling:

You could design something that would do that, if you wanted to design something that would take in the heat from the sun—just the opposite of the design presented, using the control in a different sense. However, just trying to maintain the temperature of the spacecraft, when it gets a little bit too

hot—when it is orbiting and it is on the side of the earth where the sun is, and the sun is shining on the hat structure—and the baseplate warms up and the louvers open up to dump heat. Then, when it goes around on the shadow side of the earth, away from the sun, the actuators sense the baseplate temperature and close the louvers up to keep the spacecraft from getting too cold. Certain critical components, like the battery, just can't take too wide a temperature variation, they won't work too well.

Gary Gordon:

Can you tell me what the resonant frequency is for the louver vibration?

Schilling:

Well, for the venetian-blind concept, the support bracket has a cross section 0.3 by 0.3 in. square along its length, and the actuator assembly, including the bracket, weighs about a tenth of a pound, so that can be viewed as a simple cantilever beam with its mass concentrated at the end. The natural frequency of that device in either of the lateral directions is around 99 Hz. I don't know what it is in thrust, I never calculated it. We weren't really concerned about thrust.

On the other device, if I can recall (I tested them some time ago); for the pedal concept, I believe, it was around 50 or 60 Hz. I think in most cases the spacecraft natural frequency was around 20 or 26 Hz. Most of the devices were built a little stiffer than they needed to be because a good conduction path was required; from the structural standpoint the bracket probably could have been made a little thinner.

THE APOLLO 11 LASER RANGING RETRO-REFLECTOR ARRAY

John E. McCullough
Arthur D. Little, Inc.
Cambridge, Massachusetts

The laser ranging retro-reflector now deployed at Tranquility Base consists of an array assembly housing 100 fused-silica retro-reflectors mounted on a pallet-aiming assembly resting on the lunar surface. The array assembly serves to hold, optically align, and thermally isolate the retro-reflectors to preserve optimum optical performance at all operating temperatures in the expected range from -300° F to $+250^{\circ}$ F.

I. INTRODUCTION

The Apollo 11 laser array panel, mounted on a pallet-aiming assembly, was deployed on the lunar surface at Tranquility Base on July 20, 1969, by Astronaut Neil Armstrong during the Apollo 11 lunar landing. On August 1, 1969, the reflector was acquired by detection apparatus located at Lick Observatory. Subsequent acquisitions by Lick and McDonald Observatories have established the earth-moon distance within ± 0.3 m.

This paper describes the mechanical design of the array assembly, the basic panel structure, and the manner in which the retro-reflectors are mounted.

II. DESIGN CRITERIA

The array is designed to meet the following mechanical and thermal requirements:

- (1) The array-mounted reflectors must be capable of withstanding a maximum acceleration level of 250 g without fracturing or generating debris that might contaminate the optical surfaces.
- (2) The individual reflectors must be mounted so that the maximum mechanical distortion during operation on the lunar surface does not exceed $0.5 \mu\text{in}$.
- (3) The mount must thermally isolate the retro-reflector from the array panel in order to minimize temperature gradients in the reflector and thereby ensure satisfactory optical performance. A permissible mount conductance must be of the same order as that for typical cryogenic insulating load supports for multilayer insulation systems.
- (4) The mounted reflectors will be subjected to temperatures from -300° F to $+250^{\circ}$ F during operation.
- (5) The axes normal to the front faces of the mounted reflectors must be parallel to within 2 deg.
- (6) The allowable radial thickness of the reflector mount is 0.095 in. (An increase in this thickness causes a twentyfold increase in the array panel width, which increases the array weight and lowers the natural frequency.)
- (7) The reflector mount must be appropriate for the reliable mounting of up to 100 retro-reflectors per array panel in a "clean room" environment.
- (8) The total weight of the array assembly, including the 100 retro-reflectors (each weighing 0.077 lb), must not exceed 34 lb.
- (9) The array must be fabricated of space-approved materials and, as a design goal, should have a 10-year life in the lunar environment.

III. ARRAY PANEL

The array panel was designed to accommodate 100 retro-reflectors, to be capable of withstanding the Apollo mechanical environment, and to be compatible with a method of retro-reflector mounting that would provide both thermal control and mechanical support. Very early in the program, it was decided that, on the basis of the thermal analyses, the retro-reflectors would be recessed in cavities whose heights were one-half the retro-reflector face diameter.

A design study showed that an array panel composed of orthogonal webs about 4 in. deep and spaced 3.5 in. apart would adequately support 100 retro-reflectors in groups of four between the webs (Fig. 1). In this design, a 0.05-in.-thick diaphragm is located at mid-height in the panel to provide the necessary lateral stiffness. The continuity of the orthogonal web structure from the front to back of the array panel provides maximum stiffness and minimum amplification of environmental mechanical inputs. The panel mounting brackets are bolted directly to the back edge of the web members at their intersections. The webs that connect the mounting bracket locations are thick for proper load distribution; additional local thickening provides the necessary mounting-pad surface. The bolts that secure the mounting brackets are high-strength shear bolts slide-fitted into the line-reamed bracket-panel boss hole to eliminate amplification of any mechanical input across the mounting bracket-array panel interface. To minimize the weight of the array, and also to avoid a reduction in its strength, the front face material is drilled out as much as possible; these holes are covered with thin aluminum plugs cemented in place.

The array panel was machined from a solid 6061-T6 aluminum block 4 in. thick and 18 in. square chosen for its homogeneity and uniform temper. Machining was chosen because it was much simpler to control than brazing, casting, or other fabrication procedures. The choice of material and alloy was based primarily upon availability, strength per unit weight, ease of machining, corrosion resistance, and ability to provide the correct thermal properties on the front (exposed) face. Magnesium was considered but discarded because of the

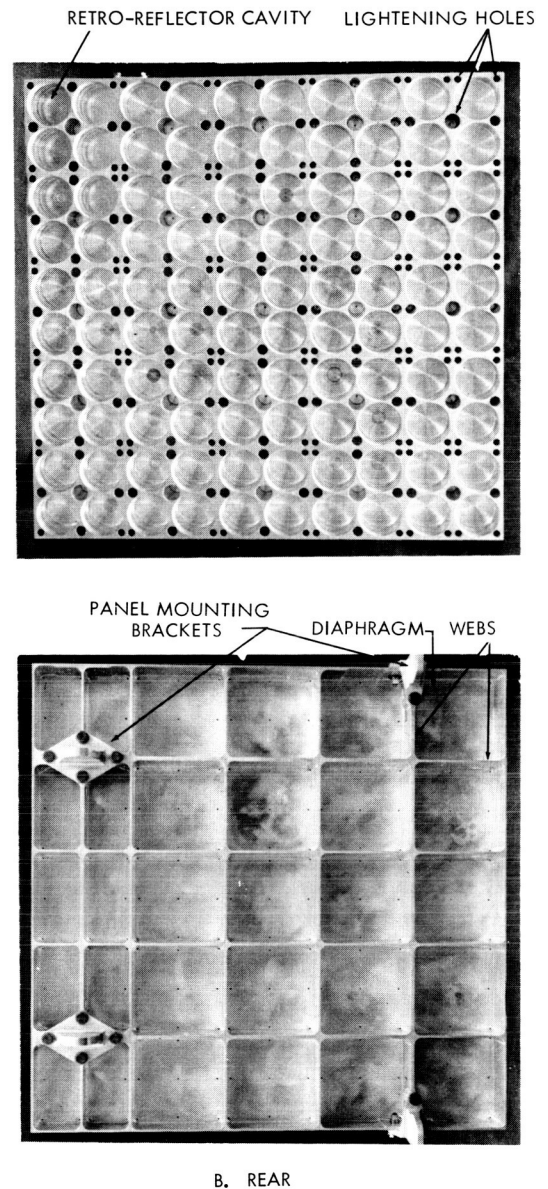


Fig. 1. Array panel structure

extensive processes required to achieve the proper thermal and optical properties and the possibility of deterioration of coatings under high humidity.

IV. RETRO-REFLECTOR MOUNTING

The design of the retro-reflector mounting provides for the overall array specifications, results of thermal analyses, and mechanical and space limitations associated with the panel configuration. The mount system had to be capable of sustaining cyclic loads of about 19.3 lb (the maximum acceleration multiplied by the mass of the retro-reflector). It had to be made of lightly loaded nonmetallic components (to minimize thermal conductance) that conformed precisely to the retro-reflector geometry (to minimize distortion) and accommodated the operating temperature range without distorting the retro-reflector. Furthermore, the mount had to be simple to design, fabricate, and assemble; possess a high spring constant (to make its natural frequency greater than the highest mechanical environment input frequency); and be compatible with the load distribution and cleanliness of precision optical elements. These design requirements appeared to be mutually exclusive because they required a mount with a stiff (high spring constant) high-load capacity which would be able to accommodate the relative shrinkage of the panel around the retro-reflector without any significant increase in contact pressure (low spring constant).

Because of the difficulty of satisfying all the requirements, several mount concepts were investigated before the final design, shown in Fig. 2, was chosen.

This design, which evolved from the analysis and testing of mechanical and thermal models, uses two Teflon mounting rings, one above and one below the tapered mounting tabs of the fused-silica retro-reflector. The lower ring has an indexing tab on its top face that fits against one of the back retro-reflector faces so that it can be used to angularly position the retro-reflector. This ring is indexed in the array panel by a slot that fits over a pin in the mounting cavity shoulder.

The retro-reflector and mounting rings are held in the array panel structure by a threaded aluminum retainer

ring. Each retainer ring has a finite axial clearance of about 0.002 to 0.003 in. to minimize thermal conductance to the retro-reflector from the surrounding hardware. This clearance allows a finite movement of the retro-reflector; however, since the retro-reflector is touched by Teflon surfaces only, no damage occurs.

The axial length of the Teflon mounting rings is such that, as the ambient temperature changes, the differential thermal expansions (radial as well as axial) between the retro-reflector, the mounting rings, and the panel are complementary; thus, they do not result in large changes in the retro-reflector mount clearance. This temperature-compensating ability of the mount depends upon the very high coefficient of expansion of Teflon (five times that of aluminum) and the taper of the retro-reflector mounting tabs. During a low-temperature excursion, the aluminum panel and the Teflon mounting rings contract while the fused-silica retro-reflector does not (near zero coefficient of expansion). As the bore of the mount contracts, it moves the Teflon rings radially inward, where they have to accommodate a greater tab thickness (because of the taper) and a reduced axial length (the panel would contract axially as well as radially). The axial length is so selected that the high thermal axial contraction of the Teflon mounting rings exactly matches the new hardware configuration. The proper axial length is easily computed once the coefficients of expansion of all the mount materials, their dimensions, and the included angle of the retro-reflector tab are known.

Teflon was selected for the mounting rings because of its favorable combination of properties; i.e., high coefficient of expansion, inertness to lunar environment, low coefficient of friction, and ability to creep and conform to the retro-reflector mounting tab surfaces.

V. ARRAY-PALLET INTERFACE

The array assembly is secured to the pallet-aiming assembly at the four mounting bracket locations. The array brackets terminate in tangs that fit into clevises on the pallet mounting posts and are secured with close-fitting pins. To guarantee proper fit, a pallet simulator and an array simulator were constructed to simulate the

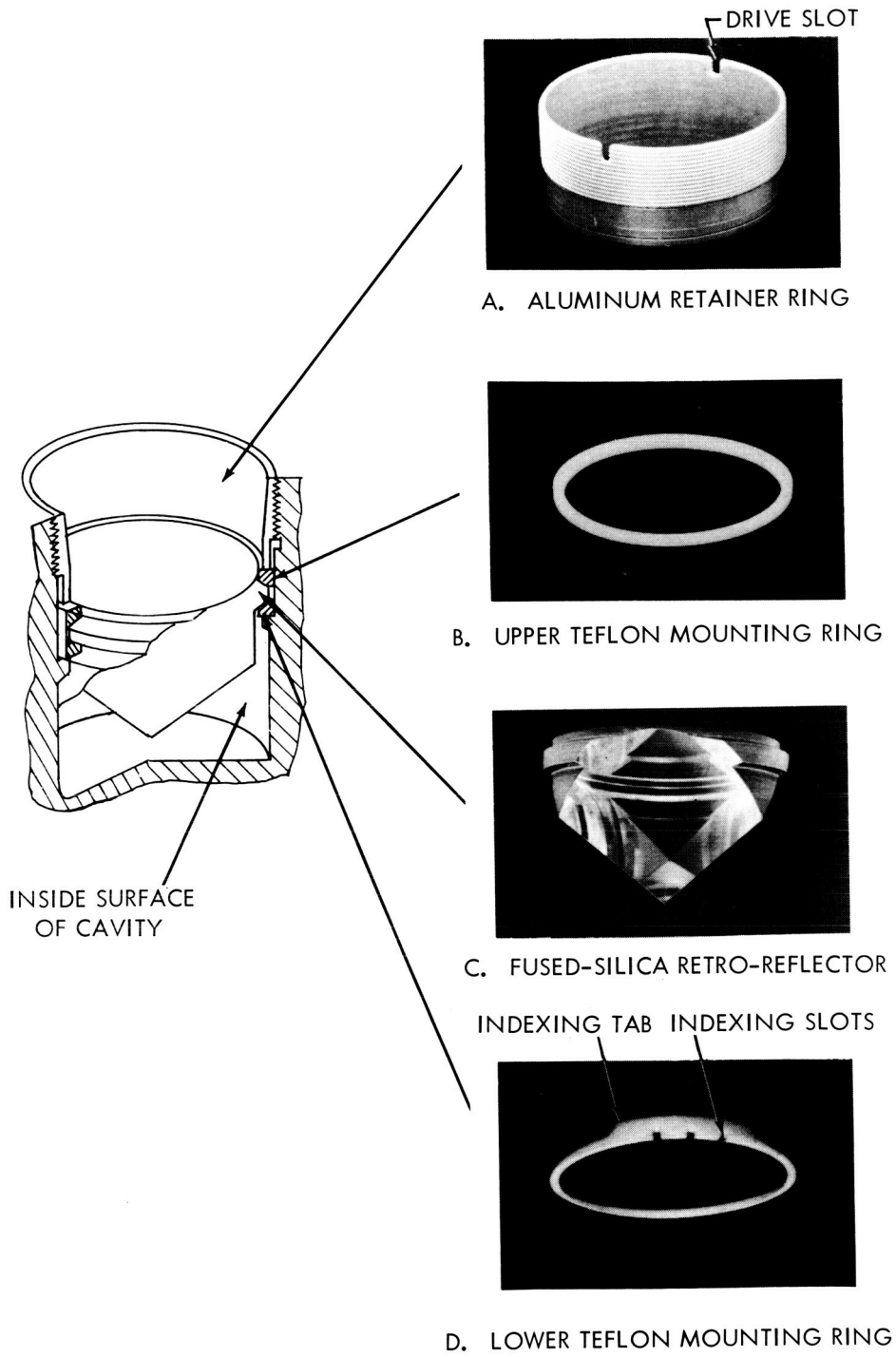


Fig. 2. Retro-reflector mounting

hardware on both sides of this interface. In both cases the simulators were combination inspection-machining fixtures.

VI. CONCLUSION

The retro-reflector mounting concept described is a simple, rugged way to mount precise optical reflectors. This mounting technique survives extreme mechanical environment factors, eliminates mechanical distortion of

the element due to clamping forces and differential thermal contraction, and minimizes thermal gradients within the element that would compromise optical performance. The retro-reflectors were manufactured to an optical precision better than 90 percent of diffraction-limited performance.

Optical alignment tests of the array panel at $+250^{\circ}$ F and -250° F demonstrated uniformity of direction-pointing of the individual reflectors within 0.3 deg.

ACKNOWLEDGMENT

The Laser Ranging Retro-Reflector experiment was conceived in 1965 by an investigator group of scientists from several institutions and headed by Professor C. O. Alley of the University of Maryland. In 1967, NASA approved the experiment for the Apollo program and provided all funding.

The array assembly was produced in conjunction with the Bendix Aerospace Systems Division, which provided the pallet-aiming mechanism and had responsibility for the integration of the experiment with the flight equipment, and the Perkin-Elmer Corporation, which produced the diffraction-limited retro-reflectors.

DISCUSSION

Ed Devine:

What tolerance did the individual reflectors have to be aligned to?

McCullough:

Well, I think the tolerance (when all of the reflectors were mounted in the panel and the pointing direction determined for each one) for an envelope drawn around the individual normals could not be any greater than about plus or minus two degrees about the average normal. Actually, the flight array tested out much better than that. I think 0.2 deg was the kind of spread we were noticing from the average normal of all retro reflectors.

Gerald Perkins:

You mentioned ten-year space life. What are the expected results of using Teflon?

McCullough:

Well, we looked into that and Teflon appeared to be one of the best materials we could select from an out-gassing point of view; and the location relative to the retro-reflector, was judged to pose no serious problems. The amount of out-gassing over that period of time, I think, would be negligibly small.

Member of the audience:

The data that they are getting back, can you describe some of this, especially the wobble data that you mentioned?

McCullough:

I don't know that they have enough data to start making any real statements. I know they are getting back information relatively reliably and they plan to watch this over some years and try to interpret it. I think at this point in time they really have established the feasibility of the concept and have been able to set up this equipment and get it to operate reliably, get signals back reliably but have not really launched into a program of getting really hard core data yet.

Member of the audience:

Who made the reflectors and what was the assembly tolerance?

McCullough:

For these retro reflectors, I think the material itself came from Heraeus-Schott in Germany, were purchased in a cube, about two inches on the side, which was split diagonally and yielded two retro reflectors. The fabrication procedure consisted of shaving off the three 90 degree faces on the back, shaving off the front face and then edging around the periphery. All of the surfaces, I think, were made flat to something better than 0.1 wavelength, very precise optical elements. These were made by Perkin-Elmer Corporation. I think that Boxtton-Beels also made some of them as well as others.

DEVELOPMENT OF PAYLOAD SUBSYSTEM-PRIMATE MISSION-BIOSATELLITE PROGRAM*

James F. Hall, Jr.
Re-entry and Environmental Systems Division
General Electric Company
Philadelphia, Pennsylvania

This paper describes and discusses the design and operation of the GE-RESD primate life-support subsystem for NASA-ARC's Biosatellite program as used during the flight of Biosatellite 3. It also describes preflight changes necessitated by the primate's (a *Macaca nemestrina* monkey) influence on the initial equipment designs.

I. INTRODUCTION

NASA-ARC's Biosatellite program required hardware for sustaining a *Macaca nemestrina* monkey during a 30-day earth orbital spaceflight. The functions required to be supplied by the experiment payload subsystem are the following:

- (1) Provide sustenance—food and water.
- (2) Provide selected waste management—feces, ammonia, carbon monoxide, and other trace gases.
- (3) Provide cyclic, day and night lighting (circadian rhythm reference).
- (4) Take single-frame and motion pictures of the primate during day and night periods and all mission phases.
- (5) Provide structural support for the restrained primate, blood pressure experiment equipment, and physiological sensor-signal conditioners through all mission phases.
- (6) Provide control for the regulation of the previous functions in accordance with preprogrammed experiment events.

The subsystem development was complicated by the unanticipated extent of the monkey's inquisitiveness, manual dexterity, tenacity, and ingenuity when left alone with complex equipment for long periods of time. Some of the feats these monkeys accomplished would have made Houdini proud.

II. POTENTIAL SOLUTIONS

Many of the functional requirements could have been satisfied through the use of various devices that performed the same function. However, since the development schedule was short, consideration of off-the-shelf hardware where possible was necessary and considerably limited the possibilities. Even so, many tradeoffs were required. Examples of two of the more basic ones are discussed in the following:

- (1) Provide Sustenance—Here the choice was between liquid and solid food. Water could either be mixed with the food, stored, or obtained from the power system (fuel-cell byproduct water).
- (2) Provide Lighting—Basically, the choice was between fluorescent or incandescent sources. More subtly, tradeoffs among multiple lamps, panel lights, direct lighting, spot lighting, voltage variation, special-purpose lamps, and/or lamp switching had to be made to result in a proper lighting arrangement.

*This paper is based on NASA CR-73424 prepared for Ames Research Center under NASA Contract NAS2-1900.

III. DISCUSSION

A. Subsystem Definition

Tradeoffs and subsequent design and development resulted in the Biosatellite Primate Experiment Payload Subsystem consisting of the following primate support equipment (PSE), supplied by GE-RESD:

- (1) Pellet feeder assembly.
- (2) Water dispenser assembly.
- (3) Feces collector assembly.
- (4) Trace gas contaminant control assembly.
- (5) Camera assembly.
- (6) Lighting assembly.
- (7) Camera/lighting controller.
- (8) Primate life-support controller.
- (9) Couch assembly.

The subsystem is a collection of assemblies unified in operation by the monkey and in function by the life-support controller (Fig. 1).

B. Equipment Details

The following paragraphs describe in more detail the features of the subsystem equipment and, in some areas, the degree of primate-induced configuration and function definition.

1. Food Dispenser (Pellet Feeder) Assembly. As previously mentioned, solid versus liquid food tradeoffs were made. Various factors, including equipment availability, led to the selection of a solid-food pellet dispenser. The pellets were attached to a nontoxic adhesive tape, much like the old candy buttons on waxed paper. To provide redundancy and minimize packaging volume, eight pellet-reel assemblies were provided (see Fig. 2). The assembly was basically mechanical rather than electronic. Although arm, lock, and unlock functions were solenoid initiated, pellet counting was switch indicated, and monkey cueing was via incandescent lamps; all other functions were mechan-

ically accomplished through the use of primate power. An electrical signal armed the feeder and lit the cue light. The monkey responded to the light by pushing the handle. The handle shaft drove a geneva and tape sprocket. These in turn indexed to the next reel and pulled the pellet and tape from the supply reel. The tape passed on to a take-up reel, while the pellet was stripped off and projected through the pellet slot. As the pellet moved into the slot, it raised a gate and tripped a switch. This was counted and registered in the life-support controller for later monitor from the ground via telemetry. The monkey managed to impart his influence on the design of the pellet dispenser through two primary factors. First, his physiological limitations imposed a limit on the amount of force required to operate the machine. Second, he caused, through his persistent tampering, what came to be known as the two-for-one problem. After many higher primates, the author included, deemed the design complete, it was turned over to the monkey. He very quickly learned that by judiciously working the handle after receiving one pellet he could get a second before the mechanism disarmed. This and several other problems led to the redesign of the machine.

A relatively equal blend of mechanical and electrical design disciplines were used to solve the feeder problems. The solenoids were removed, and their functions were performed by a single motor and mechanism. The motor also provided the force required to dispense the pellet, and the monkey's involvement was reduced to tripping a switch with the feeder handle actuation. All other features, including the mechanical and electrical interfaces to the system were identical. As a fringe benefit, the feeder could be ground initiated to dispense a pellet independent of the monkey. This feature was useful several times during the actual flight of Biosatellite 3.

2. Water Dispenser Assembly. Treated fuel-cell byproduct water was selected as a drinking water supply to minimize system weight and storage volume requirements.

The primate's influence on the design is indicated in Fig. 1. The initial design had one solenoid to shut off the supply. The primates learned that the noise of the supply solenoid signified water flow into the water dispenser. They became very proficient at cueing to the solenoid click, obtaining more water than was intended and thereby destroying the water measurement accu-

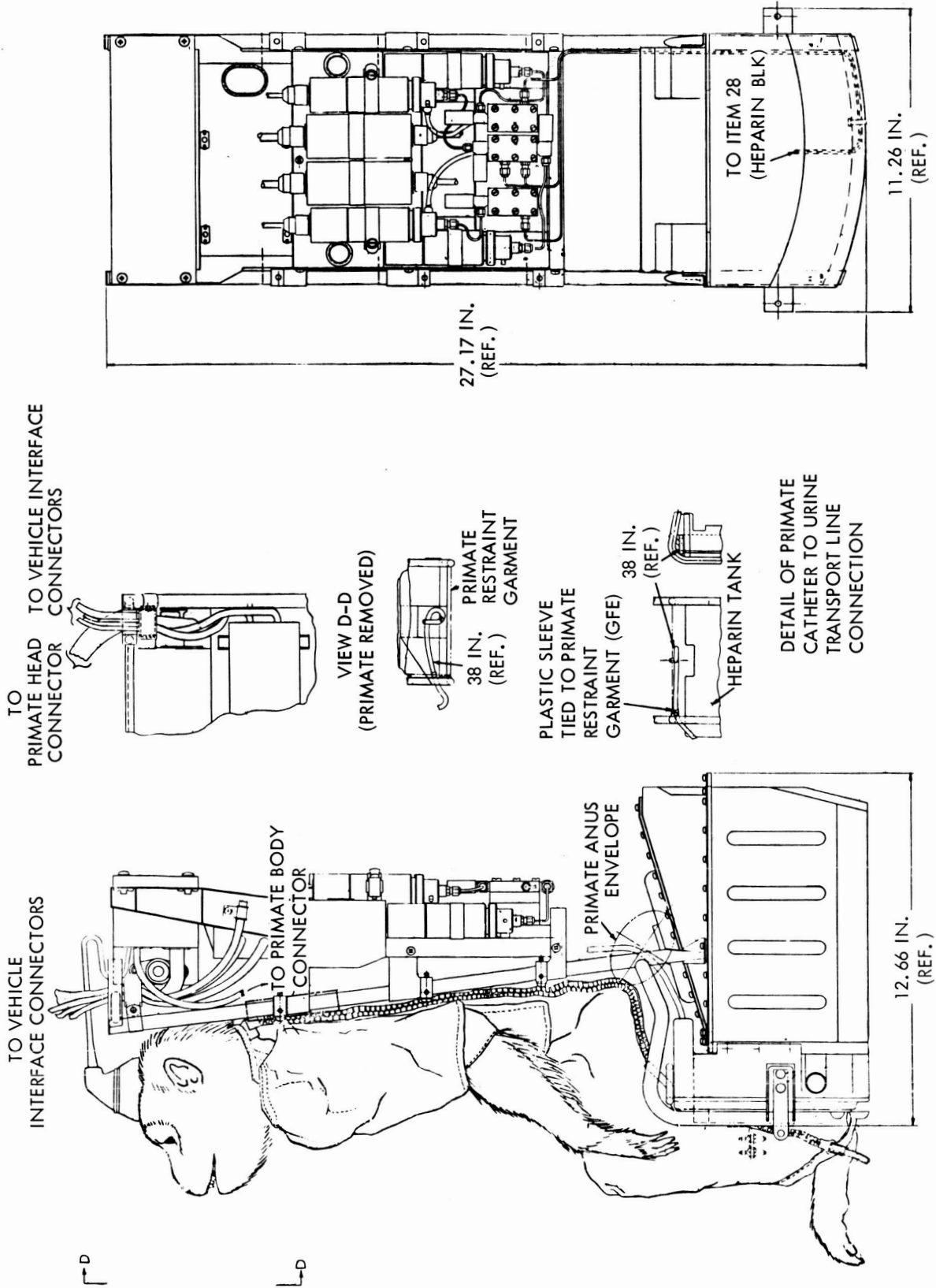


Fig. 3. Primate couch assembly

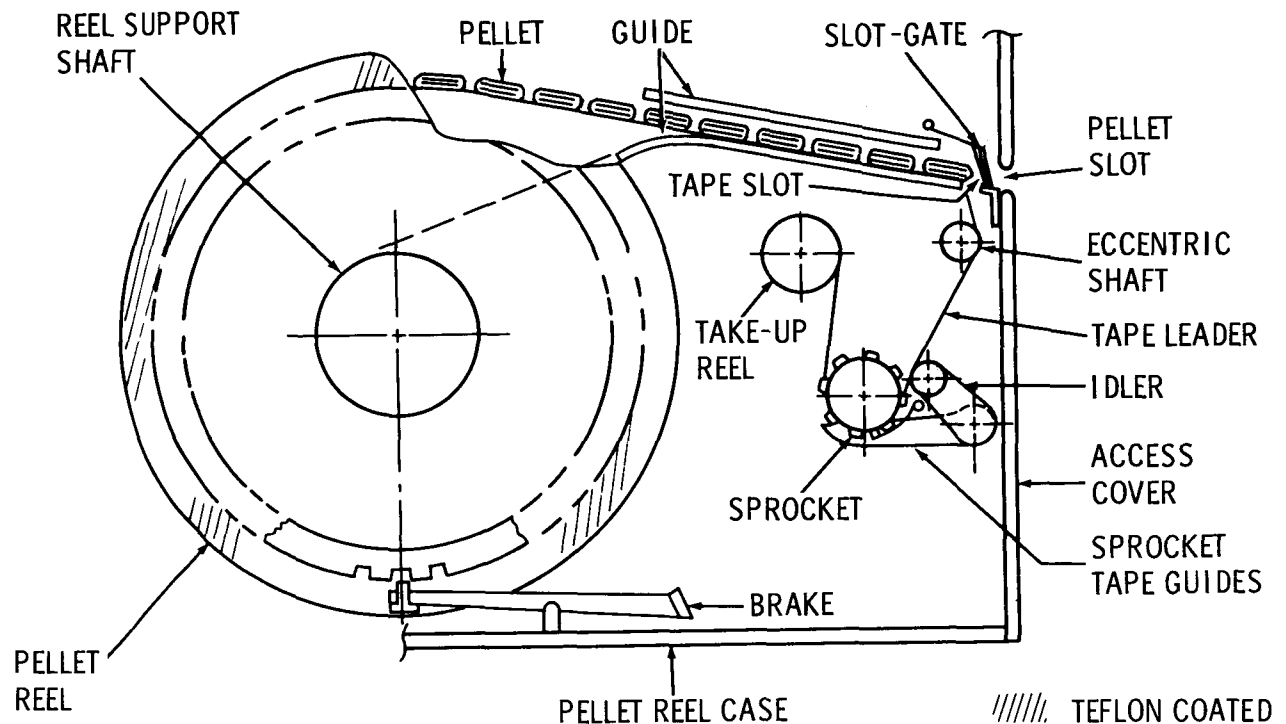


Fig. 2. Cross section of pellet feeder

racy. As a result, a nipple solenoid and related electronics were added to close the nipple solenoid before opening the supply solenoid and to keep the nipple closed until the supply solenoid had reclosed. The monkey then obtained water by sucking on the nipple which actuated the pressure demand regulator, which allowed water to flow and caused the flexible Bellofram to collapse.

A traveling contact, and associated fixed contacts and electronics, in conjunction with the life-support controller and GFE programmer initiated the fill cycle. The water dispenser was monitored by the life-support controller, which registered the water quantity for later presentation to the ground via telemetry.

3. Feces Collector and Couch Assembly. Of all the subsystem equipment, the feces collector and couch assemblies were most sensitive to the range of *Macaca nemestrina* physiological features. Since the couch had to support the restrained monkey, monkey body dimension ranges, including urine and feces envelope interfaces, were required. A limited quantity of this type of monkey was available, and of these, only a few were of the required age and weight. However, a body-measure-

ment matrix was defined, and a NASA-Ames Research Center and GE-RESD team obtained the necessary information.

In addition to the restrained primate, as shown in Fig. 3, the couch supported the University of Southern California blood pressure experiment heparin supply, pumps, transducers, and signal conditioners. It also provided support for the University of California at Los Angeles physiological sensor-signal conditioner. And last, but not least, the couch supported the feces collector. The collector provided the container for the heparin bags and support for the urine catheter line in addition to its primary function of feces collection.

The feces collector performed its function well when presented with formed stools through the use of a 1 ft³/min airflow provided by the spacecraft's gas management assembly (GMA) (Fig. 1). The airflow provided the force to move the feces into the can, prevent odor leakage (suction side of fan), and dried the feces for storage and analysis upon recovery. The air was passed through a selective gas/liquid separator membrane and a bacteria filter.

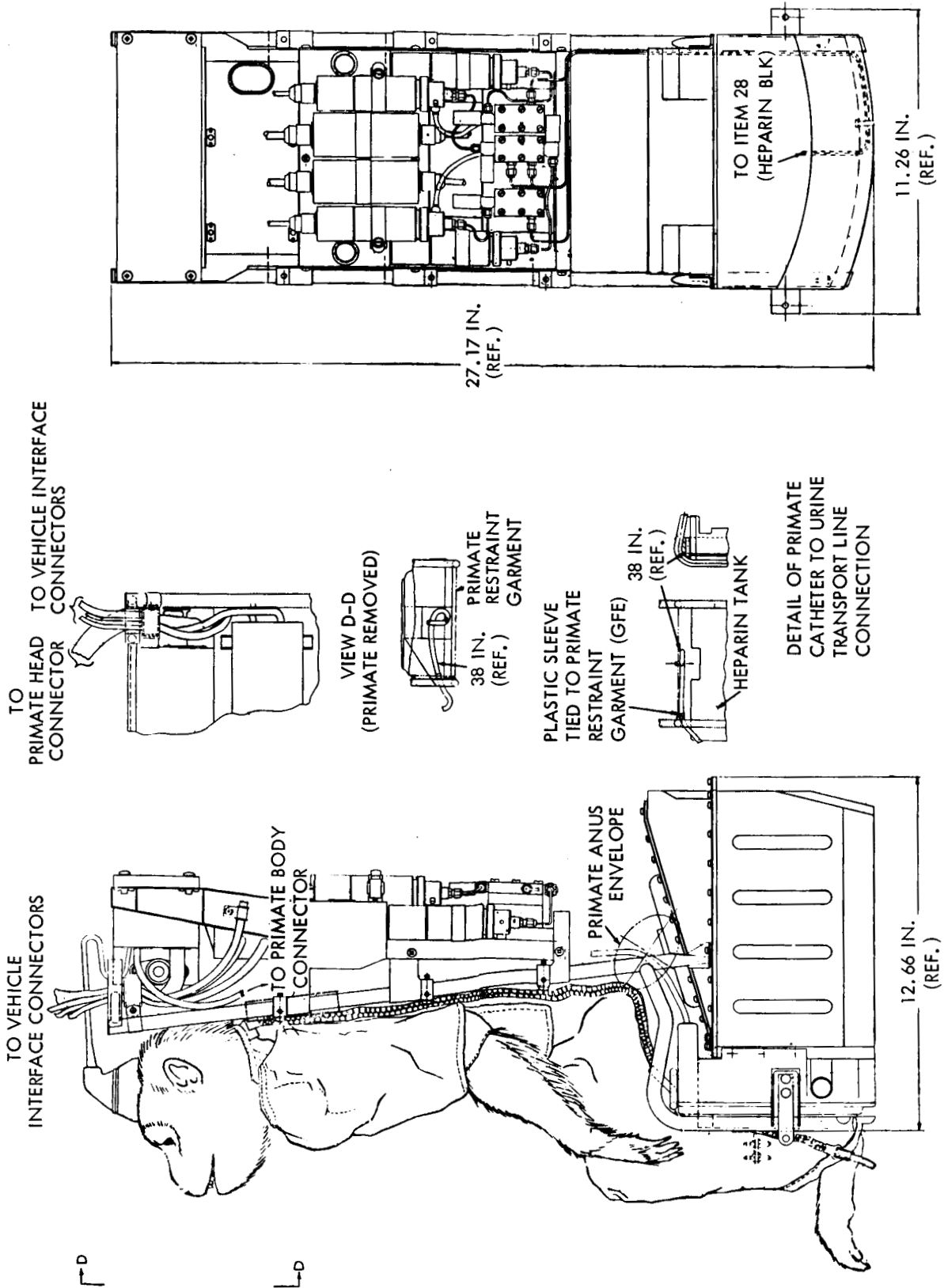


Fig. 3. Primate couch assembly

4. Trace Gas Contaminant Control Canister. As was the case with the feces collector, the trace gas contaminant control canister was located on the suction side of the GMA. Flow was set at approximately $100 \text{ cm}^3/\text{min}$ to keep the ammonia (NH_3) and carbon monoxide (CO) levels within specification limits. Amberlyst was used for NH_3 absorption and hopcalite was used to oxidize CO to CO_2 . The CO_2 was then passed to the GMA for absorption in the LiOH (Figs. 1 and 4).

5. Lighting and Camera Assemblies and Camera/Lighting Controller. Incandescent lamps were selected over fluorescent lamps primarily because of the concern early in the program over noise effects on the primate head sensors. (The lights were in the vicinity of the primate's head.) The light assembly had to perform two functions: first, provide a circadian rhythm reference for the monkey and, second, provide enough light for day and night photos.

The primate's influence on this design was found in the color of the light. It was determined that a 30-to-1, day-to-night, light-intensity (foot candles) change was required to ensure a proper day-to-night reference for the monkey. A rather clever solution to this requirement was provided by taking advantage of the difference between the monkey's eye and the film in response to light wavelengths. Since the monkey was less sensitive than the film to the red light region, a red filter was added to the night light. This provided greater than 30-to-1 (theoretically greater than 100-to-1) day-to-night light illumination ratios while providing enough light for high-resolution photos at both day and night light levels and at one camera lens setting.

Two light housings were used, one for day and one for night lighting. Each light housing contained two bulbs, a primary bulb and a redundant bulb. Only one bulb was lit at any given time. Fiber optic bundles were

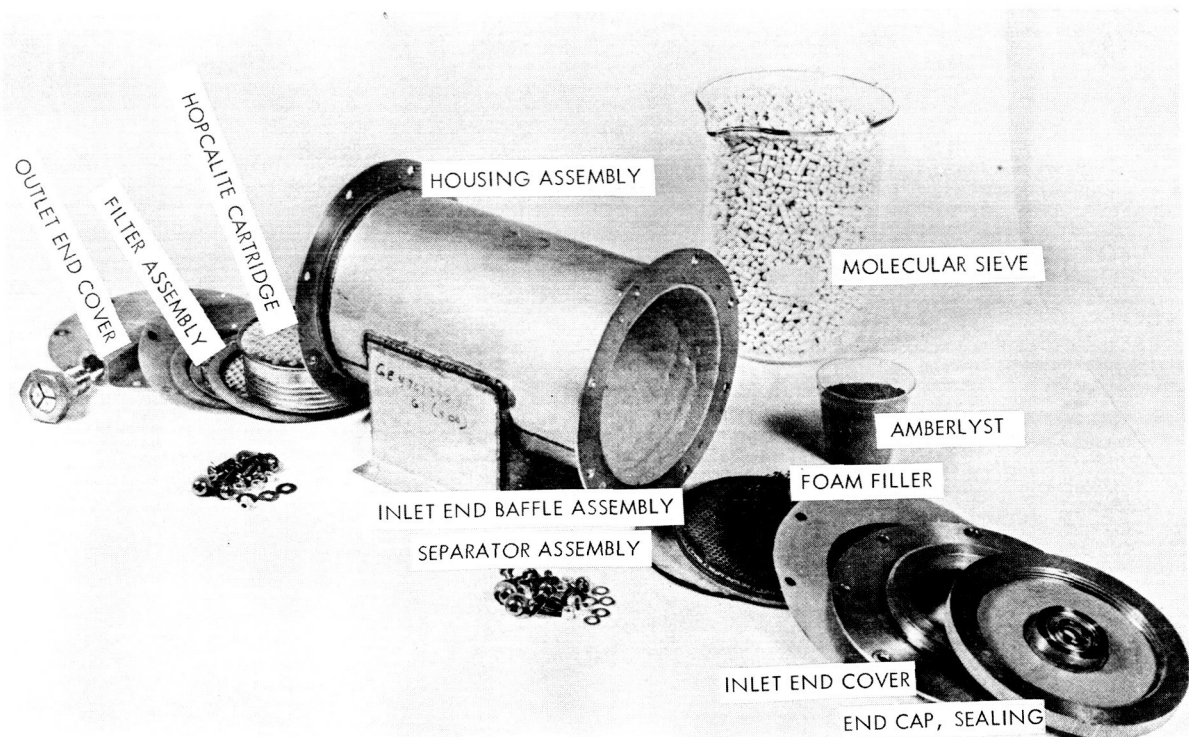


Fig. 4. Trace gas contaminant control canister

routed from the light assembly to a NASA/ARC-furnished calendar clock. This clock provided the day, hour, minute, and second record on the film.

A flight-qualified pulse camera was used to take 16-mm single-frame or motion (4 frames per second) pictures during all mission phases as preprogrammed or ground-commanded. Thin-base, high-speed, black-and-white film was used.

Both the light and camera sequences were controlled by the camera/lighting controller in conjunction with the life-support controller and government-furnished programmer.

6. Life-Support Controller. As identified in the preceding sections, the life-support controller unifies the functions of the subsystem. The significant feature in its development was the compilation of many individual component controller and monitor functions into one component with the resulting size, weight, complexity, interfacing, and cost reductions.

ACKNOWLEDGMENT

Special thanks are given to Mr. Charles Wilson, Biosatellite Project Manager, NASA-ARC, for the consideration he has given to this paper.

DISCUSSION

Member of the audience:

Would you describe a little bit the method for the blood pressure measurements that you did?

Hall:

That was part of the PSE. Very basically it involved the catheterization of the arteries and veins, which came through a standard hydraulic pressure transducer, through a signal conditioner and so on. It was a catheterization process.

Member of the audience:

The data from this took several days and the film must be

IV. CONCLUSION

It was recognized from past experience that the design of equipment that had a substantial man/machine interface was more difficult than the design of nonman-related equipment. This is due to the large variations in physiology from one person to another and the range of subjective reaction to the same stimulus, that is, the psychological variation of individuals. One is faced with an even greater challenge when these facts are coupled with the need to design for a monkey who is expending every ounce of his ingenuity in tampering with the equipment without concern for the various possible results on his own safety and/or well being and who is unable to provide routine support tasks or troubleshooting and repair.

The experiment payload subsystem operated through the system performance tests and flight mission profile without failure or serious incident. In fact, many of the assemblies exceeded their requirements by continuing to perform to specifications following re-entry and water impact.

available also. Where is this, and the results? Are they available now for use on future machines? I believe this is a case where the passenger didn't survive too long, but are the results available for future flights?

Hall:

Yes, and you would have to get them through NASA, Ames Research Center in Palo Alto, California. The head experimenter on this program is Dr. Ross Adey of UCLA. So it is a combined responsibility. In fact, I think the contract is written so that Dr. Adey owns the data, and he decides who sees it. Sometimes he doesn't let everyone see it; so you might have to contact him.

THE MARINER MARS 1971 GIMBAL ACTUATOR*

G. S. Perkins
Jet Propulsion Laboratory
California Institute of Technology
Pasadena, California

The actuator that will point the gimballed engine, thus performing the autopilot actuation function for the Mariner Mars 1971 spacecraft, is described. The gimballed engine has two axes of freedom, providing two-axis control to the spacecraft. Motion for the two axes is provided by identical and interchangeable actuators—gearless electro-mechanical linear servomechanisms. Each actuator is designed to have a long service life in the space environment (more than 50,000 hours continuous operation) and to be able to function at speeds ranging from hours per cycle to cycles per second.

I. INTRODUCTION

The Mariner Mars 1971 spacecraft (Fig. 1) is controlled in its midcourse maneuver and later into orbit about Mars by an autopilot system using a 300-lb-ft gimballed bipropellant rocket engine powered by hypergolic fuels. Orientation about the two axes of the gimballed engine is controlled by an electromechanical linear actuator (Fig. 2) capable of pointing the engine ± 9 deg about each axis. (The third axis control is provided by the attitude control system's cold-gas reaction jets on the ends of the solar panels; these jets exert millipound force.) Two gimballed actuators are required, one for each axis. Since the functional requirements for the actuators are identical, it was possible to design one actuator to be interchangeable on either axis.

The actuator was designed at the Jet Propulsion Laboratory (JPL), and the first prototype model was fabricated by the JPL model shop. Parts for the Mariner 1971 spacecraft actuators were provided by 15 companies under 18 fixed-price purchase orders. All actuator testing was performed in the JPL test laboratories. In operating tests, the actuator performance exceeded all specified performance requirements by generous margins. The simplicity of the actuator design has made it possible to manufacture the actuator for a cost of the

order of 1/10 the cost of typical actuators designed for a similar application.

This report presents the design requirements, describes the actuator's construction, and gives the results of performance, life, and environmental testing.

II. DESIGN REQUIREMENTS

The actuator is designed to meet the following performance requirements:

- (1) Motor voltage—from 0 to 30 V dc.
- (2) Motor current—limited to 1.75 A.
- (3) Stroke, fully retracted to fully extended— 0.785 ± 0.030 in.
- (4) Rate versus load—as illustrated in Fig. 3.
- (5) Backlash (total), including effects of mounting—limited to 0.004 in. of stroke under a load of at least 5 lb.
- (6) Null position—within 0.002 in. of actuator's center stroke.
- (7) Response time—less than 0.100 seconds.
- (8) Operating life—50,000 hours (continuous).

* This paper presents the results of one phase of research carried out at the Jet Propulsion Laboratory, California Institute of Technology, under NASA Contract NAS7-100.

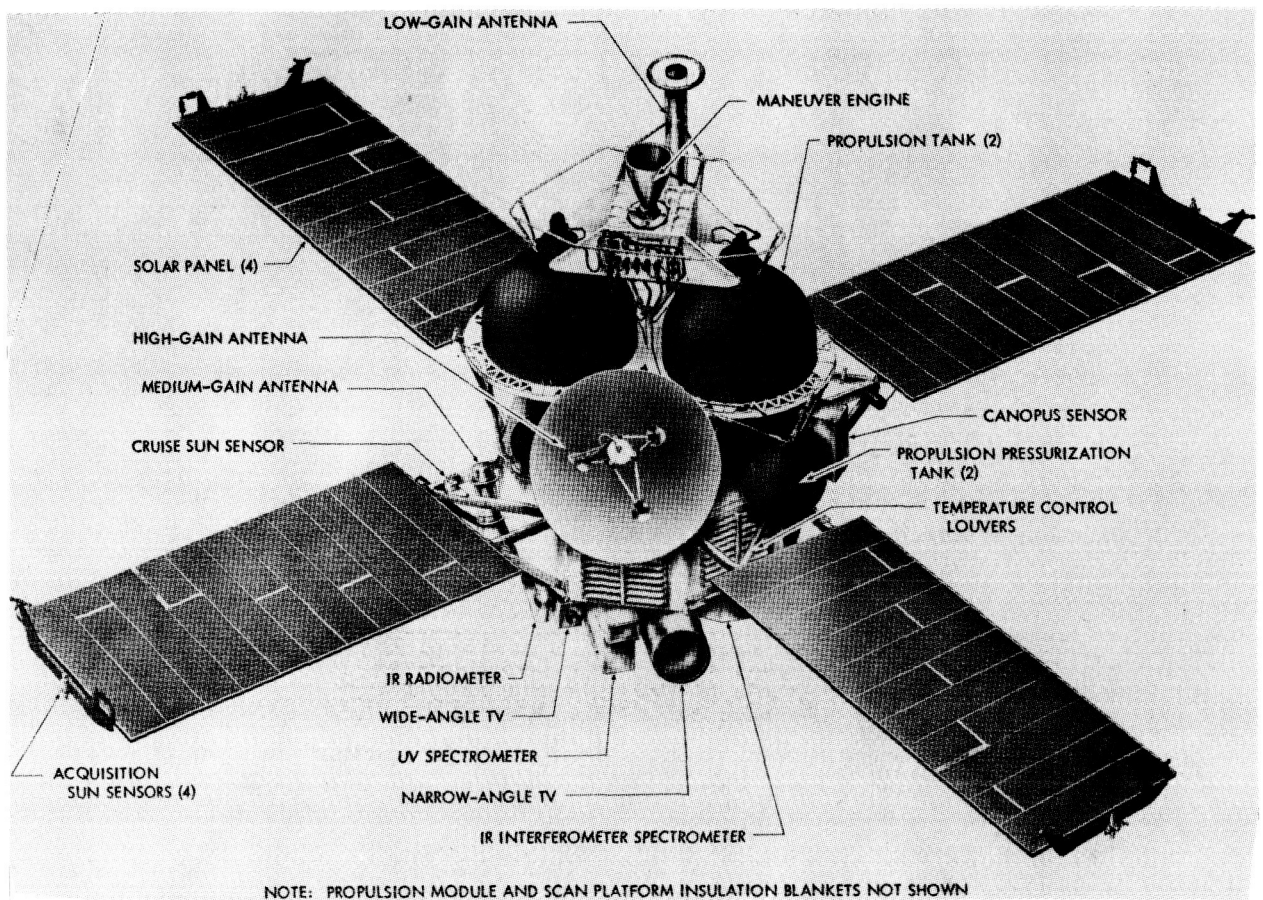


Fig. 1. Mariner Mars 1971 spacecraft (top view)

The long life of the actuator is provided by the elimination of gears, which is made possible by the ball screw assembly (described below) and which reduces the velocity of the motor with respect to the velocity of the load. The motor is designed to have a limiting top speed of 700 rpm, a speed that will drive the actuator at a rate of 1.2 in./s under no-load conditions. The actuator characteristic is linear from no-load to stall, and the current demand is also linear under the same conditions, ranging from the minimum value required for no-load operation to the maximum of 1.5 A.

III. DESCRIPTION

The gimbal actuators provide a controlled linear motion to point the gimballed engine in response to the command of the autopilot system. The actuator is a very simple device (see Fig. 2), consisting of only three major parts contained in a pressurized, O-ring-sealed housing.

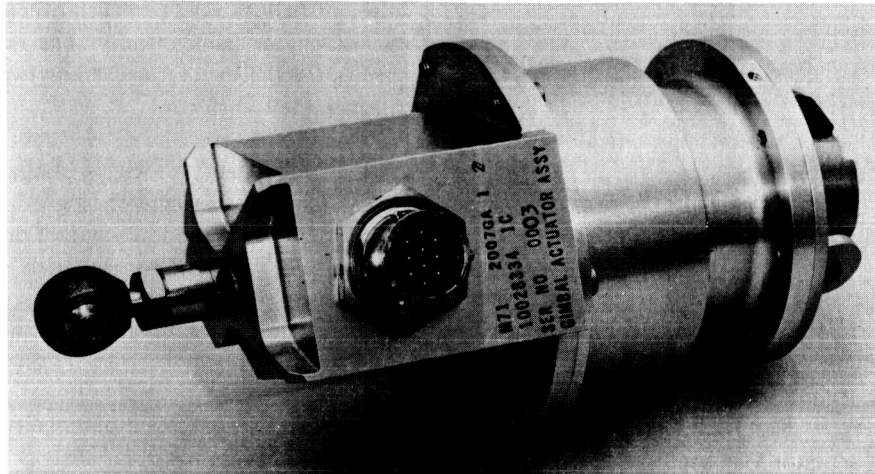
The three parts are—

- (1) A linear motion transducer.
- (2) A recirculating ball lead screw assembly.
- (3) A direct-current drive motor.

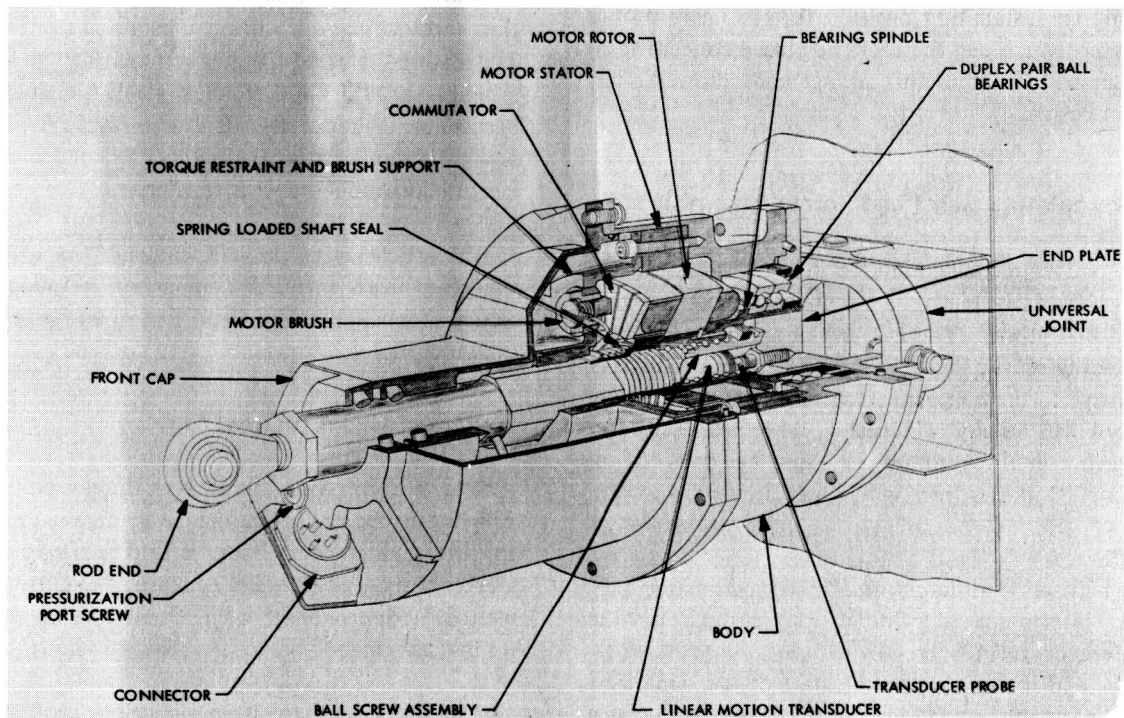
These parts and the housing are described below.

A. Linear Motion Transducer

The linear motion transducer is a linear variable differential transformer excited by sine waves at 6000 Hz at 17 V rms. The demodulated transducer readout is 3.2 V(dc)/in. of linear movement. Average power required for the transducer readout is only 0.2 W. A unique feature of the recirculating ball lead screw assembly is that the shaft of the assembly is bored out,



(a) ASSEMBLED ACTUATOR



(b) CUTAWAY VIEW

Fig. 2. Mariner Mars 1971 gimbal actuator assembly

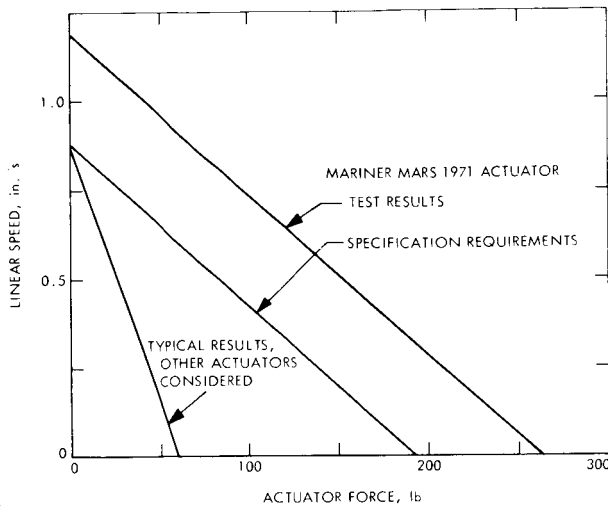


Fig. 3. Gimbal actuator load-speed performance

providing an installation position for the linear motion transducer, which can therefore be placed concentrically in the gimbal actuator. This arrangement allowed a very compact design.

B. Recirculating Ball Lead Screw Assembly

The ball screw assembly consists of a screw and mating nut, each having a specially formed concave helicoid ball groove. The nut, perfectly mated over the screw, contains the balls filling one or more circuits, which serve as the engagement medium between the nut and screw. In the gimbal actuator, three ball circuits are used, each containing about 35 balls. The pitch of the screw is 1/10 in. per turn, with a ball circuit diameter of 5/8 in.

The ball screw assembly uses 1/16-in.-diameter balls. Transfer inserts spaced symmetrically around the nut circumference form a crossover path guiding the balls from the end of the turn to the start of the same turn. This arrangement provides a continuous recirculation or closed circuit of balls, which prevents the balls in a particular circuit from entering any other race within the nut. The use of internal transfer inserts is one of the unique features of this ball screw assembly. Because the inserts eliminate external projection, the ball-nut assembly is ideally suited to be assembled inside the bearing spindle, which also supports the motor armature.

Because each circuit is only one complete turn of balls, the number of balls being recirculated is limited, therefore reducing the effect of friction produced by adjacent balls skidding on each other and eliminating the use of spacer balls entirely. The rotation of the shaft pushes the balls (never exceeding two or three at a time) through the transfer.

The ball track, which is similar to a ball-bearing groove, has a ball-diameter to groove-radius conformity of 56 percent. The initial contact angle is set up within 35 deg to 45 deg. The contact angle change under load is not drastic; therefore, it permits higher loads to be carried without fear of the contact ellipse's overlapping the shaft radius.

The load-carrying static capacity of the ball screw assembly in the gimbal actuator is 550 lb/circuit. With three circuits, this provides a static capacity of 1650 lb. The mechanical efficiency of the ball lead screw assembly is 94 percent. Under ideal conditions of configuration and loading, this value can be a point or two higher. The material selected for the recirculating ball lead screw assembly is AISI 440C stainless steel. A high-chromium, hardenable stainless steel, it attains higher hardness than any other stainless steel. In the hardened condition, it has full corrosion and wear resistance.

The efficiency of the ball lead screw is a function of the screw lead angle. A comparison between the efficiency of a ball lead screw and that of an Acme screw¹ is shown in Fig. 4.

C. Direct Current Drive Motor

The motor in the actuator is of the reversible dc type, which was chosen in preference to an ac type because, for the same power input, it is possible to develop a greater torque in a smaller package. The current requirement is in approximately linear relationship to the load on the actuator.

The actuator motor is an eight-pole configuration. A permanent-magnet stator is placed outside, around the armature. The commutator is placed axially, and the armature is wound with a 20-ohm resistance. The motor

¹Phelan, R. M., "Fundamentals of Mechanical Design," 2nd. ed. New York: McGraw-Hill Book Co., Inc., 1962, p. 195.

has a top speed of 700 rpm with a linear torque speed characteristic to a stall torque of 70 oz-in.

The relationship between motor torque and the actuator linear force is shown by the following equation:

$$T = \frac{LP}{2\pi\eta}$$

where

- T = motor torque
- L = actuator linear force
- P = thread lead of ball screw assembly
- η = efficiency of ball screw assembly

The motor current demand is linear from a minimum value required for no-load operation to a maximum value of 1.5 A at stall. The actuator has a 0.015-s time constant, which can be attributed to the configuration of the drive motor with its unusually large-diameter air gap.

D. Actuator Housing

The actuator housing is in three parts: the front cap, the actuator body, and the end cap at the base that supports the gimbal required for two-axis freedom of actuator mounting. The actuator is sealed by five O-rings: three in static-seal configuration with one at the end position, one sealing the body to the front cap, and one under the connector plug, and two carefully selected O-rings providing the dynamic seal around the output shaft.

The actuator is filled with a mixture by volume of 90 percent nitrogen and 10 percent helium at 5 psig; the allowable leak rate is in the molecular flow regime. The helium in the gas mixture inside the actuator provides a helium trace that enables the use of a mass spectrometer leak detector to measure the leak rate. This helium leak rate is modified by a conversion constant to obtain the mixture leak rate. For the gimbal actuator, this mixture leak rate is specified to be 0.07 standard cm³/h. The pressure decay caused by this leak rate is, of course, exponential. Figure 5 shows the pressure inside the actuator as a function of time in the deep-space environment, at the maximum allowable leak rate. The

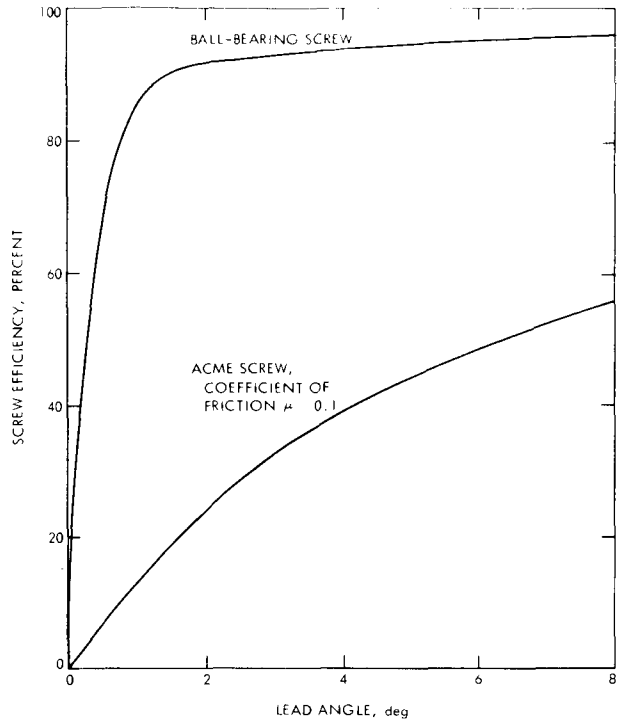


Fig. 4. Comparison of ball lead screw and Acme screw efficiency

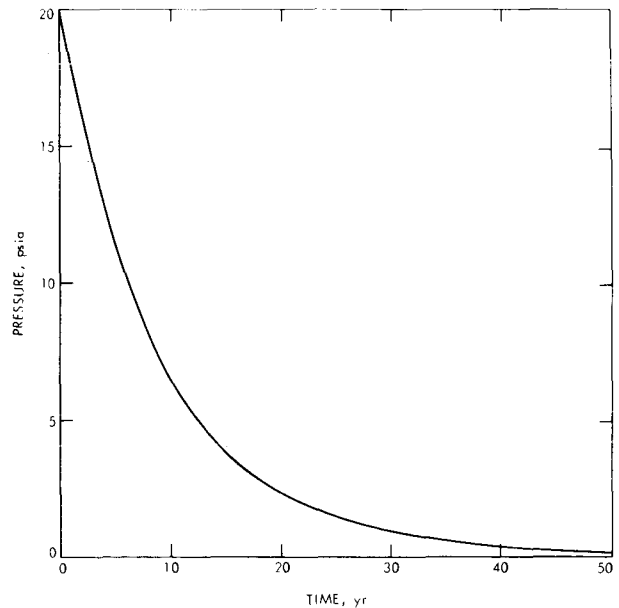


Fig. 5. Molecular regime leak rate

gas pressurization of the actuator allows it to be lubricated by conventional lubricant and also protects the brushes and bearings.

IV. TESTING AND PERFORMANCE

All components of the actuator are chosen so that they are capable of withstanding temperatures of 450° F, with the exception of the arc suppression capacitors, which will withstand only 400° F. Accordingly, the actuator is readily heat sterilizable. The actuator high-temperature test requirement is 315° F.

The axial arrangement of the brushes with respect to the commutator simplifies assembly, as the brushes can be installed from the front. Even with brush commutation, it is expected that the useful operating life of the device will be more than 50,000 hours.

The electrical efficiency of the actuator is shown in Fig. 6, and the load speed performance is shown in Fig. 3.

The actuator was life-tested by having it drive a 30-lb load at 90 percent of full amplitude through 120,000 cycles (equivalent to 100,000 hours of operation). The brush wear after the life test was 0.015 in., about 6 percent of the brush's active length. No measurable degradation was observed in any other parts of the actuator.

The actuator has been successfully qualified by environmental testing, which consisted of subjecting the actuator to temperature-vacuum and vibration tests. The actuator was heat-cycled 12 times, during a 2-week period, in a vacuum (10^{-6} torr) environment from +167° F to +315° F after being cooled to -22° F for 24

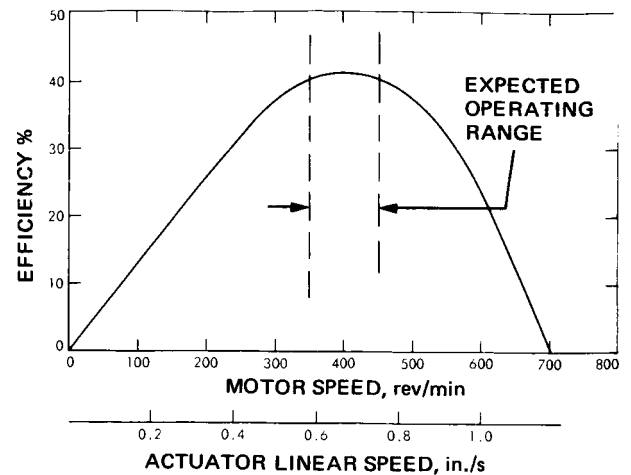


Fig. 6. Gimbal actuator electrical efficiency

hours. Vibration testing, at levels of 9 g, was conducted using both random noise and a sine sweep from 0 to 2000 Hz. The actuator was in operation during the vibration test, with good performance; no resonant disturbances were observed.

In Table 1, the performance of the JPL actuator described above is compared with the performance of other actuators designed for similar functions.

V. CONCLUSION

A simple, compact, lightweight, low-cost actuator, with an operating life expectancy of more than 50,000 hours has been described. The actuator has no gears and performs its mechanical function by transforming the rotary motion of its drive motor to linear motion through the action of a recirculating ball lead screw assembly. The actuator has been successfully qualified by environmental testing.

Table 1. Actuator performance comparison

Parameter	JPL gimbal actuator	Other typical actuators
Time constant (s)	0.015	0.050-0.150
Stall force (lb)	285	40-60
Stall current (A)	1.5	1.75-5.0
Voltage (V dc)	0-30	0-32
Weight (lb)	2.75	2-3.7

ACKNOWLEDGMENTS

John I. Tami assisted on the detail design of the actuator, directed the preparation of the drawings, and performed the production engineering required for fabrication. Ralph G. Hugo assembled and tested the actuators in the JPL actuator laboratory. Francesco Roselli-Lorenzini performed the molecular regime leak rate analysis, the results of which are shown in Fig. 5. Edward H. Kopf, Jr., designed the Mariner Mars 1971 autopilot servo system, from which the design requirements for the actuator were derived.

Actuator components were designed and manufactured by the following companies: Walter Kidde & Co., Belleville, N. Y., recirculating lead screw assembly; Curry Engineering Co., North Hollywood, Calif., actuator motor; G. L. Collins Corp., Long Beach, Calif., linear motion transducer; New Hampshire Ball Bearing Co., Peterborough, N. H., ball bearings.

DISCUSSION

Member of the audience:

Do you have any figures on the backlash that you experienced in this system or is it important to you?

Perkins:

It is important. We have the specification of less than 0.004 in. backlash in the actuators, including its mounting provision. This includes the buildup in the gimbal in the back and the gimbal, the rod end bearing in the front, the recirculating ball lead screw and the mechanism inside. Typical measurements have been on the order of 0.002 in. The recirculating ball lead screw must be designed with some free play in it, more than 0.001 in. and preferably less than 0.004 in., which would exceed our backlash. Another factor on the ball lead screw that I neglected to mention is that its operating contact angle is between 35 deg and 45 deg.

The backlash is important and is controllable, and the main control on the backlash is the external hardware to the actuator, which are the mounting provisions.

Member of the audience:

Could you comment on the selection of the brush dc motor as against the brushless? On the brushes you selected, could you comment on the compositions?

Perkins:

Yes. The brush dc motor was selected for simplicity and it

was evaluated as having a sufficiently long life. The brushes selected are a hard standard brushed-carbon alloy working against a copper commutator. I mention in my paper 50,000 hours continuous operation. One actuator, serial number one, the first one built, was tested at an equivalent of 100,000 hours of satellite operation, with about 6-percent brush wear. The brushes are 1/8-in. in diameter, 1/8-in. square, and 0.2 in. long.

Member of the audience:

How long did the 120,000 cycles driving a 30-lb load take?

Perkins:

We ran it over the Fourth-of-July weekend continuously, turning it over now and then in that load fixture to get the load and traction.

Member of the audience:

Of course, my curiosity in this is that I understand that carbon brushes dry out and show some wear characteristics, and in a time frame you couldn't drive a brush adequately to show this effect.

Perkins:

No, you see, the brushes are in a sealed actuator. We haven't had a brush problem.

I have with me one of the motors and one of the research ball links that you may see here if anyone is interested.

**ORGANIZATIONS REPRESENTED
AT THE FIFTH AEROSPACE MECHANISMS SYMPOSIUM**

Abrams Instrument Corporation	LTV Aerospace Corporation
Academy of Sciences—U.S.S.R.	Martin-Marietta Corporation
Aeroflex Laboratories, Inc.	Massachusetts Institute of Technology
Aerospace Corporation	McDonnell Douglas Astronautics Company
American Science & Engineering, Inc.	NASA—Ames Research Center
AMETEK	NASA—Goddard Space Flight Center
Arthur D. Little, Inc.	NASA—Headquarters
Avco Systems Division	NASA—Langley Research Center
<i>Aviation Week & Space Technology</i>	NASA—Manned Spacecraft Center
Ball Brothers Research Corporation	National Academy of Sciences
Beckman Instruments, Inc.	North American Rockwell Corporation
Bellcomm, Inc.	Penton Publishing
Bell Telephone Laboratories, Inc.	Pratt & Whitney Corporation
The Boeing Company	Quantic Industries, Inc.
British Aircraft Corporation	RCA Corporation
British Embassy	Sandia Laboratories
British Information Service	Santa Barbara Research Center
Computer Sciences Corporation	Society for Space Research (GFW)—West Germany
COMSAT Laboratories	Spar Aerospace Products, Ltd.
Cornell University	Sperry Rand Corporation
E. I. du Pont de Nemours & Company	TRW Systems Group
ESSA—National Environmental Satellite Center	Union Junior College
European Space Research Organization (ESTEC)—Holland	United States Air Force Armament Laboratory
Fairchild Hiller Corporation	United States Air Force Flight Dynamics Laboratory
Foreign Service Institute—Department of State	United States Naval Weapons Center
The Garrett Corporation	United States Naval Air Systems Command
General Electric Company	United States Naval Research Laboratory
Grumman Aerospace Corporation	United States Naval Weapons Laboratory
Helitarics	University of California, Berkeley
Hughes Aircraft Company	University of Maryland
Hughes Research Laboratories	University of Massachusetts
ILC Industries, Inc.	University of Santa Clara
Institute For Defense Analyses	U.S.S.R. Embassy
Jet Propulsion Laboratory	Washington Technological Associates, Inc.
The Johns Hopkins University	Westinghouse Electric Corporation
Library of Congress	Wright Components, Inc.
Lockheed Missiles & Space Company	

LIST OF ATTENDEES

- BARCLAY, RALPH G.**
 NASA-Goddard Space Flight Center
- BACHER, JOEL**
 RCA Corporation
 Astro Electronics Division
- BACHMAN, WILLIAM E.**
 Jet Propulsion Laboratory
- BEAL, ROBERT**
 U.S. Naval Research Laboratory
- BEAUMONT, JOHN B.**
 Avco Systems Division
- BELTRACCHI, LEO**
 Avco Systems Division
- BENSON, HAROLD E.**
 NASA-Manned Space Center
- BENTON, WILLIAM G.**
 General Electric Company
 Space Systems Division
- BERKO, LAWRENCE**
 RCA Corporation
 Astro Electronics Division
- BERRY, THOMAS G.**
 Fairchild Hiller Corporation
 Space and Electronics Systems Division
- BLANCHARD, DAVID L.**
 NASA-Goddard Space Flight Center
- BLOOM, KENNETH A.**
 North American Rockwell Corporation
 Space Division
- BOHLING, RAYMOND F.**
 NASA Headquarters
- BOLD, DAVID R.**
 Massachusetts Institute of Technology
 Lincoln Laboratory
- BOMKE, PAWL W.**
 Jet Propulsion Laboratory
- BOSTAIN, JAMES C.**
 Foreign Service Institute-Department
 of State
- BRADY, GEORGE W.**
 Institute for Defense Analyses
- BROWN, DAVID A.**
 Aviation Week and Space Technology
- BROWNE, WILLIAM H., JR.**
 NASA-Goddard Space Flight Center
- BURDICK, HARRY F.**
 NASA-Goddard Space Flight Center
- BURNHAM, HARTLEY M.**
 Avco Systems Division
- BURNS, GEORGE G. C.**
 McDonnell Douglas Astronautics
 Company
- BURRITT, DOUGLAS A.**
 NASA-Goddard Space Flight Center
- BUSH, KENNETH S.**
 NASA-Langley Research Center
- CAMPBELL, CHARLES E.**
 NASA-Goddard Space Flight Center
- CAMPBELL, GEORGE E.**
 North American Rockwell Corporation
 Space Division
- CAMPBELL, NORMA E.**
 North American Rockwell Corporation
- CAMPBELL, ROBERT J.**
 Avco Systems Division
- CARLSON, RONALD C.**
 TRW Systems Group
- CEPOLLINA, FRANK J.**
 NASA-Goddard Space Flight Center
- CHEN, JAY C.**
 Jet Propulsion Laboratory
- CHOBOTOV, VLADIMIR**
 Aerospace Corporation
- CHRISTY, R. I.**
 Hughes Aircraft Company
 Aerospace Group
- COKONIS, T. JAMES**
 General Electric Company
 Space Systems Division
- COMUNTZIS, MARCUS G.**
 Jet Propulsion Laboratory
- COOK, PETER L.**
 ESSA-National Environmental
 Satellite Center
- CROSSLEY, F. R. ERSKINE**
 University of Massachusetts
 Department of Mechanical and Aero-
 space Engineering
- CROUT, PRESCOTT D.**
 Massachusetts Institute of Technology
- CUNNINGHAM, A. C.**
 Hughes Aircraft Company
 Aerospace Group
- DAVIS, ROGER M.**
 Avco Systems Division
- DAWSON, FREDERICK W.**
 Martin-Marietta Corporation
- DAY, WALTER**
 Abrams Instrument Corp.
- DECKER, JAMES M.**
 The Garrett Corporation
 Airsupply Company Division
- de KRAMER, CORNELIS**
 NASA-Goddard Space Flight Center
- DEMAS, NICHOLAS L.**
 United States Naval Ordnance
 Laboratory (WO)
- DEVINE, EDWARD J.**
 NASA-Goddard Space Flight Center
- DEZIO, JOSEPH A.**
 NASA-Goddard Space Flight Center
- DRENKER, GEORGE**
 General Electric Company
 Space Systems Division
- EDSTROM, ANDREW H.**
 Quantic Industries, Inc.
- ELLIS, BERNARD**
 Lockheed Missiles & Space Company
- ENG, TON L.**
 NASA-Goddard Space Flight Center
- EVERSON, CLAUDE T.**
 Lockheed Missiles & Space Company
- FEDERLINE, M. FRANCIS**
 NASA-Goddard Space Flight Center
- FEDERLINE, ROBERT E.**
 NASA-Goddard Space Flight Center
- FEDOR, JOSEPH V.**
 NASA-Goddard Space Flight Center
- FLAVIN, STUART V.**
 Wright Components, Inc.
- FOUNTAIN, GLENN H.**
 The Johns Hopkins University
 Applied Physics Laboratory
- FORD, JOHN P.**
 Sandia Laboratories
- FRISCH, JOSEPH**
 University of California, Berkeley
 Division of Mechanical Design
- FUECHSEL, PETER G.**
 The Johns Hopkins University
 Applied Physics Laboratory
- GALBRAITH, A. D.**
 Lockheed Missiles & Space Company
- GERSON, HAROLD I.**
 COMSAT Laboratories
- GILLESPIE, VERNON P.**
 NASA-Langley Research Center
- GLUCKMAN, I. B.**
 Lockheed Missiles & Space Company
- GOLDER, DAVID G.**
 Massachusetts Institute of Technology
 Lincoln Laboratory

LIST OF ATTENDEES (contd)

- GOODWIN, FRANK A.
 Jet Propulsion Laboratory
- GORDON, GARY D.
 COMSAT Laboratories
- GOTTESMAN, TOBIAS A.
 Computer Sciences Corporation
- GRASSOT, F. R.
 COMSAT Laboratories
- GREBENSTEIN, E. B.
 Fairchild Hiller Corporation
 Space and Electronic Systems Division
- GRIFFITH, WAYLAND C.
 Lockheed Missiles & Space Company
- GROSCHOPFS, E.
 Spar Aerospace Products, Ltd.
- GROSS, FRED
 RCA Corporation
 Astro Electronics Division
- GUDIKUNST, JAMES B.
 General Electric Corporation
 Space Systems Division
- GUERSTER, RENE
 AMETEK
 Hunter Spring Division
- GUSS, HOPE H.
 NASA-Goddard Space Flight Center
- HAGERMAN, RUSSELL H.
 Grumman Aerospace Corporation
- HALL, JAMES F., JR.
 General Electric Company
 Re-entry & Environmental Systems
 Division
- HANLEIN, STUART L.
 NASA-Goddard Space Flight Center
- HAUSHALTER, CARL H.
 McDonnell-Douglas Astronautics
 Company
- HAYLECK, CHARLES R., JR.
 University of Maryland
 Department of Mechanical Engineering
- HAYNIE, H. THERON
 The Boeing Company
 Aerospace Systems Division
- HEARTH, DONALD P.
 NASA-Goddard Space Flight Center
- HEPP, A. M.
 AMETEK-Hunter Spring Division
- HERZL, GEORGE G.
 Lockheed Missiles & Space Company
- HIGHMAN, CLIFTON O.
 Ball Brothers Research Corporation
- HOEKSTRA, THOMAS B.
 Bellcomm, Inc.
- HOWEY, CHARLES K.
 Aerospace Corporation
- HUSON, GEORGE
 COMSAT Laboratories
- JABBOUR, KAHTAN N.
 NASA-Goddard Space Flight Center
- JONES, CALVIN L.
 ESSA-National Environmental
 Satellite Center
- JONES, J. LLOYD
 NASA-Ames Research Center
 Aeronautics Division
- KEYSER, WILLIAM R., JR.
 Sperry Rand Corporation
 Marine Systems Division
- KIERSARSKY, ALBERT
 Bellcomm, Inc.
- KOBUSCH, HOWARD J.
 Pratt & Whitney Aircraft
 Florida Division
 Florida Research and Development
 Center
- KRAMER, N. R.
 General Electric Company
 Space Systems Division
- KROPFELD, JOSEPH J.
 Bell Telephone Laboratories, Inc.
- KUHN, JACKSON G.
 Santa Barbara Research Center
- KULP, BERNARD A.
 United States Air Force Armament
 Laboratory (Eglin AFB)
- KUMMETH, LAWRENCE
 United States Air Force Flight
 Dynamics Laboratory (WPAFB)
- KURZHALS, PETER R.
 NASA-Langley Research Center
- LEARY, ROBERT J.
 United States Naval Ordnance
 Laboratory (WO)
- LEITER, L. D.
 AMETEK
 Hunter Spring Division
- LEONE, PETER
 NASA-Goddard Space Flight Center
- LEWIS, JOHN H.
 Aeroflex Laboratories, Inc.
- LIGHT, EARL T.
 Grumman Aerospace Corporation
 OAO Support Group
- LILLY, JAMES L.
 General Electric Company
 Space Systems Division
- LINDBERG, FRANK A.
 Westinghouse Electric Corporation
 Aerospace and Electronics Division
- LOGAN, WILLIAM S.
 NASA-Goddard Space Flight Center
- LUCIER, ERNEST R.
 Computer Sciences Corporation
- MCCARTHY, DENNIS K.
 NASA-Goddard Space Flight Center
- McCLAVE, KENNETH A.
 The Garrett Corporation
 Airsupply Company Division
- McCULLOUGH, JOHN E.
 Arthur D. Little, Inc.
- McGREEN, THOMAS C.
 United States Naval Ordnance
 Laboratory (WO)
- McLARIN, MAITLAND
 Union Junior College (N.J.)
- McLEAN, HOWARD J.
 Pratt & Whitney Aircraft
 Florida Division
- MacLAREN, ARTHUR P.
 British Embassy
- MacVEIGH, GEORGE E.
 NASA-Goddard Space Flight Center
- MANNHEIMER, HARRY
 NASA Headquarters
- MARTIN, ERNESTO R.
 COMSAT Laboratories
- MARTIN, FRANK T.
 NASA-Goddard Space Flight Center
- MATILAINE, JOHN
 Cornell University
- MATOS, DOMINICK
 Grumman Aerospace Corporation
 OAO Support Group
- MATTEY, ROBERT A.
 The Johns Hopkins University
 Applied Physics Laboratory
- MATTINGLY, ROBERT D.
 NASA-Goddard Space Flight Center
- MAYER, NORMAN J.
 NASA Headquarters
- MAYER, R. W.
 Ball Brothers Research Corporation
- MEEKS, C. R.
 Hughes Aircraft Company
 Space Systems Division
- MELROSE, DAVID
 RCA Corporation
 Astro Electronics Division
- MENTZELL, J. C.
 Westinghouse Electric Corporation
 Aerospace and Electronics Division
- MILLER, DONALD L.
 NASA-Goddard Space Flight Center
- MONTGOMERY, HARRY E.
 NASA-Goddard Space Flight Center
- MORAN, ALBERTA C.
 NASA-Goddard Space Flight Center
- MORSE, FREDERICK H.
 University of Maryland
 Department of Mechanical Engineering
- MOYER, X. WILLIAM
 NASA-Goddard Space Flight Center
- MUNDY, EDWARD C., JR.
 NASA-Goddard Space Flight Center
- MYERS, DAVID
 American Science & Engineering, Inc.

LIST OF ATTENDEES (contd)

- NEMECEK, JOSEPH J.
United States Naval Research
Laboratory
- NEWKIRK, HORACE L.
United States Naval Weapons Center
(China Lake)
- NOLL, CARROLL G.
Washington Technological Associates,
Inc.
- NORTON, DORIS M.
NASA-Goddard Space Flight Center
- O'BRIEN, JOHN J.
NASA-Goddard Space Flight Center
- OFODILE, E. I.
E. I. du Pont de Nemours & Company
Textile Fibers Dept.
- OKHOTSIMSKY, D. E.
Academy of Sciences-U.S.S.R.
Institute for Applied Mathematics
- OLSON, LARRY J.
Penton Publishing Company
- PADDACK, STEPHEN J.
NASA-Goddard Space Flight Center
- PAPICH, RAYMOND
Aerospace Corporation
- PARADISE, JOHN J.
Lockheed Missiles & Space Company
- PARKS, MICHAEL J.
British Aircraft Corporation
GW Division
- PAUL, WALTER S.
Helitarics
- PEACOCK, WILLIAM M.
NASA-Goddard Space Flight Center
- PEFLEY, RICHARD K.
University of Santa Clara
Mechanical Engineering Department
- PENTLICKI, C. J.
COMSAT Laboratories
- PERKINS, GERALD S.
Jet Propulsion Laboratory
- PERRIN, B. J.
Ball Brothers Research Corporation
- PHILLIPS, Baxter M.
The Johns Hopkins University
Applied Physics Laboratory
- PHILLIPS, KEVIN J.
RCA Corporation
Astro Electronics Division
- PLATONOV, A. K.
Academy of Sciences-U.S.S.R.
Institute for Applied Mathematics
- PLOUGH, JAMES A.
Aerospace Corporation
- PLUSH, PETER
RCA Corporation
Missile and Surface Radar Division
- PODOSKI, JOSEPH J.
Library of Congress (Ret.)
- PRICE, JACK E.
The Boeing Company
- RATERMANIS, JOHN O.
ILC Industries, Inc.
- RAY, GEORGE, III
Washington Technological Associates,
Inc.
- REDLIN, MICHAEL
Cornell University
- REW, J. A.
Westinghouse Electric Corporation
Aerospace and Electronics Division
- RICE, RICHARD W.
NASA-Goddard Space Flight Center
- RICHARDSON, CHARLES H.
Sperry Rand Corporation
Support Facility-GSFC
- RINALDO, ALFRED L.
Lockheed Missiles & Space Company
- ROBINSON, JOHN E.
NASA-Goddard Space Flight Center
- ROSCHKE, MELVIN G.
NASA Headquarters
- ROWLEY, REGINALD C.
United States Naval Air Systems
Command
- RYDER, E. R.
Aerospace Corporation
- RUDERMAN, MYRON
Aeroflex Laboratories, Inc.
- SABELMAN, ERIC E.
Jet Propulsion Laboratory
- SAJHIN, ALEX I.
U.S.S.R. Embassy
- SAMBUROFF, SERGE N.
The Johns Hopkins University
Applied Physics Laboratory
- SCAGNELLI, H. J.
Bell Telephone Laboratories, Inc.
- SCHER, MARK P.
TRW Systems Group
- SCHILLING, KEITH L.
RCA Corporation
Astro Electronics Division
- SCHUERMANNS, HORST
Society for Space Research (GFW)-
W. Germany
- SEN, ASIM K.
National Academy of Science
- SIMMONS, DELFORD E.
United States Naval Research
Laboratory
- SIMPSON, WILLIAM E.
Grumman Aerospace Corporation
- SINCLAIR, JOHN D.
The Boeing Company
- SMITH, GILBERT R.
ESSA-National Environmental
Satellite Center
- SMITH, WILLIAM G.
Aerospace Corporation
- SOTHERLUND, ARTHUR W.
LTV Aerospace Corporation
Missiles & Space Division
- SOUKHANOV, IVAN M.
Library of Congress
Fed. Research Division
- SPEIGHT, KEVIN M.
General Electric Company
Space Systems Division
- SPENCER, THOMAS M.
Ball Brothers Research Corporation
- STANHOUSE, R. W.
General Electric Company
Space Systems Division
- STEIMLE, HAUSULRICH
Society for Space Research (GFW)-
W. Germany
- STEPHENSON, BERTRAND H.
NASA-Goddard Space Flight Center
- STEURI, ROBERT E.
Hughes Research Laboratories
- STOCKWELL, B.
European Space Research Organization
- STRAKOSCH, JOHN
Grumman Aerospace Corporation
- STUDER, PHILIP A.
NASA-Goddard Space Flight Center
- SUDEY, JOHN, JR.
NASA-Goddard Space Flight Center
- SULLIVAN, CORNELIUS M.
Massachusetts Institute of Technology
Lincoln Laboratory
- SULLIVAN, J. J.
Lockheed Missiles & Space Company
- SWEET, VICTOR T.
General Electric Company
Space Systems Division
- SYROMYATNIKOV, V. S.
Academy of Sciences-U.S.S.R.
Institute for Machine Technology
- TALCOTT, JAMES M.
Fairchild Hiller Corporation
Space and Electronics Systems Division
- TANNER, ROBERT L.
NASA-Goddard Space Flight Center
- THOMAS, EDWARD M.
Grumman Aerospace Corporation
OAO Project
- THORSTED, KENNETH G.
United States Naval Weapons
Laboratory (Dahlgren)
- TOSSMAN, BARRY E.
The Johns Hopkins University
Applied Physics Laboratory
- TRAVIS, ELMER W.
NASA-Goddard Space Flight Center

LIST OF ATTENDEES (contd)

VAN ELKAN, HARRY RCA Corporation Astro Electronics Division	WATSON, ROBERT J. Lockheed Missiles & Space Company	WILLIAMS, GEORGE A. United States Naval Weapons Laboratory (Dahlgren)
VEST, CHARLES E. NASA-Goddard Space Flight Center	WEIDLER, D. E. TRW Systems Group	WINSTON, DONALD C. Aviation Week and Space Technology
WALLIS, DAVID C. B.I.S.	WEILBACH, AUGUST Beckman Instruments, Inc.	WITKIEWICZ, KASMIR W. NASA-Goddard Space Flight Center
WALTHALL, J.L., JR. United States Naval Ordnance Laboratory (WO)	WEISSENBERGER, STEIN University of Santa Clara Mechanical Engineering Department	WRIGHT, W. A. Wright Components, Inc.
WARD, BOWDEN W., JR. NASA-Goddard Space Flight Center	WELLS, ALAN Spar Aerospace Products, Ltd.	YEZHOV, YURI V. U.S.S.R. Embassy
	WEYMAN, H. N. Spar Aerospace Products, Ltd.	

PRIOR SYMPOSIA IN THIS SERIES

First Aerospace Mechanisms Symposium

May 19-20, 1966

University of Santa Clara

Santa Clara, California

Proceedings, AD 638 916, are available from:

The Clearinghouse for Federal Scientific and Technical Information

Department of Commerce

Washington, D.C.

Second Aerospace Mechanisms Symposium

May 4-5, 1967

University of Santa Clara

Santa Clara, California

Proceedings, TM 33-355, are available from:

Jet Propulsion Laboratory

California Institute of Technology

Pasadena, California

Third Aerospace Mechanisms Symposium

May 23-24, 1968

Jet Propulsion Laboratory

Pasadena, California

Proceedings, TM 33-382, are available from:

Jet Propulsion Laboratory

California Institute of Technology

Pasadena, California

Fourth Aerospace Mechanisms Symposium

May 22-23, 1969

University of Santa Clara

Santa Clara, California

Proceedings, TM 33-425, are available from:

Jet Propulsion Laboratory

California Institute of Technology

Pasadena, California